THE UNIVERSITY OF HULL

A Matrix Isolation Study of Main Group and Transition Metal Atom Cryochemistry

being a Thesis submitted for the Degree of Doctor of Philosophy
in the University of Hull

by

Neil Harris, BSc

March 2001

Abstract

The majority of the work described in this thesis is concerned with the isolation of transition metal and main group atoms in dilute reactive ligand matrices. The previously uncharacterised matrix isolated species were characterised using IR, UV-Vis-NIR and XAFS spectroscopic techniques. Various metal atom sources were investigated for the production and subsequent isolation of atomic species in both inert and reactive ligand matrices.

Some 4d and 5d transition metals atoms were produced from a hollow cathode sputtering source (laser ablation was also employed as an atom source in some of the work) and isolated in argon matrices. The isolation of both platinum and palladium atoms in chlorine containing argon matrices has been shown to result in the formation of linear $PtCl_2$ and $PdCl_2$ molecules. The isolation of gold atoms has led to the formation of a monomeric chloride, suspected to be either $AuCl_3$ or $AuCl_2$. The structure of the silver chloride remains undetermined. The *pseudo*-gas phase structure of these monomeric species is presented for the first time.

In addition to this work tellurium atoms have been generated from the photodecomposition of matrix isolated H_2Te. The use of CO containing matrices has led to the isolation and characterisation of carbonyl telluride, OCTe, the structure and composition of which (either in the solid or gas phase) is presented for the first time.

In complementary work, an investigation into carbonyl complexes formed on isolation of some 3d transition metal bromides in dilute carbon monoxide / argon matrices is also presented, together with their photochemistry in neat CO matrices.

Acknowledgements

Many people have contributed to the work presented in this thesis and its preparation, but the biggest debt of gratitude is owed to my supervisor, Dr Nigel Young, for his continued help, guidance and training throughout the past 3 years of study. I would also like to thank EPSRC for funding the project.

The assistance and opinions of Dr Owen Wilkin are also greatly appreciated; I particularly enjoyed the swearing. Further thanks to the members of the inorganic department past and present, especially the contribution from Ian Blackmoore during the course of his masters degree.

Thanks to the station managers Fred Mosselmans, Mark Surman and Bob Billsborrow at Daresbury stations 9.2, 16.5 and 13.3 for their assistance, availability and interest.

Many thanks to the technical staff at Hull University, in particular to Paul Monk for his assistance in the laser ablation work. The chemistry department mechanical workshops, electricians and glassblowers are also thanked for their patience and help.

On a personal note this thesis could not have been completed without the constant support of my family and friends. In particular to my parents for their help and support throughout my years at university and to Claire, for being there.

Contents

Chapter

1

Introduction

Section 1.1: **Matrix Isolation**

Introduction

The matrix isolation technique was first proposed in 1954 simultaneously by I. Norman and G. Porter[1] and E. Whittle, D. A. Dows and G. C. Pimentel[2] as a method for trapping highly reactive chemical species for further study. The majority of the pioneering work is credited to Pimentel, with the first clear definition of conditions and requirements for isolation of molecules in nitrogen or noble gas matrices being proposed by Becker and Pimentel in 1956.[3]

Matrix isolation experiments involve the preparation of a rigid lattice that acts as a host for preserving and immobilising the molecular species of interest indefinitely, when they would normally only be present as short lived species in high temperature vapours and discharges. The nature of the matrix isolation experiment, that of high dilution and low temperature, prevents these unstable species from undergoing unimolecular decomposition or bimolecular collisions that may occur under normal conditions. This allows it to be used to study weakly bound molecular species, usually formed by rapid quenching with an excess of the matrix gas, or species prepared *in-situ*, which are often photochemically generated from isolated precursors.

The matrix cage extends the lifetime of the trapped species indefinitely allowing spectroscopic detection and characterisation to be completed at relative leisure. This allows the conventional techniques such as IR, UV-Vis, ESR, Raman and Mössbauer spectroscopy to be used for characterisation.

Matrix isolation experiments are generally based around four main areas of interest:

1) Fundamental Spectroscopy: matrix isolation techniques provide important data to assist in the detailed understanding of geometric and electronic structure, particularly in free radicals, high temperature molecules and molecular ions.

2) Matrix Perturbations: the interaction between host and trapped species can be examined by matrix isolation studies, essentially treating the isolated species as probes to gain information on the matrix environment.

3) Chemistry in Matrices: trapping products of a reaction in matrices.

4) Interstellar Chemistry: in the study of diffuse interstellar bands.

Matrix Materials

a) General Requirements of a Matrix Material

To be used as a matrix, a substance requires several properties without which it will be unsuccessful as a support for trapped species.

1) Purity: an impure matrix will provide non-reproducible spectra.

2) Vibrational Spectrum: as well as having no absorption bands in the same region as the species of interest, the use of matrices that appear clear or opaque in the visible region should reduce the amount of scatter in the infrared region.

3) Inertness: in most cases a matrix is used that does not react with the isolated species, therefore the type of matrix that is used will depend on the type of experiment and species to be isolated. Often a matrix gas is used that will give rise to chemistry under certain conditions, a good example of this is nitrogen which is a very common matrix gas but is relatively reactive when compared to a noble gas (for example, the use of nitrogen as both the matrix gas and the reactive gas in the

formation of the metal nitrides of yttrium and lanthanum[4]). No matrix will be completely unreactive however, since even noble gases alter the energy levels of the trapped species and therefore affect the vibrational frequencies.

4) Rigidity: rigidity is a very important property since lack of rigidity of a matrix gas can cause diffusion of the trapped species and lead to aggregation which defeats the whole purpose of the isolation experiment. The rigidity of the matrix gas governs the temperature at which the deposition surface must be held for a suitable matrix to form, this is the diffusion temperature (T_d), that is the temperature at which the solidified gas will begin to diffuse. The rigidity of the matrix gas is highly temperature dependent and often the melting point is a good guide as to the rigidity of the material as a matrix.

5) Volatility: the matrix material needs to have a sufficiently high vapour pressure (V.P.) at room temperature to be handled in a vacuum line and a low enough vapour pressure at the temperature of refrigeration to avoid loss of the matrix material.

6) Latent Heat of Fusion (L_f): for the matrix gas (@ ~295K) to condense on the deposition surface (@ ~10K) heat must be removed from the sample area. This energy is the latent heat of fusion (L_f) and is essentially the energy required to form a lattice at 0 K. This also relates to the energy required for a molecule to diffuse from within the lattice.

7) Thermal Conductivity: the L_f that is released on condensation must be absorbed by the support surface for the matrix to form. As deposition continues the layer of gas thickens and must act as a conductor for the heat being supplied by the continually condensing gas. If the conductivity of the gas is poor then local heating may occur which would result in a poor matrix and increased scatter. this may also

promote localised diffusion of the isolated species, leading to monomer loss and multimer formation. This is not always the case however, as in some instances local heating may actually improve the matrix as gentle annealing can remove lattice defects improving the quality of the matrix and reducing scatter. The thermal conductivity (γ) of the matrix therefore can control the rate of deposition, and hence the deposition time, since if the deposition rate is decreased then deposition time must be increased to achieve the same amount of deposition (assuming that the deposition of reactive species remains proportional to the rate of matrix deposition).

Although all these characteristics are important the main two properties of the material to be considered are its rigidity at the deposition temperature and its transparency in the desired spectral region. All the others vary from experiment to experiment.

Thermochemical data for some matrix materials is given in the table below.[5]

Gas	T_d (K)	m.p. (K)	b.p. (K)	v.p. of 10^{-3}mm at (K)	L_f (Jmole^{-1})	γ (20 K) (Wm^{-1} K^{-1})	γ (5 K) (Wm^{-1} K^{-1})
Ne	10	24.6	27.1	11	335	0.4	-
Ar	35	83.3	87.3	39	1190	1.3	2.0
Kr	50	115.8	119.8	54	1640	1.2	0.7
Xe	65	161.4	165.0	74	2295	2	-
CH_4	45	90.7	111.7	48	971	0.1	-
N_2	30	63.2	77.4	34	721	0.4	5.0

Table 1.1: thermochemical data for some matrix gases.

b) The Most Common Matrices

The noble gases are the most obvious choice as a matrix material since they are chemically inert and have no absorption bands in the infrared. Argon is the most commonly used since it forms good matrices and is relatively cheap.

Molecules such as ethylene and acetylene are used to form reactive matrices. The wide range of properties supplied by the gases nitrogen, oxygen, carbon dioxide, carbon monoxide, carbon disulphide, sulfur dioxide, sulfur hexafluoride, nitric oxide, hydrogen sulphide and chlorine when acting as matrices have been investigated as well as halocarbons.

c) Crystal Data

The spherical nature of noble gas atoms means that they adhere to the principle of close packing. Spherical atoms or molecules crystallise in a close packed structure to maximise intermolecular Van der Waals forces by achieving the maximum number of nearest neighbours. There are two simple ways that close packing can be achieved, both of which use the same volume (74%) of the total space. They are hexagonal close packing (h.c.p.) and cubic close packing (c.c.p.).

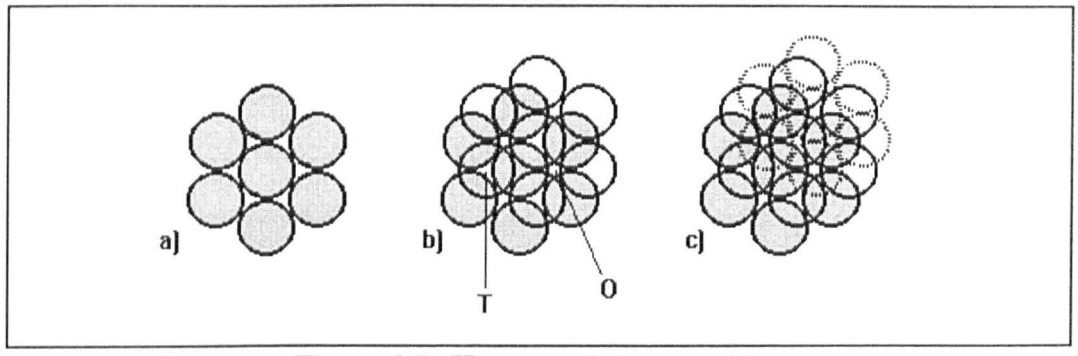

Figure 1.1: Hexagonal close packing.

Hexagonal close packing of spheres showing the build up of layers through a, b and c and the formation of tetrahedral (T) and octahedral (O) holes.

For cubic close packing the structure is built up in layers where the third layer is above the first, making the stacking order *abababab*.... With hexagonal close packing the third layer (c) is not above a or b, giving rise to the stacking order *abcabc*... shown in figure 1.1 above.

Close packed lattices have three types of guest sites. A substitutional site (the replacement of one of the lattice spheres with a trapped species) and two kinds of interstitial sites, an octahedral hole and a tetrahedral hole, shown as O and T on the diagram. The octahedral hole has six adjacent spheres and the tetrahedral hole has four adjacent spheres.

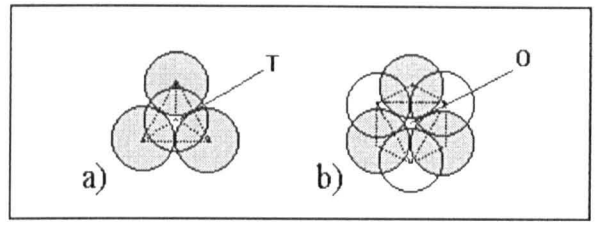

Figure 1.2: tetrahedral and octahedral holes

The trapping site is important as its geometry dictates the perturbations that the reactive species will experience.

It has been shown that all noble gas solids will form a face centred cubic (or cubic close packed) lattice except helium and on occasion argon, which sometimes assumes a hexagonal close packed structure, especially in the presence of impurities.[5]

The type of trapping site occupied is largely dependent on the type and size of the trapped species.[2] The following table shows the sizes of the various trapping sites for different noble gas matrices.[6]

Solid (4 K)	a_o^*	Substitutional Hole	Octahedral Hole	Tetrahedral Hole
Ne	4.46 Å	3.16 Å	1.31 Å	0.71 Å
Ar	5.31 Å	3.75 Å	1.56 Å	0.85 Å
Kr	5.64 Å	3.99 Å	1.65 Å	0.90 Å
Xe	6.13 Å	4.34 Å	1.80 Å	0.97 Å

*a_o - *lattice parameter (f.c.c. unit cell edge length).*

Table 1.2 trapping site sizes for the noble gasses.

d) Lattice Dislocations

The nature of matrix isolation experiments, that is the rapid condensation of gas to cryogenic temperatures, means that the crystal lattices formed are likely to be imperfect due to the presence of lattice dislocations. Lattice dislocations are imperfections in the crystal structure that provide additional trapping sites and give diffusion pathways in the solid state. The two simplest types of lattice dislocation are edge dislocations and screw dislocations.

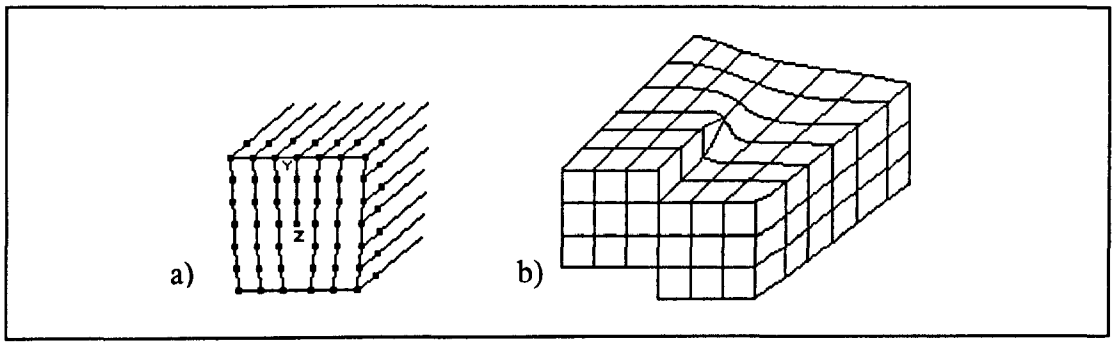

Figure 1.3: lattice dislocations.

a) a pure edge dislocation and b) a screw dislocation

An edge dislocation can be described as the insertion of an extra half plane of atoms (YZ on the diagram) into the lattice. Screw dislocations involve part of the lattice being displaced with respect to the other part.

e) Matrix Effects

As has already been briefly mentioned, even a noble gas matrix will affect the energy levels of a species trapped within the matrix. It is therefore important to establish the degree of perturbation that the matrix will cause to the vibrational frequencies, electron transition energies, g-values, hyperfine coupling constants and other information that can be elucidated from the experiment. The disturbances

caused by the matrix can interfere with the characterisation of unusual molecular species but they can also help to give information on intermolecular forces within the matrix. The effects which the matrix exerts on the species, which are often revealed through multiplet spectral features, are:

1) Vibrational Shift: the absorption bands of the species will normally undergo a red shift from the gas phase to the condensed phase value. It is the commonest and most easily identified matrix effect and has been observed for rotational, vibrational and electronic transitions. This is analogous to a solvent shift in solution and allows calculation from equations based around the solvent effect:

$$\Delta\nu = (\nu_{gas} - \nu_{solvent})$$

which can be used to derive an equation to be applied to matrices that takes into account the internal forces of the matrix. The intermolecular potential energy can be expressed as the sum of dispersive, inductive, electrostatic and repulsive contributions so that the matrix shift is given by:

$$\Delta\nu = \nu_{matrix} - \nu_{gas} = \Delta\nu_{dis} + \Delta\nu_{ind} + \Delta\nu_{elec} + \Delta\nu_{rep}$$

matrix shifts are generally around 1%, although they have been observed as up to 10%, of that of the gas phase data.

2) Matrix Site Effects: further complications can arise with a group of effects associated with the intimate properties of the matrix site enclosing the guest species. These effects may be due to:

a) different orientations of a guest within a matrix.

b) Multiple trapping sites: the isolated species may be trapped in two or more distinct sites. The effect of the species being isolated in different matrix cage environments will be a different vibrational shift for each different site occupied.

c) Occupation of cages which include guest as well as host molecules as nearest neighbours. This is known as an aggregation site effect and is usually very weak.

3) Rotation or Other Motion of the Trapped Species Within the Lattice: movement is rare at low temperature, although the lowest rotation energy levels can be occupied. Therefore, it is only the smallest of isolated species that can undergo rotation. For larger species isolated in the matrix, rotation is quenched.

4) Splitting of Degenerate Frequencies, or the Appearance of an 'Infrared Inactive' Band: the matrix may perturb the trapped species sufficiently to lift the degeneracy of two levels, or to induce Infrared inactive bands. The low temperature and the isolation of monomer often causes near degenerate bands to be resolved.

5) External and Lattice Vibrations: due to the presence of an impurity.

Advantages of Matrix Isolation

The matrix isolation technique has several advantages over high temperature spectroscopic techniques:

1) It simplifies the problems associated with containment of high temperature molecular vapours.

2) Spectra can be obtained for species with vapour pressures of around 10^{-4} to 10^{-5} atm below 2800 K, requiring only around 10^{-5} to 10^{-7} mol of material, that can be deposited in haste or at leisure.

3) The absence of rotational structure simplifies and sharpens the spectral features of the observed vibrational and electronic spectra. A consequence of this is that when isotopic data is available bond angles can be calculated from IR data.

4) Interpretation is simplified since transitions all occur from the spectroscopic ground state due to the matrix environment (with the exception of molecules which are small enough to undergo rotation).

4) In mixed vapour species the experimental conditions can be varied so that the bands which originate from the same species can be determined by comparison.

Conversely there are also some difficulties associated with the technique:

1) The lack of rotational data prevents the determination of interatomic distances from the moments of inertia and the lack of band contour shapes also means that they cannot be used to help assign frequencies to specific vibrational modes.

2) When isotopic data is not available, the vibrational assignments must be based solely on an assumed model.

3) Matrix splitting may cause single frequencies to appear as a multiplet, although isotopic substitution and the use of different matrices helps to remove this problem.

4) Matrix shifts have a slight effect on thermodynamic calculations of vapour phase behaviour due to their difference from true gas phase data.

Section 1.2: **Generation of Reactive Species**

Introduction

The generation of the reactive species that are to be isolated in the matrix and studied can be achieved in a number of different ways. The generation method chosen is usually determined by the nature of the chemical species that is to be isolated. Pimentel proposed the use of the Knudsen cell in 1960[7] which was first used successfully in an experiment by Linevsky in 1961.[8] Since then a number of other techniques have been successfully applied to the generation of highly reactive species. The following is a list of some of the methods that have been used to generate molecular and atomic species for spectroscopic examination in matrix isolation experiments.

a) Direct Vaporisation

Metal atoms and molecular compounds can be produced by the direct heating of a bulk metal, such as a ribbon, rod or filament by applying a low-voltage and high current. This method has difficulty with metals such as manganese and chromium which cannot be machined into filaments and with gold, silver and copper due to their high conductivities. In the case of Au, Ag and Cu the problem is usually solved by mounting them on a support filament, such as molybdenum, tantalum or tungsten.

b) Induction Heating and pyrolysis

Knudsen cells can be heated indirectly by an external heating coil or *via* induction heating. A high power radio frequency field is produced to induce eddy

currents in the cell material. This then heats the cell as a result of dissipative processes within it.

This is generally used in the heating of impure materials, which act as precursors, to sublimation temperature in the Knudsen cell.

c) Sputtering

Atoms or molecules are 'sputtered' when a suitable target of the sample is ion bombarded. A hollow cathode sputtering source involves a low pressure inert gas discharge being used to 'sputter' metal atoms from inside the cathode. The atoms are then carried to the matrix by a continuing stream of inert gas.

d) Electron Bombardment

High energy electrons are thermionically produced from a hot tungsten filament and electrostatically accelerated towards the target material held in a water-cooled crucible. The electron beam is magnetically deflected and focused onto the target by a permanent magnet.

e) Laser Ablation

A laser beam is directed to a sample of target material which is thermally dissociated by the focused beam.

Sputtering

In these experiments a hollow cathode sputtering source was used to create the reactive species which could then be trapped in inert matrices. Metal atoms were generated by the method first described by Carstens, Kozlowski and Gruen in 1972,[9] although the sputtering theory was first used experimentally in conjunction with matrix isolation by Shirk and Bass.[10]

The technique involved a low pressure gas discharge being used to 'sputter' metal atoms from the surface of a metal cathode. The discharge was maintained between a hollow metal cylindrical cathode and a platinum anode. The metal atoms were then swept along with the matrix gas and isolated on the cold deposition surface in an inert gas matrix.

The addition of small concentrations of reactive gas to the inert gas allowed the generation of highly reactive novel transition metal species. UV/Vis, Infrared and EXAFS spectroscopies were then used to characterise the isolated species.

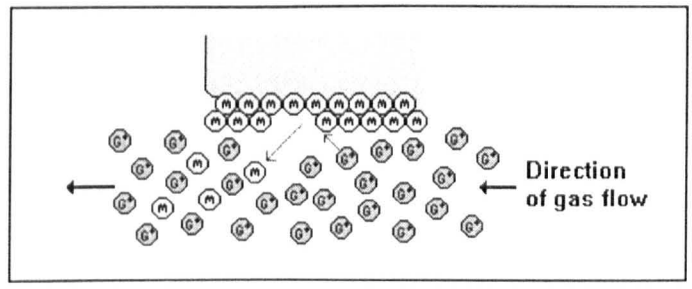

Figure 1.4: the sputtering process: a simplistic view.

metal atom *ionised gas atom or molecule.*

The dislocation of atoms from the metal surface was caused by bombardment of the cathode by ions. It has been shown that sputtered material leaves the cathode in all directions[11] and a large proportion, if not all, were shown by Von Hippel to be in an uncharged state.[12] The sputtering experiments described in this research use a

hollow cathode sputtering source similar to that proposed by Gruen and Bates for the isolation of metal atoms,[13] which has been described more recently and in greater detail by Beattie *et. al.*.[14] The hollow cathode technique involves the discharging gas being passed through the centre of the cathode material on a direct route to the deposition surface. This dislocates metal atoms from the cathode surface which are then swept along with the discharging gas to the cold deposition surface. At the deposition surface the discharging gas is quenched and solidifies, forming the matrix environment, trapping and isolating the atomic species contained within it. The hollow cathode device used is described in more detail in chapter 3.

Laser Ablation

Rare gas halide laser, or EXCIPLEX (Excited Complex) lasers as they are alternatively known, are based on a molecular reaction between rare gas (argon krypton or xenon) and halide (generally fluorine or chlorine) atoms. The EXCIPLEX molecules formed by the collision of excited state rare gas and halide species have a finite lifetime (around 10 ns). The decay of the EXCIPLEX emits a photon which for rare gas halides is in the ultra violet spectral region. The frequencies of light emitted by some EXCIPLEX lasers are given in the table below.[15]

EXCIPLEX	Frequency of Laser Light (nm)
ArF	193
KrF	248
XeCl	308
XeF	351

Table 1.3 : frequencies of EXCIPLEX lasers

The rare gas halide laser can only be generated by pulsed electron discharges due to the short lifetime of the EXCIPLEX species generated.

By focusing the laser output onto a sample, the energy of the beam can be used to heat the sample and generate atomic species. The heating of a sample with laser light is fundamentally different to conventional heating methods in that it is the sub-surface layers which become heated, causing fragmentation of the outer surface rather than straight forward thermolysis.

The heating is caused by the absorption of photons and depending on the optical and thermal properties of the target is thought to proceed by three possible mechanisms.[16] The heating can occur by either photolytic, pyrolytic or hydrodynamic sputtering processes. The photolytic process is caused by photon induced excitation of solid species such that they overcome the lattice energy. This is a more realistic mechanism for impurity removal and generally degassing a sample. The pyrolytic mechanism is the straightforward heating of the lattice, with hydrodynamic sputtering being the result of liquification of the lattice subsurface resulting in the internal expansion of the substrate causing explosive evaporation. Whichever mechanism results in the evaporation the intense nature of the laser evaporation results in thermally driven removal of material.

The intense and focused nature of the laser beam also results in minimal heating of the sample. Even though the area on which the beam is focused should be totally removed it is not inconceivable that a portion of the excess energy is not removed from the sample area on evaporation. This excess energy may remain in the substrate and cause general heating of the sample.

Section 1.3: **Research Objectives**

The aims of this work are to generate and characterise novel molecular species. This is to be achieved by the development of a method to provide metal atoms from bulk material which can be isolated in reactive ligand matrices to form novel molecules.

The stimulus for the majority of this work is the observation of the formation of novel nitride and nitrogen complexes upon isolation of laser ablation products in nitrogen and nitrogen containing matrices.[17] The laser ablation method has been shown to provide novel metal oxides[18] and nitrogen oxides[19] by isolation in O_2 and NO containing matrices.

The work presented represents an investigation into the use of different methods for the generation of atomic species and characterisation of the products formed on isolation in a reactive medium. The intention is not to offer an alternative method to the isolation of vapour phase species which can be obtained through vaporisation, but to provide a route to the formation of novel vapour phase species which are not directly observed by simple thermolysis of a precursor.

In conjunction with the metal atom work, a complementary study on carbonyl complexes of the 3d transition metal dibromides has also been undertaken. This was completed due to the availability of a new far infrared source allowing the spectrum to be determined down to very low energy (50 cm^{-1}).

The isolated species are chiefly investigated using infrared and UV-Vis spectroscopy, although occasionally EXAFS spectroscopy is employed to determine interatomic distances. Mass spectrometry was also used to provide an insight into vaporisation products where applicable.

Section 1.4: **References**

[1] I. Norman and G. Porter, *Nature,* Lond., **174**, 508 (1954).

[2] E. Whittle, D. A. Dows and G. C. Pimmentel, *J. Chem. Phys.*, **22**, 1943 (1954).

[3] E. D. Becker and G. C. Pimmentel, *J. Chem. Phys.*, **25**, 224 (1956).

[4] G. V. Chertihin, W. D. Bare and L. Andrews, *J. Phys. Chem.*, **102**, 3697 (1998).

[5] H. E. Hallam (editor), *Vibrational Spectroscopy of Trapped Species*, Wiley-Interscience, London (1973) *and references therein.*

[6] M. Moskovits and G. A. Ozin (editors), *Cryochemistry,* Wiley-Interscience, Toronto, (1974).

[7] G. C. Pimmentel, *Forming and Trapping Free Radicals.*, ed. A. M. Bass and H. P. Broida, Academic Press, New York, 109 (1960).

[8] M. J. Linevsky, *J. Chem. Phys.*, **34**, 587 (1961).

[9] D. H. W. Carstens, J. F. Kozlowski and D. M. Gruen, *High Temp. Sci.*, **4**, 301 (1972).

[10] J. S. Shirk and A. M. Bass, *J. Chem. Phys.*, **49**, 5156 (1968).

[11] C. H. Townes, *Phys. Rev.*, **65**, 319 (1944).

[12] A. Von Hippel, *Ann. d. Physik.*, **80**, 672 (1926).

[13] D. M. Gruen and J. K. Bates, *Rev. Sci. Instrum.*, **47**, 1506 (1976).

[14] I. R. Beattie, P. J. Jones, K. R. Millington and A. D. Willson, *J. Chem. Soc. Dalton Trans.*, **1988**, 2759 (1988).

[15] F. X. Wagner, *PhD Thesis*, The University of Hull, (1996).

[16] P. H. Key, *PhD Thesis*, The University of Hull, (1989).

[17] L. Andrews, A. Citra, G. V. Chertihin, W. D. Bare and M. Neurock, *J. Phys. Chem.*, **102**, 2561 (1998).

[18] A. Citra and L. Andrews, *J. Phys. Chem.*, **103**, 4182 (1999).

[19] L. Andrews, M. Zhou and D. W. Ball, *J. Phys. Chem.*, **102**, 10041 (1998).

Chapter

2

Vibrational Theory and EXAFS

Section 2.1: **Theory of Vibrational Spectroscopy**

Introduction

The following section describes a brief introduction into the theoretical basis for the observation of infrared spectra and the assignment of infrared bands. For a more in-depth discussion on the subject the reader is referred elsewhere.[1]

Vibrations of a diatomic molecule

For simplicity, a diatomic molecule is considered first. The vibration of a molecule with 2 nuclei x and y to be to be reduced to the motion of a single particle of mass μ, whose displacement q from its equilibrium position is equal to the change in intermolecular distance. μ is referred to as the reduced mass and represented by:

$$\frac{1}{\mu} = \frac{1}{m_x} + \frac{1}{m_y}$$

where m_x and m_y are the masses of the two nuclei x and y. The kinetic energy is then expressed quantum mechanically as:

$$T = \frac{1}{2}\mu\dot{q}^2 = \frac{1}{2\mu}p^2$$

where p is the conjugate momentum $\mu\dot{q}$. The potential energy (V) for vibrations resembles the Morse potential, however, this cannot be easily solved so is approximated by Hook's law:

$$V = \frac{1}{2}kq^2$$

where k is a force constant and representative of the curvature of the potential energy well and not the bond dissociation.

These energy terms can then be entered into the vibrational Schrödinger equation:

$$H_{vib}\Psi_{vib} = E_{vib}\Psi_{vib}$$

to give:

$$\left\{\frac{-\hbar^2}{2m}\frac{d^2}{dq^2} + \frac{1}{2}kq^2\right\}\Psi_{vib} = E_{vib}\Psi_{vib}$$

Solving this equation, providing that Ψ_{vib} must be a single value, finite and continuous function, gives the eigenvalues:

$$E_n = \left(n + \frac{1}{2}\right)h\nu = \left(n + \frac{1}{2}\right)hc\tilde{\nu}$$

where n is the vibrational quantum number and ν and $\tilde{\nu}$ represent the vibrational frequency in s^{-1} and cm^{-1} respectively. The frequency of vibration is given by:

$$\nu = \frac{1}{2\pi}\sqrt{\frac{k}{\mu}} \quad \text{or} \quad \tilde{\nu} = \frac{1}{2c\pi}\sqrt{\frac{k}{\mu}}$$

ψ_{vib} is then given by the corresponding eigenfunctions:

$$\psi_{vib} = \frac{N}{\left(2^n n!\right)^{\frac{1}{2}}} e^{-\frac{\alpha q^2}{2}} H_n\left(\sqrt{\alpha} q\right)$$

where the normalisation factor, $N = \left(\frac{\alpha}{\pi}\right)^{\frac{1}{4}}$ and $\alpha = 2\frac{\pi\nu\mu}{\hbar}$.

$H_n\left(\sqrt{\alpha} q\right)$ are the Hermite polynomials of order n in the variable $\sqrt{\alpha} q$ with n being the vibrational quantum number.

Polyatomic Molecules

For diatomic molecules there is only one vibrational mode, but in the case of polyatomic molecules the case becomes more complicated due to the presence of 3N-6 vibrational degrees of freedom (or 3N-5 for linear molecules). This essentially means that the complex vibration undergone by the molecule as a whole is merely a superposition of a number of normal vibrations.

Each normal vibration is related to a normal coordinate (Q) which describes the atomic motion. These are then included into the vibrational wave equation with

the product of each wavefunction for each normal co-ordinate given the overall vibrational wavefunction:

$$\frac{\hbar^2}{2}\sum^{3N-6}\frac{d^2\psi_k^2}{dQ_k^2}+\frac{1}{2}\sum_{k=1}^{3N-6}\lambda_k Q_k^2\psi_k = E_{vib}\psi_{vib}$$

Selection Rules

In addition to the harmonic selection rule ($\Delta n = \mp 1$), the infrared activity of fundamental absorptions of a polyatomic molecule are governed by a set of symmetry selection rules. The rule is expressed as "energy can only be absorbed or emitted if the change in vibrational state is accompanied by a change in the molecular dipole moment." This translates quantum mechanically as:

$$\langle \psi_0 | \mu_q | \psi_1 \rangle \neq 0$$

For the two integrals to be non-zero, the direct product of the totally symmetric vibrational ground state (ψ_0), the symmetry properties of the component of the dipole moment along a particular cartesian axis q (x, y, or z) (μ_q) and the vibrational wavefunction of the excited state (ψ_1) must be, or contain, the totally symmetric representation.

The symmetry of vibrational modes can be determined simply by the use of Group Theory.[2] For example, considering the bent molecule XY_2,

University
Library
Hull

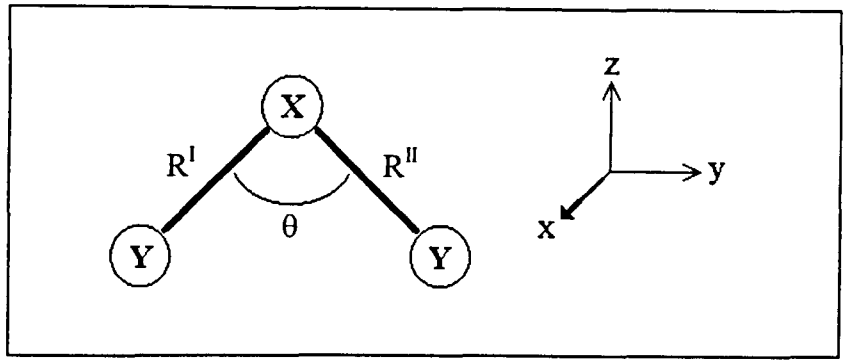

Figure 2.1: representation of a bent triatomic molecule.

a set of symmetry operations can be carried out for the specific molecular point group to determine the irreducible representation, Γ_{3N}, which is merely the sum of all vibrational, rotational and translational molecular motion.

$$\Gamma_{3N} = \Gamma_{vib} + \Gamma_{rot} + \Gamma_{trans}$$

This is usually calculated using a series of equations based on determining the number of unshifted Cartesian axes per symmetry operation (known as the reducible representation) in a summation with the irreducible characters for each symmetry species.

The sum of all vibrational motion, Γ_{vib} can then be divided into stretching and deformation modes:

$$\Gamma_{vib} = \Gamma_{str} + \Gamma_{def}$$

Γ_{str} can then be determined by repeating the symmetry operations using the number of bond stretching modes unshifted per symmetry operation.

The assignment of internal co-ordinates and projection operators, such as R^{I}, R^{II} and θ shown in figure 2.1 above are then used to determine the change in R^{I} relative to the change in R^{II} and therefore the nature of the bond stretch.

Wilson's GF Method

When the changes in the internal co-ordinates are represented by the column matrix R and its transpose $\tilde{R}$

$$R = \begin{bmatrix} \Delta R^{I} \\ \Delta R^{II} \\ \Delta\theta \end{bmatrix} \qquad \tilde{R} = \left[\Delta R^{I} \Delta R^{II} \Delta\theta\right]$$

the potential energy can be written as:

$$2V = \tilde{R}FR$$

where F is a matrix composed of force constants. The F matrix is used to describe the principal force constant for each vibrational stretching mode, f_r, and an interaction force constant, f_{rr}.

The kinetic energy is much more difficult to describe in terms of internal co-ordinates, but Wilson[3] showed that it can be written as:

$$2T = \dot{\tilde{R}}G^{-1}\dot{R}$$

where $\dot{R}$ is the derivative of R with respect to time and the reduced mass and internal displacement co-ordinates are used to provide the G matrix, of which the reciprocal is taken.

Wilson showed that the vibrational frequency could then be determined by the use of the secular equation:

$$|GF - E\lambda| = 0$$

where E is the identity matrix and λ is given by:

$$\lambda = 4\pi^2 c^2 \tilde{\nu}^2 \quad \text{and} \quad \tilde{\nu} = 1302.83\sqrt{\lambda}$$

Predicted spectra presented in this work have been calculated using the FG method with the computer program SOTONVIB[4] which requires the input of Cartesian co-ordinates to determine the G matrix and solve the secular equation. The F matrices were solved by applying reasonable force constant values from previous work and refining until a good correspondence between experimentally observed and calculated values were found.

Determination of Bond Angles

By resolving the IR active bands to observe the isotopic structure contained within them, matrix isolation experiments allow bond angles to be determined. The

simplest example of this is the ν_3 stretch of a bent XY_2 molecule. Solving the secular equation gives:

$$\lambda = 4\pi^2\nu_3^2 = \left[\frac{1}{M_Y} + \frac{2}{M_X}\sin^2\alpha\right](f_r - f_{rr}) \qquad \text{where } \alpha = \frac{\theta}{2}.$$

This shows that the angle Y-X-Y is equal to 2 α. By rearranging in terms of $\sin^2$ and assuming that the force constants remain the same after isotopic substitution, θ can be determined directly from the equation:

$$\sin^2\alpha = \frac{M_X M_X^i\left[M_Y(\nu_3)^2 - M_Y^i(\nu_3^i)^2\right]}{2M_Y M_Y^i\left[M_X^i(\nu_3^i)^2 - M_X(\nu_3)^2\right]}$$

where M_X, M_Y, M^i_X, and M^i_Y are the masses of the X and Y atoms and the associated isotopes. Thus allowing the calculation of the bond angle for the XY_2 unit by the use of vibrational frequencies observed in the isotopic molecules. However, this only applies to strictly C_{2v} molecules and therefore only XY_2, X^iY_2 and XY^i_2 but not XYY^i.

Section 2.2: **EXAFS**

Introduction

X-ray absorption fine structure (XAFS) refers to the wave-like features in an X-ray absorption spectrum. EXAFS (extended X-ray asorption fine structure) refers more specifically to the oscillations occurring after the absorption edge in an X-ray absorption spectrum as a function of proton energy. A typical X-ray absorption spectrum is shown in figure 2.2 below.[5]

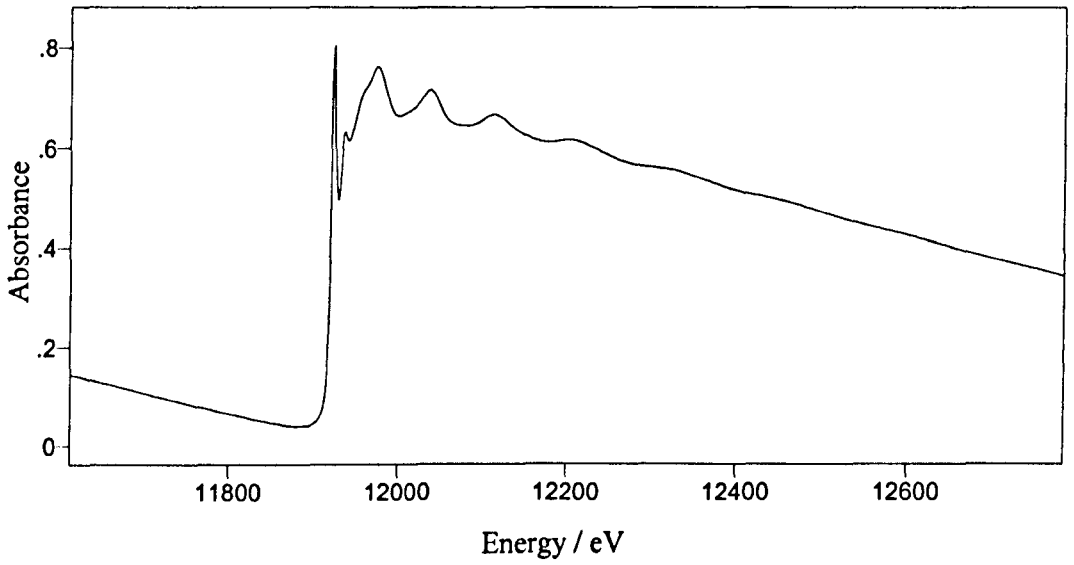

Figure 2.2: X-ray absorption edge of a gold chloride compound.[5]

The edge step corresponds to an atom absorbing enough photon energy for a core electron to overcome the binding energy and be ejected from the absorbing atom. The ejected electron can be visualised as a photoelectron wave originating and propagating from the absorber. The energy of the photoelectron is directly proportional to the incident photon energy.

The outgoing wave is then partially backscattered by surrounding atoms resulting in an incoming photoelectron wave. Interaction between the outgoing and

incoming wave results in constructive and destructive interference as the photon energy is increased.

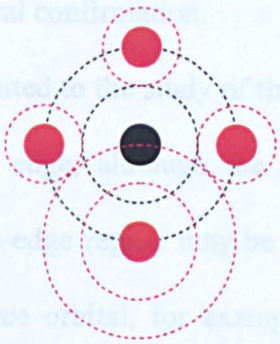

Figure 2.3: schematic representation of outgoing and backscattered photoelectron waves.
(Black dashed lines indicates the outgoing portion, the red dashed lines indicate portions of the scattered wave from the surrounding atoms).

This interference will therefore raise or lower the absorption coefficient relative to that for a free atom resulting in the characteristic EXAFS oscillations.

Since the absorption coefficient is a direct consequence of the interaction between the photoabsorbing atom and its local environment, EXAFS can be used to provide structural information and characterisation of the photon absorber and its local environment. More specifically it allows a quantitative determination of:

1) the distances between the absorber and back-scatterers.

2) The types and numbers of back-scatterers.

3) The degree of thermal and static disorder within the system.

4) Ligand arrangement (by the inclusion of multiple scattering).

Since the technique does not require long range order, these parameters can be determined from samples in any physical state. For dilute samples synchrotron

radiation is often used as this provides greater beam intensity. The element specific nature of the analysis allows the observation of one edge in the presence of others. This allows the analysis of multiple edges (for example the Ni and Br edges in $NiBr_2$ complexes)[6] to further structural confirmation.

EXAFS is generally limited to the study of the X-ray spectrum between 40 to 1000 eV after the absorption edge, although the pre-edge region often contains structural information. The pre-edge region may be structured due to transitions of core electrons to a high valence orbital, for example the iron K-edge[6] has been shown to contain a pre-edge feature due to the transition of a 1s electron to the 3d orbital. This can often allow the pre-edge region to provide information on the oxidation state and the geometry and co-ordination of the absorber. For L-edges the 2p to nd (n =3, 4 or 5) are fully allowed and hence very intense.

EXAFS Analysis

To gain a simplified view for EXAFS and its analysis the plane wave approximation is employed. The EXAFS equation given is a simplified derivation developed by Stern, Sayers and Lytle[7] rather than the single and multiple scattering fast spherical wave expression[8] used in the curve fitting program EXCURV98 which was employed in the analysis presented in this work as this is extremely complex.

$$\chi(k) = -S_0^2 \sum_S \left[\left(\frac{N_s}{kR_{as}^{\ 2}} \right) \left| F_s(\pi,k) \right| . e^{(-2k^2\sigma^2_{as})} . e^{(-2R_{as}/\lambda(k))} . \sin(2kR_{as} + 2\delta_a + \alpha_s) \right]$$

Definition of terms:

N_s - Number of equivalent scatterers (i.e. the same atom types at the same distance).

R_{as} - Distance between the absorbing and backscattering atoms.

$2\delta_a$ - Phaseshift experienced by the photoelectron on leaving and re-entering the absorbing atom *a*.

α_s - Phaseshift experienced by the photoelectron when it is backscattered by the scattering atom *s*.

$|F_s(\pi, k)|$ - Amplitude and phase of the backscattered photoelectron at given *k*.

$e^{(-2k^2\sigma^2_{as})}$ - Debye-Waller factor, which models the thermal and static disorder in the system.

$e^{(-2R_{as}/\lambda(k))}$ - Term reflecting the finite lifetime of the photoelectron, where $\lambda(k)$ is the electron mean free path.

S_0^2 - Shake up and shake off factor, which accounts for the fact that not all the photoelectrons participate in the EXAFS.

Data Analysis

The initial stage of EXAFS analysis is the conversion of the absorption data from the experiments from to $\chi(k)$ in *k* space which was completed using the PAXAS computer program.[9] The monochromator position was first calibrated using the edge position obtained from a metal foil of the sample edge to be analysed. Experimental spectra of the sample were then averaged together and adjusted as required by the calibration and converted from monochromator position to energy. The averaged

spectrum was then background corrected in the pre and post-edge regions to leave only the pure EXAFS oscillations in *k* space.

Once the data have been converted, structural information can be extracted by fitting the theoretical and experimentally observed EXAFS spectra using the curve fitting program EXCURV98.[10] Setting the types of atoms present and adjusting and refining the variables of atom distance (R) and coordination number (N) allows a theoretical model to be produced. Direct comparison between the pure EXAFS oscillations and monitoring the values of the thermal and static disorder (A) and the 'goodness of fit' (R) shows the most likely structure of the molecule present. A Fourier Transform of the EXAFS curve then provides a distance for the interaction.

Multiple Scattering

To gain further structural information multiple scattering terms can be included in the calculations. Multiple scattering describes the ejected photoelectron wave being 'doubly backscattered' as shown below. Figure 2.4 describes a triatomic molecule, for instance a metal halide, MX_2.

Figure 2.4: representation of multiple scattering.

An outgoing photoelecton wave is shown to propagate from the absorbing atom (M) and be backscattered by the adjacent atom (X^{II}). The backscattered wave then travels through the absorbing atom and onto the second atom (X^{I}) of the linear molecule and is again backscattered towards the absorbing atom. This manifests itself in the

Fourier Transform as an additional feature of much weaker intensity at twice the inter-atomic distance. Although multiple scattering for linear units, such as M-C-O is common, this type of multiple scattering in MX_2 molecules has only recently been identified.[11-13].

The presence of a multiple scattering feature is important as although a slight bend may still result in some multiple scattering it is generally associated with a linear unit.[6]

Section 2.3: **References**

[1] K. Nakamoto, *Infrared and Raman Spectra of Inorganic Co-ordination Compounds,* 5th ed., Wiley, New York (1997).

[2] R. L. Carter, *Molecular Symmetry and Group Theory,* Wiley, New York (1998).

[3] E. B. Wilson, J. C. Decius and P. C. Cross, *Molecular Vibrations,* McGraw Hill, New York (1955), Dover (1980).

[4] I. R. Beattie, N. Cheetham, M. Gardner and D. E. Rogers, *J. Chem. Soc. A,* **1971,** 2240 (1971).

[5] $HAuCl_4.3H_2O$. Taken from this work, chapter 4.

[6] O. M. Wilkin, PhD Thesis, the University of Hull (1999).

[7] D. E. Sayers, E. A. Stern and F. W. Lytle, *Phys. Rev. Lett.,* **27,** 1204 (1971).

[8] S. J. Gurman, N. Binsted and I. Ross, *J. Phys. C: Solid State Phys.,* **17,** 143 (1984), S. J. Gurman, N. Binsted and I. Ross, *J. Phys. C: Solid State Phys.,* **19,** 1845 (1986).

[9] N. Binsted, EXCURV98, CCLRC Daresbury Laboratories Computer Program (1998).

[10] N. Binsted, PAXAS, Program for the Analysis of X-Ray Absorption Spectra, University of Southampton (1988).

[11] A. van der Gaauw, O. M. Wilkin and N. A. Young, *J. Chem. Soc., Dalton Trans.,* **1999,** 2405 (1999).

[12] N. Binstead, A. van der Gaauw, O. M. Wilkin and N. A. Young, *J. Synchr. Radiat.,* **6,** 239 (1999).

[13] A. Munoz-Paez, S. Diaz-Moreno, E. S. Marcos and J. J. Rehr, *Inorg. Chem.,* **39,** 3784 (2000).

Chapter

3

Experimental

Introduction

The following chapter outlines the various deposition techniques used in conjunction with general matrix isolation experiments which are also described. With the exception of the furnace deposition of transition metal halides, all other experimental procedures described have been developed from previous experimental accounts and optimised during the course of the research. New apparatus has been designed and constructed when required in the development of the deposition techniques. As an example the design of two vacuum chambers purpose-built for UV-Vis-NIR experiments and far infrared work completed at Daresbury laboratories are included in Appendix A.

Gas Preparation

The gases used for the matrix isolation experiments are shown, along with their supplier, in table 1. Isotopic gas mixtures ($^{14}N_2$ / $^{15}N_2$ and ^{12}CO / ^{13}CO) and reactive / inert mixtures (Cl_2, HCl, O_2 and CO in argon) were prepared using standard vacuum line techniques.

The chlorine and hydrogen chloride supplied was further purified by vacuum distillation cycles in bulk to ensure a standard high purity.

Before commencing an experiment all matrix gas supply lines were subjected to three 'pump and flush' cycles to ensure the high purity of the matrix gas was maintained.

Gas	Purity	Supplier
Ar	99.999%	Messer Griesheim
$^{14}N_2$	99.999%	Messer Griesheim
$^{15}N_2$	97.4% (^{15}N)	Cea Euriso-top
$^{16}O_2$	99.998%	Messer Griesheim
$^{12}C^{16}O$	99.997%	Messer Griesheim
$^{13}C^{16}O$	99% (^{13}C)	Cambridge Isotopes
$^{12}C^{18}O$	99% (^{18}O)	Cea Euriso-top
Cl_2	99.9%	Energas
HCl	99+%	Aldrich

Table 3.1: Matrix gases

Section 3.1: **General Matrix Isolation Apparatus.**

In this section the apparatus used to generate, maintain and monitor the matrix environment, *i.e.* that of high vacuum and low temperature, is described in detail.

Matrix Isolation Fourier Transform Infrared (FTIR) Spectroscopy.

A schematic representation of the experimental apparatus used during a standard matrix isolation FTIR Experiment is shown in figure 3.1 below.

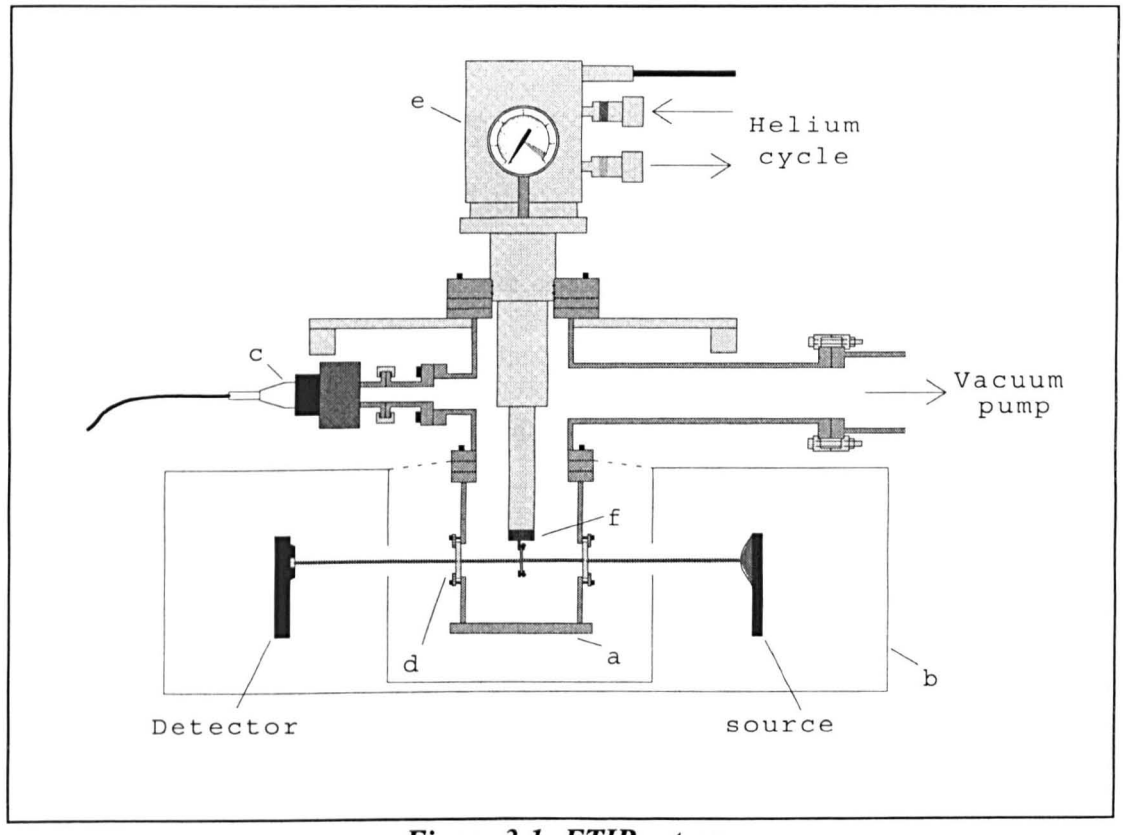

Figure 3.1: FTIR set-up

The diagram shows the main vacuum chamber (a) which was incorporated into the sample compartment of the Bruker IFS66 FTIR spectrometer (b) and maintained under high vacuum by either an Edwards turbomolecular pump (250 l / s) or an

Edwards vapour pump (600 l / s). Both were fitted with a liquid nitrogen trap and backed by an Edwards two-stage rotary pump. The vacuum in the main chamber was monitored with an Edwards Penning gauge (c). The typical vacuum achieved in the chamber was in the region of 5 x 10^{-7} mbar at room temperature. At cryogenic temperatures the chamber pressure improved to the region of 1 x 10^{-8} mbar due to cryopumping. The vacuum chambers used in all experiments consist of a number of ports which can be used as optical windows by the attachment of a CsI or CaF_2 disc. Any ports which were not required were covered by blanking plates, which were made usually in the form of aluminium but occasionally stainless steel or perspex plates were employed. For infrared work the chamber was fitted with CsI optical windows which transmit infrared radiation above 200 cm^{-1}. All vacuum seals on the chamber ports were made with Viton 'O'-rings.

The deposition surface was also in the form of a CsI window mounted in a copper block attached to the tip of the cryostat. Indium gaskets were used on these couplings to improve the thermal contact between deposition surface and cryostat. A close-up of the sample compartment is shown below in figure 3.2.

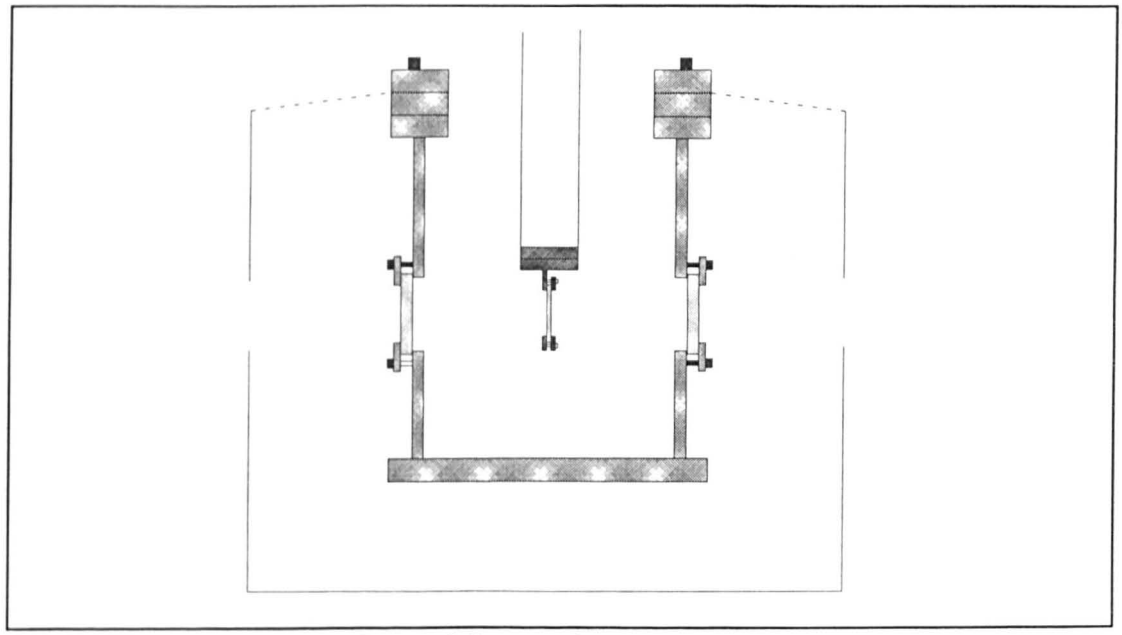

Figure 3.2: sample compartment

Experimental temperatures in the region of 8 to 13 K were achieved using an APD cryogenics Displex closed cycle He refrigerator (models DE-204SL, D-202 were used). The temperature of the deposition surface was monitored using a Scientific Instruments 9650 (SI9650) digital temperature controller which could also be used for warming the deposition surface using a heating element embedded in the tip of the cryostat. This could maintain the deposition surface at a temperature higher than the base temperature of the cryostat.

The rotatable seal on the cryostat permitted rotation of the sample window during experiments. This allowed the sample to be deposited at 90° to the scan position and the deposition window to be rotated at will, exposing the sample to either more depositing material or IR radiation. The diagrams above shows the apparatus in the 'scan' position during experiment.

Spectra were recorded in transmission mode with the FTIR spectrometer which has a working range of 4000 to 400 cm^{-1} for the mid infrared (MIR) using a KBr beamsplitter and CsI windowed DTGS detector. The far infrared (FIR) working range was 600 to 150 cm^{-1} (although the use of CsI windows meant that only radiation >200 cm^{-1} was transmitted) and required the use of a Mylar beamsplitter and polyethylene windowed detector. Data acquisition and manipulation was completed with a conventional PC using the Bruker Opus 3.0 Software. Samples were usually monitored with short scan cycles at 2 cm^{-1} resolution and as transmission, but could easily be converted to absorbance *via* the software used for data collection. Once deposition had been completed an averaged spectrum was recorded (around 500 scans) to reduce the noise level and generally improve the data quality. Further scans at higher resolution were recorded if required, with an increase of resolution up to the instrument maximum of 0.25 cm^{-1} being realistically achievable.

Water vapour and CO_2 were removed from the sample compartment by a Peak Scientific CO_2 desiccant air dryer. The integrity of the air purge was maintained by covering the sample compartment in a thick rubber sheet (shown as a dashed line in figure 3.2) sealed to be air tight around the sample cavity. A Perkin Elmer recirculating dryer / purger was also used to assist in the removal of water vapour for FIR experiments.

Photolysis could be completed on the isolated sample during and after deposition with an Oriel 660022 200 W Hg / Xe lamp fitted with a fibre optic extension with the light directed through a calcium fluoride window mounted on a chamber port. The efficiency of the photolysis process was increased by the use of a small focusing lens on the end of the light cable. The deposition window was rotated to directly face the CaF_2 window in post deposition photolysis both to maximise the energy on the sample and to allow the sample to be scanned during photolysis (at 45° to the incident IR radiation). Annealing cycles could also be completed using the temperature controller mentioned earlier.

Additional Infrared Apparatus.

For laser ablation experiments (described in more detail in section 3.3) a Perkin Elmer PE983G infrared spectrometer was used, operating in the region 180 to 4000 cm^{-1}. Data was extracted to a PC in the form of an ASCII X,Y file. Spectra were recorded as transmission with respect to a reference beam and obtained initially at a resolution of 6 to 10 cm^{-1}, with the highest resolution achievable being at around 2 cm^{-1}. Prior to any deposition the light travelling through the deposition window and reaching the detector did not exceed 30% of that of the reference beam. This led to a poor signal-to-noise ratio and meant higher resolution spectra were of low quality.

The chamber and deposition windows were again CsI and a purge shield maintained the dry air supplied by a Perkin Elmer recirculating dryer / purger. The vacuum pumping arrangement provide a vacuum in the region of 2 x 10^{-5} mbar at room temperature which improved to 2 x 10^{-6} mbar when the base temperature of 12 K had been achieved by the DE-204SL cryostat.

Matrix Isolation UV-Vis-NIR Spectroscopy

A near identical arrangement of apparatus was used for the UV-Vis-NIR experiments as that described for the FTIR. The vacuum chamber was mounted inside the sample compartment of a Varian Cary 5E spectrometer and spectra were generally recorded within the range 4000 to 50000 cm^{-1}. CaF_2 deposition and chamber windows were used in all cases. The spectra were stored as absorbance using Cary 5 3.0 OS/2 software on a conventional PC.

Although the experimental apparatus was arranged in a similar way to that of the FTIR, the different pumping arrangements meant that the typical vacuum when warm reached around 2 x 10^{-6} mbar at room temperature. Cryopumping improved the vacuum to the region of 2 x 10^{-7} mbar.

Section 3.2: **Deposition Techniques**

The deposition of the matrix gas and the generation of reactive species to be isolated was completed using a variety of different methods. The deposition techniques used are described in the following section with any variation in the experimental set-up from those described in the previous section detailed. All the deposition techniques described were designed or adapted to fit on the designated deposition port of the main vacuum chamber described previously.

3.2.1. Sputtering

a) Experimental Apparatus

A schematic representation of the experimental set-up used when using a hollow cathode sputtering device as the deposition source is shown in figure 3.3 below.

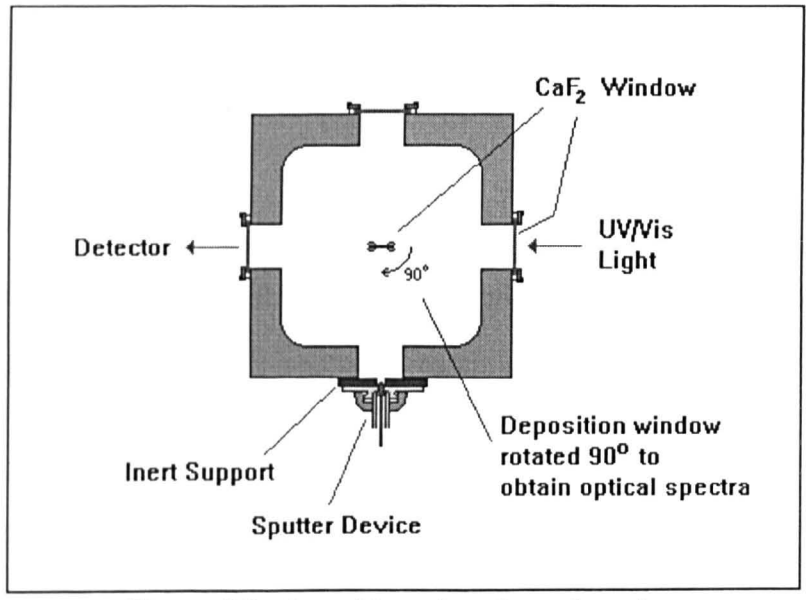

Figure 3.3: deposition chamber, plan view.

The vacuum chamber is shown arranged for UV-Vis-NIR experiments as described previously, with the sputter device mounted on the front face of the chamber. A more detailed view of the sputter device can be seen in figure 3.4.

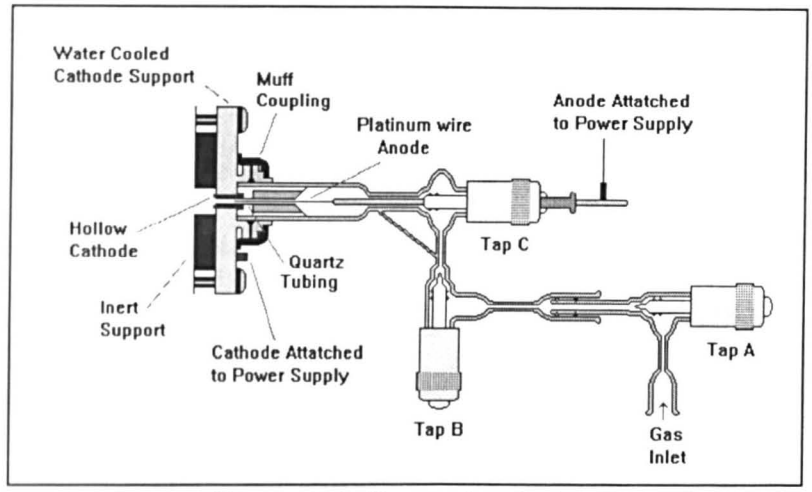

Figure 3.4: Sputtering device.

The sputtering device consisted of a cathode area, a glassware section and an anode. The cathode section mainly consists of the cathode support which was machined from stainless steel with a 4 mm threaded hole in the centre to hold the cathode. The cathode itself was in the form of a screw, manufactured from high purity copper (Goodfellows, 99.95% O.F.H.C.), with a 2.5 mm hole through the centre. When depositing materials other than copper metal foils of 0.025 mm thickness (Goodfellows 99.95%) and of 25 mm x 25 mm in size were rolled into the form of a tube and inserted inside the hollow copper cathode. This resulted in the foil forming a metal coating inside the hollow cathode approximately 0.1 mm thick.

The cathode support was attached directly to the vacuum chamber (*via* an inert support in the form of a Quartz ring) with insulated screws to prevent the chamber becoming live when a voltage was applied. The cathode support was also machined to support the glassware section of the sputter device with the use of a Viton 'O'-ring sealed muff coupling.

The glassware section essentially acted as a guide for the matrix gas. The gas supply used was generally from a two litre glass bulb, attached to the inlet point shown on tap A. Tap A was used as the main flow regulator, with tap B allowing fine control. The gas was directed inside the hollow cathode area by a small piece of quartz tubing attached to the end of the glassware.

The anode was made from platinum wire 0.4 mm in diameter (Goodfellows, 99.99%) which was attached to a stainless steel rod. The rod was inserted through a Young's tap and sealed with a PTFE 'O'-ring. The use of the tap allowed the position of the anode to be finely altered with respect to the cathode and glassware sections. The positioning of the quartz tube inside the cathode is shown in figure 3.5.

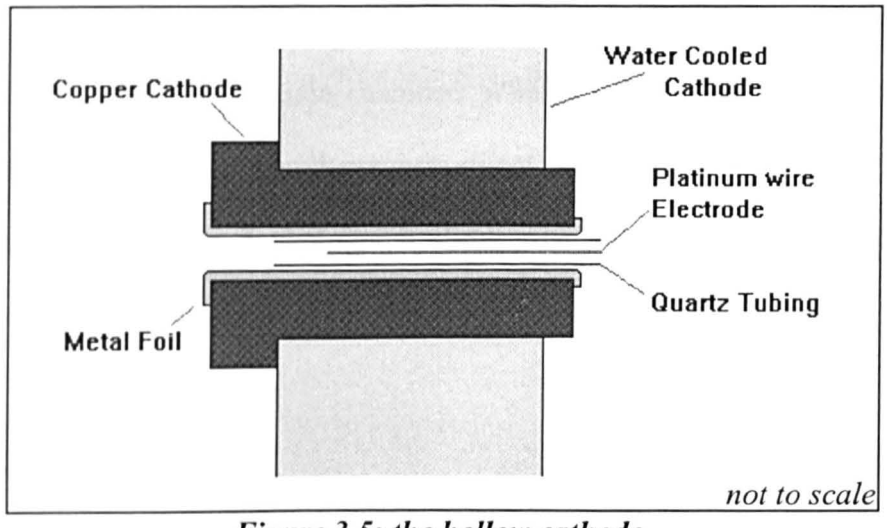

Figure 3.5: the hollow cathode.

The positioning of the quartz tubing within the hollow cathode was found to be critical in maximising the amount of sputtered products reaching the deposition surface. It was found that the yield was greatest when the quartz tube was positioned towards the end of the hollow cathode nearest the deposition surface. For this reason the positioning of the quartz tubing in the glassware was adjusted until the optimum conditions were achieved.

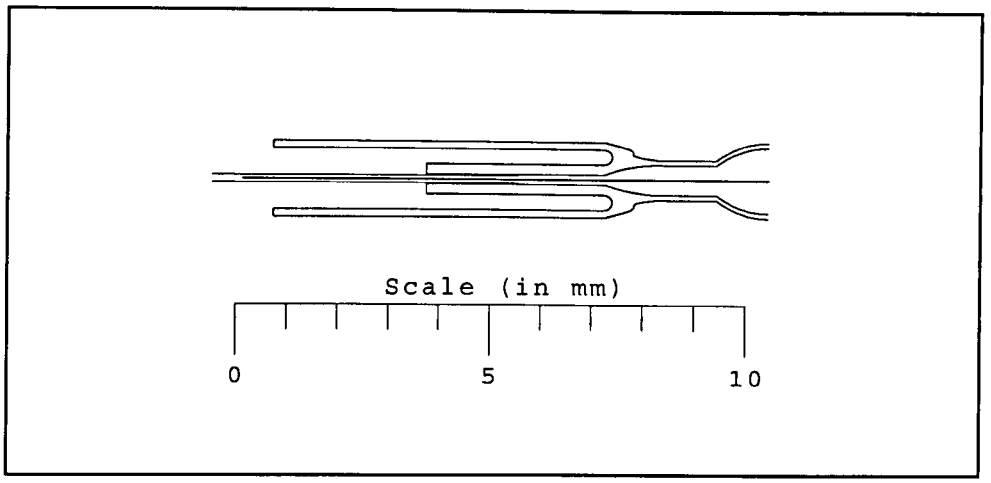

Figure 3.6: Positioning of the glassware.

The DC power supply (Ion Tech 150 V.A. Power Supply) was attached to the anode with a BNC high voltage connector and could be clipped to the cathode support and earthed on the main chamber area.

To begin depositing the gas flow was first established and monitored by the change in pressure in the main chamber. When a voltage was applied a discharge occurred and the sputtered products were swept along with the discharging gas to the cold deposition surface. A photograph of the experimental apparatus arranged for an FTIR experiment is shown in figure 3.7.

b) Deposition Conditions.

The discharge conditions were varied, but a general experimental procedure could be followed. With pressures in the vacuum chamber of the order 1 x 10^{-8} to 2 x 10^{-7} mbar, a gas flow producing a chamber pressure of around 2 x 10^{-5} mbar was found to be required to sustain the gas discharge.

Once the gas flow had begun the power supply could be switched on and the current increased to the maximum the supply would allow, around 15 mA (0.5 kV). Deposition times were varied, but generally lasted around 10 minutes for infrared or 2

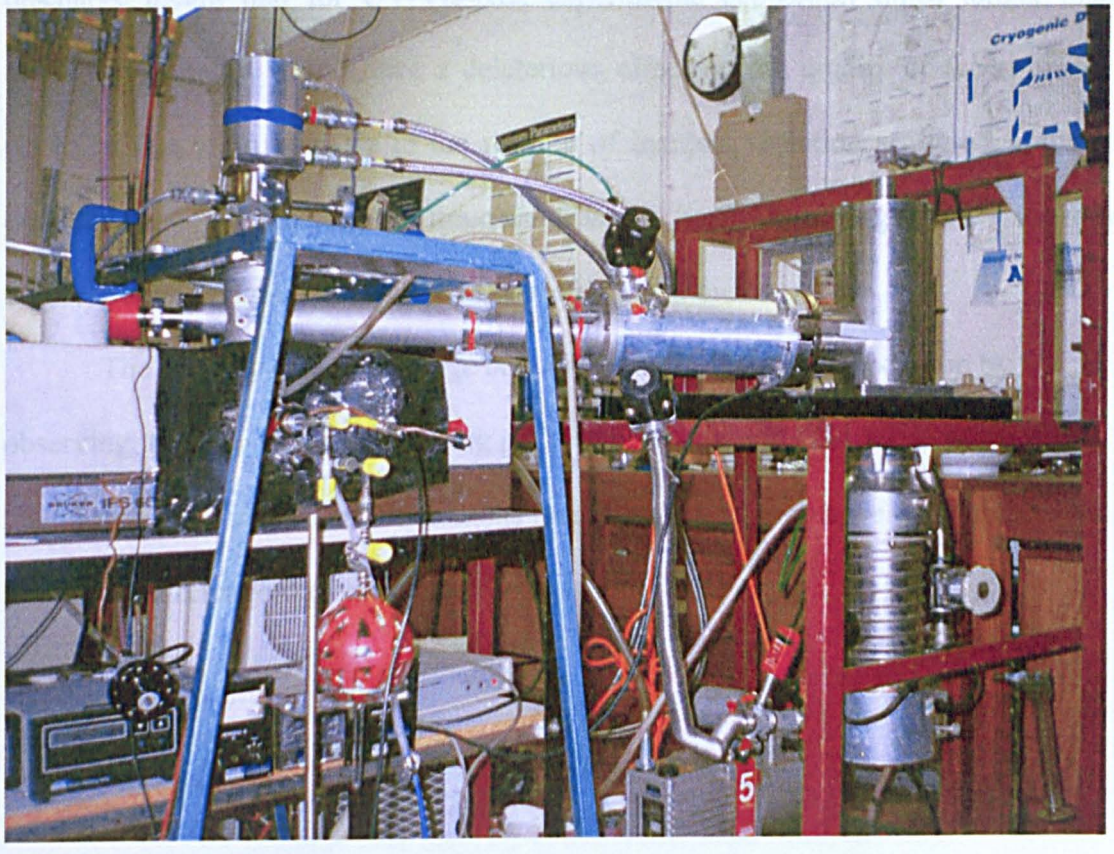

Figure 3.7: photograph of sputtering FTIR apparatus.

minutes for UV-Vis-NIR. The relatively large volumes of gas required to sustain the discharge meant that for UV-Vis-NIR experiments deposition times longer than around 10 minutes would have a deleterious effect on the quality of the spectrum observed due to an increase in the amount of incident radiation scattered. Infrared experiments could generally continue for around 1 hour (depending on the gas used) before too much light was lost due to scattering from the matrix.

The stability of the discharge could be monitored during deposition by observing the glow of the discharging gas. For best results the discharge was maintained with an even and continuous nature providing an intense glow observable in the post-discharge region through the inert support.

3.2.2. EXAFS Experiments

a) Experimental Apparatus

A plan view of the experimental set-up used for the EXAFS studies of sputtering products is shown in figure 3.8. The experiments were completed at Daresbury Laboratories Stations 9.2 and 16.5.

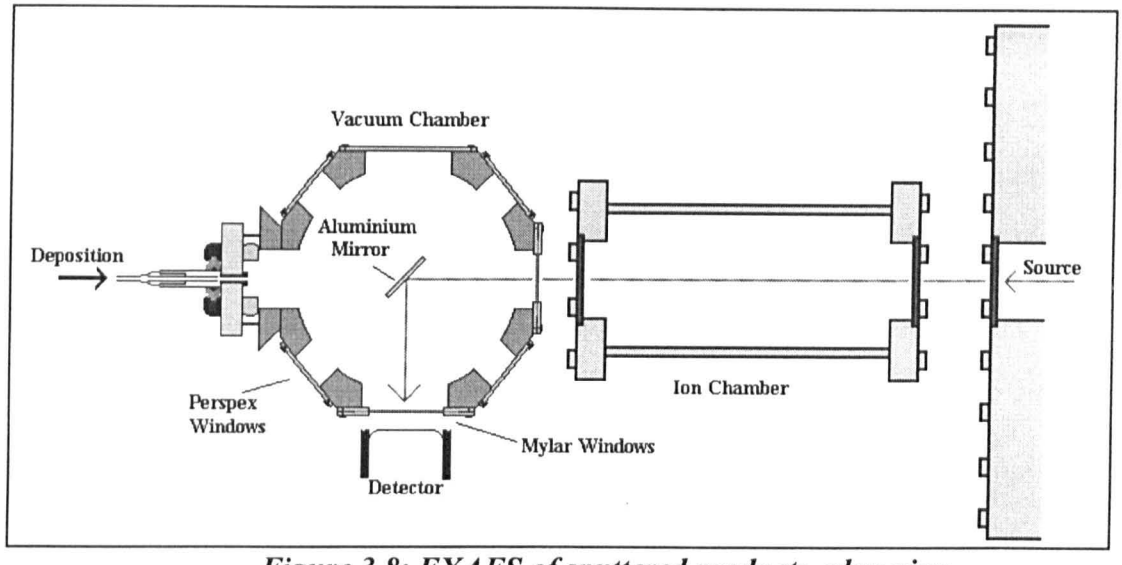

Figure 3.8: EXAFS of sputtered products, plan view

The X-ray radiation from the source was made monochromatic by either a double crystal harmonic rejecting Si220 (station 9.2) or Si311 (station 16.5) monochromator. The size and shape of the beam was determined by pre-monochromator slits producing typical beam dimensions of 6 x 1 mm. Post-monochromator exit slits were used to remove scatter before the beam entered the experimental hutch. The beam travelled through the ion chamber (I_0) to normalise the fluorescence signal with respect to the incoming intensity. The ion chamber was filled with an inert gas mixture with the ratio of the 2 gases tailored to the specific absorption edge under study.

The deposition surface was a polished aluminium mirror, again mounted on the tip of the DE-204SL cryostat. The two chamber windows through which the beam passed were Mylar and the remaining chamber windows were perspex. The

deposition source was mounted on the opposite face of the chamber to the incoming radiation and deposition was completed directly onto the aluminium mirror as described in the previous section. The deposition surface was then rotated 135° and the fluorescence recorded. The angle of incident beam onto deposition surface could then be finely altered to increase the total fluorescence counts reaching the detector. The detectors were either a 13 element solid state detector using germanium diodes (9.2) or an array of 30 high purity germanium diodes (16.5).

A vacuum in the region of 2 x 10^{-7} mbar could often be achieved in these experiments when cryopumping. Figure 3.9 shows a photograph of the EXAFS sputtering experiments at Daresbury laboratories station 9.2.

b) Deposition Conditions

Deposition conditions were kept as identical as possible with those used for infrared and UV-Vis-NIR experiments. Deposition times varied between around 5 to 10 minutes between scans with the average deposition being completed after around 20 to 30 minutes of total deposition. An Edwards diaphragm gauge was connected to the glassware adjacent to the gas bulb to allow the relative flow rate of the depositing gas to be monitored. The flow could be further checked by noting the change in pressure of the vacuum chamber before and after deposition. During deposition the growth of the X-ray absorption was monitored by scanning a short region around the metal edge under study. The scans concentrated on the region from 50 eV before the absorption edge to 100 eV after the edge and generally took around 10 minutes to record. Deposition was completed when further sputtering resulted in no net growth of the absorption edge, which was generally after around 20 to 30 minutes depending on the flow rate of the gas and the energy of the incident x-rays. This signalled that

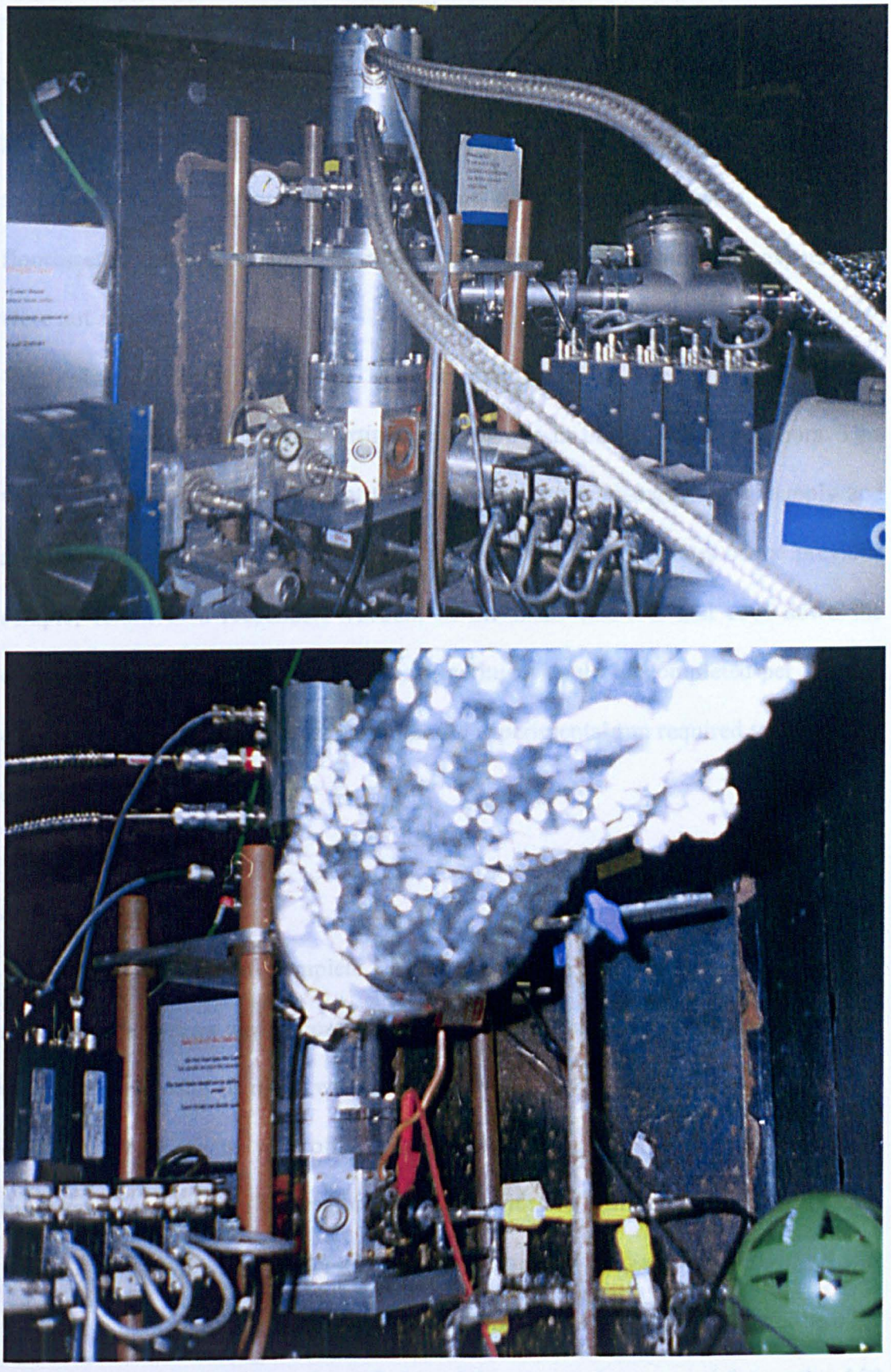

Figure 3.9: photograph of the sputtering experiments at Daresbury laboratories station 9.2.

the penetration depth of the argon matrix had been reached and that further deposition would be counter-productive. A deposition of 30 minutes used on average one litre of gas. These flow rates were higher than those used in other sputtering experiments due to the different pumping arrangements but since the spectra were recorded as fluorescence the light scattering problems associated with transmission experiments were not a factor.

The turnaround time for these experiments (the time required between finishing one experiment and starting another) was in the region of 10 hours. This was required to warm the cryostat to room temperature, change the gas supply and sample if required, clean the deposition surface to remove all traces of the previous sample, return to a reasonable vacuum in the main chamber and cool down the deposition surface. This meant that one experiment could be completed per full day of beam time, with a day before and after the experimental run required to set up and dismantle the apparatus.

c) Data Acquisition.

With deposition complete, X-ray absorption spectra were recorded for analysis. The spectra were recorded in k space with a maximum range of 15 $Å^{-1}$ after the absorption edge using k^3 weighting. However, since the noise levels increased with k space the spectra were often only recorded to 14 $Å^{-1}$ for weaker samples. Scan times were generally in the region of 1 hour with the scanning range divided into three regions. Typically the pre-edge region began 200 eV before the edge and was recorded with a step interval of 20 eV for 150 eV. At around 50 eV before the edge the step interval was decreased to 1.5 eV and the edge region scanned for another 150 eV. The final post-edge region was then scanned at a step interval commonly around

0.03 $Å^{-1}$ and collected out to 14 or 15 $Å^{-1}$ depending on the noise level. The monochromators were de-tuned to reject 50 % (9.2) or 10 % (16.5) of the beam intensity to eliminate harmonic reflections from the crystals. The harmonic rejection was set every 4 or 5 scans at an energy in the middle of the post-edge region to allow for fluctuations in the intensity of the beam. Matrix spectra were generally noisy and required in the region of 10 scans to reduce the noise to acceptable levels, although in some instances more scans were required when the absorption edge was particularly low in intensity. A calibration scan was recorded at each metal edge by placing a 5 or 10 μm metal foil in front of the I_0 ion chamber. This allowed the XANES region to be recorded and compared to previously reported edge data.[1]

The analysis of the data was completed by the method discussed earlier using the PAXAS and EXCURV98 programs.

3.2.3. Laser Ablation

a) Experimental Apparatus

A plan view of the alterations to the general experimental apparatus for laser ablation are shown in the diagram below.

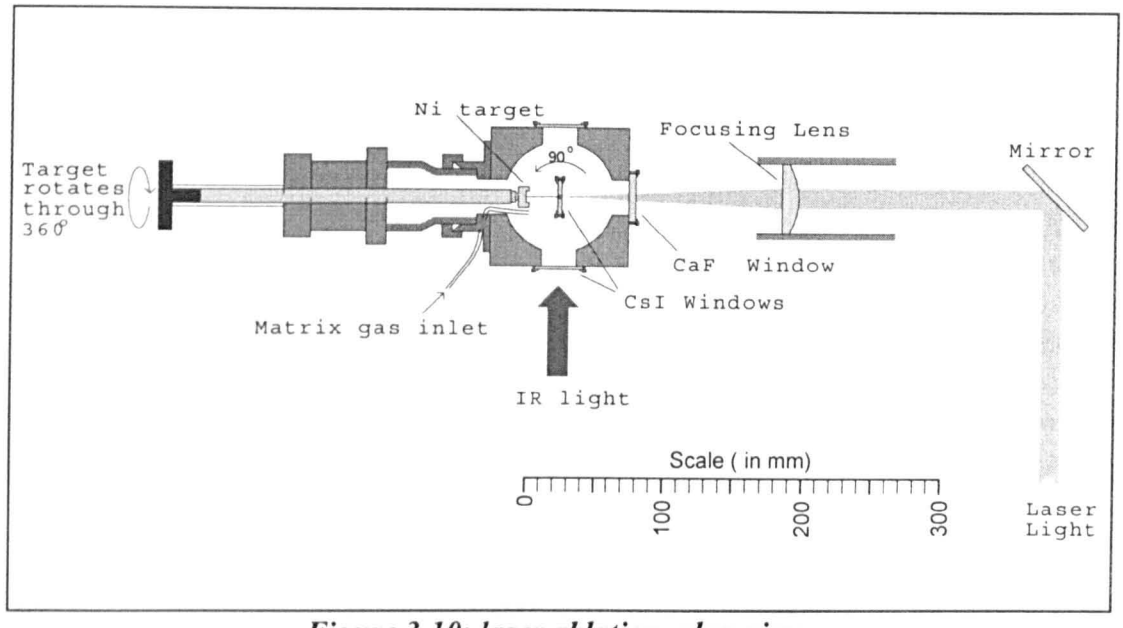

Figure 3.10: laser ablation, plan view.

The vacuum chamber was mounted inside the cavity of the Perkin Elmer 983G spectrometer. The sample to be ablated, which was initially in the form of a nickel stud, was mounted on the tip of a rotating probe. The probe was fixed to the front face of the vacuum chamber with a brass coupling. The deposition surface was again a CsI window maintained at *ca.* 12K during experiments by the DE-204SL cryostat. The window is shown in figure 3.10 in the deposition orientation, but was rotated after deposition by 90° to obtain a spectrum as transmission through the sample. A CaF_2 window was placed on the back face of the chamber which would transmit a laser beam of the frequency used (308 nm).

The laser beam was supplied by a xenon chloride excimer laser operating at 100 mJ per pulse. The light travelled through a series of filters which reduced the energy to 50 mJ and was then deflected towards the sample chamber by a mirror

placed 2400 mm from the source and 300mm from the sample. A lens was then used to focus the beam onto the target through the CaF_2 and CsI windows. Since the frequency of light used would not be transmitted by the CsI deposition window a small hole (~2 mm) was drilled in the window to allow the beam to pass through. The beam was deliberately focused slightly off the centre of the target as this allowed rotation of the target to reduced the likelihood of a hole being ablated through the centre spot.

When the laser output was set to give 100mJ the energy measured immediately after the lens was 67 mJ (∓ 7 mJ). This energy would be further reduced by the CaF_2 chamber window (by around 15%) and also by the sample window (by approximately 10%) due to the difference in the shape of the laser light and the hole in the CsI window. The aperture on the exit of the laser was 15mm x 8mm. The distance from source to target resulted in a demagnification factor of 8 which should produce an image spot of 1.875mm x 1mm. By taking into account that the energy was further reduced by 50% with a series of filters, the energy impinging on the sample surface per unit area (fluence) is estimated to be 16 mJ per mm^2.

When ablating metals other than nickel several layers of foil were placed over the tip of the nickel target (usually around 10, each of 0.025 mm thickness) and the ablation took place on the surface of the foil.

The ablated products were matrix isolated in a number of gases which were bled into the chamber during deposition through the gas inlet which was again an $^1/_8$ inch OD (outer diameter) copper pipe mounted on the brass coupling shown. The pressure in the vacuum chamber was monitored by a Balzers PKR 250 Full Range Gauge and was found to be of the order of 2×10^{-6} mbar at base temperature.

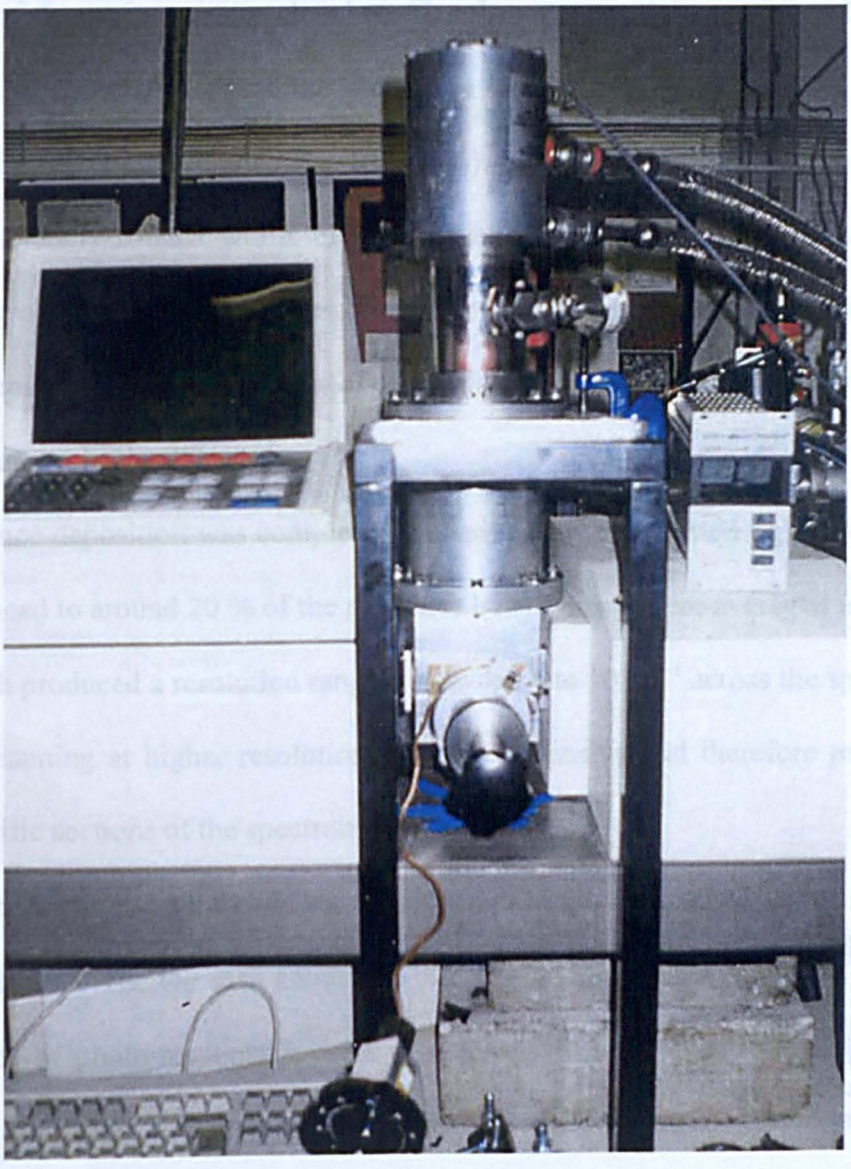

Figure 3.11: photograph of the apparatus used for IR analysis of matrix isolated laser ablation products.

b) Deposition Conditions

After a series of background scans had been recorded at the base temperature the flow rate of the matrix gas was established by monitoring the change in the pressure of the main vacuum chamber. The flow rate, which was controlled with a needle valve, typically reduced the vacuum in the chamber by an order of magnitude (usually from 2 x 10^{-6} mbar to 2 x 10^{-5} mbar). The laser was then activated and the sample manually rotated whilst being exposed to the radiation which had a pulse frequency of 10 Hz in most cases. Deposition times were generally 30 minutes in total, completed in 5 minute cycles of deposition and scanning. Gas flow was stopped during scan cycles in all cases.

Once deposition was completed the amount of transmitted light had typically been reduced to around 20 % of the reference beam. Scans were averaged using mode 5, 1 which produced a resolution ranging between 4 to 10 cm^{-1} across the spectrum.

Scanning at higher resolution was time intensive and therefore restricted to very specific sections of the spectrum.

The pictures on the right shows the effect of the laser on the sample area. The top scan shows the effect of a single pulse on a piece of photo-responsive paper which was fixed to the target area and exposed to a single pulse. The paper shows a reasonable image of the laser which is purposely slightly out of focus. The second scan shows the effect of laser ablation on the gold foil covering the nickel stud. The foil is shown after around 90 minutes of ablation. It is evident from this scan that rotation of the target is effective in prolonging the lifetime of the sample to be ablated.

Laser ablation target: after single shot

Laser ablation target: after 90 minutes of ablation

3.2.4. Sublimation Experiments

a) Sample Preparation.

The majority of the metal halides used in sublimation experiments were purchased from the suppliers in a high purity (99+ %) and preferentially in the high purity form. The exceptions to this were the samples of $CoBr_2$, $NiBr_2$ and AgCl. Samples of $NiBr_2$ and $CoBr_2$ were obtained from previous work[2] in which they were generated from the heating of the high purity metal foil in HBr and purified by sublimation under vacuum.

Silver chloride was prepared by the addition of an aqueous solution of silver nitrate to potassium chloride solution over gentle heating with AgCl being formed as the precipitate. The solid was then washed with water, ethanol and diethyl ether before being oven dried (at 60 °C)

b) Experimental Apparatus

Figure 3.12 below shows the furnace set-up used for the generation of molecular species from a furnace for a UV-Vis-NIR experiment.

The furnace was attached to the front of the vacuum chamber by a brass coupling which clamped the cooling water jacket in place and sealed with two Viton 'O'-rings. Cooling water was circulated through the copper electrodes and around the water jacket to maintain the integrity of the vacuum by cooling the various seals and prevented the glassware overheating. Power was supplied to the electrodes using a variac in series with a transformer operating at a maximum of 20 volts and 10 amps. The tantalum wire furnace was resistively heated by increasing the variac voltage, this in turn heated the sample contained in a silica pot within the tantalum wire windings.

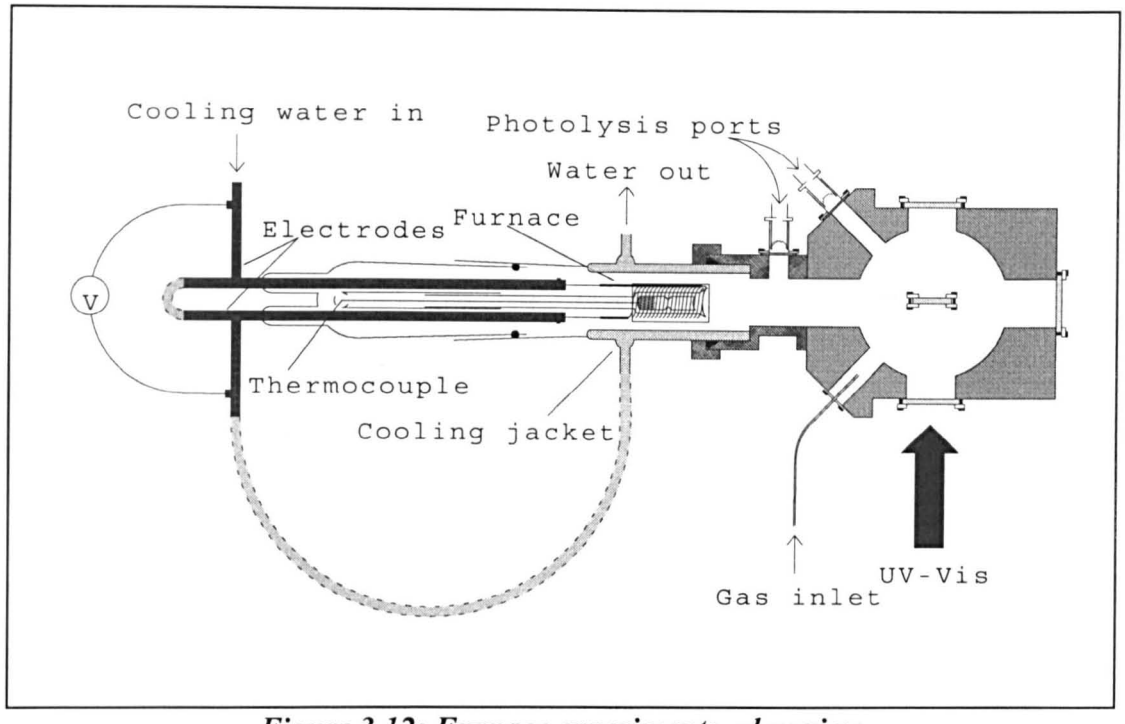

Figure 3.12: Furnace experiments, plan view

A close-up of this area of the furnace is shown in greater detail in figure 3.13 below.

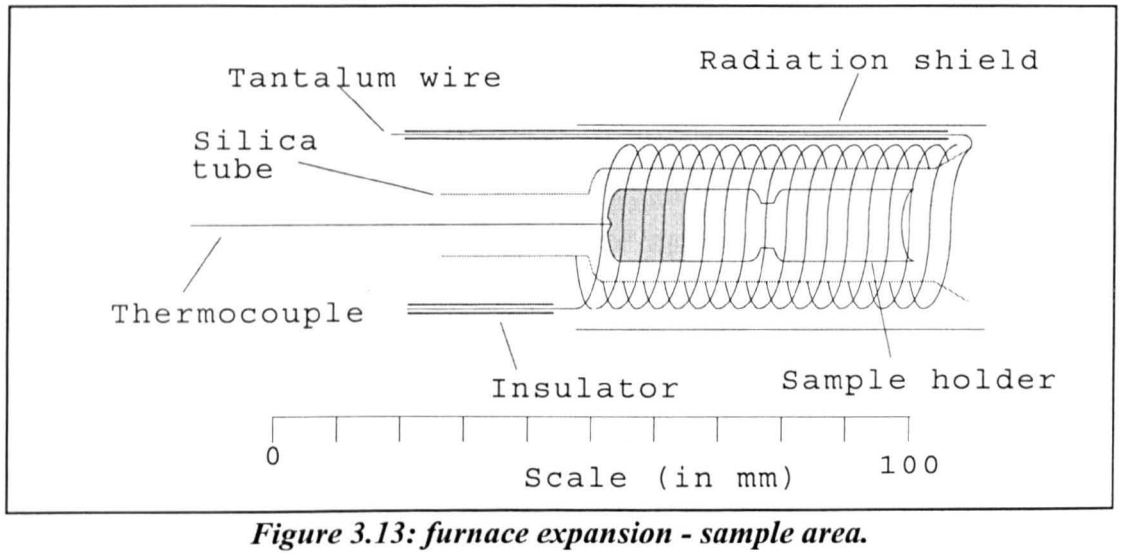

Figure 3.13: furnace expansion - sample area.

The insulators were simply thin ceramic tubes which were placed over the wires to prevent a short across the windings. The windings were tightly wrapped around the silica tube which supported the sample holder and were themselves encased in a larger section of silica tube which acted as a radiation shield. A type K thermocouple was used in an attempt to provide a reproducible sublimation temperature and was

placed as close as possible to the sample container. Although this did not give a truly accurate reading of the actual sublimation temperature it was found to act a reproducible guide to the furnace conditions required to achieve sublimation.

Figure 3.14 shows a close-up of the adaptations made to the furnace when subliming atoms from bulk metal.

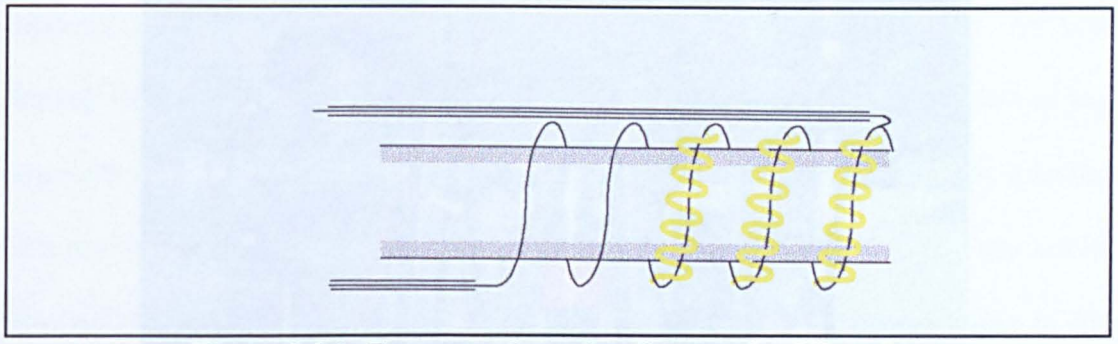

Figure 3.14: Furnace adaptation for metal sublimation.

The sublimation of atoms was achieved by tightly wrapping thin strips of gold foil (0.025 mm thick) around the tantalum windings. To obtain the higher temperatures required for the sublimation of metals two variacs with maximum outputs of 270 V and 8 and 15 amps were used to generate the resistive heating required. The first variac (8 A) was generally set at around 30 V and the second increased gradually until sublimation was achieved.

Isolation of the sublimed material was achieved by co-deposition on the cold window with the matrix gas. This was delivered through the gas inlet shown in figure 3.8. The inlet is an 1/8 inch OD copper pipe connected to an Edwards Pirani gauge and needle valve. This method only gave relative flow rate values but was found to be an effective way of reproducing the flow rates required for successful matrix isolation of the sublimed species. Figure 3.15 shows a photograph of the experimental apparatus used for UV-Vis-NIR furnace evaporation experiments.

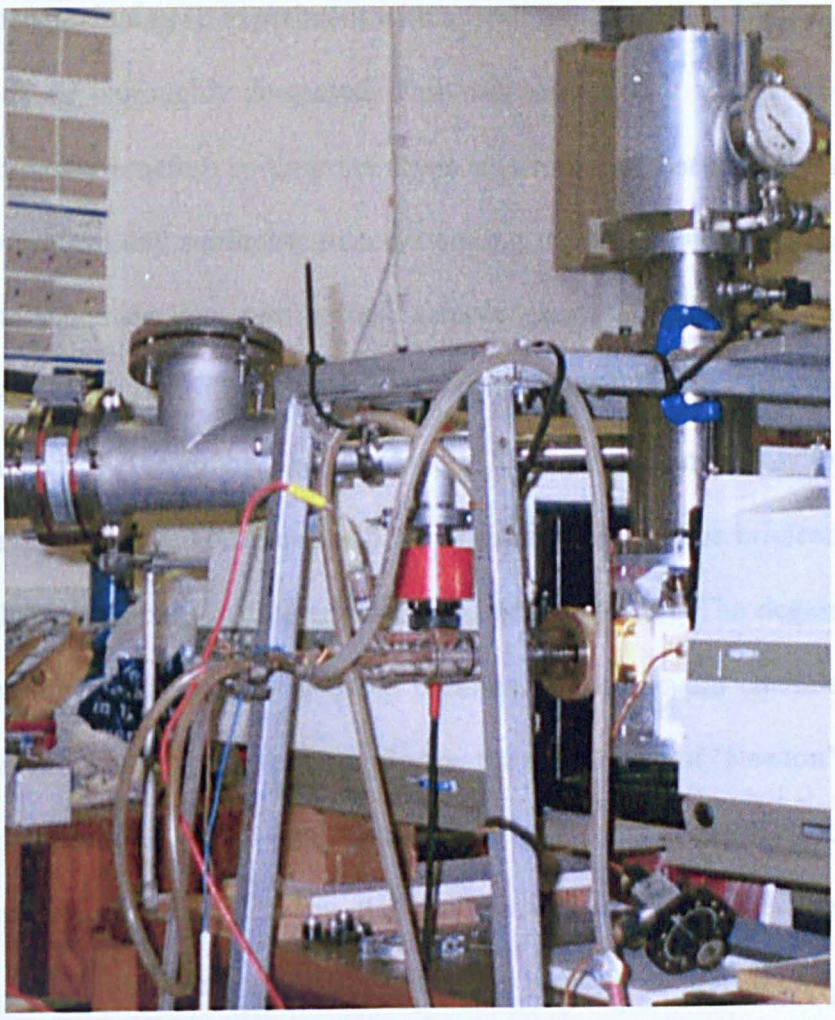

Figure 3.15: photograph of the apparatus used for UV-Vis-NIR analysis of matrix isolated furnace sublimation products

b) Experimental Procedure

When beginning an experiment with a fresh sample to be sublimed the sample had to firstly be thoroughly de-gassed. This was achieved by slowly increasing the furnace temperature before cooling the cryostat, which had been rotated to the scan position to prevent any subliming material soiling the window prior to the isolation experiment. When dealing with a fresh sample great care was taken at this first heating stage to increase the temperature slowly and reduce the likelihood of the sample being ejected from the silica pot holder. Typically moisture was first released by any sample which had been exposed to normal air for even the briefest amount of time and then commonly hydrogen halide was often released. The degassing of the sample was monitored by the change in pressure of the vacuum chamber until the sublimation temperature could be identified by the appearance of 'Newton's rings' - a fine film of deposited sample - on the water jacket at the end of the furnace. Any CO_2 which may have been present on the furnace windings was then removed by increasing the temperature above this sublimation point for a short period of intense heating.

Once the cryostat had been cooled to its base temperature and a series of background scans completed the matrix isolation of the vapour species could begin. The flow rate of the matrix gas was first established to an even and continuous manner at the desired relative flow rate. With the matrix now forming on the cold surface the furnace was heated to the previously established sublimation temperature and the vapour phase species isolated on the deposition window, which had been rotated 90° from the scan position to directly face the depositing material.

The progress of the deposition was monitored every 15 to 20 minutes with short scan cycles recording over the spectral region where the characteristic

absorption bands should occur. When sufficient sample had been deposited the furnace was switched off and allowed to cool. The gas flow was maintained for a short period (around 5 minutes) to provide a protective coating and to ensure complete isolation before being shut off. Deposition times for these experiments were generally in the region of one to two hours (maximum of 1 hour for UV-Vis-NIR experiments). In the infrared region deposition was usually monitored in the far infrared for the metal halides investigated. MIR scans were mainly recorded when deposition had been completed.

The isolated samples could then be photolysed and / or annealed as described previously.

c) Far Infrared

Sublimation experiments were also completed at Daresbury Laboratories Station 13.3. A plan view of the apparatus used in these experiments is shown in figure 3.16.

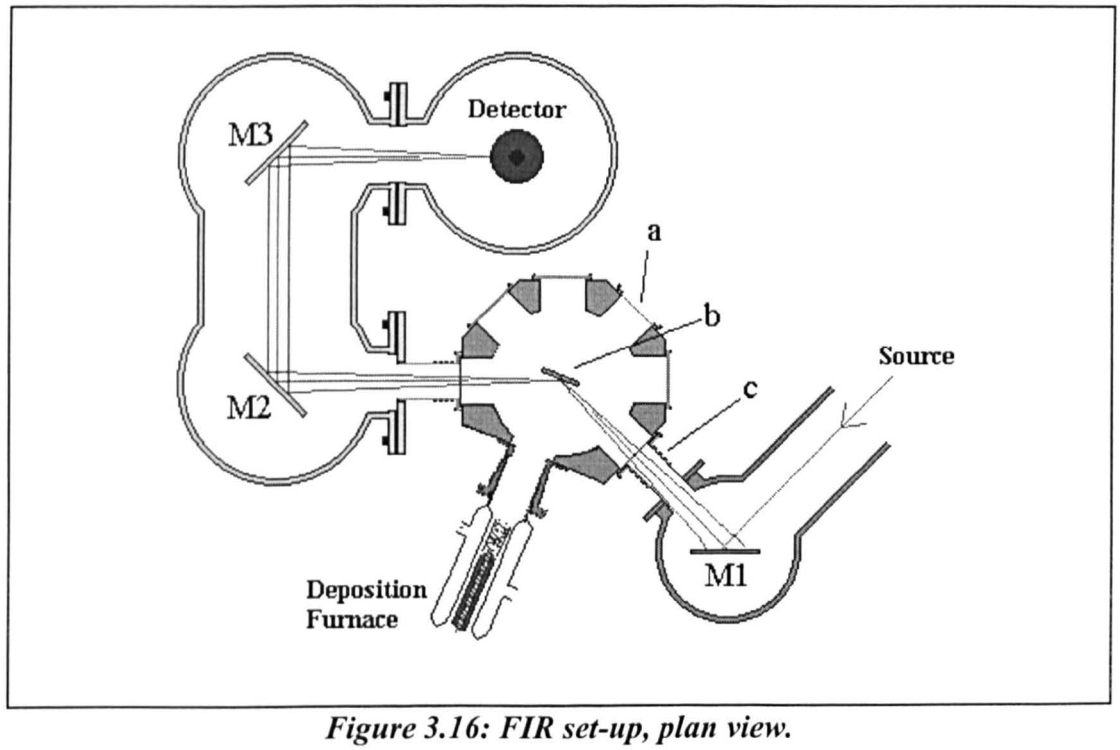

Figure 3.16: FIR set-up, plan view.

The infrared region of the radiation supplied by the synchrotron was deflected onto the optical path shown above by a series of deflecting, steering and focusing mirrors with a vacuum Nicolet FTIR bench being used to access the region 20 to 2500 cm^{-1}. The optical windows on the main vacuum chamber were polyethylene, sealed with Viton 'O'-rings by purge tubes (c) which maintain the integrity of the vacuum purge along the optical path to the detector . For these experiments an Infrared Laboratories bolometer was used, which has a detection range of 20 to 600 cm^{-1}. The furnace was mounted on the front face of the vacuum chamber with the brass coupling described earlier and the deposition surface (b) was in the form of a copper mirror which acted as part of the optical path from source to detector. A perspex window (a) was fitted onto one of the chamber ports to assist in the alignment of the light.

Further to the standard FTIR set-up described earlier (Fig 3.1) a short section of supported bellows was incorporated into the vacuum apparatus. This was placed between the flanges joining the cryostat collar and the chamber pump-out arm. The bellows acted as a 'shock-absorber' and removed a great deal of vibrations from the detector caused by the cryostat during refrigeration. Figure 3.17 shows a side view of the front face of the custom built chamber which has two smaller ports at 35° to the deposition face above and below the brass coupling.

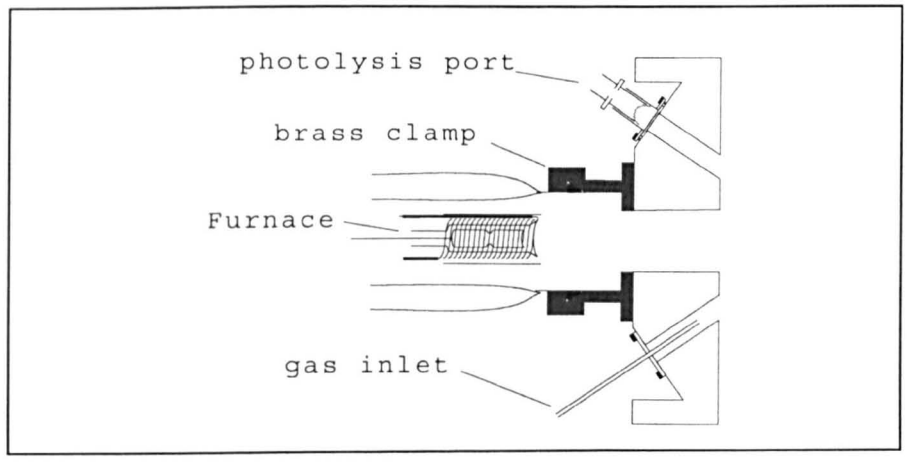

Figure 3.17: Deposition face of main vacuum chamber, side view.

These are fitted with an $^1/_8$ inch copper pipe gas inlet and small photolysis port designed to support the focused optical cable.

Identical deposition conditions were used as described for the FTIR characterisation, but with deposition times generally being increased (2 to 3 hours) to develop the weaker bands under study. Scans were recorded throughout deposition to monitor the growth of the characteristic bands without needing to rotate the cryostat. This also helped in keeping the optical path in the optimised position established in the initial alignment stage. Spectra were recorded at $2cm^{-1}$ with only around 250 scans being required to gain a relatively noise free spectrum. With the deposition completed photolysis and annealing cycles were then carried out on the isolated sample. Figure 3.18 shows a close-up of the vacuum chamber on station 13.3. The picture clearly shows the furnace attached to the front face of the main vacuum chamber, with the small window above the furnace used for photolysis of the isolated sample also evident. The flexible vacuum purge tubes attached to the optical windows and the bellows placed between the cryostat and the vacuum chamber can also be seen on the photograph.

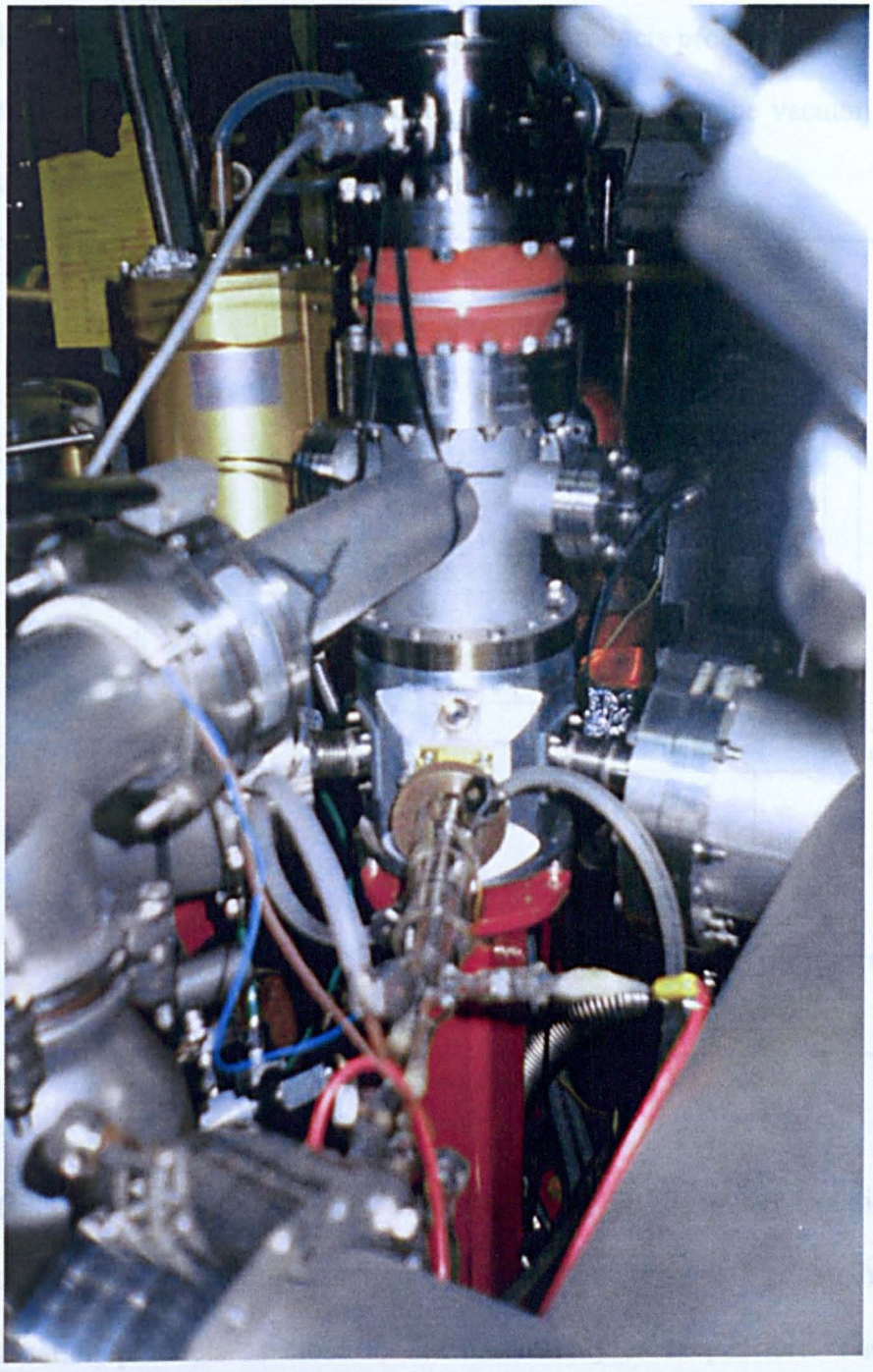

Figure 3.18: photograph of the apparatus used at Daresbury laboratories station 13.3 for FIR matrix isolation experiments.

3.2.5. Mass Spectrometry

To further identify some of the sublimation products produced during furnace evaporation experiments the furnace could be fitted directly to the vacuum chamber containing the quadrupole mass analyser as shown below.

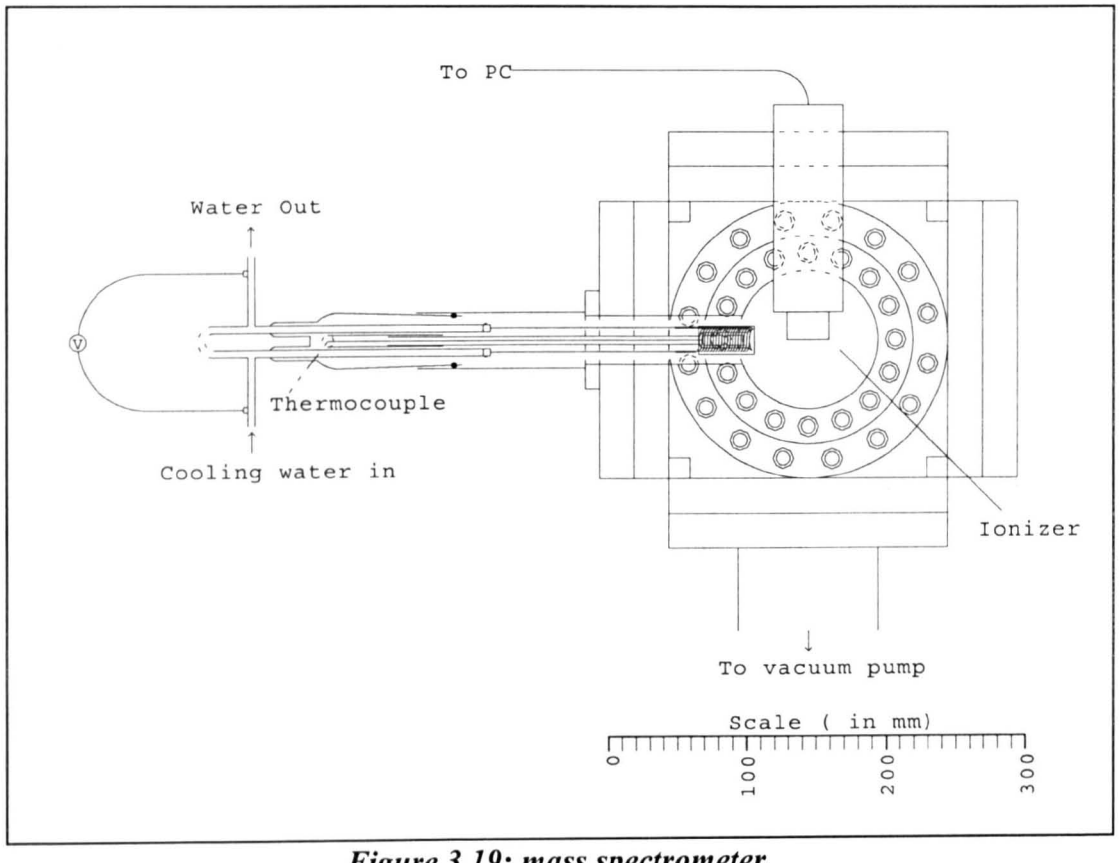

Figure 3.19: mass spectrometer.

The furnace is essentially the same as that used for the matrix isolation of the sublimation products with the exception that it has been increased in length to place the sublimation products as close to the mass analyser as possible. The copper electrodes are again water cooled and coupled to the variac as described previously. The vacuum achieved in the chamber was generally in the region of 5×10^{-8} mbar.

For vapour analysis the variac was increased to heat the material to its sublimation point and maintain the temperature to provide subliming material at a constant pressure in the region of 5×10^{-6} mbar.

The vapour was ionised by electron bombardment generated by thermionic emission of a heated tungsten filament. The energy of the electrons was varied by altering the accelerating potential between the filament and the ion source cage which also acts as the electron trap. The ions are injected into the mass filter which consists of four parallel rods which are polarised by an applied RF voltage to provide a positive and negative plane. An increase in the potential of the RF field increases amplitude of the oscillatory motion of the ions in the positive plane, which leads to neutralising collisions with the polarised rods. Therefore by altering the field potential the polarised rods act as a low mass pass filter. In the negative potential plane the RF gradients near the electrodes exert focusing force on the ions. This force also increases with mass and thereby acts as a high mass pass filter. These filters are then made to overlap, providing an overall band pass mass analyser with only those ions in the range specified reaching the detector.

The ions are detected by a wide bore channeltron multiplier. This electron multiplier consists of a funnel shaped piece of glass with a resistive coating which is held at negative potential. When ions collide with the detector electrons are liberated from the resistive coating which increases the current as the ions travel along the resistive surface to the collector, liberating more electrons as they do so. The current that arrives at the detector is the fed to the amplifier and on to the interfaced microcomputer. The data is analysed using the data review package 'Postsoft' run from a conventional PC.

3.2.6. Photodissociation of Tellurium Compounds

The alterations to the experimental set-up for the isolation of H_2Te and its photodissociation are outlined in figure 3.20 below.

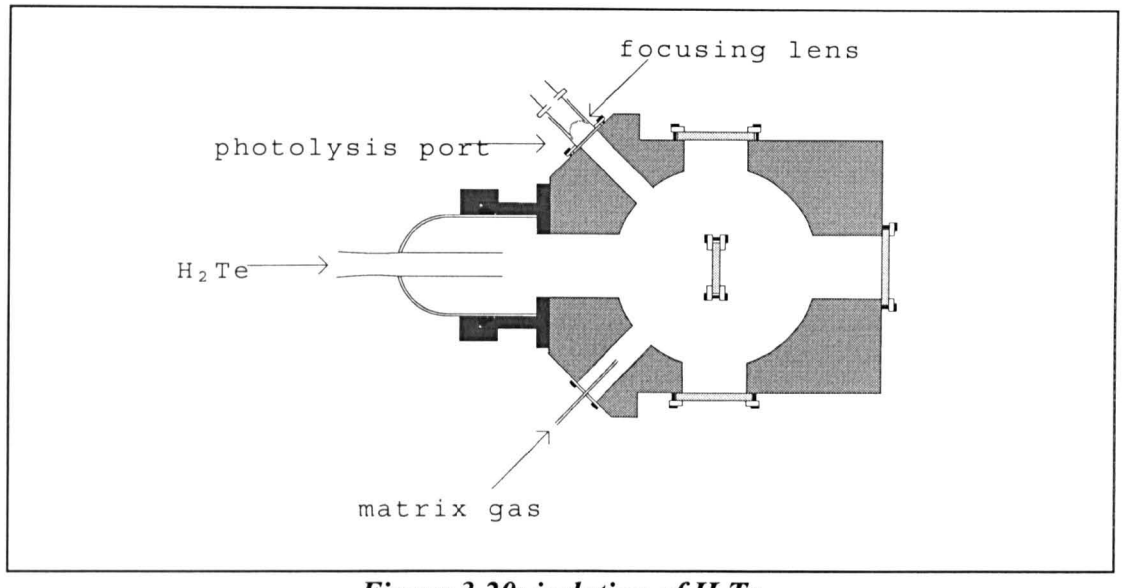

Figure 3.20: isolation of H_2Te

A glass dome was attached to the front of the vacuum chamber with the brass coupling used in previous experiments. Before beginning the experiment the flask containing H_2Te was stored in liquid nitrogen to solidify the sample and fixed to the glass dome using a double 'O'-ring glass joint. The preparation of H_2Te is described in more detail in chapter 5.

When starting the experiment, the sample temperature was first raised to allow sublimation of the H_2Te. To accomplish this the flask was immersed in a slush bath containing methylcyclohexane cooled with liquid nitrogen to just above its melting point, thus maintaining the temperature of the H_2Te in the range 147 to 163K. At this temperature H_2Te has been shown to have a vapour pressure of 0.01 to 0.08 mm Hg.[3]

First the matrix gas was deposited on to the deposition window, with the flow maintained by a needle valve and monitored with an Edwards Pirani gauge to ensure

a standard flow rate throughout the deposition. The H_2Te was then allowed to flow through the glassware and onto the deposition surface. The flow was maintained by a series of taps on the glassware and also by control of the vapour pressure of the sample via the slush bath temperature. The glassware sections of the experiment were kept dark to avoid decomposition of the sample.

Photolysis was completed on the sample both during and after deposition with the Oriel 660022 200 W Hg / Xe lamp as described earlier.

Section 3.4: **References**

[1] J. A. Bearden and A. F. Burr, *Rev. Mod. Phys.*, **39**, 125 (1967).

[2] O. M. Wilkin, *PhD. Thesis*, University of Hull, 1999.

[3] D. M. Chizhikov and V. P. Shchastlivyi, *Tellurium and Tellurides*, Collet's Ltd, London (1970) - English translation by E. M. Elkin.

Chapter

4

Late 4d and 5d Transition Metal Halides

Introduction

In this chapter the results of a study on late 4d and 5d transition metal atoms isolated in inert and reactive matrices as a source of novel transition metal halides are presented. The experiments outlined in this chapter were designed to form novel transition metal halide molecules that had not been previously characterised and as they are co-ordinatively unsaturated this must be carried out in the vapour phase. Matrix isolation techniques were therefore employed to allow conventional spectroscopic techniques to be used in the characterisation of the molecular species formed.

The most common route to isolated transition metal halide molecules is by furnace sublimation experiments. As described earlier a purified sample of the solid compound is heated *in-vacuo* with the high temperature vapour species produced being trapped in an inert matrix and characterised spectroscopically. These types of experiments often produce one major molecular gas phase species with the metal usually in the same oxidation state as in the solid sample.

Presented in this chapter are the results of an investigation into the formation of transition metal halide molecules formed by direct combination of metal and chlorine atoms. This is used as a route to the formation of gas phase transition metal molecules which cannot be observed by the simple heating of the solid to sublimation temperature. Metal atoms of gold, silver, platinum and palladium were isolated in argon matrices doped with small concentrations of chlorine to determine if transition metal chlorides would form as isolated molecules in the matrix. UV-Vis-NIR, EXAFS, infrared and mass spectral data is presented where appropriate, along with any previous available data.

The metals used in this study were chosen mainly due to availability of source material and encouraging initial results. Different generation methods were used as sources of metal atoms for matrix isolation experiments to improve spectral quality and to assist in the complete assignment of the bands present. Unfortunately, experimental constraints limited the application of these sources and prevented their use in all analyses. More explicitly, laser ablation experiments were limited to infrared analysis and the sputtering products could not be monitored by mass spectrometry. Neither of these techniques were used with far infrared work below 200 cm^{-1}.

Infrared spectra were routinely recorded from 600 to 200 cm^{-1} (or as low as 20 cm^{-1} in extreme far-infrared work), however for convenience and clarity of presentation, IR spectra are often truncated to show the region of interest more clearly. Any regions absent from the spectra presented should be assumed to contain no observable absorption bands or those bands unambiguously assigned to the presence of low level impurities such as water and carbon dioxide. Mid-infrared spectra were also routinely recorded but are not presented in this section since they provided no additional information. UV-Vis-NIR spectroscopy was used to confirm the isolation of atomic species by comparison with previously observed results. UV-Vis-NIR spectra of any molecular species formed were used to assist in the characterisation based on the assignment of possible charge transfer bands and d-d transitions to contribute in the determination of molecular structure.

Section 4.1: **Gold Chloride.**

Introduction.

The purpose of this study on gold chloride was to generate and characterise monomeric gold chloride molecules. The most common method for the generation of metal halide vapours for matrix isolation experiments is by sublimation of a stable precursor. However, it was shown by Fischer and Blitz[1] in 1928 that the vapour of gold(III) chloride contained only the dimer, Au_2Cl_6, and that the monomer $AuCl_3$ was not formed by direct vaporisation. With further investigations[2] they proved that the monomer could be formed, along with the other species AuCl and Au_2Cl_2 by heating gold under a flowing chlorine atmosphere, and suggested that the species formed was dependent on the temperature of the gold. The formation of $AuCl_3$ had also been reported in the same year by introducing the vapour from the solid into a stream of "active nitrogen".[3, 4] The work of Fischer *et. al.*[2] also served to settle an old argument over the existence of $AuCl_2$ and the dimer Au_2Cl_4 which were first reported by Thomsen in 1876,[5] formed by passing chlorine over a gold sponge and measuring the amount absorbed. This claim was disputed 11 years later by Krüss and Schmidt[6] who failed to reproduce the work. Thomsen then went on to reconfirm the findings[7] only to have them again discredited.[8] The "non-existence" of these molecules was later to be confirmed by Corbett and Druding[9] and also by Janssen *et. al.*[10]

Further investigations on the products formed by heating gold in the presence of chlorine have been presented[11-15] and these results confirm that AuCl and $AuCl_3$ can be formed in the vapour phase with the species produced dependent on the temperature of the gold. Ivashentsev and Timonova[13] showed that, when using gold powder, reaction begins at 143 °C forming solid gold (III) chloride up to 260 °C

whereupon it decomposes to AuCl, which itself then decomposes to the elements at 283 °C. The reaction is said to proceed with the corresponding vapour phase species formed above the respective solid.

Mass spectral data on the vapour products from heated gold (III) chloride presented by Shannon and Swan[16] shows consecutive loss of a chlorine *molecule* from the parent ion $Au_2Cl_6^+$, rather than loss of a chlorine *atom*. This was thought to be due to the relative instability of the Au(II) oxidation state. A high temperature mass spectrometry study was also employed to confirm the predominance of gold (I) chloride above 127 °C in a chlorine stream.[17-19] Below this temperature Au_2Cl_6 was shown to be the major species produced with all the mass spectrum components being the products of the dissociative ionisation of this species.

The predominance of the dimer in the vapour above solid state gold (III) chloride was complemented by the work of Clark, Templeton and MacGillavry[20] who confirmed that the crystal structure of solid gold (III) chloride was the planar Au_2Cl_6, in agreement with the structure predicted by Wells in 1947.[21] The single-crystal X-ray structure has been re-determined more recently to improve the data quality.[22]

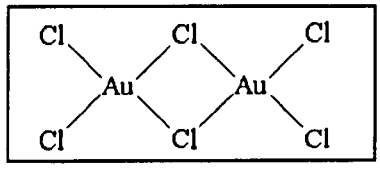

Figure 4.1: the structure of molecular gold (III) chloride

The vibrational spectra for this dimer have also been assigned, with some band assignment changes being given in the later work.[23-25]

Although AuCl is a metastable molecule which disproportionates at room temperature to Au and Au_2Cl_6[26] the solid state crystal structure[26-28] and vibrational

spectra[29,30] of this molecule have also been reported with the solid state structure said to be of *zig-zag* chains with a gold chlorine bond distance of 2.36 Å.

Further studies in the past decade have been used to characterise the UV-Vis[31, 32] and Raman spectra[33] of gas phase Au_2Cl_6, with the latter report predicting the nature of the infrared spectrum. In 1999 a report on the FT emission spectroscopy of the visible transitions of AuCl (first reported by Fischer *et.al.* in 1928) at 0.05 cm^{-1} resolution was also published.[34]

In the following experiments gold atoms were isolated in a cryogenic matrix of inert gas doped with a small concentration of chlorine in an attempt to form the monomeric gold halides which cannot be formed by direct sublimation. The experiments were also intended to determine if the co-ordination number of the gold atom could be governed by the chlorine concentration in the matrix or if only the most stable gold chloride would form in all cases.

Theoretical papers have been published on the target molecules, many are concentrated around the discussion of relativistic effects,[22,35,36] but predictions have been made to show that both AuCl[35] and $AuCl_3$[22] could form, with the former having a vibrational stretching frequency of 369.5 cm^{-1} and the latter being 'T-shaped'.

Figure 4.2 shows predicted spectra for the gold chlorides $AuCl_x$ (x = 1 to 4) completed using the computer program 'SOTONVIB'.[37] The calculations show the isotope patterns that are expected for the possible shapes of the gold mono-, di- , tri- and tetrachlorides. The calculated spectra are shown at 0.5 cm^{-1} resolution and the pattern observed is due to the chlorine isotope pattern (3 : 1 for ^{35}Cl : ^{37}Cl) as gold has only one major isotope (100 % ^{197}Au). Clearly observing the number of vibrational bands present in the spectrum and the isotope pattern contained within the

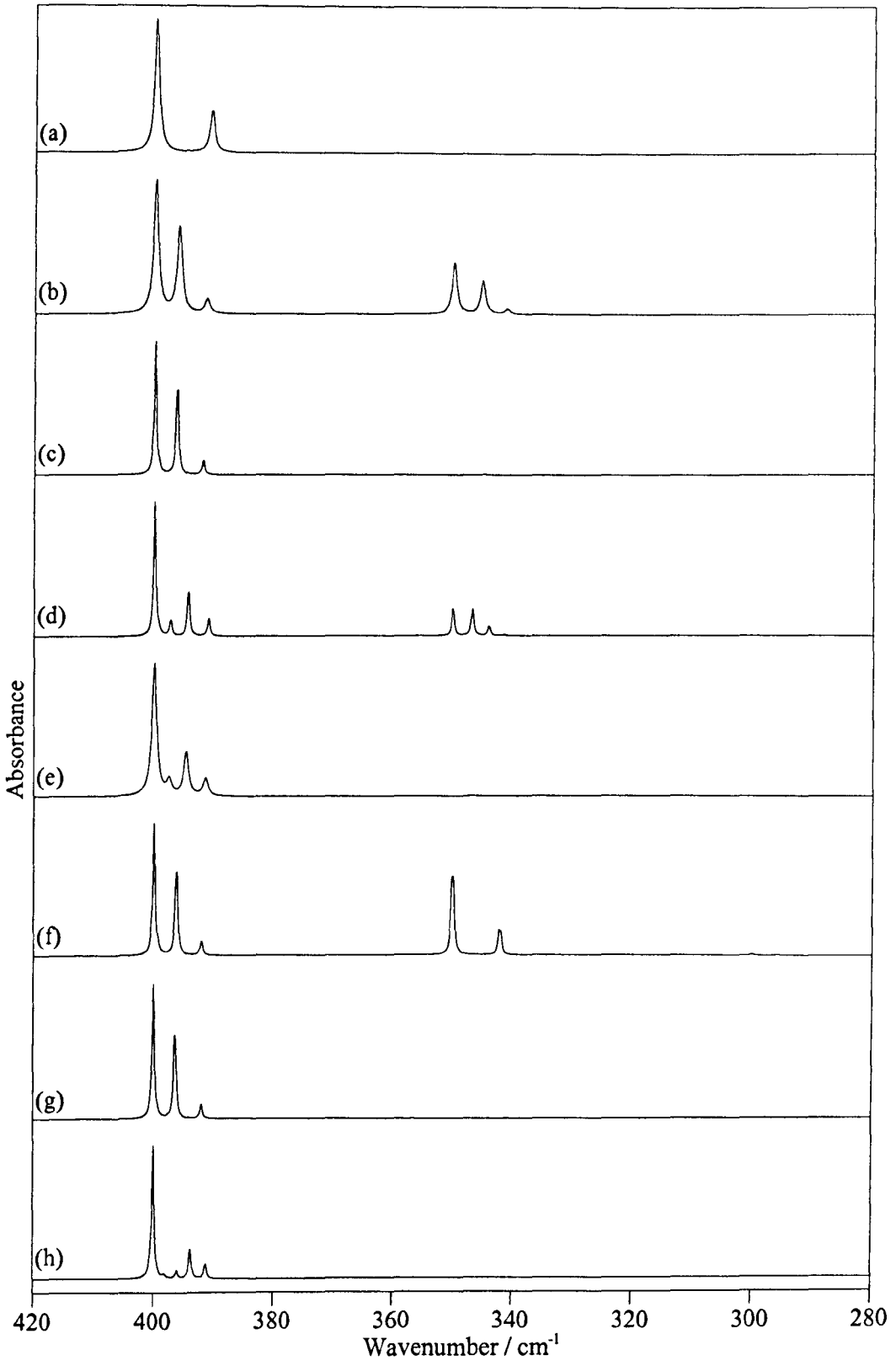

Figure 4.2: calculated infrared spectra for different gold chloride species.

(a) $AuCl$, (b) $AuCl_2$ bent, (c) $AuCl_2$ linear, (d) $AuCl_3$ pyramidal, (e) $AuCl_3$ planar; (f) $AuCl_3$ 'T-shaped', (g) $AuCl_4$ square planar, (h) $AuCl_4$ tetrahedral.

bands should assist in the determination of the co-ordination number and geometry of any gold chloride isolated in the matrix. The positioning of the high frequency band is set to 400 cm^{-1} in the calculations and the low frequency band set to 350 cm^{-1} if applicable. Table 4.1 lists the principle force constant (F_r) and the interaction force constant (F_{rr}) values for the calculated spectra shown in figure 4.2.

Molecule	Geometry and Point Group	F_r (mdyne / Å)	F_{rr} (mdyne / Å)
AuCl	$C_{\infty v}$	2.80	-
$AuCl_2$	Bent (120°), C_{2v}	2.46	-0.14
$AuCl_2$	Linear, $D_{\infty h}$	2.49	0.05
$AuCl_3$	Trigonal pyramidal (110°), C_{3v}	2.57	-0.09
$AuCl_3$	Planar, D_{3h}	2.58	-0.03
$AuCl_3$	T-Shaped, C_{2v}	2.15, 2.16	-0.28, 0.12
$AuCl_4$	Tetrahedral, T_d	2.61	-0.03
$AuCl_4$	Square planar, D_{4h}	2.18	0.17

Table 4.1: force constant values for predicted $AuCl_x$ spectra (x = 1 to 4).

For the trichlorides the isotope pattern expected statistically is 27 : 27 : 9 : 1. However, if degenerate modes are present, the isotope pattern is no longer binomial as the symmetry is lowered by isotopic substitution and the pattern becomes distorted. In the case of the 'T-shaped' molecule shown in figure 4.2(f) the pattern observed can be split into the vibrational modes of a linear or bent Cl-Au-Cl and a Cl-Au unit. The spectrum shown is the simplest scenario possible, with the interaction force constant between *cis*-AuCl units set to a minimum (0) in the initial calculation and the active frequencies sufficiently separated to reduce the interaction. As the interaction is increased the spectrum becomes more complicated as the lower energy modes become split and increase in intensity.

The predicted spectra for the tetrachloride also shows a different pattern from that which is statistically expected. The square planar molecule presents a 9 : 6 : 1 pattern as it is effectively observed in this simplest scenario as two overlapping linear dichloride molecules. The bands predicted for the tetrahedral tetrachloride spectrum are again distorted by the lowering of symmetry due to isotopic substitution.

Results and Discussion

Sublimation Experiments

Sublimation experiments were first carried out on a solid sample of gold (III) chloride, which was heated to sublimation temperature (around 80 °C) in order to confirm the characterisation of the major vapour phase species produced.

On heating gold chloride the mass spectrum shown in figure 4.3 was observed along with an expansion of the regions which contained the major peaks also given. The presence of the $Au_2Cl_6^+$ ion at around 606 mass units was clear, along with all ions produced from the breakdown of the Au_2Cl_6 molecule, with the notable exception of $Au_2Cl_5^+$. The intensities of the $Au_2Cl_6^+$ peaks are somewhat misleading, as the sensitivity of the instrument was greatly reduced at such high masses. This means that the presence of such an intense peak at this high mass and the lack of peaks due to $AuCl_3$ (at 302 amu) and its daughter ions suggested it was present in a proportionally large amount and therefore the predominant species in the vapour phase. Truncated regions of the spectrum where the major gold chloride mass ions are also presented along with the predicted mass peaks for gold chloride produced using the computer program 'Massspec'[38] also given to confirm the assignments. Miscellaneous bands which remain unassigned in the mass spectrum which appear to have characteristic chlorine and bromine isotope patterns (at 206, 252, 288 and 321

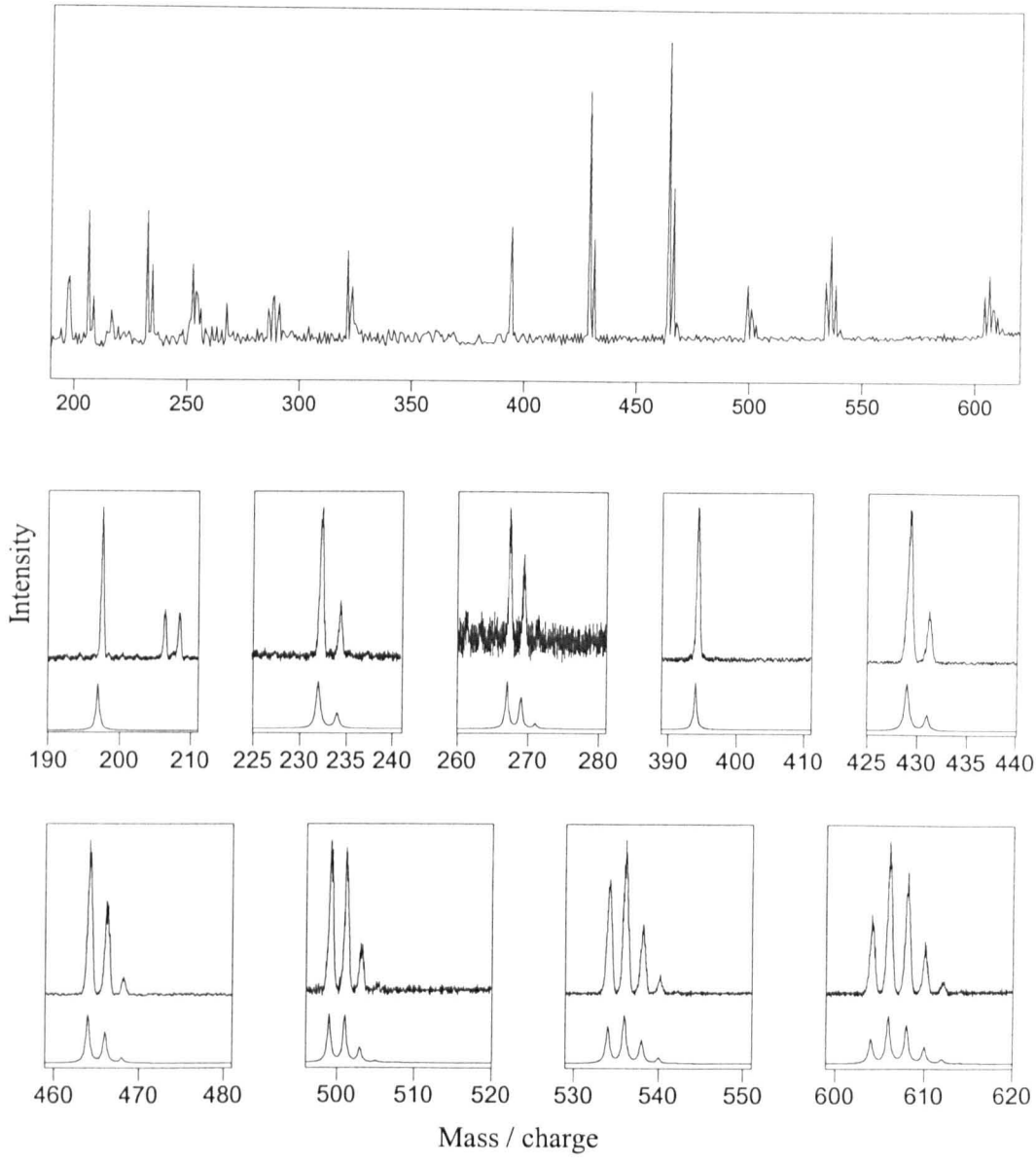

Mass	Assignment	Mass	Assignment	Mass	Assignment
197	Au^+	394	Au_2^+	499	$Au_2Cl_3^+$
232	$AuCl^+$	429	Au_2Cl^+	534	$Au_2Cl_4^+$
267	$AuCl_2^+$	464	$Au_2Cl_2^+$	604	$Au_2Cl_6^+$

Figure 4.3: mass spectrum of the vapour above gold (III) chloride with assingments. (a) observed mass spectrum, (b) predicted mass spectrum.

mass units) are assumed to be due to the presence of impurities. These peaks are observed at different relative intensities in consecutive spectra when compared to the gold chloride peaks and are thought to be due to residual sample from previous experiments. A good example of the relative intensity difference in these impurity peaks is shown by the 206 peak which can be seen in the truncated mass spectrum to be of a proportionally different intensity when compared to the adjacent gold peak than it is in the whole mass spectrum given at the top of figure 4.3. These spectra were recorded separately and illustrate that this impurity band is not due to a gold chloride mass ion.

The infrared spectrum of the gold (III) chloride sublimation products isolated in an argon matrix at 12 K is shown in figure 4.4 with the assignments given in the table below.

Observed	**Reported solid state value[33]**	**Predicted gas phase value[33]**	**Assignment[33]**
$^{\blacklozenge}$386 cm^{-1} ($395.4\ cm^{-1}$, $389.6\ cm^{-1}$, $385.7\ cm^{-1}$, $377.5\ cm^{-1}$)	383, 373 cm^{-1}	379.2, 375.2 cm^{-1}	ν_{12}, ν_{16} (terminal Au-Cl stretch)
$^{\blacklozenge}$312 cm^{-1} ($314.7\ cm^{-1}$, $311.7\ cm^{-1}$, $308.8\ cm^{-1}$, $305.2\ cm^{-1}$)	313, 309 cm^{-1}	309.2, 307.1 cm^{-1}	ν_{13}, ν_{17} (bridging Au-Cl stretch).
*146.5 cm^{-1}	135 cm^{-1}	155 cm^{-1}	ν_9 (deformation)

$^{\blacklozenge}$approximate value of most intense peak, *tentative assignment.

Table 4.2: assignments of vibrational modes for Au_2Cl_6.

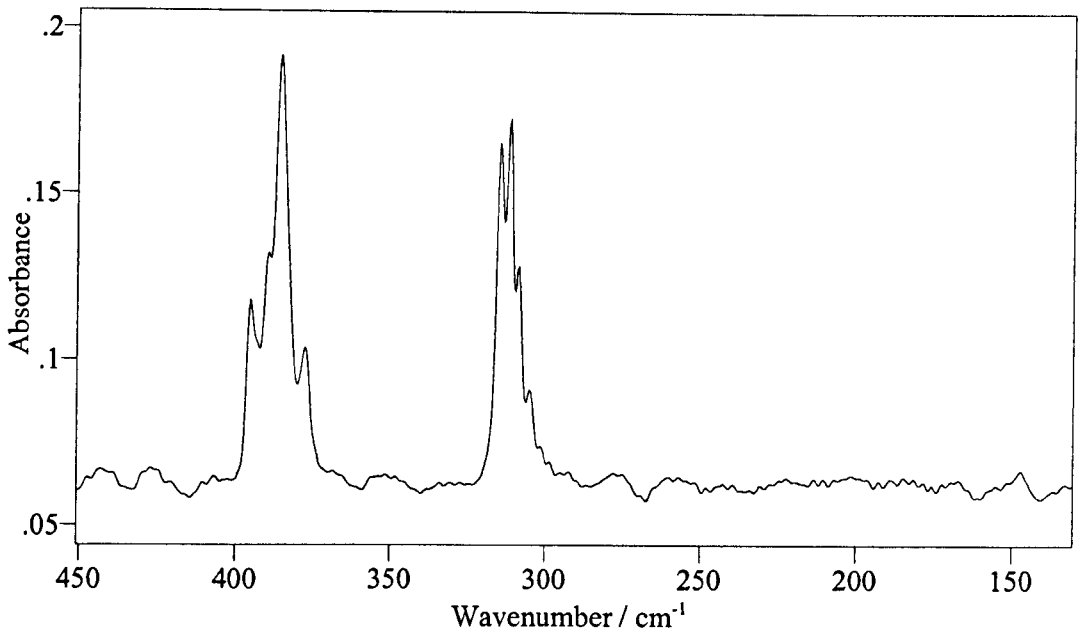

Figure 4.4: infrared spectrum of gold chloride sublimation products isolated in an argon matrix at 12 K.

Increasing the spectrometer resolution resulted in no improvement in the quality of the isotopic structure observed for the vibrational bands shown in figure 4.4 at 2 cm^{-1} resolution. The vibrational modes at 386 and 312 cm^{-1} are due to the vibration of the terminal and bridging Au-Cl bonds respectively, and each contains two vibrational modes within the band structure, which is complicated by the chlorine isotope pattern.

Along with the assignment of the two vibrational bands, the weak band at 146.5 cm^{-1} was tentatively assigned as a deformation mode of Au_2Cl_6. This assignment was based on the similar photolytic behaviour of this weak band in comparison to the stretching modes. Unfortunately the weak intensity of the band prevented the observation of any isotopic data contained within it.

Photolysis experiments showed the instability of the molecule to visible light as observed by Rustad and Gregory.[31] They observed that vapour phase Au_2Cl_6 was

dissociated by white light but recombined when it was left in the dark for a short time. The experimentally observed vibrational bands of the matrix isolated Au_2Cl_6 were also reduced in intensity after exposing the sample to combined UV and visible light but no spontaneous recombination was observed after leaving the sample for a short time (around 15 minutes) in the dark. The sample was then exposed to visible light, which caused a further reduction in the vibrational bands, presumably due to the further dissociation of the isolated molecule. On exposing the sample to ultra-violet light the bands increased in intensity, suggesting a recombination of the dissociated molecules. Annealing experiments only resulted in a further reduction in intensity of the vibrational bands caused by either loss of sample or the formation of multimers. No new bands were observed in the spectrum after photolysis or annealing.

The UV-Vis-NIR spectrum for matrix isolated gold (III) chloride (figure 4.5) confirms the assignment with the presence of two previously assigned intense ligand to metal charge transfer bands present in the spectrum and a close up of the low energy region (figure 4.5(b)) highlighting the presence of the weaker d-d transitions.

Observed frequency	Gas phase frequency[31]	Gas phase frequency[32]	Assignment[32]
46100 cm^{-1}	45045 cm^{-1}	45800 cm^{-1}	$M \leftarrow L_t^*$
40600 cm^{-1}	40983.6 cm^{-1}	41100 cm^{-1}	$M \leftarrow L_b^*$
32900 cm^{-1}		32000 cm^{-1}	d-d transition
22300 cm^{-1}	21739.1 cm^{-1}	21700 cm^{-1}	d-d transition

**metal - ligand charge transfer bands (L_t terminal ligand, L_b bridging ligand).*

Table 4.3: electronic transition band assignments for gold (III) chloride in an argon matrix at 12 K.

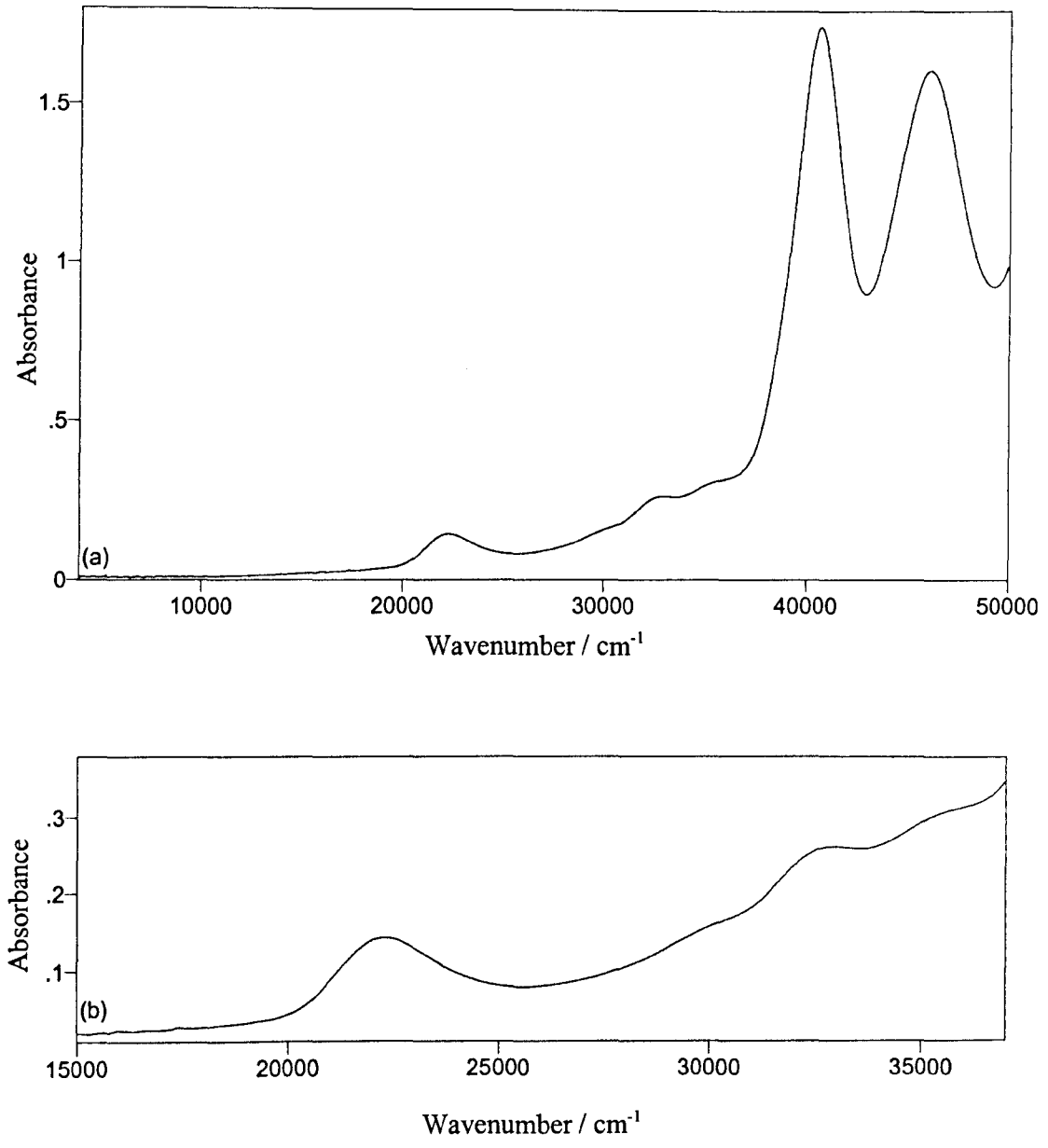

Figure 4.5: UV-Vis-NIR spectrum of gold (III) chloride in argon at 12 K.

Sputtering Experiments

In an attempt to make monomeric gold chloride, sputtered gold atoms were isolated in an argon matrix at 10 to 13 K with dilute amounts of chlorine.

a) UV-Vis-NIR Results

Figure 4.6 shows the UV-Vis-NIR spectrum of gold sputtered with argon and condensed at 13 K on a calcium fluoride window. The results are in good agreement with those previously reported and assigned using both argon and nitrogen matrices by Gruen and Bates[39(a)] and show no evidence of the presence of dimeric species.[39(b)]

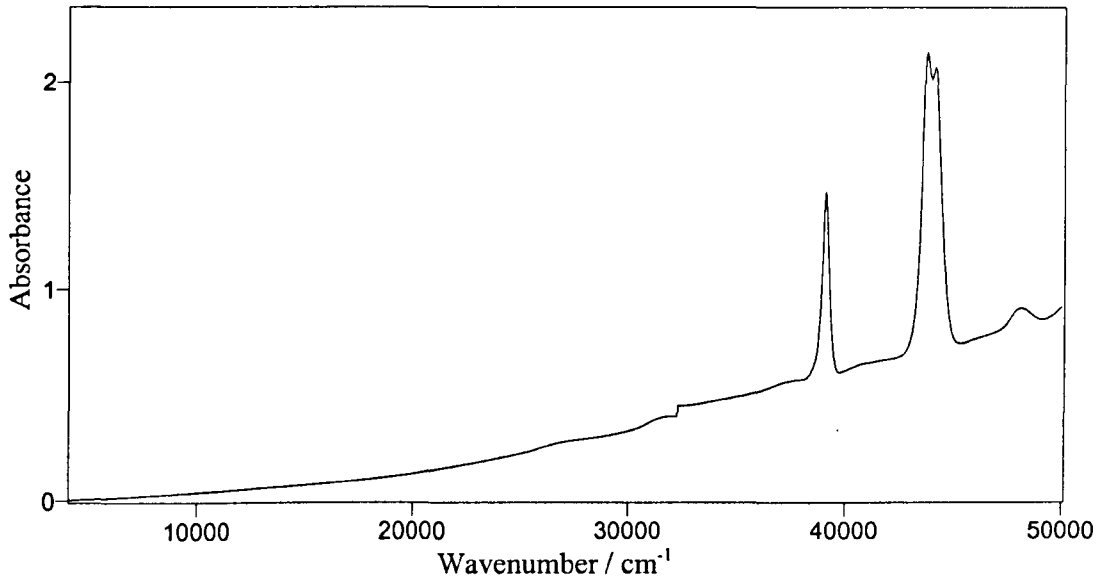

Figure 4.6: UV-Vis-NIR spectrum of gold atoms isolated in argon at 13K.

Observed	Reported[39(a)]	Assignment[39(a)]
39120 cm^{-1}	39175 cm^{-1}	E_1 ($^2P_{1/2}$)
43782 cm^{-1}	43763 cm^{-1}	E_2 ($^2P_{3/2,3/2}$)
44128 cm^{-1}	44375 cm^{-1}	E_2 ($^2P_{3/2,1/2}$)

Based on ^2S ground state.

Table 4.4: electronic transitions of isolated gold atoms in an argon matrix.

It is clear from this spectrum that the sputtering of gold foil inside a hollow copper cathode was in fact producing isolated gold atoms without traces of the underlying copper. When small concentrations of chlorine were added to the argon, subtle changes occurred in the UV-Vis-NIR spectrum which pointed towards a possible reaction between the gold atoms and chlorine. Figure 4.7 shows the UV-Vis-NIR spectra of gold atoms sputtered with 1 % and 5 % Cl_2 in argon. They are shown along with the observed spectra after a similar deposition time of 1 % and 5 % chlorine in argon matrix without the deposition of gold atoms. Subtraction spectra were attempted using these results but provided no additional clarity.

The 1 % chlorine in argon spectrum clearly displays the major atomic transitions of isolated gold atoms, along with a broad band at around 29000 cm^{-1} which was due to chlorine (band centre of gas phase chlorine is 30300 cm^{-1}).[19] In addition to these features, new bands are also present at 40000 cm^{-1} and 16000 cm^{-1}. These new bands, and importantly the vibrational fine structure present on the 16000 cm^{-1} absorption, indicate molecule formation, with the higher energy band clearly in the charge transfer region and the lower energy band more likely to arise from a d-d transition. When the chlorine concentration was increased to 5 % the spectrum clearly displayed the more intense chlorine band but with a noticeable absence of the atomic transitions. Signs again of molecular formation were evident in the lower energy band with vibrational fine structure again present at 16000 cm^{-1} along with a sharper band at 42000 cm^{-1}. The loss of light above 45000 cm^{-1} was a result of the increased chlorine concentration in the matrix absorbing and scattering light above that frequency. The frequencies of the peaks of the vibrational fine structure present on the 16000 cm^{-1} band are given in tables 4.5 and 4.6 along with the frequencies of the other bands present.

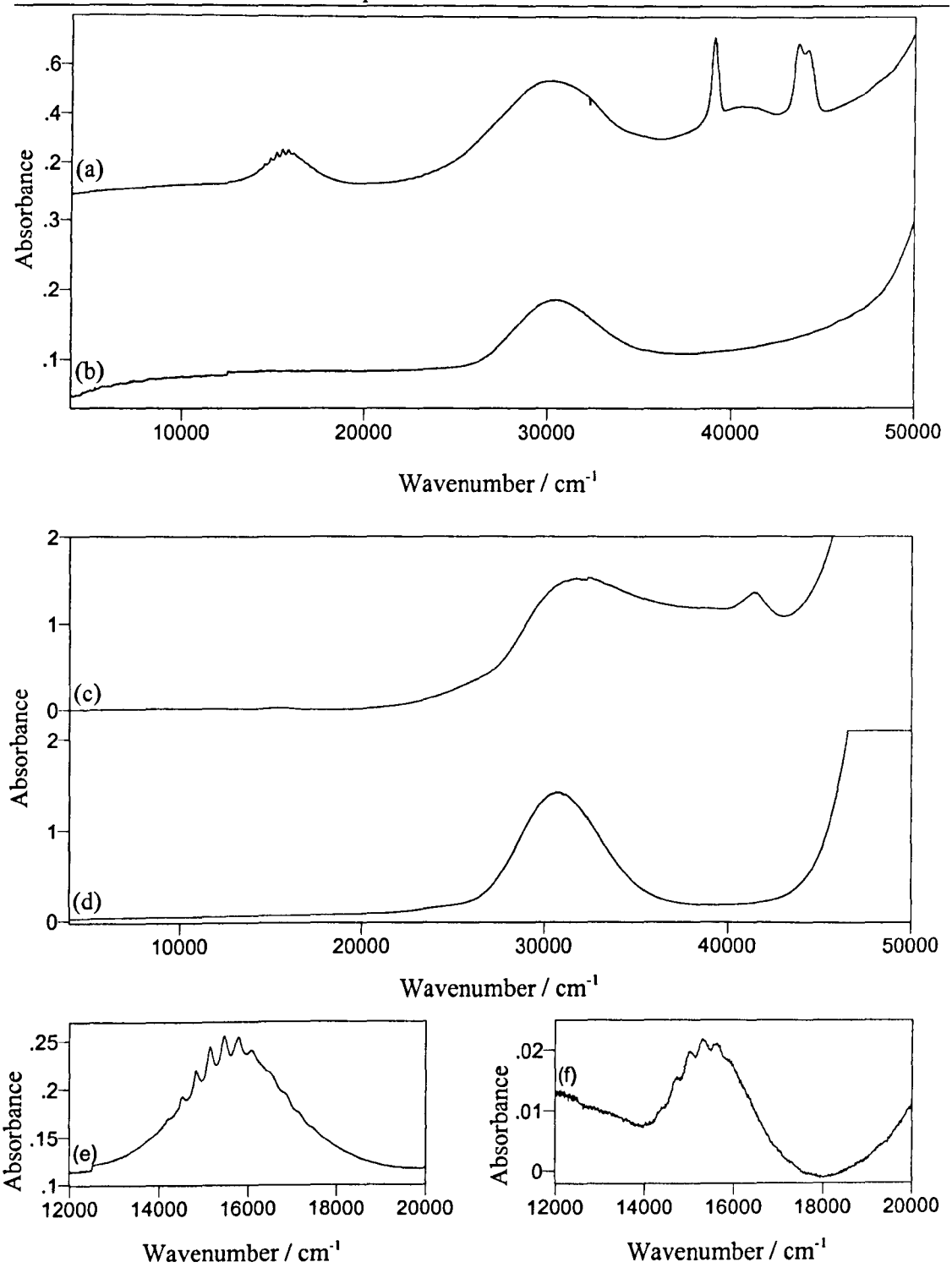

Figure 4.7: UV-Vis-NIR spectra of gold atoms isolated in chlorine doped argon matrices at 13K.

(a) gold atoms in 1 % chlorine in argon, (b) 1 % chlorine in argon matrix, (c) gold atoms in 5 % chlorine in argon, (d) 5 % chlorine in argon matrix, (e) 1 % chlorine in argon - expansion, (f) 5 % chlorine in argon - expansion.

Wavenumber / cm^{-1}	Assignment
44200	Au
43700	Au
40000	Au_xCl_y?
39080	Au
30000	Cl_2
16000	Au_xCl_y?
vibrational fine structure:	
16081	
15787	Average peak gap
15458	312 cm^{-1}
15146	
14833	
14521	

Table 4.5: UV-Vis-NIR data for Au atoms isolated in a 1 % Chlorine in argon matrix at 12 K.

Wavenumber / cm^{-1}	Assignment
42000	Au_xCl_y?
31000	Cl_2
16000	Au_xCl_y?
vibrational fine structure:	
15610	
15307	Average peak gap
15020	294 cm^{-1}
14729	

Table 4.6: UV-Vis-NIR data for Au atoms isolated in a 5 % Chlorine in argon matrix at 12 K.

The fine structure describes the vibrational energy levels of the excited state of the 16000 cm^{-1} transition and suggests the formation of an excited state species with a symmetric vibrational frequency of around 300 cm^{-1}. Since the band at 16000 cm^{-1} is also less intense in the 5 % Cl_2 spectrum than in the 1 % it may also suggest the formation of a second species, prevalent at lower concentration but less so as the chlorine concentration is increased. This may be compensated for slightly by the fact that the 1 % Cl_2 spectrum was recorded after 30 minutes deposition and the 5 % spectrum after only 15 minutes, making the intensity difference somewhat misleading. The supposition that this band is due to a d-d transition is based only on the fact that at 16000 cm^{-1} it is rather too low in energy to be a charge-transfer band. If this is accurate then the relative intensity is too great to be due to a molecule containing an inversion centre because of the La Porte selection rule. One could therefore assume that the molecule formed is not linear $AuCl_2$ or square planar $AuCl_4$. The presence of this band also makes it unlikely that the molecule is AuCl as Au^I is d^{10} and therefore has no d-d transitions.

From these results it was inferred that lower chlorine concentrations (1 %) do provide some molecular species, which since the only constituents of the matrix are gold, chlorine and argon, must be some form of gold chloride. However, it was evident from the spectrum that not all the gold atoms had reacted with the chlorine by the continued presence of atomic transitions in the spectrum. The presence of atomic bands in the 1 % matrix suggests that not enough chlorine is present in the average matrix site for each gold atom to react. When larger concentrations of chlorine were added (5 %) it appeared that the majority of the atoms had reacted, since there were no obvious atomic transitions present. It can therefore be assumed that a dopant level of 5 % is sufficient for all traces of isolated gold atoms to be removed from the

spectrum, presumably due to the combination of the atoms with the dopant leading to the formation of molecular species. What is unclear at this stage is the actual identity of the gold chloride being formed. Different energies of the transitions are observed in the 1 % and 5 % spectra at higher energies which points towards different species being formed. However, changing the concentration of the chlorine present in the matrix shifts the broad band due to chlorine by around 1000 cm^{-1}. This shift in energy is due to the matrix effects discussed earlier and could also explain the different transition energies observed for the other bands.

At this stage it was clear that a reaction was occurring between the gold and chlorine atoms isolated in the matrix forming a molecule which was unlikely to be the dimer due to the new band present at 16000 cm^{-1}, although it cannot be completely ruled out due to the majority of the spectrum at higher energy being obscured by to the presence of chlorine.

b) Infrared Results

Infrared analysis was applied to assist in the confirmation of the gold chloride formed. The result of sputtering of gold with various dilute concentrations of chlorine in argon are shown in figure 4.8.

5 % Cl_2 in argon was used at first since it was thought that the atoms were the yield determining content of the matrix and the UV-Vis-NIR spectrum of 5% chlorine showed no sign of atomic transitions. The infrared spectrum (figure 4.8(a)) shows one major feature at 420 cm^{-1} accompanying the bands at 546.7, 539.5 and 532.3 cm^{-1} which can be assigned as the activated Cl-Cl stretch of molecular chlorine, previously assigned at 538.6, 531.0 and 523.5 cm^{-1}.[40] The previously reported position of the Cl_2 bands differs from the observed results by around 8 cm^{-1}.

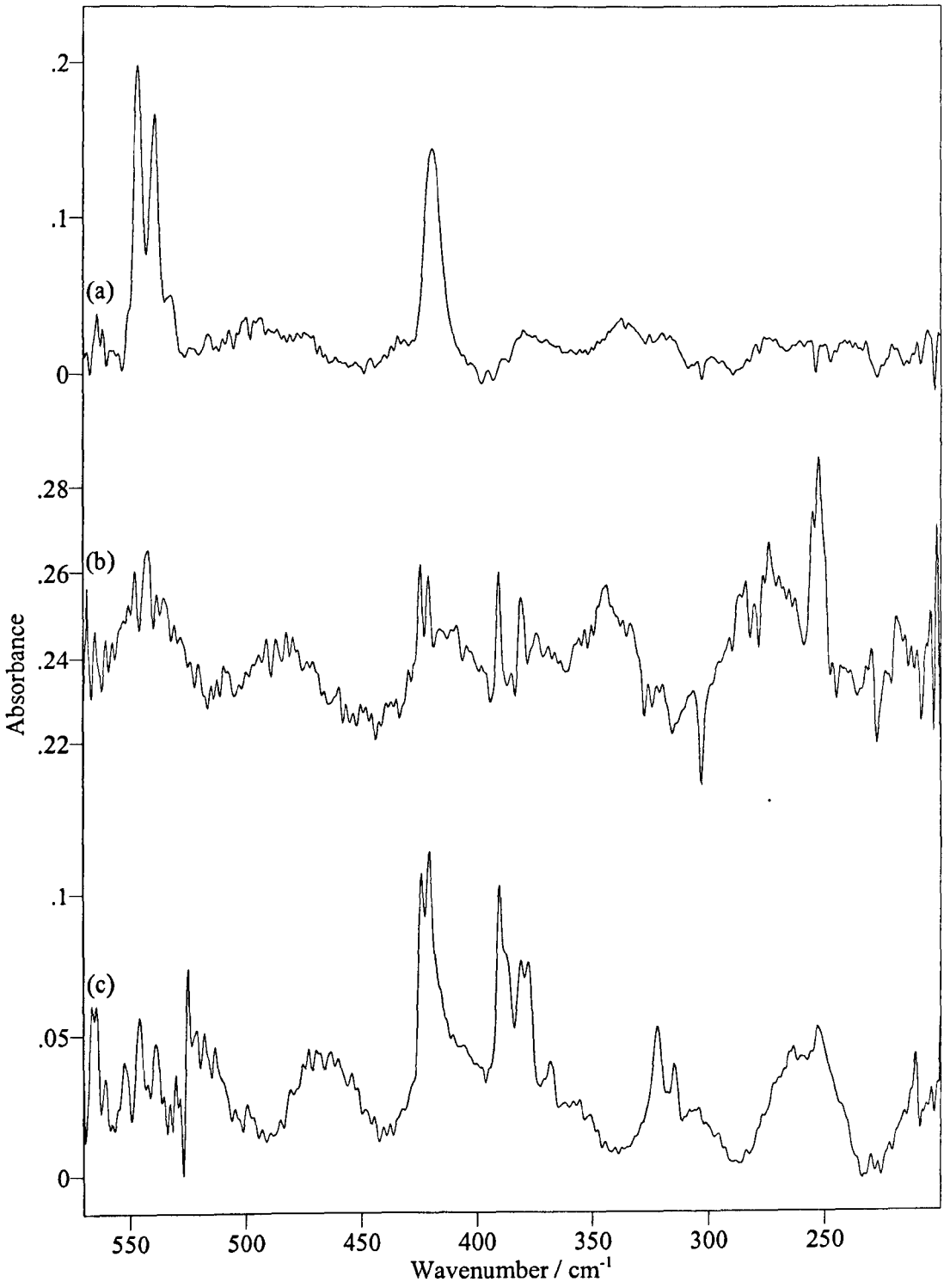

Figure 4.8: infrared spectra of sputtered gold isolated in dilute chlorine / argon matrices. (a) 5 % chlorine in argon, (b) 1 % chlorine in argon, (a) 3 % chlorine in argon,

Again this is probably due to the chlorine present in the matrix, with the reported results recorded using a dopant level of 1 % Cl_2 in argon rather than 5 %. Unfortunately the peak at 420 cm^{-1} could not be further resolved due to the perturbing nature of a 5 % Cl_2 in argon matrix causing broadening of the vibrational band, it does however suggest the formation of one major species. The lack of any other infrared active band allows possible structures for the gold chloride formed to be ruled out. It is now unlikely that the molecule formed is bent $AuCl_2$ as two active vibrational modes are expected, although if the molecule was only partially bent the symmetric stretch would be of very low intensity and if it was bent to 90° then the 2 modes could overlap. For similar reasons both 'T-shaped' and trigonal pyramidal $AuCl_3$ are unlikely, although again the second vibrational mode may be too low in intensity to be identified.

What could be confirmed from this result was that sputtered gold atoms isolated in dilute chlorine / argon matrices were not providing the same result as the isolation of the sublimation products from solid gold (III) chloride. Since reduction of the chlorine concentration would hopefully improve the resolution of the vibrational band, lower concentrations of chlorine were employed in an attempt to observe the underlying isotopic structure. As expected from the UV-Vis-NIR data, lowering the chlorine concentration lowered the amount of atoms that reacted and in effect lowered the yield to an extent where the bands were not strong enough to be assigned to any particular species, as is shown in the 1 % chlorine in argon spectrum (figure 4.8(b)). The experiments with 1 % chlorine did however appear to be providing evidence that at lower chlorine concentrations more than one species was present. The chlorine concentration was then increased in order to increase the intensity of the bands present in 1 % chlorine, but without losing the resolution. The

best result was achieved with 3 % chlorine in argon (figure 4.8(c)) and clearly shows multiple bands which are presumably due to different species, along with sharper bands, helping to more clearly define the underlying isotopic structure. Unfortunately higher resolution scans still proved ineffective at this concentration and the isotope patterns could not be further resolved. It is also possible that the new bands observed could be due to the formation of Au_2Cl_6 as they occur at a similar frequency even though they are clearly absent from the 5 % chlorine in argon spectrum. A table of the observed infrared frequencies is listed in table 4.7 below.

5 % Cl_2 in argon	1 % Cl_2 in argon	3 % Cl_2 in argon
546.7 cm^{-1}		
539.5 cm^{-1}		
532.3 cm^{-1}		
419.4 cm^{-1}	424.5 cm^{-1}	424.0 cm^{-1}
	420.9 cm^{-1}	420.5 cm^{-1}
	390.5 cm^{-1}	390.1 cm^{-1}
	380.9 cm^{-1}	380.9 cm^{-1}
	252.6 cm^{-1}	377.8 cm^{-1}
		368.0 cm^{-1}
		321.8 cm^{-1}
		314.8 cm^{-1}

Table 4.7. Observed infrared frequencies after the deposition of gold atoms in 1 %, 5 % and 3 % Cl_2 in argon matrices at 12 K.

c) XAFS Results

To assist in the characterisation of the matrix isolated gold chloride, XAFS analysis was applied to the products formed when sputtering gold with 5 % chlorine in argon. Since XAFS analysis becomes more complicated when dealing with

multiple species these experiments were completed using 5 % chlorine in argon only, as this was thought to provide only one major product.

As a comparison with the XAFS spectra obtained from the sputtering experiments a spectrum of aurochloric acid ($H[AuCl_4].3H_2O$) was recorded. The sample was ground to a fine powder and diluted with boron nitride (BN) before being mounted in a sample plate. The EXAFS oscillations and Fourier Transform (FT) produced for the model compound are shown in figure 4.9 with the fitting parameters outlined in table 4.8 below.

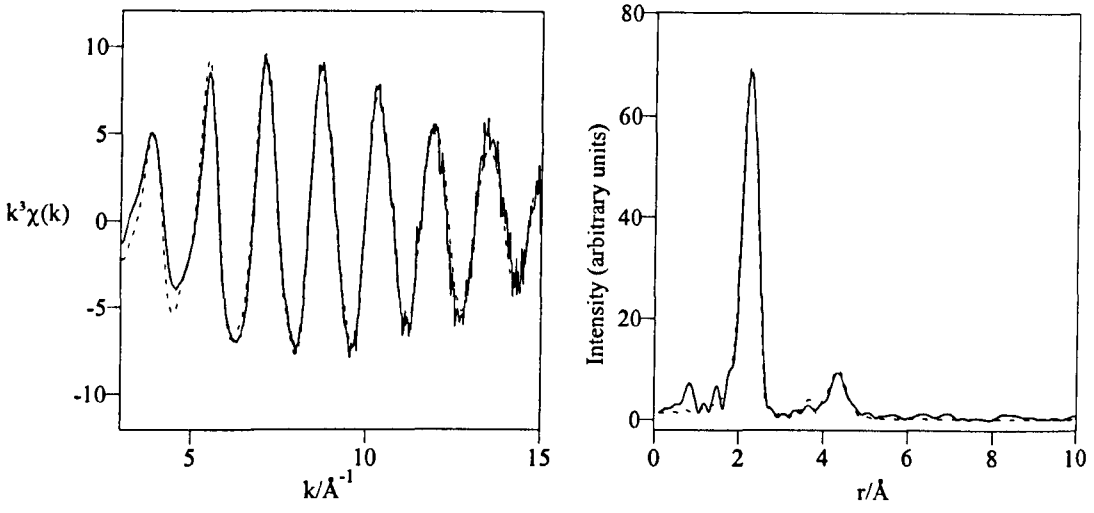

Figure 4.9: Au L_3-edge EXAFS and Fourier Transform for $H[AuCl_4].3H_2O$ in BN at room temperature.

(——— observed, ····· theoretical)

r_{Au-Cl} / Å	$2\sigma^2_{Au-Cl}$ [a] / Å²	E_f [b] / eV	R
2.282 (2)	0.006 (0.2)	-11.7 (4)	19

[a] *Debye-Waller factor,* [b] *Reflection of differences in experimental and theoretical Fermi levels.*

Table 4.8: refined EXAFS parameters for $H[AuCl_4].3H_2O$ in BN at room temperature.

The theoretical best fit data, which were fixed to a co-ordination number of four to allow multiple scattering to be taken into account, identified the average gold environment to be one which is surrounded by four chlorine atoms at a distance of 2.282 Å. The feature at around 4 Å is a multiple scattering feature at double the bond length which confirms the linearity of the Cl-Au-Cl units within the molecule. The relatively low Debye-Waller and E_f values are also acceptable for a reasonably well defined solid, with the low R factor reflecting the use of multiple shells in the refinement. These results are in good agreement with the previously reported crystal structure of $H[AuCl_4].4H_2O$[41] which shows a square planar $[AuCl_4]^-$ structure with Au-Cl bond lengths of 2.283 and 2.286 Å. Further refinement including the co-ordination number (N_1) is given in table 4.9. The data refinement shows the co-ordination number of 4 given in the initial refinement to be accurate.

r_{Au-Cl}	$2\sigma^2_{Au-Cl}$[a] / Å^2	E_f[b] / eV	N_1[c]	R
2.282 (2)	0.005 (0.5)	-11.9 (6)	3.6 (2)	24

[a] *Debye-Waller factor,* [b] *Reflection of differences in experimental and theoretical Fermi levels,* [c] *co-ordination number.*

Table 4.9: EXAFS parameters For H[AuCl4].3H$_2$O in BN at room temperature with co-ordination number refined.

The EXAFS oscillations and the Fourier transform observed from the XAFS sputtering experiments are shown in Figure 4.10. Experimental results were found to provide no reasonable fit for any Au-Au or Au-Ar_{matrix} interactions, providing further evidence for the formation of a monomeric gold chloride. By refining the EXAFS parameters a best fit for the data was found and is given table 4.10 with the EXAFS and Fourier Transform displayed in figure 4.10(a).

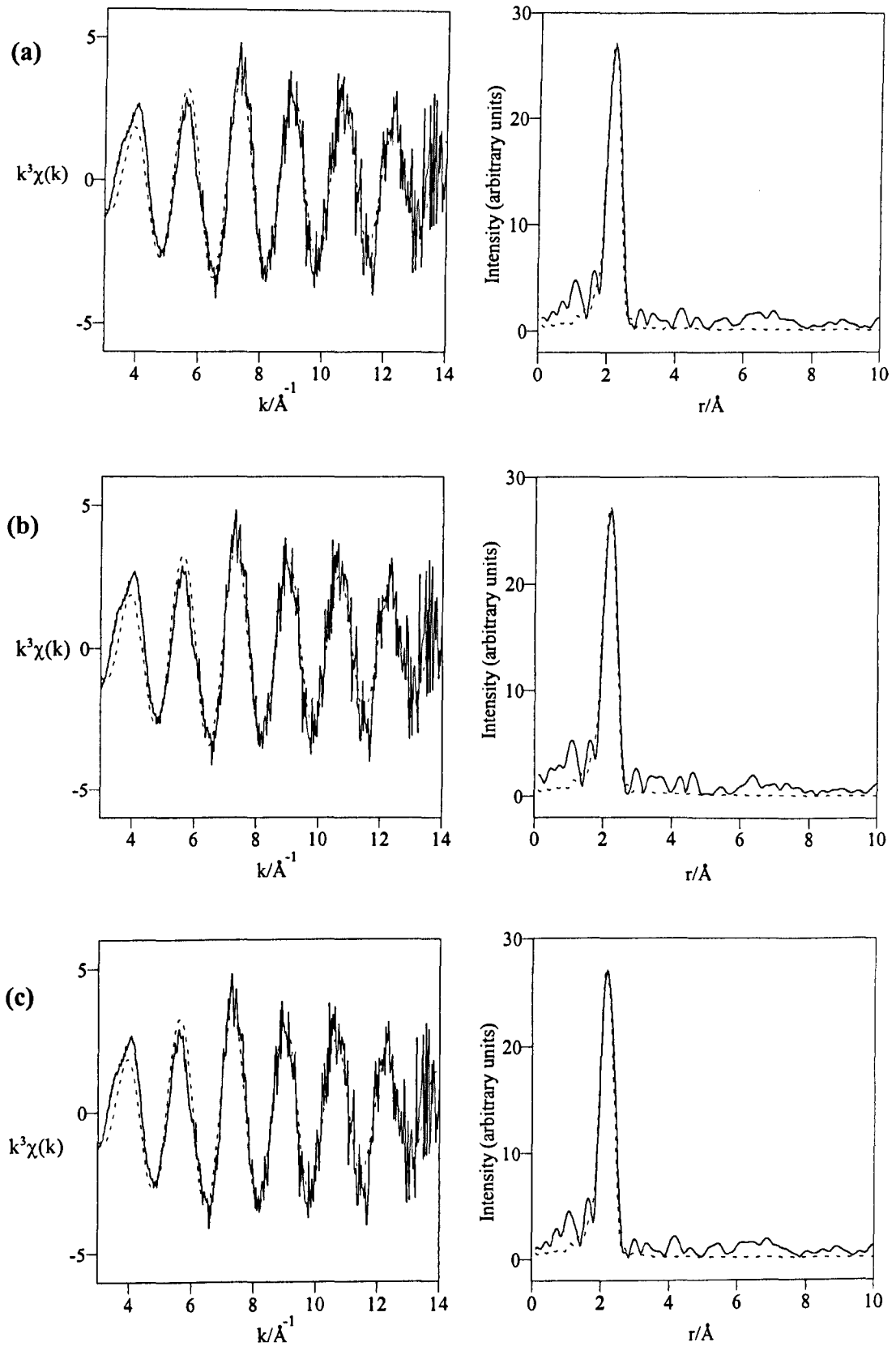

Figure 4.10: Au L_3-edge EXAFS and Fourier Transforms for gold sputtered with 5% Cl_2 in argon at 12 K.

(a) single cluster refinement, (b) $AuCl_3$ and AuCl, (c) $AuCl_3$ and Au.

(——— observed, - - - - - theoretical)

r_{Au-Cl}	$2\sigma^2_{Au-Cl}$ [a] / Å^2	E_f [b] / eV	N_1 [c]	R
2.228 (+2)	0.006 (0.2)	-11.7 (4)	1.7 (2)	41

[a] *Debye-Waller factor,* [b] *Reflection of differences in experimental and theoretical Fermi levels,* [c] *co-ordination number.*

Table 4.10: refined EXAFS parameters for gold atoms in a 5 % chlorine in argon matrix at 12K.

The refinement has clearly produced an experimental best fit with the co-ordination number (N_1) refined providing evidence of the presence of a gold dichloride. However, since previous work[2,9,10] has established that Au^{II} is a less stable oxidation state and the dichloride is unlikely to form, then other factors must be taken into account. Since the EXAFS data provides only details of the average gold environment the presence of species with a lower co-ordination number in the matrix would artificially reduce the oxidation state of the main component. By including more than one cluster in the EXAFS calculations multiple species could be taken into account and the refinement recalculated. Since the major species is most likely to be $AuCl_3$ the refinement was recalculated with either AuCl or Au atoms also present. Refining the value of N_0 (the contribution from gold atoms of the main cluster) whilst maintaining that the value of N_2 (the contribution from gold atoms of the second cluster) to 1 - N_0 effectively calculates the contribution to the EXAFS made by each cluster. So for a matrix containing $AuCl_3$ and AuCl the contribution from the gold atom in $AuCl_3$ molecules (N_0) is refined whilst maintaining that the total number of gold atoms in the refinement never exceeds unity. Figure 4.10(b) shows the EXAFS and Fourier Transform for this refinement. To alter the parameters and complete the refinement for a matrix containing $AuCl_3$ and Au atoms the co-

ordination number of the second gold cluster was changed to 0.01, i.e. removing all chlorine co-ordination to the second gold centre. The results of this refinement are plotted in figure 4.10(c) with the data for both refinements shown in table 4.11 below.

	r_{Au-Cl}	$2\sigma^2_{Au-Cl}$[a] / Å^2	E_f[b] / eV	N_0[c]	R
$AuCl_3$ and AuCl	2.228 (6)	0.006 (1)	-8 (1)	0.42 (4)	41
$AuCl_3$ and Au	2.224 (6)	0.007 (1)	-8 (1)	0.56 (5)	41

[a] Debye-Waller factor, [b] Reflection of differences in experimental and theoretical Fermi levels, [c] contribution from the gold atoms of $AuCl_3$.

Table 4.11: refined EXAFS parameters for $AuCl_3$ with AuCl or Au atoms in an argon matrix at 12K.

Comparison of the data in the table above demonstrates a similar fit when the calculation involves multiple clusters is compared to the refinements with a single species, either $AuCl_2$ or $AuCl_3$. This suggests the formation of $AuCl_3$ in the matrix along with AuCl or gold atoms is acceptable, with the latter providing marginally better data fitting and suggesting a matrix in which 56% of the gold present is in the form of $AuCl_3$ with a bond length of 2.22 Å.

On the assumption that the major species formed is $AuCl_3$ further calculations can be completed to help determine the geometry of the molecule formed by including multiple scattering in the calculations. Figure 4.11(a) shows the EXAFS oscillations and Fourier Transform for the 'T-shaped' $AuCl_3$ molecule in comparison to the experimentally observed EXAFS. The absence of the predicted multiple scattering feature at twice the bond length in the theoretical Fourier Transform suggests that the previously predicted shape of $AuCl_3$[22] does not correspond to the geometry of the molecule formed in the sputtering experiments. However, figure

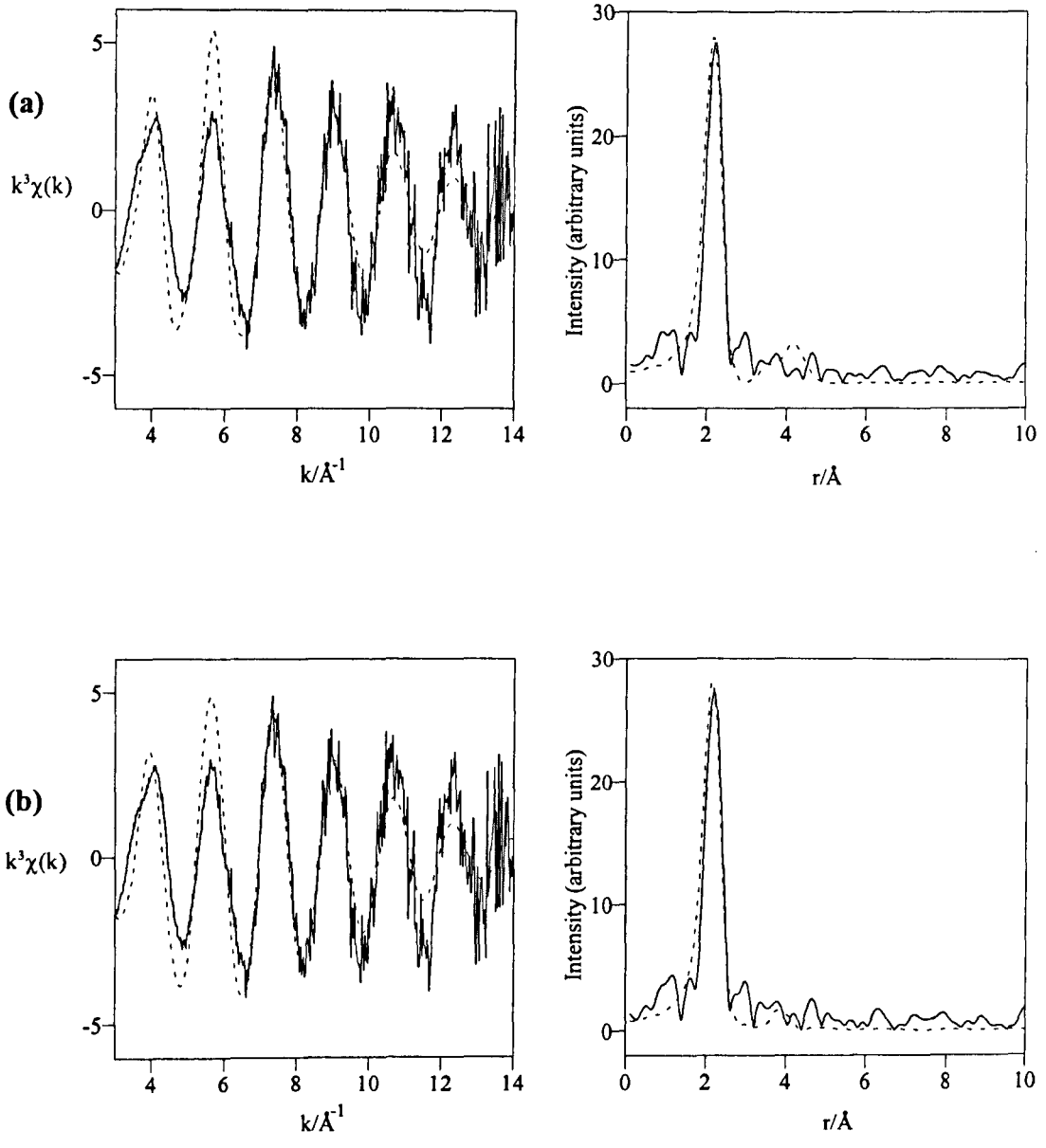

Figure 4.11: Au L_3-edge EXAFS and Fourier Transforms for $AuCl_3$ in argon at 12 K with multiple scattering.

(a) 'T-shaped' (b) pseudo 'T-shaped'

(——— observed, - - - - - theoretical)

4.11(b) shows the EXAFS and Fourier Transform predicted when the linear Cl-Au-Cl bond in the 'T-shaped' molecule is bent by only 20° from 180° to 160°. The multiple scattering feature at a distance of twice the bond length is still present but below the noise level. It is therefore possible that the molecule formed is Jahn-Teller distorted from trigonal planar as previously predicted[22] but does not convert to a complete 'T-Shaped' geometry with a precisely linear Cl-Au-Cl bond.

The fitting parameters obtained from the EXAFS refinements for the 'T-shaped' and *pseudo* 'T-Shaped' ('Y-shaped') $AuCl_3$ molecules are given in the table below.

	r_{Au-Cl}	$2\sigma^2_{Au-Cl}{}^a$ / Å^2	$E_f{}^b$ / eV	R
'T-shaped' $AuCl_3$	2.222 (7)	0.015 (1)	-6 (1)	51
pseudo 'T-Shaped'	2.221 (7)	0.015 (1)	-6 (1)	51

[a] Debye-Waller factor, [b] Reflection of differences in experimental and theoretical Fermi levels.

Table 4.12: refined EXAFS parameters for $AuCl_3$ in an argon matrix at 12 K with multiple scattering - 'T-shaped' and pseudo- 'T-Shaped'.

Figure 4.12 below shows the XANES (x-ray absorption near-edge structure) spectra of the model compound $H(AuCl_4).3H_2O$ compared to the edge observed after the sputtering experiments. The edge step observed from gold foil (0.25 mm thick) is also shown for comparison and the edge positions are given in the accompanying table.

The white line intensity (the intensity of the pre-edge feature) observed in the model compound corresponds to an atomic transition ($2p_{3/2}$ to 5d and 6s). Previous work on Au XANES spectra[42] reports the white line intensity to be significant in terms of the oxidation state of the gold atom. The reduced spatial overlap between s and p-orbitals when compared to d and p-orbitals makes the electronic transition

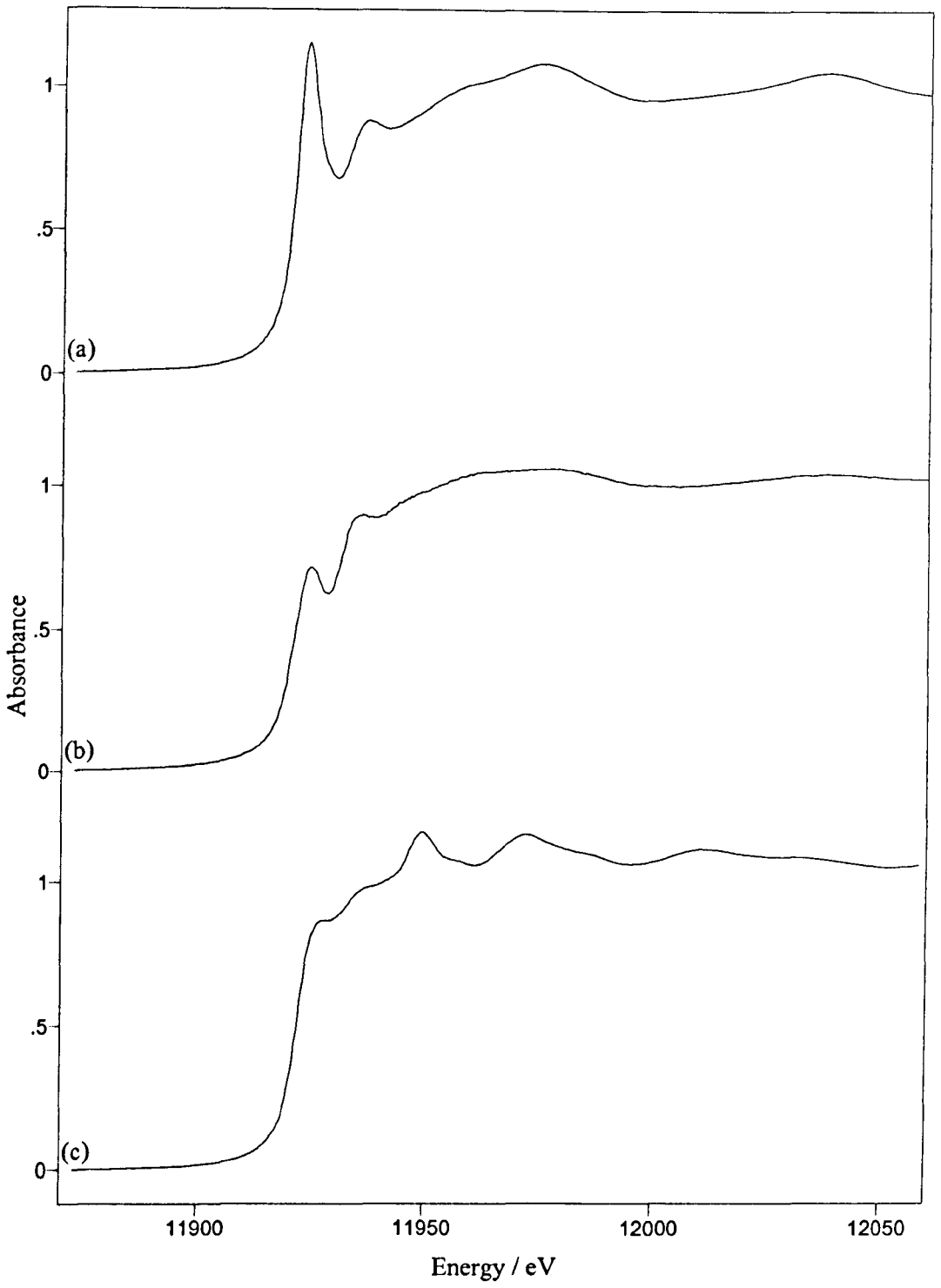

Figure 4.12: Au L_3-edge XANES spectra observed in gold XAFS experiments.

(a) $H(AuCl_4)$ in BN at room temperature.

(b) Sputtered sample of gold atoms in a 5 % chlorine in argon matrix at 12 K.

(c) 0.25 mm gold foil at room temperature.

weaker, and therefore the white line intensity is assumed to be diagnostic of the $2p_{3/2}$ to 5d transition. Since gold foil and AuCl have closed d-shells (d^{10} $6s^1$ and d^{10} $6s^0$ respectively) this transition is orbitally forbidden and the pre-edge feature is of much lower intensity. This evidence suggests that the sputtered sample also contains gold in a lower oxidation state, as the pre-edge feature is significantly weaker than that observed from the sample of gold (III) chloride. The presence of atomic species which is assumed from the previous results in this section would compensate for this, making the white line intensity reasonable for a mixture of Au^{III} and Au^0. Although this reasoning would explain the intensity differences it could also simply be due to the different orbital occupancy between D_{4h} and D_{3h} molecules (D_{4h} has an empty $d_{x^2-y^2}$ orbital whereas D_{3h} has two half empty d_{xy} and $d_{x^2-y^2}$ orbitals).

The edge position should also assist in assigning the oxidation state of the gold present, as a shift to higher energy is expected as the gold oxidation state increases. Unfortunately the exact edge position is masked by the pre-edge feature at the Au-L_3 edge and the exact edge position cannot be determined precisely (although the estimated position is given in table 4.13).

Sample	Edge Position / eV
$H(AuCl_4).3H_2O$ in BN at 298 K	11920
Au in 5 % Cl_2 / Ar at 12 K	11913
Gold foil at 298 K	11919

Table 4.13: edge positions for gold XAFS experiments

Furnace Evaporation

Sputtering experiments show that isolated atoms of chlorine and gold will react to form a novel gold chloride which is most probably $AuCl_3$. The high gas flow rate required to maintain the sputtering discharge combined with the relatively high concentration of chlorine results in a poor matrix, resulting in broad absorption bands. Furnace evaporation experiments should allow atoms to be isolated in a matrix with a more controlled deposition rate. This should provide a more even and undistorted matrix environment and allow the isotopic structure contained within the vibrational absorption bands to be defined.

Figure 4.13 shows the UV-Vis-NIR spectra observed when the vapour species from heated gold foil on a tungsten filament furnace are trapped in argon and chlorine / argon matrices at 13 K.

The results show good agreement with those observed for the sputtering of gold with argon and chlorine / argon mixtures. Figure 4.13(a) shows clearly the absorption bands of isolated gold atoms in an argon matrix (39100 cm^{-1}, 43700 cm^{-1} and 44200 cm^{-1}). The spectrum for 1 % chlorine matrix shown in figure 4.13(b) is again in good agreement with the sputtering counterpart, with the presence of absorption bands due to gold atoms and chlorine (~ 31000 cm^{-1}) evident along with the weak band at 16000 cm^{-1} again showing vibrational fine structure.

When increasing the chlorine concentration to 5 % the UV-Vis-NIR spectrum observed is shown in figure 4.13(c). The increase in intensity of the band at 16000cm^{-1} shows signs of an increase in yield of the gold chloride but signs of unreacted gold are still evident with the presence of the atomic transition of gold at around 39000 cm^{-1} and as weak shoulders at around 44000 cm^{-1}. The feature

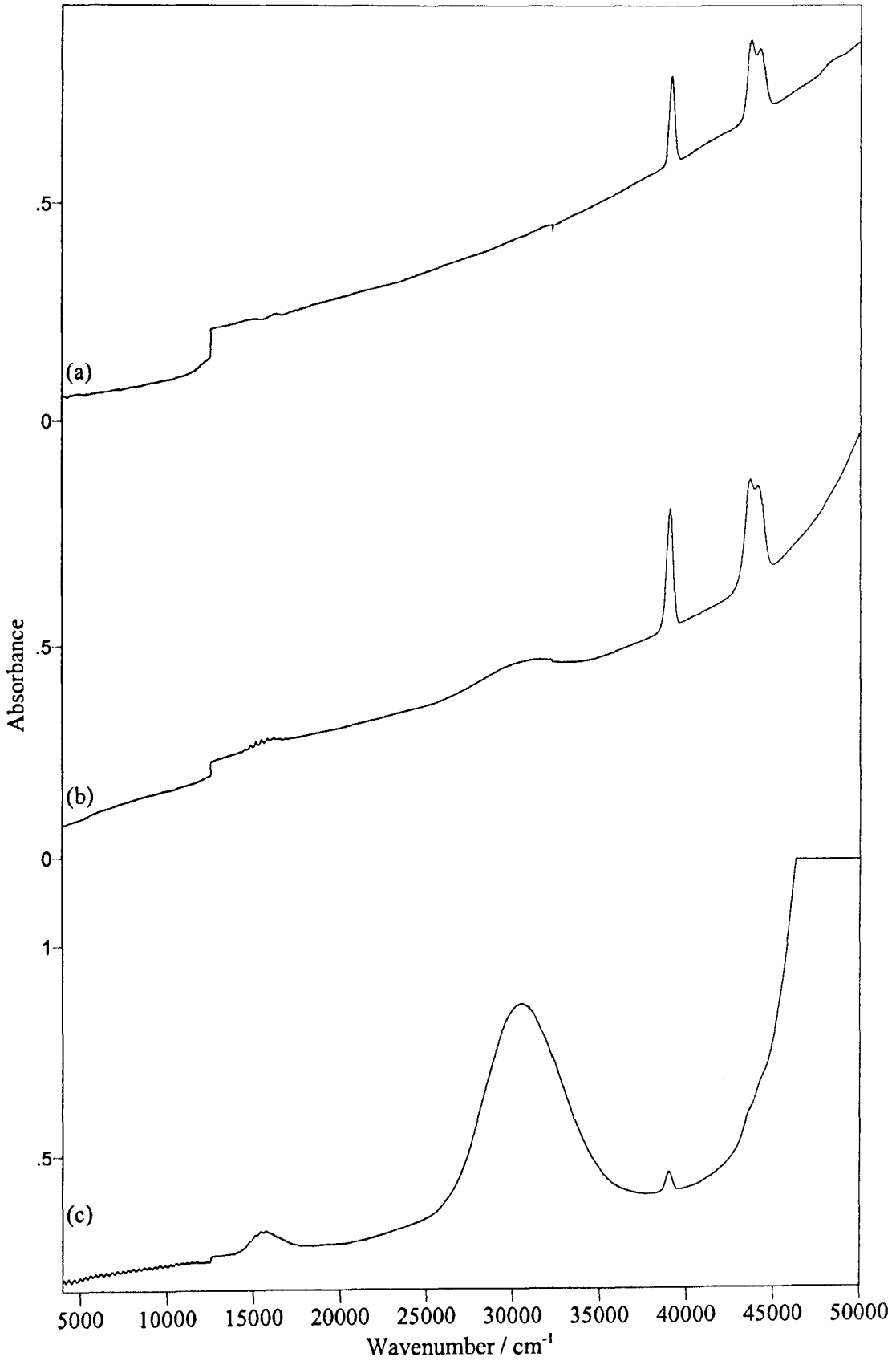

Figure 4.13: matrix isolation of gold vapour in Argon and chlorine / argon matrices at 13 K.

(a) argon matrix, (b) 1 % Cl_2 in argon matrix, (c) 5 % Cl_2 in argon matrix.

observed in the sputtering experiments at around 42000 cm^{-1} also appears to be absent from this spectrum.

argon	1 % Cl_2 in argon	5 % Cl_2 in argon
44240 cm^{-1}	44150 cm^{-1}	44300 cm^{-1}
43720 cm^{-1}	43670 cm^{-1}	43600 cm^{-1}
39130 cm^{-1}	39060 cm^{-1}	39040 cm^{-1}
	31500 cm^{-1}	30550 cm^{-1}
	15500 cm^{-1}	15500 cm^{-1}
	vibrational fine structure:	vibrational fine structure:
	14519 cm^{-1}	
	14832 cm^{-1}	
	15137 cm^{-1}	15109 cm^{-1}
	15462 cm^{-1}	15417 cm^{-1}
	15786 cm^{-1}	15697 cm^{-1}
	16513 cm^{-1}	
	16873 cm^{-1}	

Table 4.14. Observed UV-Vis-NIR frequencies after the deposition of gold atoms by furnace sublimation in argon, 1 % and 5 % Cl_2 in argon matrices at 12 K.

The overall yield of these experiments is apparently low, with deposition times needing to be increased by an order of magnitude to achieve the comparatively weak bands shown in figure 4.13. This increase in deposition time increases the light scattering caused by the matrix formation on the optical window, which in turn decreases the spectral quality. For this reason further furnace evaporation experiments were not completed in favour of an alternative metal atom source.

Laser Ablation

Laser ablation of a gold target was used as an atom source in the further investigations of the nature of the gold chloride formed by isolation of gold atoms in a chlorine containing argon matrix. Experimental constraints meant that all spectra could only be recorded on a PE983G IR spectrometer. This meant that the UV-Vis-NIR spectrum could not be recorded and that the scans produced were generally at lower resolution than those produced using the FTIR spectrometer. The infrared spectrum produced after laser ablation of a gold sample for 30 minutes with the products trapped in a 5 % Cl_2 chlorine in argon matrix is shown in figure 4.14.

The initial spectrum of the region 600 to 300 cm^{-1} is recorded at a resolution ranging between 7 and 10 cm^{-1} over the region scanned, with the average resolution being 8 cm^{-1}. Increasing the resolution also increased the noise level and thus a greater number of averaged scans were required. It is still evident that at the highest resolution shown in figure 4.14 that the noise level is high, making definite assignment of isotopic structure difficult to confirm. Scans such as figure 4.14(c) were recorded at 2 cm^{-1} resolution, the spectrum is plotted after 300 scans (recorded over a period of 14 hours).

Further laser ablation experiments at reduced chlorine concentration showed the formation of the same band at 420 cm^{-1} but with lower intensity, rather than bands of different energy as was observed with the sputtering experiments.

Although these experiments contain little new information they do provide evidence that sputtering and laser ablation give rise to identical products, as the 420 cm^{-1} band is clearly the dominant feature in both IR spectra. This offers an alternative source to the gold chloride which may lead to the determination of the underlying isotopic structure should the experimental conditions be improved.

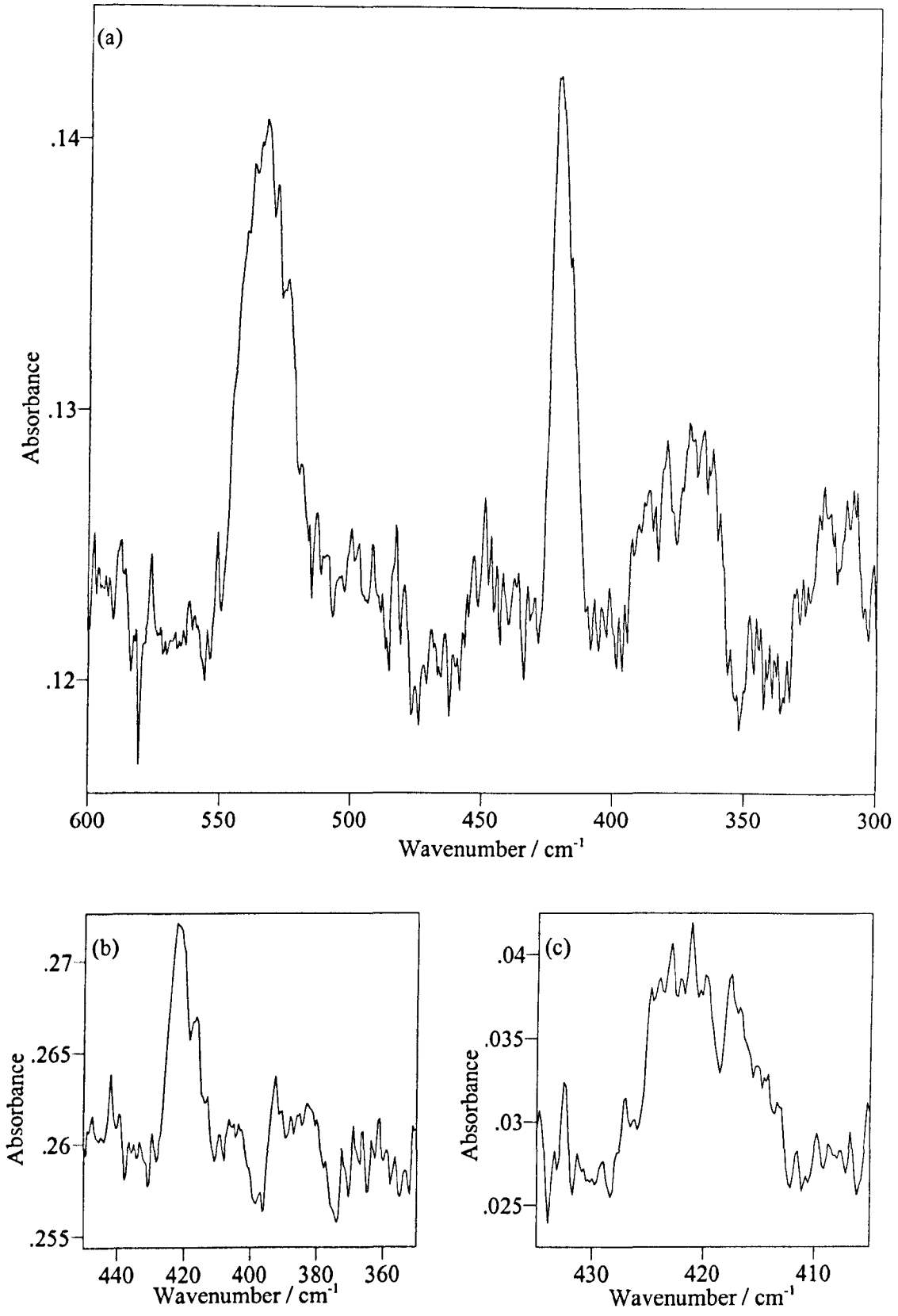

Figure 4.14: infrared spectrum of the isolated products formed by laser ablation of a gold target trapped in a 5 % Cl_2 / argon matrix at 12K.
(a) 8 cm^{-1} resolution, (b) 4 cm^{-1} resolution, (c) 2 cm^{-1} resolution.

Conclusion

These experiments have confirmed previous reports that the major gas phase species formed by the sublimation of gold (III) chloride is the dimer Au_2Cl_6. Mass spectrometry, UV-Vis-NIR and infrared spectroscopic data confirm the structure and shape of the dimer with the matrix isolation spectra of the molecule presented for the first time.

A sputtering source has been used effectively as a method of generating gold atoms which, when sputtered with an inert gas doped with a low concentration of chlorine, led to the formation of a gold chloride. It is clear from the spectra presented that the species formed is not the same as that produced from the furnace evaporation experiments with solid gold (III) chloride.

The gold chloride isolated has been investigated using FTIR, UV-Vis-NIR and EXAFS spectroscopy in order to fully characterise the species formed. The nature of the sputtering source was found to provide a matrix environment which prevented the characterisation being completed since the gas flow and dopant concentrations resulted in significant matrix perturbation. This led to the formation of a particularly distorting matrix environment and prevented the observation of the chlorine isotope pattern contained within the vibrational absorption bands.

In an attempt to determine the isotopic structure alternative atom sources were employed which allowed matrix gas flow rates to be reduced. The reduction of the flow rate should provide sharper bands which could be further resolved. Unfortunately neither furnace evaporation or laser ablation provided the information required, although both techniques did show signs of the gold chloride forming. Infrared analysis of the products formed with laser ablation showed the same species

forming, but unfortunately spectrometer limits meant the resolution required could not be achieved.

Although there can be no clear and unambiguous characterisation of the species formed on isolation of gold atoms in chlorine containing matrices, the evidence presented does offer some clues to its structure.

1) EXAFS experiments showed no reasonable gold-gold interaction, identifying the formation of a monomeric species. The co-ordination number provided by the EXAFS for the gold-chlorine interaction was originally refined to 2, but taking into account the presence of residual gold atoms or lower co-ordinate gold species this can easily be shown to be 3.

2) UV-Vis-NIR spectra show that the species formed does not have an inversion centre and is therefore not a linear molecule. This rules out all probable structures other than bent $AuCl_2$, $AuCl_3$, and tetrahedral $AuCl_4$. The consistency of the weak band at around 16000 cm^{-1} and the associated vibrational fine structure in both the 1 % and 5 % chlorine cases suggest these bands arise from the same species.

3) The IR spectrum observed after isolation in 5 % chlorine in argon matrices provides evidence of one major species at this concentration and only one active infrared mode of reasonable intensity. This rules out the presence of bent $AuCl_2$ as two reasonably intense IR active modes would be expected, unless the molecule was only slightly bent. However, if the molecule was bent to 90° then the two bands would overlap and would probably appear as a single band under relatively low resolution. At lower concentration evidence exists for the possible presence of multiple species.

The data therefore point to the formation of $AuCl_3$ in 5 % chlorine / argon matrices and from the data presented the molecule is most obviously trigonal planar.

However, referring to the previous report on AuF_3[43] the most obvious shape for the molecule would be 'T-shaped' since the trigonal planar molecule is expected to be Jahn-Teller distorted. EXAFS data suggests the molecule does not contain a linear unit, although it has been shown that the molecule could be distorted to 'Y-shaped' and still be consistent with the EXAFS and IR results. The low energy band expected in the IR for the 'Y-shaped' molecule would be lower in intensity than the band predicted for the 'T-shaped' molecule which could explain its absence from the observed infrared spectrum as it may be too weak to be observed above the spectral noise.

Although the gold chloride formed has been shown to most likely be Y-shaped $AuCl_3$ recent data has suggested another possibility should be considered. DFT calculations[93] have shown that although the previously assigned trichloride is the most energetically favourable gold chloride to form, the linear dichloride has the closest active vibrational frequency to that observed in the sputtering experiments. A value of 422 cm^{-1} is produced from the calculations, which is very close to that of the major band at 419.4 cm^{-1} observed in the sputtering and laser ablation experiments. This is much closer than the predicted value of 399 cm^{-1} for 'T-shaped' $AuCl_3$. The laser ablation experiments also have the suggestion of the 9 : 6 : 1 isotopic ratio expected on the vibrational band at 4 cm^{-1} resolution, although it is possible that this could be a convenient artefact of the spectral noise.

The DFT calculated values of the vibrational frequencies provided for the gold chloride dimer, Au_2Cl_6 compare very well with those observed experimentally, with a values of 389, 298 cm^{-1} provided by the calculations corresponding to the bands observed experimentally at 386 and 312 cm^{-1}.

From the EXAFS spectra the data clearly fit readily to the dichloride, although it has been shown that this can be manipulated to take into account the presence of multiple species and there is no evidence to suggest the presence of a multiple scattering feature. The XANES spectra are remarkably similar for the square planar $AuCl_4^-$ ion and the sputtering experiment, with the exception of the white line intensity which is again explicable by the lowering of the co-ordination number and more importantly the oxidation state.

However, if this is the case the band at around 16000 cm^{-1} containing the vibrational progression remains unexplained. The band is thought to be too intense to be due to a forbidden transition and was therefore taken as proof of a La Porte allowed transition and used to discount the formation of linear $AuCl_2$ in the previous analysis. The only explanation could be that this feature is due to a charge-transfer band, although it was previously considered to be of too low an energy to arise from such a transition.

Therefore, although a new gold chloride species has been identified, further experiments are required for the clarification of its stoichiometry and molecular geometry.

Section 4.2: **Silver Chloride**

Introduction.

In 1957 Rosenstock *et al.* first proposed that the vapour above gaseous silver (I) chloride was not simply composed of monomeric AgCl molecules.[44] The mass spectral data presented showed evidence of the existence of the trimeric molecule Ag_3Cl_3 in the vapour phase as well as the monomer after heating a solid sample of AgCl to an estimated temperature of 500 °C. The absence of the dimer was noted in this mass spectrum and was further investigated by Gusarov and Gorochov[45] who likewise could only confirm the presence of monomer and trimer. They also found only a slight relative intensity variation with temperature and concluded that the monomer to trimer ratio is only marginally temperature dependent. A further study was completed by Visnapuu and Jensen[46] which concurred with the previous findings and described the presence of Ag_2Cl_2 as a vapour phase species above molten AgCl as being "very improbable". These results led to the suggestion of the existence of a third vapour phase species Ag_3Cl_2, which would account for the formation of mass spectral ions such as Ag_2Cl^+ which they felt were unlikely to be formed from the fragmentation of the Ag_3Cl_3 parent molecule. The report of this species could not be confirmed by the further account presented by Gräber and Weil[47] whose investigation on the appearance potentials and fragmentation scheme of the gas phase silver chloride species identified Ag_2Cl_2 for the first time, which was present in low concentration.

Further mass spectrometric investigations have been presented in the years since these publications continuing the investigation into the gas phase species present in AgCl vapour, [18, 48-51] all of which showed that the major species present

were the monomer and trimer but were unable to confirm the presence of the dimer and led to the suggestion of higher multimer formation.

An argon matrix isolation study has already been employed to further characterise the gas phase species produced from the sublimation of solid AgCl.[52] The matrix experiments determined the presence of AgCl, Ag_2Cl_2 and Ag_3Cl_3 molecules as sublimation products, with the band assignments calculated and confirmed by annealing experiments. The report predicts the formation of cyclic multimers from vaporised AgCl molecules, with the formation of distorted 4-membered and 6-membered rings as described in figure 4.15 below.

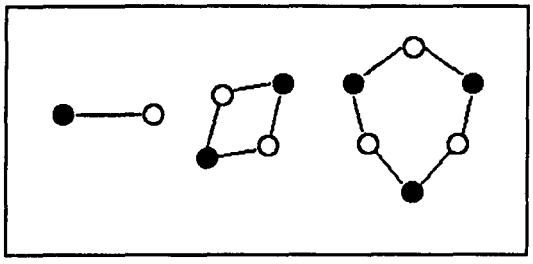

Figure 4.15: gas phase molecular structure of Ag_xCl_x (x = 1 to 3).[52]

This report suggests the presence of monomer, dimer and trimer to be roughly equivalent, with the cyclic multimers formed by collisions between gas phase AgCl molecules.

Investigations on the photoelectron spectroscopy of AgCl vapour have also been presented to determine the nature of the bonding in the AgCl molecule.[53-6] In a similar fashion to the presented mass spectral data a consistency is lacking in the observed results and conclusions drawn from them.

In the following section experimental results are presented from an investigation into the formation of monomeric silver chloride molecules isolated in an inert matrix for spectroscopic study.

Results and Discussion.

Furnace Experiments

To confirm the structure of the vapour phase products from the heating of solid silver chloride the sublimed species were isolated in an argon matrix and characterised using FTIR and UV-Vis-NIR spectroscopy as described previously. Figure 4.16 below shows the observed infrared spectrum which is in good agreement with that previously reported,[52] with the assignments given in the accompanying table (table 4.15).

The spectrum produced shows the monomer (345 cm^{-1}), dimer (255 cm^{-1}) and trimer (324 cm^{-1}) of Ag_xCl_x with the chlorine isotope pattern being evident in the monomer, while the underlying structure is clearly suggested in the dimer and trimer bands. A reduction in intensity of the vibrational bands after photolysis experiments appeared to underline the instability of the silver (I) chlorides to both visible and ultra-violet light, suggesting the decomposition of the isolated molecules. Annealing experiments provided no further assistance in the confirmation of the band assignments.

The UV-Vis-NIR spectrum of silver chloride vapour isolated in an argon matrix is shown in figure 4.17. The spectrum shows multiple band features at high energy which presumably arise from charge transfer transition in the isolated monomer, dimer and trimer molecules. No d-d transitions are expected or observed as the silver is present as d^{10}.

These experiments confirmed the previously reported sublimation products of silver chloride although the geometry of the multimers cannot be confirmed.

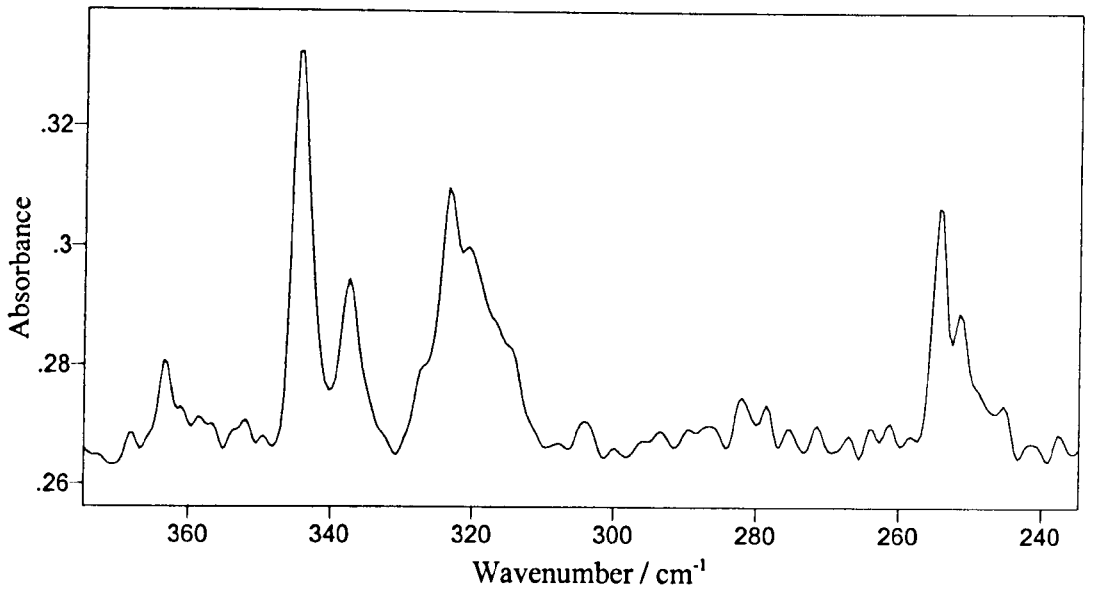

Figure 4.16:infrared spectrum of silver chloride sublimation products isolated in argon at 10 K.

Observed frequency	Previously reported[52]	Assignment
344.5 / 337.5 cm^{-1}	339 cm^{-1}	monomer
254.5 / 251.5 / 248.5* cm^{-1}	255 cm^{-1}	dimer
323.5 cm^{-1}	322 cm^{-1}	trimer

**tentative assignment.*

Table 4.15: vibrational assignments for silver chloride sublimation products isolated in argon at 10 K.

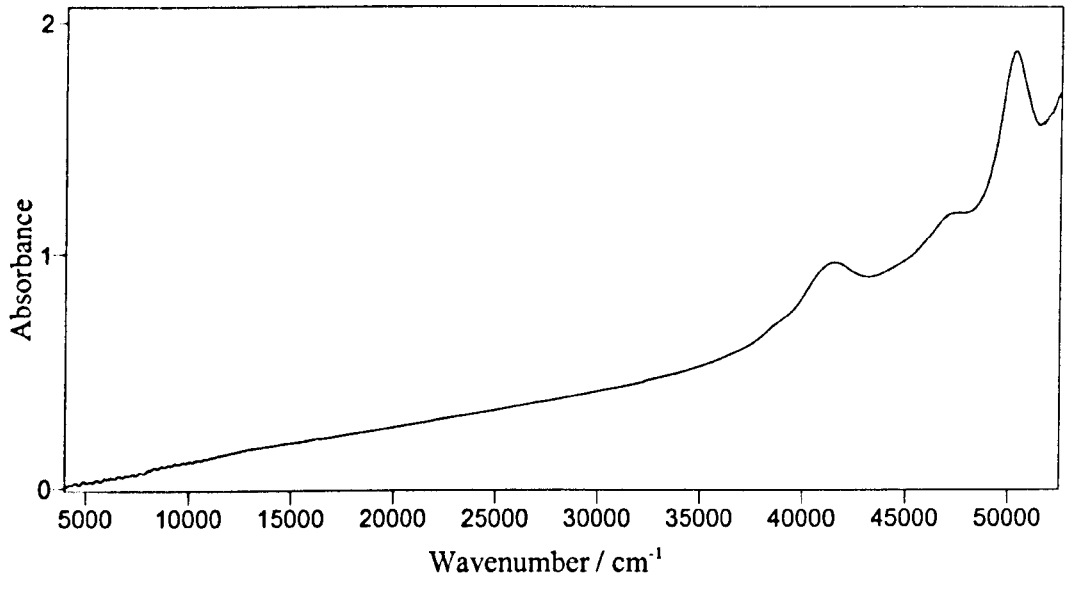

Figure 4.17: UV-Vis-NIR spectrum of silver chloride sublimation products isolated in argon at 10 K.

Sputtering Experiments

To generate the monomer as the single isolated species silver atoms were isolated in an argon matrix doped with a low concentration of chlorine (typically 1 to 5 %) from a sputtering source.

a) UV-Vis-NIR Results

Figure 4.18(a) shows the UV-Vis-NIR spectrum of silver atoms isolated in an argon matrix and the assignments given by previous work.[39(a)] The results are in good agreement with those previously reported for silver atoms isolated in an argon matrix given in table 4.16 and again show no evidence of the presence of dimers or higher multimers.[39(c)] When silver foil was sputtered with argon doped with 1 % chlorine similar results were observed as those discussed for the corresponding gold experiment. The UV-Vis-NIR spectrum produced after a 5 minute deposition is shown in figure 4.18(b). The atomic transitions of the isolated silver atoms are still present in the spectrum along with the evidence of chlorine content (the broad band at around 30000 cm^{-1} and the increased scattering of light at high energy). The spectrum also shows evidence of a new band at 41400 cm^{-1} which suggests the formation of a new molecule between the isolated silver atoms and chlorine in the matrix. Increasing the chlorine concentration to 5 % produced the spectrum shown in figure 4.18(c). As expected the bands due to chlorine show an increase in intensity with the sample completely absorbing above 47000 cm^{-1} (again due to the high chlorine content). Further signs of molecular formation are evident with the continued presence of the band at around 41000 cm^{-1} and evidence of new absorptions at 26300 cm^{-1} and 17600 cm^{-1}. There is also the possibility of a weak band at around 8200 cm^{-1} which appears to be present in both the 1 % and 5 %

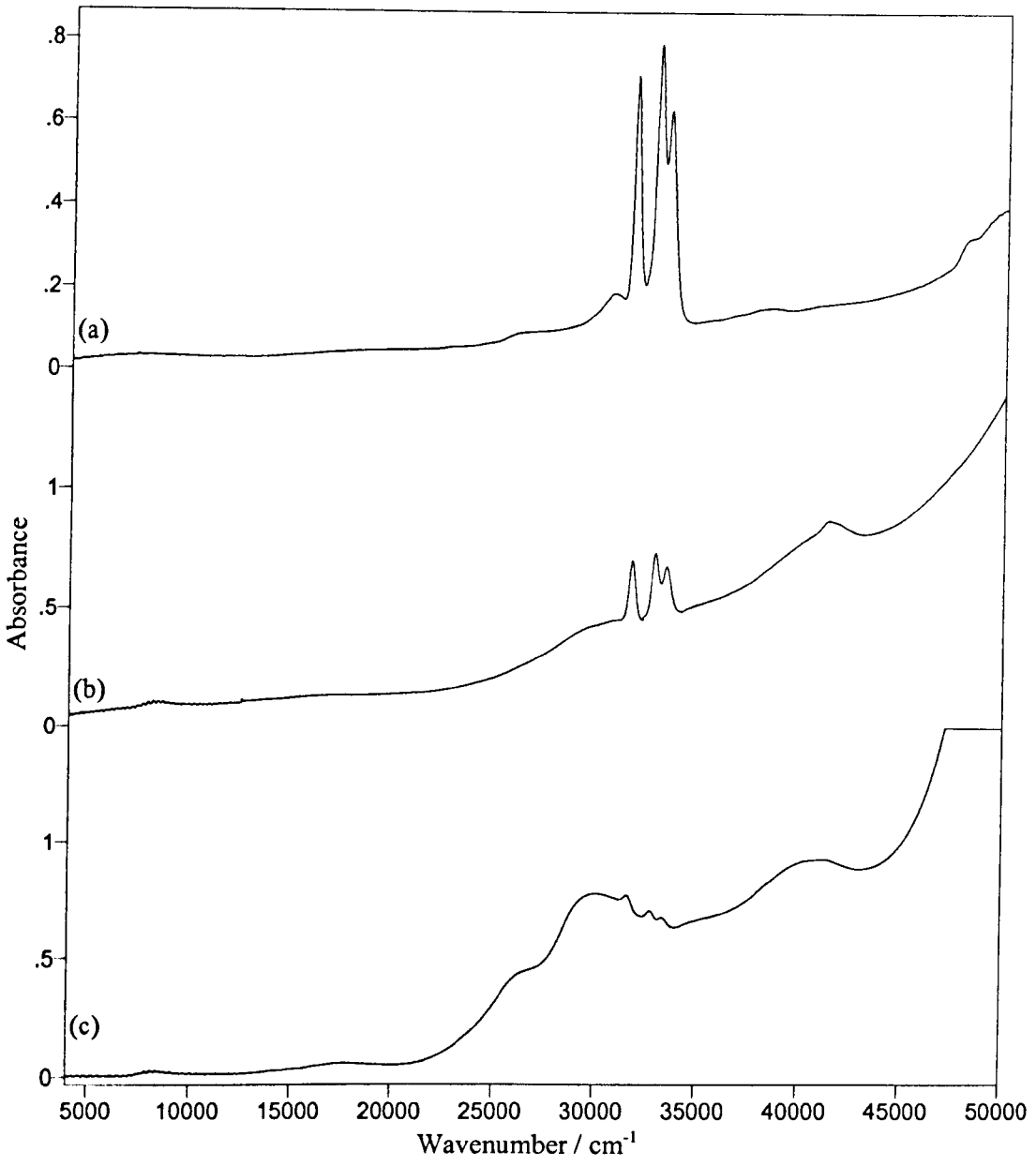

Figure 4.18: UV-Vis-NIR spectra of silver isolated in argon and chlorine / argon matrices at 13 K with assignments. (a) argon, (b) 1 % chlorine in argon, (c) 5 % chlorine in argon.

Observed Frequency	Previously Reported[39(a)]	Assignment[39(a)]
31730 cm^{-1}	31749 cm^{-1}	E_1 ($^2P_{1/2}$)
33416 cm^{-1}	33489 cm^{-1}	E_2 ($^2P_{3/2, 1/2}$)
32868 cm^{-1}	32908 cm^{-1}	E_2 ($^2P_{3/2, 3/2}$)

Based on ^2S ground state.

Table 4.16: assignments of atomic transitions for silver atoms isolated in argon.

chlorine in argon matrices. Unfortunately this band is too weak to identify the presence of any vibrational fine structure. A notable difference between the silver and gold sputtering with 5 % chlorine in argon is the continued presence of the metal atom transitions in the silver spectrum indicating that not all the silver atoms have reacted with the chlorine in the matrix.

From comparison of the sputtering results with the solid AgCl sublimation experiments a simplistic conclusion could be drawn that both spectra share a common feature at around 41000 cm^{-1} which could possibly originate from the same species in both experiments. However, this is indeed an oversimplification since a large proportion of the spectra from the sputtering experiments is obscured by the chlorine absorption bands. The chlorine content masks the areas around 48000 to 50000 cm^{-1} where other transitions in the sublimation experiments occur and therefore their presence in the matrix cannot be categorically refuted. In addition the presence of new bands in the sputtering experiments with broad bands at 17600 and 26300 cm^{-1} and at very low energy which are not immediately apparent in the sublimation spectrum appear to indicate the formation of a different species. However, this hypothesis is also easily discredited when the intrinsic nature of both deposition techniques is taken into account. The furnace experiments cause a general fouling of the optical window as the experiments continue and result in increased light scatter throughout the spectral region. This would result in these weak broad bands at low energy appearing to be even lower in intensity. The light scattering problems associated with the sputtering experiments however are due to the chlorine content, which absorbs and scatters light at high energy, so while the high energy bands may be obscured by a scattering matrix the low energy bands are still observable as the matrix is still fully transmitting in that region.

b) Infrared Results

The matrix isolated products of silver foil sputtered with both 1 % and 5 % chlorine in argon produced no absorption bands in the infrared region other than those which could be readily assigned to low level impurities in the matrix gas or chlorine. This suggests that any silver chloride present in the matrix was not in sufficient quantity for the infrared active vibrational mode(s) to be visible above the noise level in the spectrum. The lack of spectral features in the infrared region, coupled with the continued presence of atomic absorption bands in the UV-Vis-NIR spectra suggests that the isolated silver atoms do not react completely with the chlorine in the matrix. An increase in the concentration of chlorine in the matrix gas produced no improvement in the quality of the spectra observed and also failed to provide any new infrared absorption bands.

(c) EXAFS Results

When EXAFS was employed to analyse the products of sputtering silver with 5 % chlorine in argon the results were very weak and resulted in an increase in the noise level at high k space. This is assumed to be due to the low yield of silver chlorides from the sputtering source. The experimental and observed EXAFS and Fourier Transforms for silver sputtered with 5 % chlorine in argon and isolated at 12 K are shown in figure 4.19 below along with the fitting parameters which are given in table 4.17.

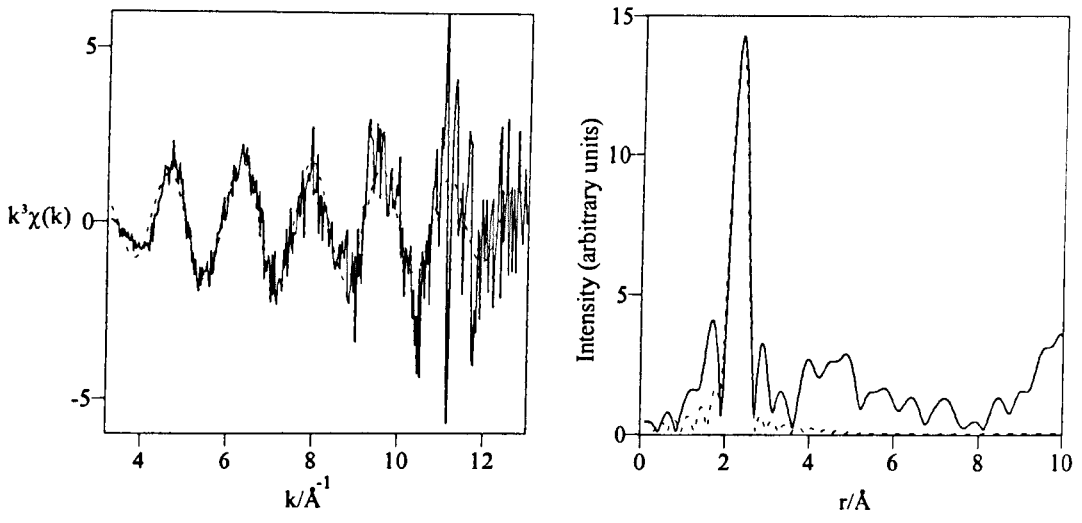

Figure 4.19: Ag K-edge EXAFS and Fourier Transform for silver atoms isolated in a 5 % chlorine / argon matrix at 12 K.

$r_{Ag\text{-}Cl}$	N_1[c]	$2\sigma^2_{Ag\text{-}Cl}$[a] / Å^2	E_f[b] / eV	R
2.33 (1)	1.0 (2)	0.006 (3)	-2 (3)	63

[a] *Debye-Waller factor,* [b] *Reflection of differences in experimental and theoretical Fermi levels,* [c] *Co-ordination number.*

Table 4.17: refined EXAFS parameters for silver atoms isolated in a 5 % chlorine / argon matrix at 12 K.

The EXAFS for silver atoms isolated in a 5 % chlorine in argon matrix show the formation of silver (I) chloride, with the above parameters refined with a co-ordination number of one after initial co-ordination number refinements showed it to be the most probable value. The large errors evident in the parameters are most probably due to the high noise levels at high *k* space.

Conclusion

The vapour phase species produced from the sublimation of solid silver chloride have been confirmed as the monomer, dimer and trimer of silver (I) chloride. The UV-Vis-NIR spectrum of the sublimation products isolated in an inert matrix has been presented for the first time.

UV-Vis-NIR and EXAFS experiments have been employed to show that the isolation of silver atoms in an argon matrix doped with 5 % chlorine leads to the formation of a silver chloride. The characterisation has not been fully completed due to the lack of any observable vibrational bands in the infrared region.

When the comparison is made to the gold sputtering experiments the evidence points towards the silver chloride forming less readily than the gold chloride under these conditions. The experiments with gold appeared to suggest the atomic species as being the yield determining component, especially in 5 % chlorine matrices. If enough chlorine is present in a 5 % matrix to form gold (III) chloride then one would naively assume that if chlorine were the yield determining component then a greater amount of the potentially less co-ordinated silver chloride could be isolated. Even after taking into account that the major vibrational band may be intrinsically weaker than that of gold (III) chloride some evidence would be expected in the infrared spectrum. Therefore, since chlorine is present in excess and the UV-Vis-NIR spectrum shows that some silver atoms are still isolated, the conclusion must be that the isolated silver atoms are less reactive towards the chlorine present in the matrix, and as a result a very low yield of the silver chloride is observed. This apparently low reactivity appears to be the continuation of a trend through this group, as similar sputtering experiments with copper and chlorine have also provided experimental

evidence of copper atoms present in a 5 % chlorine in argon matrix and no observable bands in the far infrared.

The EXAFS data clearly identifies the most likely structure to be silver (I) chloride, although through comparison with the results of the previous section when atomic species are present (as they clearly are in the case of silver) the co-ordination number may be artificially reduced. Further, the weak band that is again present at low energy in the UV-Vis-NIR spectra at 16000 cm^{-1} is very similar to that observed with gold. It is unlikely at such a low energy that this is a charge transfer band and is therefore probably a d-d transition. If this is the case then the formation of silver (I) chloride can be ruled out since no d-d transition are observed for silver (I) compounds (d^{10}).

Section 4.3: **Platinum Chloride**

Introduction.

Information on the gas phase structure of the platinum chlorides is relatively sparse. The solid state molecules have been shown to decompose on heating, even in a chlorine atmosphere, to the elements following the scheme outlined below.[57]

$$PtCl_4 \longrightarrow PtCl_3 \longrightarrow PtCl_2 \longrightarrow PtCl \longrightarrow Pt$$

Further investigations[58-67] have shown that the decomposition occurs readily with the majority of work presented suggesting it is more likely to proceed *via* the even oxidation states only, and that $PtCl_3$ and PtCl are unlikely to form as direct decomposition products. These reports also show reaction between metallic platinum and atmospheric chlorine as a source of platinum chlorides to be very slow and ineffective.

More recently the thermodynamic properties of the platinum chlorides have been studied by mass spectrometry and the first evidence presented for the existence of $PtCl_4$ and $PtCl_2$ in the gas phase.[68] These molecules are shown to form in low concentration along with the decomposition products by sublimation of the solid. This paper also confirms the decomposition of $PtCl_4$ to $PtCl_2$ does not proceed via $PtCl_3$.

Results and Discussion.

Sublimation Experiments

The vacuum sublimation of $PtCl_4$ and $PtCl_2$ confirmed the previous reports of the thermal decomposition of the solid. Mass spectral data showed chlorine (Cl_2^+) as the major gas phase product and the silica sample pot was coated in a platinum film (figure 4.20), showing the direct decomposition to the elements. No trace of $PtCl_4$ or $PtCl_2$ was observed in the mass spectrum.

Figure 4.20: Silica sample pot after sublimation of $PtCl_4$.

Sputtering Experiments

Sputtering experiments were again employed to attempt to generate a platinum chloride by the isolation of the metal atoms in dilute chlorine / argon matrices.

a) UV-Vis-NIR Results

Figure 4.21 shows the UV-Vis-NIR spectrum observed after sputtering platinum foil with argon and isolating the products at 13 K. The observed bands are in reasonable agreement with previously reported data for the absorption bands of matrix isolated platinum atoms.[69,70(a)] and do not show any evidence of the presence of Pt_2.[70(b)] The previously observed frequencies and their assignments are outlined in the table accompanying the spectrum (table 4.18).

When the matrix gas was doped with 1 % and 5 % chlorine the UV-Vis-NIR spectra observed are shown in figure 4.22 and are consistent with the previous

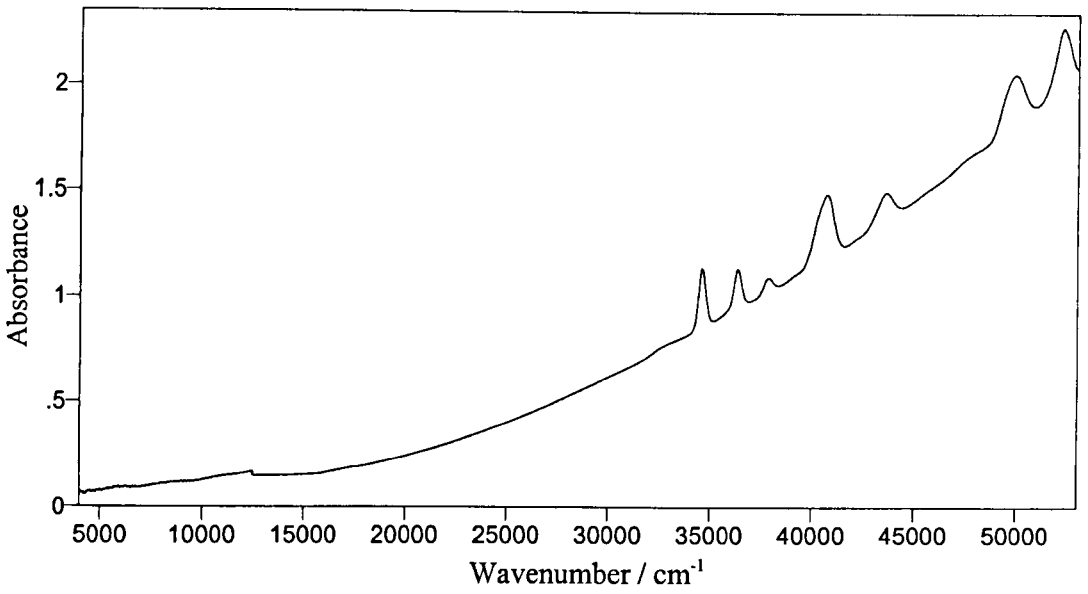

Figure 4.21: UV-Vis-NIR spectrum of sputtered platinum products isolated in an argon matrix at 13 K.

Observed Frequency	Previously Reported[70(a)]	Assignment[70(a)] *
52290 cm^{-1}	52083 cm^{-1}	$5d^8\ 6s^1\ 6p^1$
49920 cm^{-1}	50251 cm^{-1}	$5d^9\ 6s^0\ 6p^1$
43610 cm^{-1}	43859 cm^{-1}	$5d^8\ 6s^1\ 6p^1$
40710 cm^{-1}	40983 cm^{-1}	$5d^9\ 6s^0\ 6p^1$
37860 cm^{-1}	38022 cm^{-1}	$5d^8\ 6s^1\ 6p^1$
36350 cm^{-1}	36496 cm^{-1}	$5d^9\ 6s^0\ 6p^1$
34610 cm^{-1}	34600 cm^{-1}	$5d^9\ 6s^0\ 6p^1$

**assignments based on $5d^9\ 6s^1$; $^3D_3$ ground state.*

Table 4.18: observed absorption bands for platinum atoms isolated in an argon matrix at 12 K and assignments.

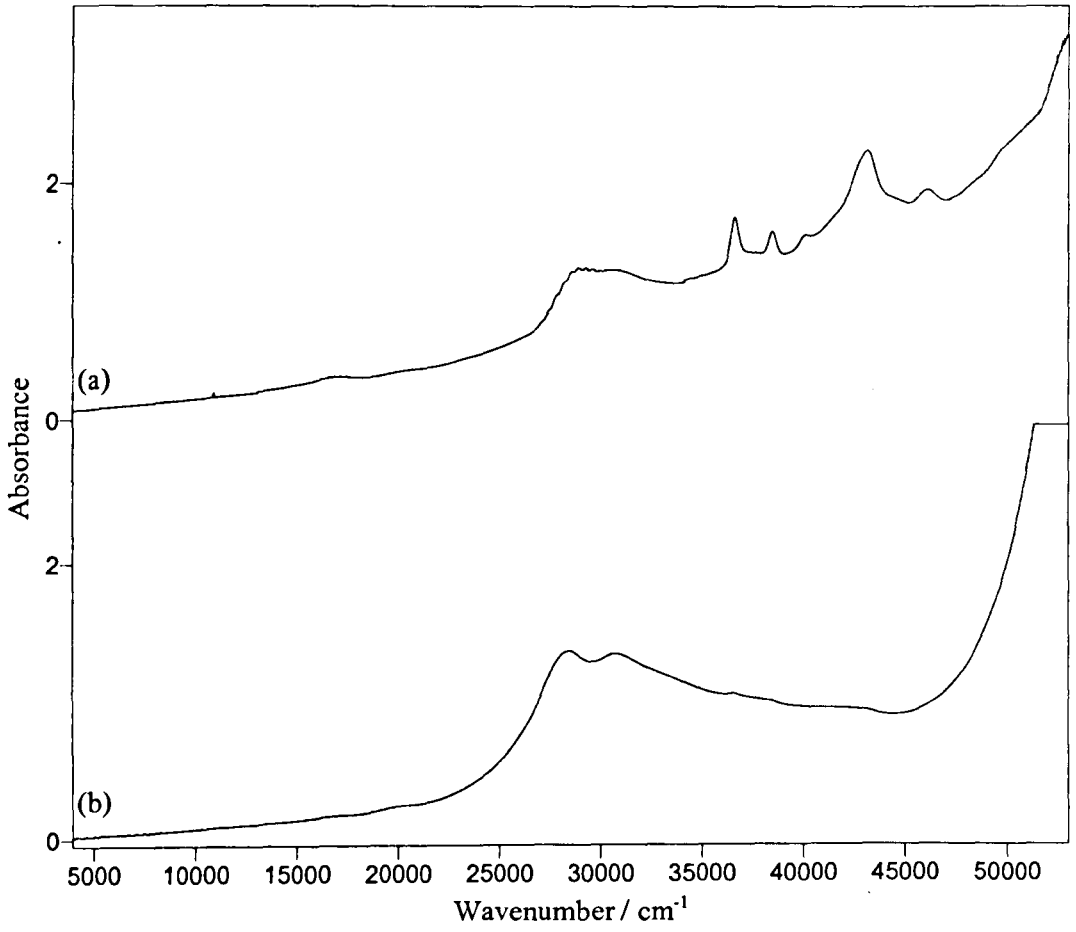

Figure 4.22: UV-Vis-NIR spectra of platinum atoms isolated in chlorine containing argon matrices at 13 K and expansion of low energy region. (a) 1 % chlorine, (b) 5 % chlorine.

observations with gold and silver. Figure 4.22(a) shows platinum atoms isolated in a 1 % chlorine matrix and evidently still contains traces of platinum atoms along with evidence of new molecular species, most obviously the new band present at 27000 cm^{-1}, slightly lower in energy than the chlorine transition. The 5 % chlorine spectrum shown in figure 4.22(b) shows the expected reduction of atomic bands (the spectrum still shows the slightest traces of the atomic transitions at 35000 to 40000 cm^{-1}) along with the apparent effects of increased chlorine concentration. The spectra of chlorine containing matrices have not been extended to include the region above 50000 cm^{-1} which contains atomic transitions since the light scattering and absorption caused by the chlorine concentration made the scanning of this region uninformative.

1 % Cl_2 in argon	5 % Cl_2 in argon
43520 cm^{-1}	
40720 cm^{-1}	40670 cm^{-1}
37880 cm^{-1}	
36350 cm^{-1}	36240 cm^{-1}
34620 cm^{-1}	34550 cm^{-1}
28950 cm^{-1}	29100 cm^{-1}
27370 cm^{-1}	26980 cm^{-1}
16100 cm^{-1}	

Table 4.19. Observed UV-Vis NIR transition after the isolation of platinum atoms in Cl_2 / argon matrices at 12 K.

Both the 1 % and 5 % chlorine in argon spectra show one major new band caused (presumably) by the same species at around 27000 cm^{-1}. This band is present at roughly the same energy in both spectra with the shift in position easily being accounted for by a matrix shift due to the differing chlorine concentration in the two matrices (from 27400 cm^{-1} in 1 % chlorine in argon to 27000 cm^{-1} in 5 % chlorine /

argon). Closer examination of the new band in the 1 % chlorine in argon matrix also suggests the presence of vibrational fine structure on the major absorption band at 27400 cm^{-1}. A weak band is also present at 16100 cm^{-1} which shows similar vibrational fine structure. An expansion of these regions is given in figure 4.23 with the corresponding data in table 4.20. In the 5 % chlorine in argon matrix spectrum the vibrational fine structure is not observed and the 16100 cm^{-1} band is absent. The 5 % chlorine spectrum also appears to still contain very weak bands due to the presence of atomic species.

	27370 cm^{-1} band	**16110 cm^{-1} band**
	28024 cm^{-1}	16880 cm^{-1}
	27712 cm^{-1}	16610 cm^{-1}
	27384 cm^{-1}	16340 cm^{-1}
	27080 cm^{-1}	16064 cm^{-1}
	26690 cm^{-1}	15804 cm^{-1}
	26360 cm^{-1}	15542 cm^{-1}
Average peak gap	333	268

Table 4.20: wavelength data for the vibrational fine structure in figure 4.22.

The expansion of the region 7000 to 17000 cm^{-1} presented in figure 4.24 shows further interesting features. The vibrational fine structure is evident at around 16000 cm^{-1} but is accompanied by three very sharp low energy bands at 8216, 10448 and 10849 cm^{-1}. The origin of these bands is unknown, but since they do not appear in the 5 % chlorine in argon spectrum and no other similar bands are observed in other matrix spectra they could possibly be spin forbidden transitions.

Figure 4.25 shows the effect of annealing the 5 % chlorine / argon matrix after deposition. The growth of a new broad band at 40000 cm^{-1} clearly suggests that

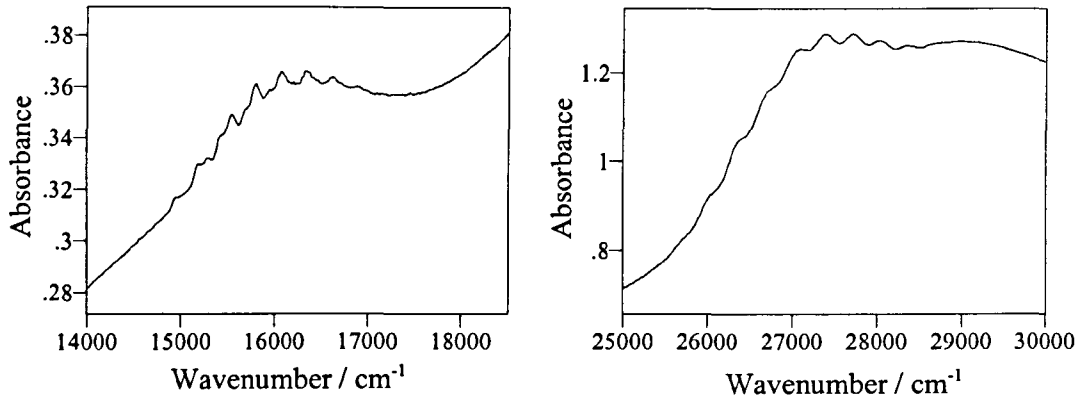

Figure 4.23: expansion of vibrational fine structure observed in figure 4.21.

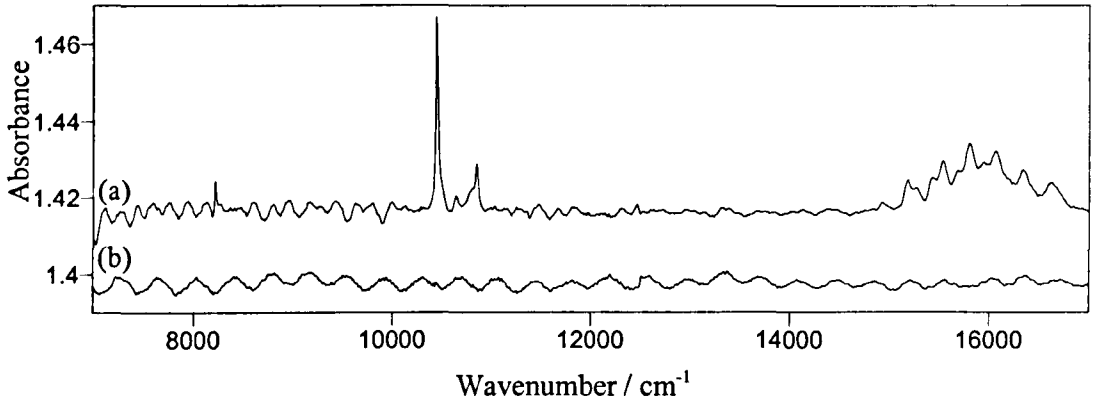

Figure 4.24: expansion of the region 7000 to 17000 cm^{-1} in figure 4.21.

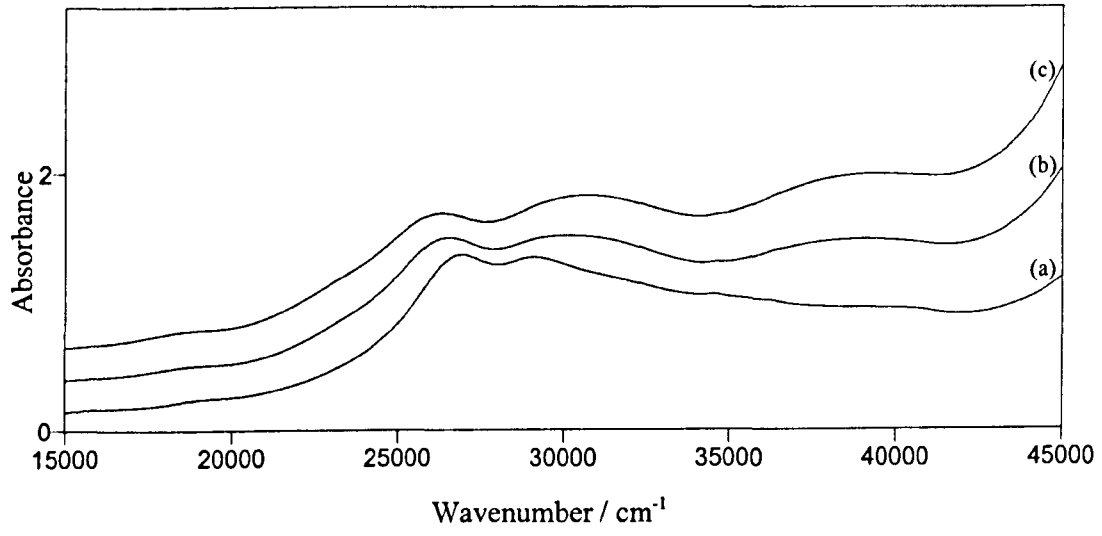

Figure 4.25: UV-Vis-NIR spectra of platinum atoms isolated in 5 % chlorine / argon matrices at 13 K.

(a) Deposition, (b) after warming to 25 K, (c) after warming 30 K.

a new species is being formed when the matrix is warmed. Since warming the matrix allows movement of the molecules within the matrix it is likely that this new species is either a higher co-ordination complex or a multimer formed by agglomeration of previously isolated molecules.

b) Infrared Results

The predicted infrared spectra for $PtCl_x$ (x = 1 to 4) are similar to those given in figure 4.2 for the gold chlorides. Although under high resolution platinum isotope patterns should be observable within the vibrational bands, the platinum isotope splitting pattern is small enough not to distort the chlorine isotope patterns predicted for the gold chlorides.

The best infrared experimental result was achieved using a 0.5 % chlorine in argon gas mixture as the matrix gas. The observed infrared spectrum is shown in figure 4.26. Larger chlorine concentrations provided only the same bands with no net gain in intensity since the use of 0.5 % chlorine allowed the deposition time to be increased to 50 minutes. This increased the intensity of the major band to similar levels as those achieved by using more concentrated chlorine matrices but provided sharper bands, allowing high resolution scans to be employed to further investigate the isotopic structure contained within the vibrational bands. Figure 4.26 shows a close up of the vibrational band at 430 cm^{-1} scanned at 0.25 cm^{-1} resolution. The increase in resolution has sharpened the bands but no new isotopic structure is observable above the noise level.

The infrared spectrum presents a relatively strong band at 430 cm^{-1} which has a 9 : 6 : 1 intensity pattern characteristic of the asymmetric stretch of a linear or bent dichloride. Comparison with the predicted spectra presented earlier shows the

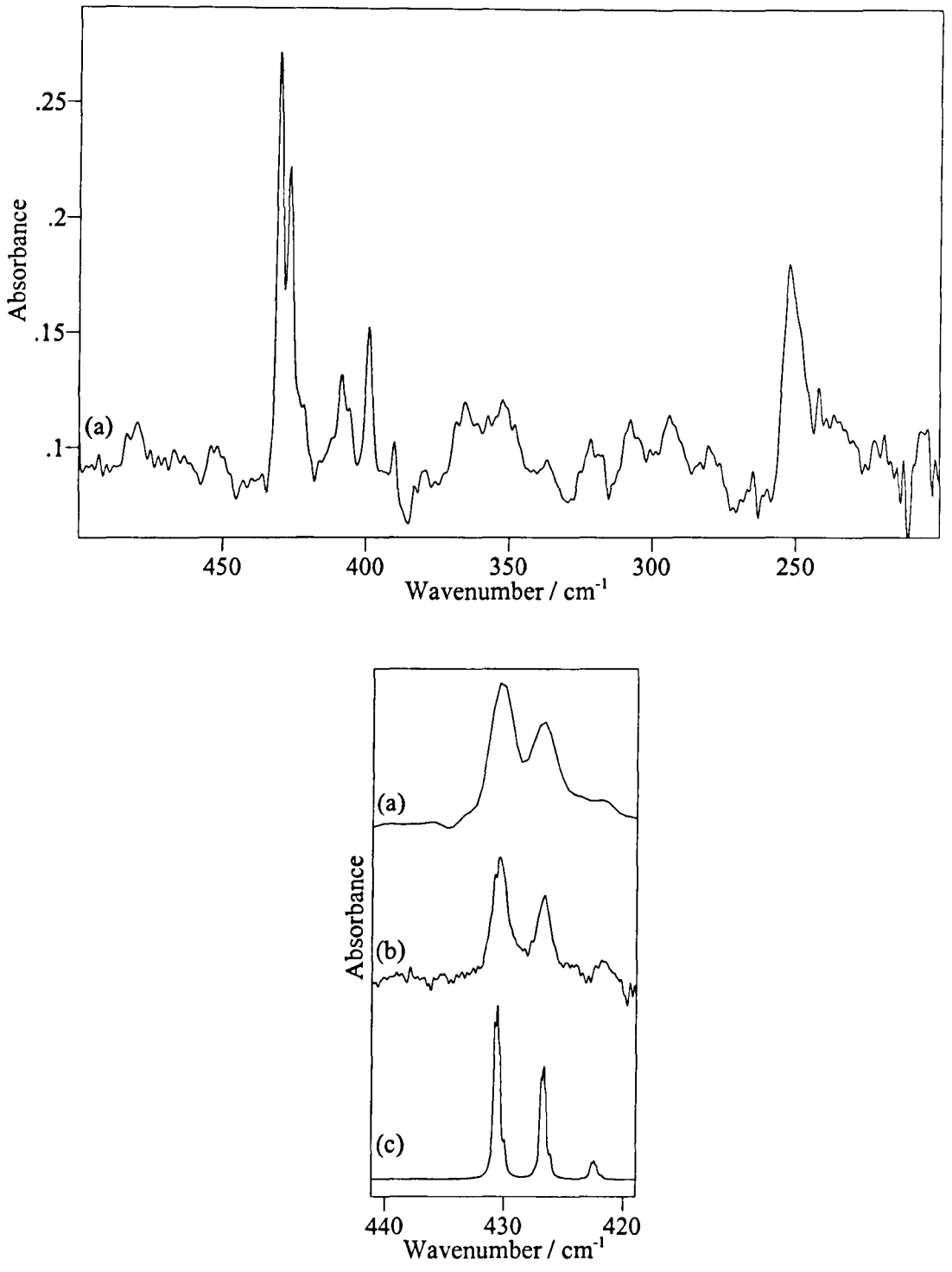

Figure 4.26: infrared spectra of platinum atoms isolated in a 0.5 % chlorine in argon matrix at 12 K and expansion of the major absorption band (a) 2cm^{-1} resolution, (b) 0.25 cm^{-1} resolution, (c) predicted isotope pattern at 0.5 cm^{-1} bandwidth for linear $PtCl_2$.

intensity distribution provides a good fit to either $PtCl_2$ geometry as only the separation in the isotopic peaks is dependent on the bond angle. The presence of a second feature at 250 cm^{-1} suggests either the presence of another species or alternatively this could be the symmetric stretch of a bent $PtCl_2$ molecule. The results of a second experiment with Pt atoms in a 0.5 % chlorine in argon matrix are shown in figure 4.27. This second experiment immediately helps the assignment of the major absorption band as the other features at 400 and 250 cm^{-1} are present in the deposition spectrum at different relative intensities than in figure 4.26. The annealing experiment also shows clearly through the subtraction spectrum given (fig. 4.27(c)) that as the major absorption band at 430 cm^{-1} decreases, the band at 250 cm^{-1} increases while the band at 400 cm^{-1} undergoes very little change in intensity. Accompanied by the fact that the band at 400 cm^{-1} also has no obvious chlorine isotope pattern, this identifies the bands as being due to the presence of different species. The growth of the 250 cm^{-1} band on annealing tends to suggest this is due to the formation of a multimer species, formed by agglomeration of isolated molecules as the matrix is warmed. The frequencies of the observed infrared absorptions accompany the spectra in table 4.21. High resolution provided no further evidence as to the underlying isotopic structure of these other bands at 400 and 250 cm^{-1}.

By the use of the spectral prediction program 'SOTONVIB' the position of ν_1 can be determined from the isotopic splitting pattern shown in figure 4.26(b). Setting the value of the major isotope bands within the calculations and allowing the force constants and ν_1 to be refined a prediction can be made for the position of ν_1. The values for the calculated position of ν_1 for a bent and linear $PtCl_2$ molecule are given in table 4.20 below. The calculated positions for ν_1 of the bent molecule are reasonably close to ν_3, at 410 cm^{-1}, and could be present in the observed spectrum as

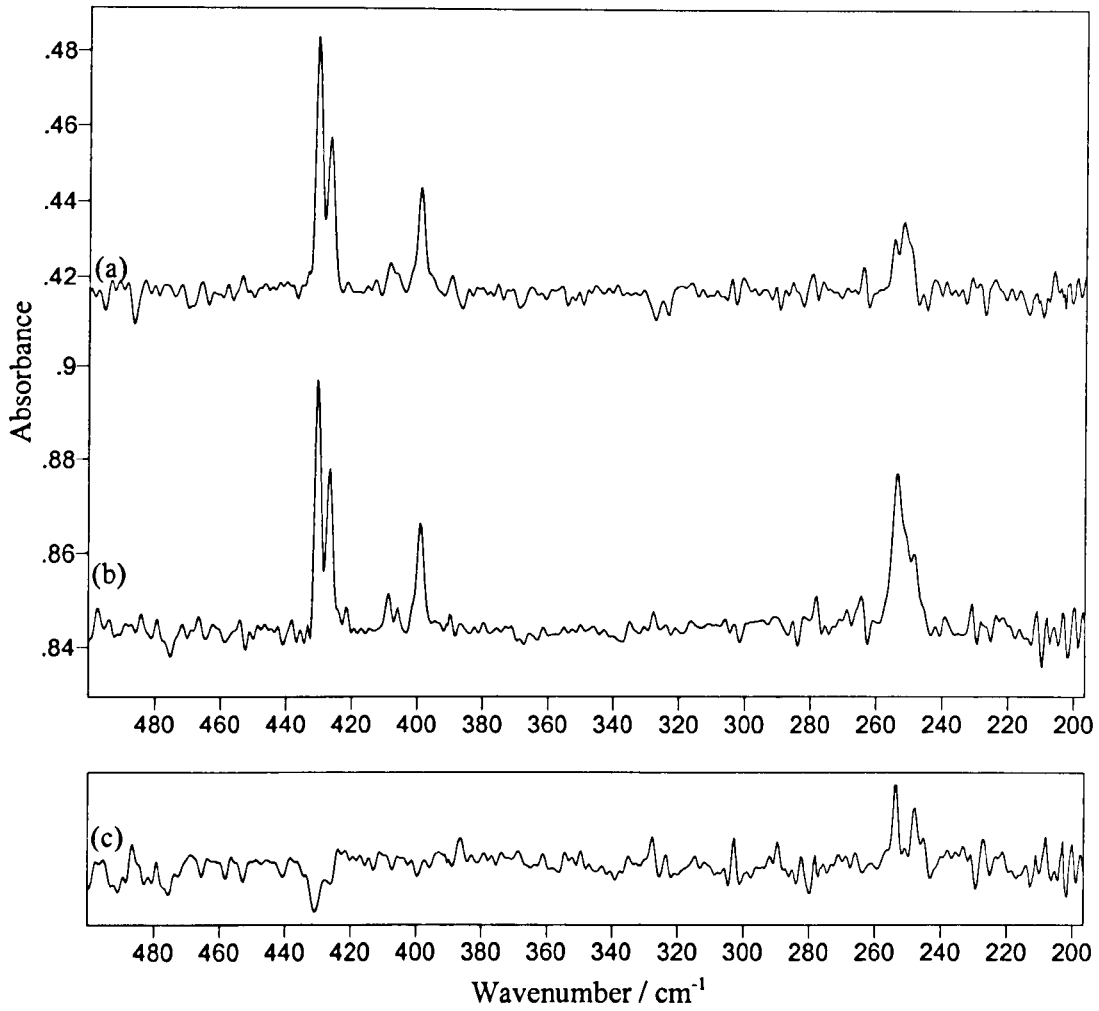

Figure 4.27: infrared spectra of platinum atoms isolated in a 0.5 % chlorine in argon matrix at 12 K.

(a) deposition, (b) at 12 K after annealing to 25 K, (c) subtraction spectrum (b - a).

Observed Frequency / cm^{-1}	Calculated frequency / cm^{-1}
430.3	ν_3 ($^{195}Pt\ ^{35}Cl\ ^{35}Cl$): 430.3* ($C_{2v}$, 120°), 430.3# ($D_{\infty h}$)
426.8	ν_3 ($^{195}Pt\ ^{35}Cl\ ^{37}Cl$): 426.8* ($C_{2v}$, 120°), 426.8# ($D_{\infty h}$)
421.9	ν_3 ($^{195}Pt\ ^{37}Cl\ ^{37}Cl$): 421.1* ($C_{2v}$, 120°), 421.7# ($D_{\infty h}$)
408.5	
399.2	Calculated position of ν_1:
390.1	410.65, 404.36, 400.30
252.7	

**Force constant values: F_r = 3.1 mdyne / Å, F_{rr} = 0.1 mdyne / Å,*
#Force constant values: F_r = 3.1 mdyne / Å, F_{rr} = 0.27mdyne / Å.

Table 4.21. infrared data for platinum atoms isolated in 0.5 % chlorine in argon matrix at 12 K.

bands are evident at a similar wavelength. However, since these bands have been shown to behave inconsistently on annealing it is unlikely they arise from the same species.

c) XAFS

To complete the analysis, XAFS experiments were undertaken on the platinum sputtering products. The experiments were completed using a matrix gas of 5 % chlorine in argon, which UV-Vis-NIR experiments had shown to remove the majority of the platinum atoms.

To assist in the characterisation of the sputtering products the XAFS of K_2PtCl_4 and K_2PtCl_6 diluted in BN were recorded and analysed. After initial refinement of co-ordination number to 3.5(2) and 5.5(4) respectively the calculations were completed and refined with the co-ordination numbers set at 4 and 6 for the inclusion of multiple scattering terms, with the results given in figure 4.28. The EXAFS curves and Fourier transforms show good agreement with crystal data which gives bond lengths of 2.309 Å for K_2PtCl_4 and 2.311 Å for K_2PtCl_6.[71] The fitting parameters given in table 4.22 describes reasonably well structured solids of platinum atoms co-ordinated to 4 and 6 chlorine atoms at a distance of 2.31 and 2.32 Å respectively.

Compound (in BN)	r_{Pt-Cl}	$2\sigma^2_{Pt-Cl}$ [a] / Å^2	E_f [b] / eV	R
K_2PtCl_4	2.309 (3)	0.0068 (3)	-10.8 (6)	26
K_2PtCl_6	2.323 (4)	0.0061 (4)	-11.3 (8)	22

[a] *Debye-Waller factor,* [b] *Reflection of differences in experimental and theoretical Fermi levels.*

Table 4.22: refined EXAFS parameters For K_2PtCl_4 and K_2PtCl_6 in BN at room temperature.

The calculated and observed Fourier Transforms show a low intensity peak at double the bond length showing multiple scattering and is an indication of the linearity of the Cl-Pt-Cl unit, showing that $PtCl_4^{2-}$ is square planar in both K_2PtCl_4 and K_2PtCl_6.

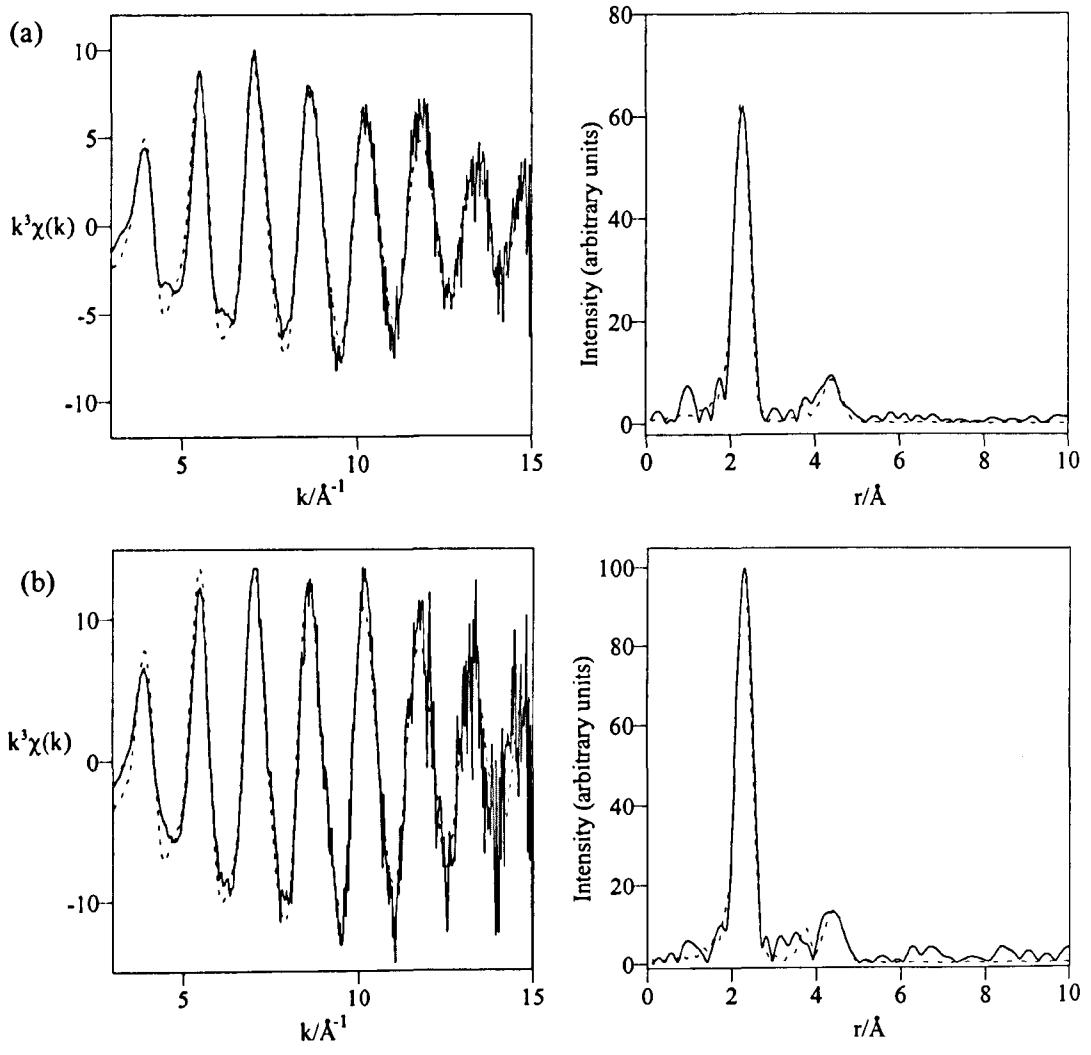

Figure 4.28: Pt L_3-edge EXAFS and Fourier Transform for (a) K_2PtCl_4 and (b) K_2PtCl_6 in BN at room temperature.

(——— observed, - - - - - theoretical)

The EXAFS and Fourier Transform from the experiments with platinum atoms isolated in an argon matrix doped with 5 % chlorine are presented in figure 4.29 below along with the fitting parameters in the accompanying table.

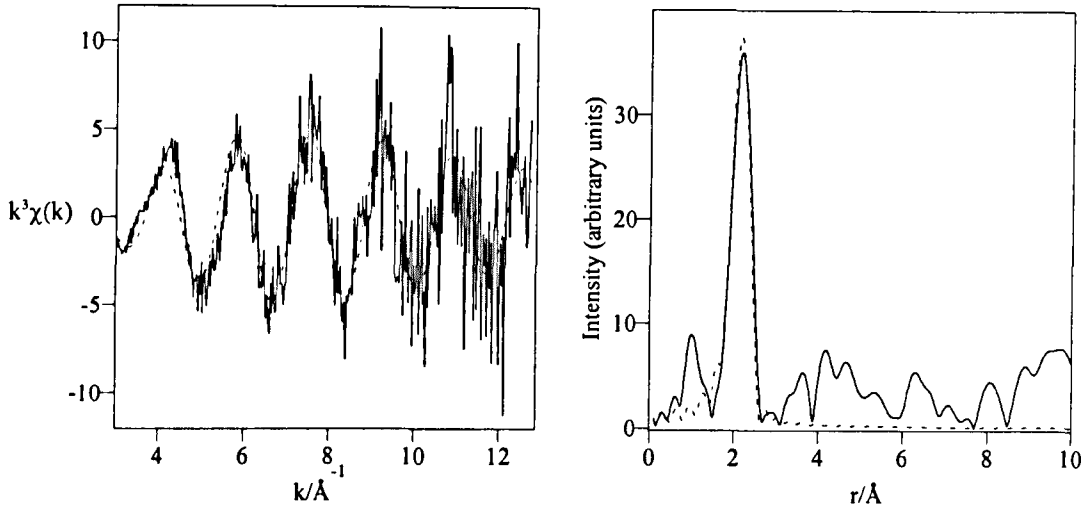

Figure 4.29: Pt L_3-edge EXAFS and Fourier Transform for platinum sputtered with 5 % chlorine in argon and isolated at 12 K.

r_{Pt-Cl}	$2\sigma^2_{Pt-Cl}$ [a] / Å²	E_f [b] / eV	N_1 [c]	R
2.19 (1)	0.008 (2)	-7.8 (2)	2.3 (4)	58

[a] *Debye-Waller factor,* [b] *Reflection of differences in experimental and theoretical Fermi levels,* [c] *co-ordination number.*

Table 4.23: refined EXAFS parameters For platinum sputtered with 5 % chlorine / argon and isolated at 12 K.

The parameters above show a reasonable fit to the dichloride and provide a bond length of 2.19 Å with reasonable degrees of disorder for the sample under study. The relatively large refinement errors are probably due to the poor quality of the data with respect to the high level of noise present in the oscillations, again presumably due to the sample weakness (deposition times of only 10 minutes could be employed before the penetration depth of argon was reached and further deposition provided no net gain in intensity). This relatively high noise level meant that calculations involving

multiple scattering terms were ineffective as the peak produced in a linear molecule (figure 4.30) was not of sufficient intensity to be above the baseline noise level in the experimental Fourier Transform. Further analysis showed a poor fit and unacceptable disorder values for $PtCl_4$ or mixtures of $PtCl_4$, $PtCl_2$ and Pt atoms. Further calculations incorporating metal-metal and metal-argon interactions were refined and showed the existence of dimers and isolated atoms to be extremely unlikely.

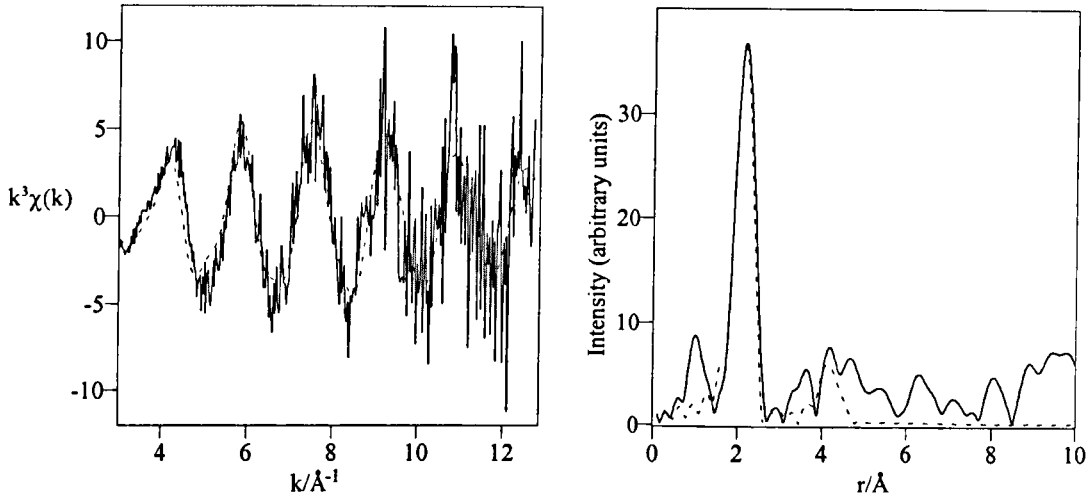

Figure 4.30: Pt L_3-edge EXAFS and Fourier Transform for platinum sputtered with 5 % chlorine in argon and isolated at 12 K. With multiple scattering on.

r_{Pt-Cl}	$2\sigma^2_{Pt-Cl}$ [a] / Å²	E_f [b] / eV	R
2.19 (1)	0.006 (1)	-8 (2)	59

[a] Debye-Waller factor, [b] Reflection of differences in experimental and theoretical Fermi levels.

Table 4.24: refined EXAFS parameters for linear $PtCl_2$ including multiple scattering terms from 5 % chlorine in argon matrix data.

The XANES spectra observed for the model compounds and the platinum sputtering experiments are given in figure 4.31 along with the data observed from a 0.25 mm thick platinum foil. By comparison of the white line intensity (the intensity of

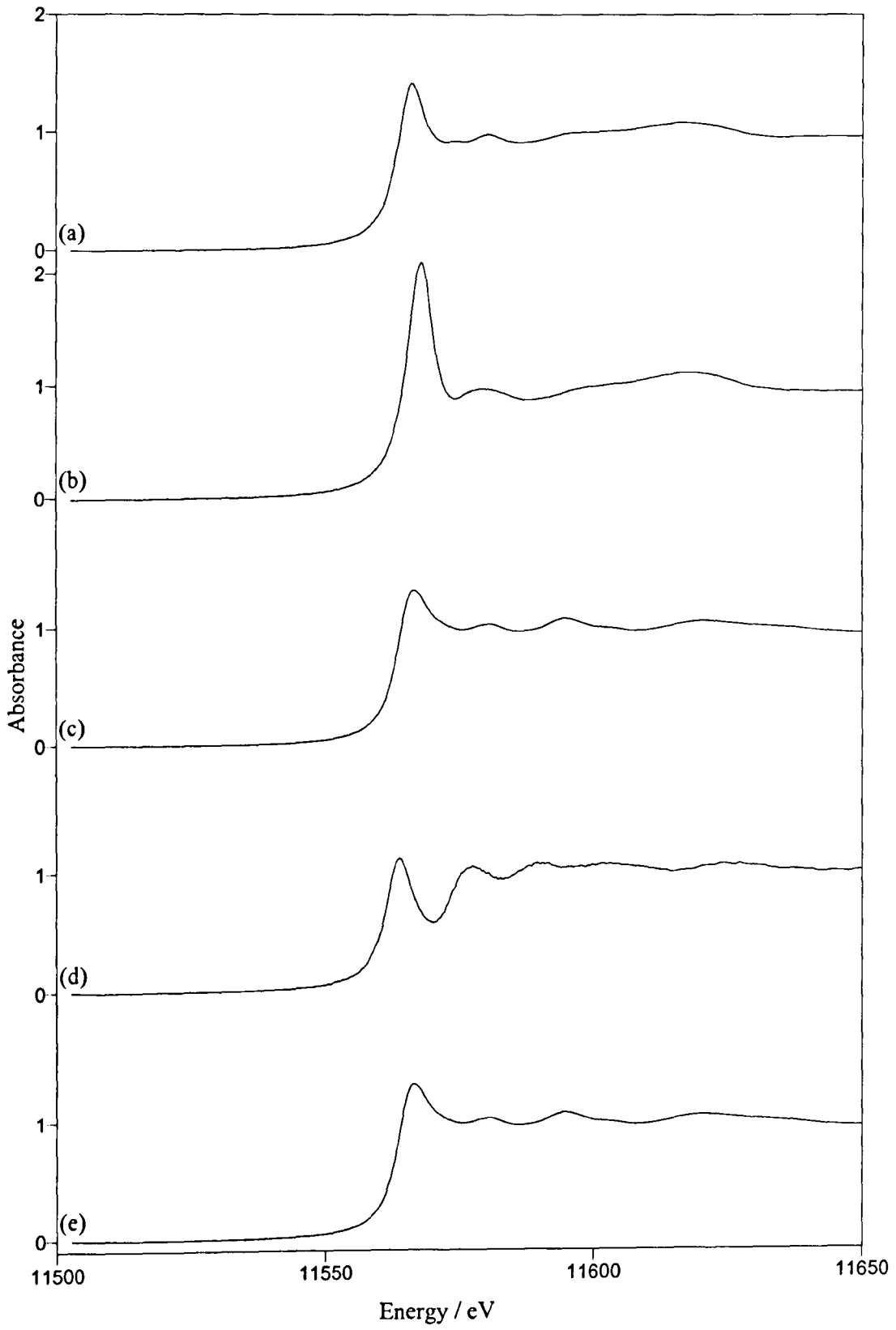

Figure 4.31: Pt L_3-edge XANES spectra observed in platinum XAFS experiments. (a) K_2PtCl_4 in BN at room temperature, (b) K_2PtCl_6 in BN at room temperature, (c) sputtered sample of platinum atoms in a 5 % chlorine in argon matrix at 12 K, (d) sputtered sample of platinum atoms in an argon matrix at 12 K, (e) 0.25 mm palladium foil at room temperature.

the pre-edge peak which corresponds to an atomic transition) for the two model compounds, a difference is clearly observed between Pt^{II} and Pt^{IV}. The greater intensity of the pre-edge feature in K_2PtCl_6 is characteristic of a Pt^{IV} compound[72] and offers further experimental evidence to suggest that the compounds formed by the sputtering experiments are more likely to be Pt^{II} than Pt^{IV}. The energy of the edge positions observed are listed in table 4.25 below.

Sample	Edge Position / eV
K_2PtCl_4 in BN at 298 K	11566
K_2PtCl_6 in BN at 298 K	11564
Pt in 5 % Cl_2 / Ar at 12 K	11567
Pt in Ar at 12 K	11562
Platinum foil at 298 K	11564

Table 4.25: edge positions for Pt L_3-edge XAFS experiments

Conclusion

Solid $PtCl_2$ and $PtCl_4$ have been shown to dissociate to their constituent atoms when the solids are heated under vacuum, with the only species present in the gas phase in any appreciable quantity being chlorine. This confirms previous work and explains the lack of gas phase data available on the chlorides of platinum.

By the isolation of platinum atoms in an argon matrix doped with low levels of chlorine, molecular platinum dichloride has been isolated for the first time. FTIR, UV-Vis-NIR and EXAFS spectroscopy have been use to identify and characterise the structure and geometry of the *pseudo* gas phase species. From the spectroscopic data observed in these experiments coupled with previous reports of gas phase behaviour of platinum chlorides, the molecule formed is assigned as the dichloride, $PtCl_2$.

Experimental evidence presented in this chapter has shown that the structure of molecular $PtCl_2$ is most likely linear, with a bond length of 2.19 Å.

Section 4.4: **Palladium**

Introduction

Similar to the platinum dichlorides, experimental evidence previously presented shows that solid palladium (II) chloride decomposes on heating to palladium metal and chlorine gas.[73-75] The decomposition was shown to begin to occur at around 600 °C[74] when the solid begins to melt. Evidence for the existence of $PdCl_2$ in the gas phase was first presented by Bell, Merten and Tamagi in 1961,[76] whose work on the vaporisation of solid $PdCl_2$ also identified the presence of polymeric Pd_5Cl_{10} as a vapour phase molecule along with the decomposition products. Experiments on the formation of solid $PdCl_2$ by the heating of palladium powder in the presence of chlorine have reported the formation of gas phase $PdCl_2$.[77,78] The molecule was observed to be a stable decomposition product as the solid formed began to melt and decompose in a chlorine atmosphere.

The first mass spectral data on gas phase palladium chlorides was presented by Schäfer *et al.*[79] and identified the sole molecular species from vacuum sublimed $PdCl_2$ as the hexamer, Pd_6Cl_{12}. A more recent thermodynamic study[80] concurred with the existence of this species in the vapour, along with other smaller multimers. This was said to account for the previous identification of Pd_5Cl_{10} as the major species, this being the average composition of the hexamer and lower molecular weight species.

The only report of the infrared spectrum of the vapour above $PdCl_2$ also identifies Pd_6Cl_{12} as the major gas phase species observed after trapping the gas phase sublimation products in argon.[81] A reproduction of the spectrum presented is shown in figure 4.32, vibrational frequencies are reported for the weaker bands

evident at 466 and 485 cm^{-1} but no values are quoted for the remaining spectral features. The structures shown in figure 4.32 are calculated as the probable structure of the Pd_6Cl_{12} molecule in the gas phase. The most stable calculated structure was low symmetry (C_{1h}) and therefore expected to have 48 infrared active vibrational modes. To account for the nature of the infrared spectrum observed the structure shown on the left (O_h symmetry, 4 active vibrational modes) is suggested as the most likely geometry of Pd_6Cl_{12} based on the infrared spectrum observed with the bold lines on figure 4.32 representing the calculated intensity of the active infrared bands. The second structure is presented to account for the additional two weak transitions present at 400 cm^{-1} not accounted for in the spherical structure which could be due to "dangling chlorine ions".

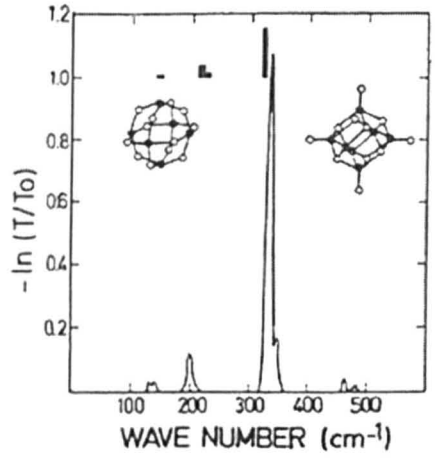

Figure 4.32: previously reported[81] IR spectrum of Pd_6Cl_{12} in argon.

The following section describes the results obtained from a series of experiments designed to generate monomeric palladium chloride and characterise the *pseudo* gas phase structure of the isolated molecule, as it has been predicted that the ground state has a 98° bond angle.[82,83]

Results and Discussion.

Furnace Experiments

Mass spectral data recorded on the sublimation products only provided evidence of the decomposition of the solid on heating, with only chlorine peaks being present in the spectrum and a film of palladium present on the inside of the silica pot. These findings are inconsistent with the previous reports, however those experiments dealt with the sublimation products from a Knudsen cell type furnace. The Knudsen cell furnace is more likely to provide molecular species as the evaporation proceeds under a vapour pressure, despite being a vacuum sublimation technique. This creates a thermodynamic equilibrium in which the molecule is stable. Since the aim of the experiments was to generate the monomer $PdCl_2$ the furnace adaptation required to produce the previously assigned hexameric vapour phase species was not pursued further.

Sputtering Experiments

In an attempt to form a monomeric palladium chloride, palladium foil was sputtered with argon doped with low levels of chlorine and the products isolated in chlorine containing argon matrices.

a) UV-Vis-NIR Results

Figure 4.33 shows the UV-Vis-NIR spectra observed when the product of palladium foil sputtered with argon / chlorine gas mixtures was isolated at 12 K with the discharge gas acting as the matrix. The figure shows the sputtering products isolated in (a) argon, (b) 1 % chlorine in argon and (c) 5 % chlorine in argon. The observed bands in the argon matrix are in good agreement with those previously

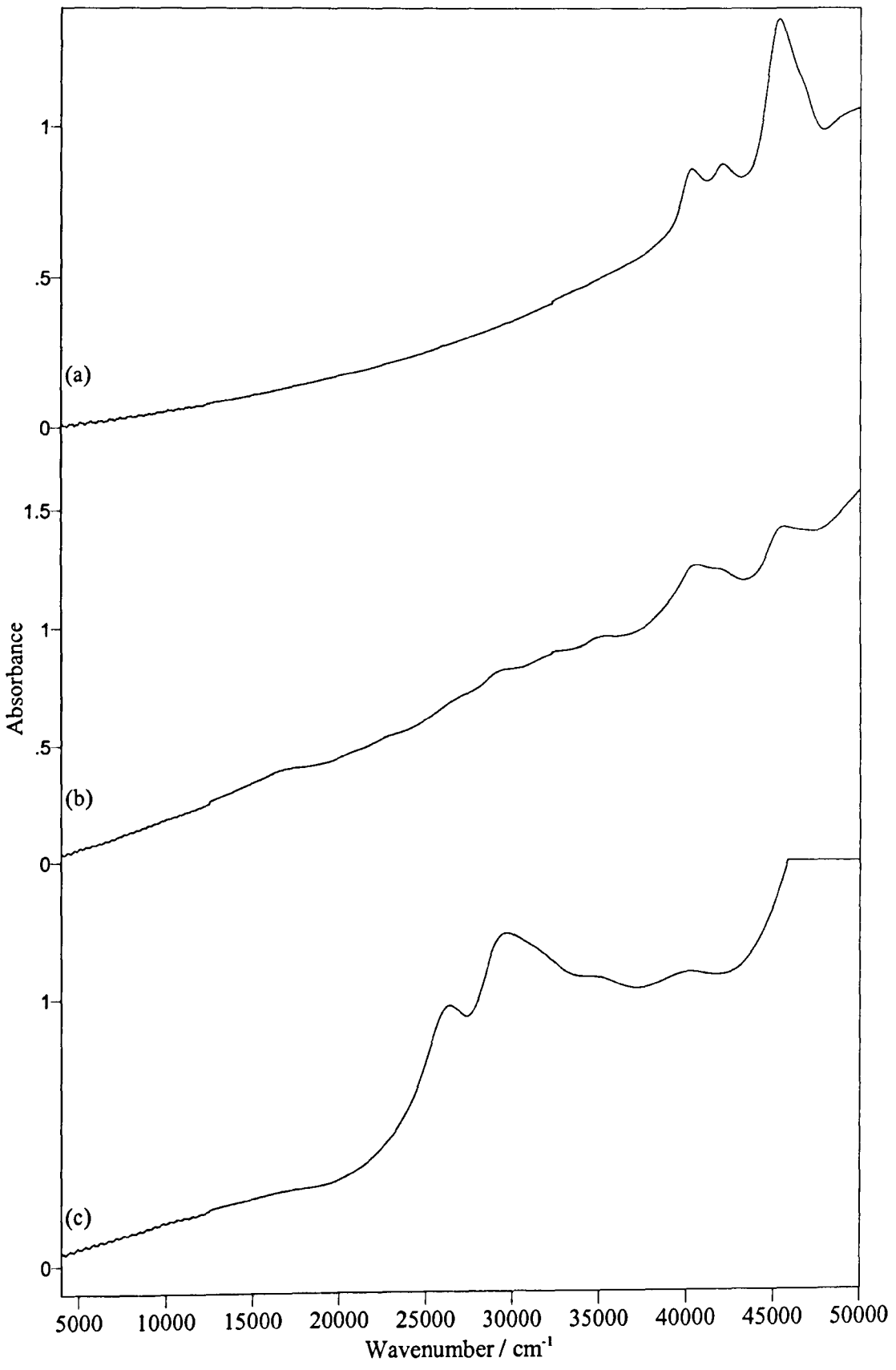

Figure 4.33: UV-Vis-NIR spectrum of sputtered palladium products isolated at 13 K.

(a) argon, (b) 1 % chlorine / argon, (c) 5 % chlorine / argon.

reported for palladium atoms isolated in an argon matrix[84(a)] and do not show any bands associated with the presence of the dimer.[84(b)] These values are given in table 4.26 below along with frequency of the absorption bands in chlorine containing matrices and the assignments of the previously reported transitions.

Observed Frequency (Ar)	Observed Frequency (1% Cl_2 / Ar)	Observed Frequency (5% Cl_2 / Ar)	Previously Reported[84(a)]	Assignment[84(a)]*
46700 cm^{-1}			47169 cm^{-1}	$4d^9\ 5p;\ ^1P_1$
45600 cm^{-1}	45520 cm^{-1}		45454 cm^{-1}	$^3D_1$
41850 cm^{-1}	41950 cm^{-1}		42372 cm^{-1}	$^3F_2$
40650 cm^{-1}	40630 cm^{-1}		40322 cm^{-1}	$^3P_1$
		40210 cm^{-1}		
	34950 cm^{-1}	34810 cm^{-1}		
	29560 cm^{-1}	29710 cm^{-1}		
	27100 cm^{-1}	26340 cm^{-1}		
	17150 cm^{-1}			

**assignments based on $4d^{10}$; $^1S_0$ ground state.*

Table 4.26: observed absorption bands for palladium atoms isolated in an argon and chlorine containing argon matrices at 12 K and assignments.

The assignment of the highest energy transition is somewhat tentative although it does appear to be present as a weak shoulder on the intense 45600 cm^{-1} band. The spectrum of the 1 % chlorine in argon matrix shows a similar pattern to those previously reported for gold, silver and platinum sputtering products being that the atomic transitions are still evident in the spectrum along with signs of other (presumably) molecular species. The evidence of new molecules forming is only very weak, with the undulations in the region 15000 to 40000 cm^{-1} showing signs of other species isolated in the matrix. As the chlorine concentration was increased to 5 %

(figure 4.33(c)) the chlorine band at 30000 cm^{-1} becomes the dominating feature but a new band at 26340 cm^{-1} is also evident. Weak bands at 34810 and 40210 cm^{-1} may also be absorption bands from a molecular species in the matrix but these are less defined due to the dominance of chlorine and the atomic transitions in that spectral region.

b) Infrared Results

The infrared spectrum observed when palladium foil was sputtered with 5 % chlorine in argon and isolated at 10 K shown in figure 4.34. The spectrum shows one major feature at 336 cm^{-1} and the possibility of a weak shoulder at 329 cm^{-1}.

The presence of only one major absorption band in the far infrared immediately leads to some conclusions being made about the geometry of the molecule. Comparison with the predicted spectra shown in figure 4.2 appear to suggest that the molecule formed is linear $PdCl_2$, trigonal planar $PdCl_3$ or $PdCl_4$ square planar or tetrahedral (with tetrahedral being the more likely structure for a palladium d^6 complex).

The expansion of the absorption band shown in figure 4.34(a) along with the predicted isotope patterns for linear $PdCl_2$ (b) show the problems in attempting to resolve the experimentally observed vibrational band. The isotope patterns shown in figure 4.34 are more complicated than those predicted for gold chloride as the metal isotope splitting pattern distorts the characteristic chlorine isotope pattern. This means that even a partially resolved band is unlikely to provide the structure required to determine the co-ordination number. The experimentally observed band is also rather broad (4 cm^{-1} at the peak half height), which is probably due to the large amount of isotopic structure contained underneath the band envelope. However, the

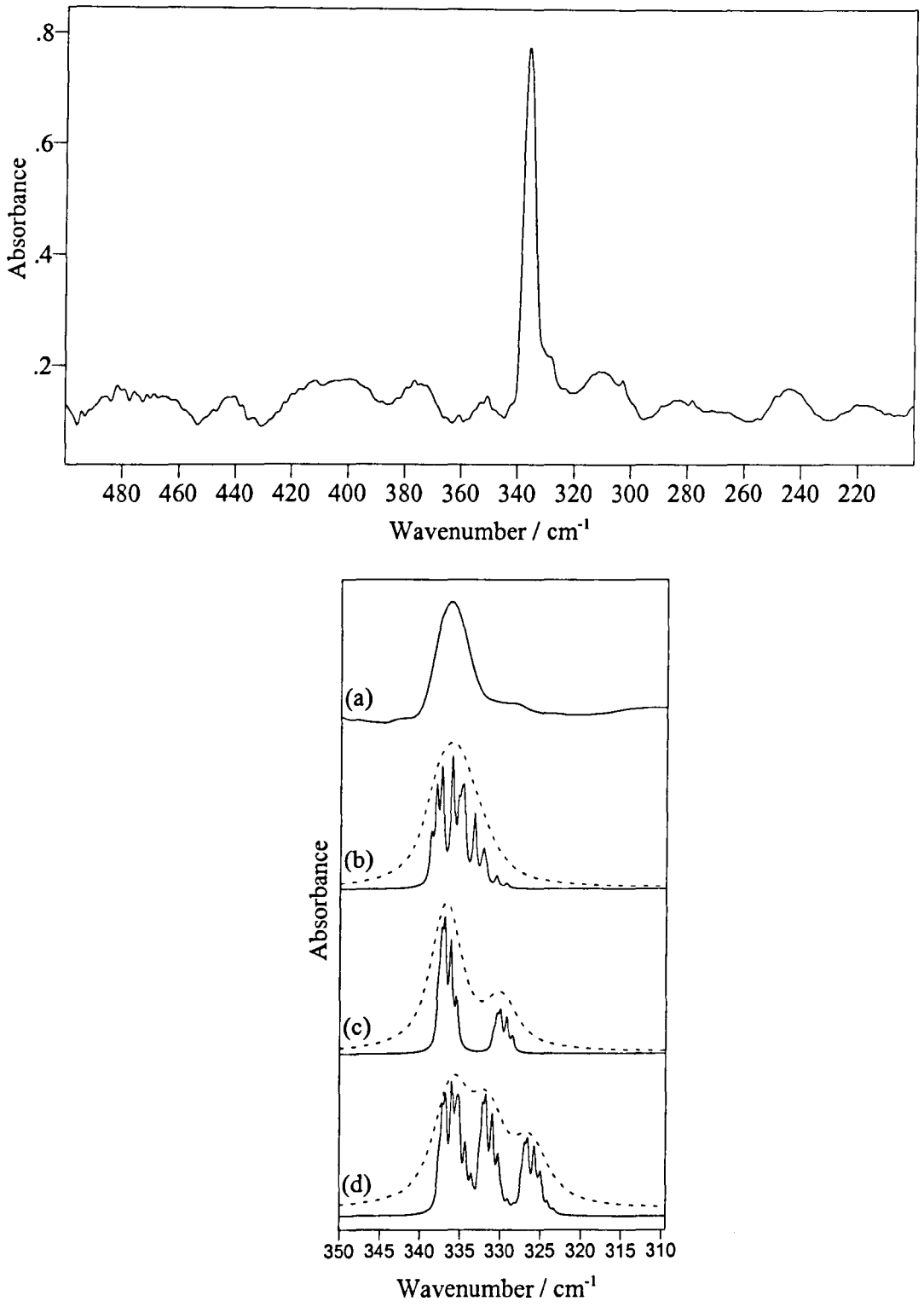

Figure 4.34: infrared spectrum of sputtered palladium products isolated at 10 K in 5 % chlorine / argon. (a) experimentally observed spectrum at 2 cm^{-1} resolution, (b) predicted spectrum for $PdCl_2$ (linear), (c) predicted spectrum for bent $PdCl_2$ (ν_1 and ν_3 overlapping), (d) predicted spectrum for bent $PdCl_2$ (ν_1 and ν_3 separated by 5 cm^{-1}).

——— 0.5 cm^{-1} resolution, ····· 4 cm^{-1} resolution.

band can still be used to assist in the characterisation of the species present. Included in the figure are the predicted patterns for bent $PdCl_2$ with a bond angle of 98° (as previously predicted[82,83]) which would result in a symmetric and asymmetric stretch of near identical frequency. In the figure 4.34(c) both the symmetric and asymmetric stretching modes overlap and interact, this results in the 3 : 1 isotope pattern shown. The interaction force constant refines to a negligible value in this instance and the molecule is effectively two identical Pd-Cl units, hence the pattern observed. If the frequencies of ν_1 and ν_3 are separated by 5 cm^{-1} the spectrum given in figure 4.34(d) is observed and is effectively two 9 : 6 : 1 bands overlapping. The dashed lines on figure 4.34 show each of the predicted spectra plotted at 4 cm^{-1} bandwidth to identify the shape and width of the band envelope. It is immediately obvious that the predicted spectra for the bent $PdCl_2$ molecule do not represent that experimentally observed. The 3 : 1 ratio in 4.34(c) is still clearly evident even at low resolution, making it significantly different from that observed. The broadness of the band in figure 4.34(c) is predicted to be significantly larger than that observed in the deposition spectrum and also still presents some structure. From these calculations it would appear that the band envelope predicted for the linear $PdCl_2$ molecule matches the experimentally observed vibrational band much better than those predicted for bent $PdCl_2$.

As may be expected further scans at higher resolution produced no improvement in the observed experimental spectrum and reducing the chlorine concentration to 1 % reduced the intensity in a similar manner to that previously described in the platinum experiments without allowing the band to be resolved further.

c) XAFS

To determine the accuracy of the palladium XAFS experiments the spectra of model compounds were again recorded and analysed. Figure 4.35(a) shows the experimentally observed and theoretical EXAFS and Fourier Transform for solid $PdCl_2$. A reasonable fit can be found for the dichloride with the bond length observed being close to that of the reported literature value (2.31 Å)[85] although the co-ordination number refines to around 3. This value can be explained when the crystal structure of palladium dichloride is taken into account. The published crystal structure[85] shows the central palladium atom surrounded by four chlorine atoms in a square planar arrangement at around 2.31 Å and also has two adjacent palladium atoms at around 3.33 Å. Figure 4.35(b) shows the EXAFS and Fourier Transform for a second model compound, K_2PdCl_4. A reasonable fit is again produced on refinement for a complex identified in the solid state as being square planar $PdCl_4$ with a Pd-Cl bond length of 2.298 Å.[86] The EXAFS refinements for both structures given in table 4.27 describe reasonably well defined solid state structures with the co-ordination number and bond length values in good agreement with the previously reported crystal structures.

	$r_{Pd\text{-}Cl}$	$2\sigma^2_{Pd\text{-}Cl}$ [a] / Å^2	E_f [b] / eV	N_1 [c]	R
$PdCl_2$	2.324 (6)	0.004 (1)	-8 (1)	3.2 (4)	46
K_2PdCl_4	2.295 (4)	0.005 (0.9)	-3 (1)	3.7 (3)	35

[a] *Debye-Waller factor,* [b] *Reflection of differences in experimental and theoretical Fermi levels,* [c] *co-ordination number.*

Table 4.27: refined EXAFS parameters for $PdCl_2$ and K_2PdCl_4 in BN at room temperature.

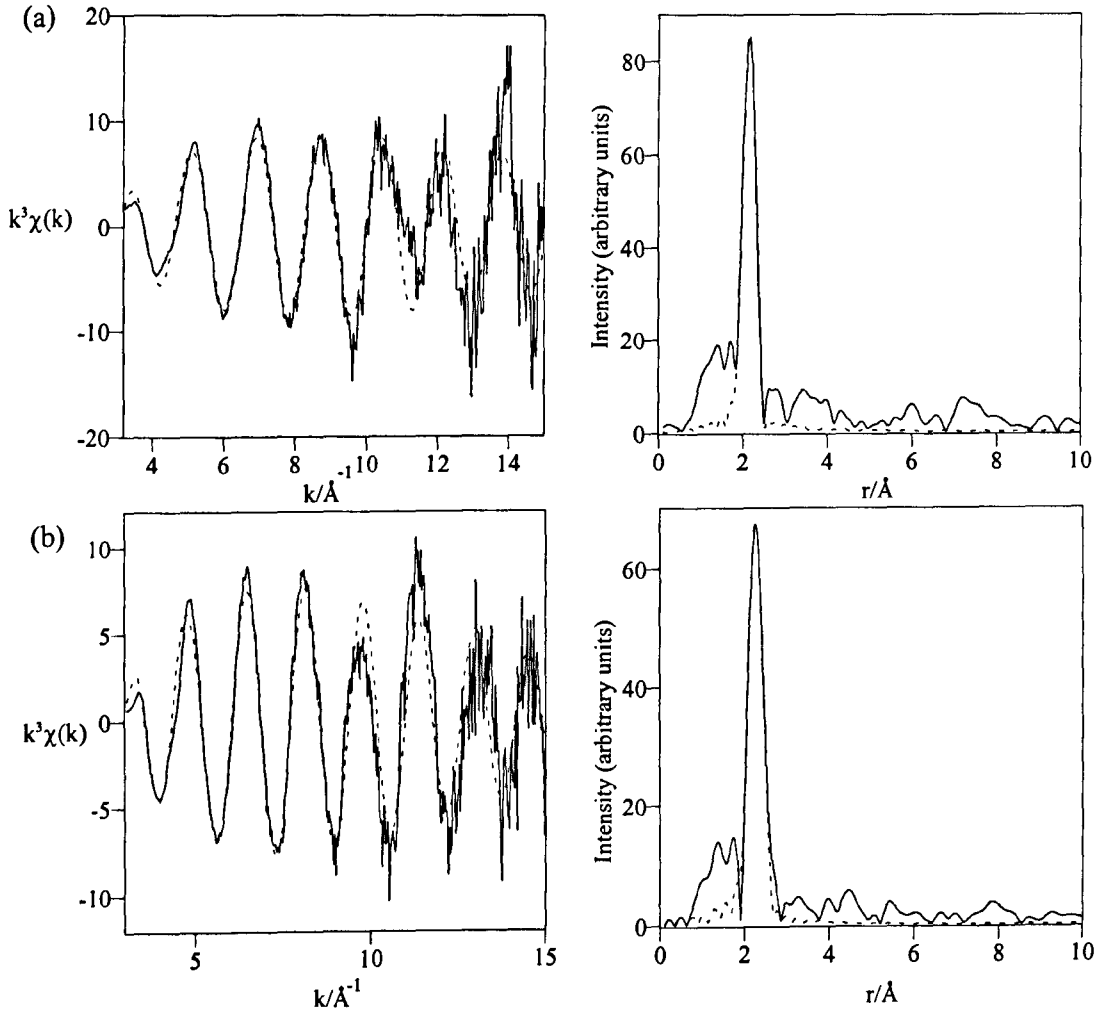

Figure 4.35: Pd K-edge EXAFS and Fourier Transform for palladium model compounds in BN at room temperature. (a) $PdCl_2$, (b) K_2PdCl_4

The observed and calculated EXAFS curves and Fourier Transforms from the X-ray spectroscopic study of palladium foil sputtering products isolated in a 5 % chlorine in argon gas mixture at 12 K are presented in figure 4.36 with the refined parameters given in the accompanying table (table 4.28).

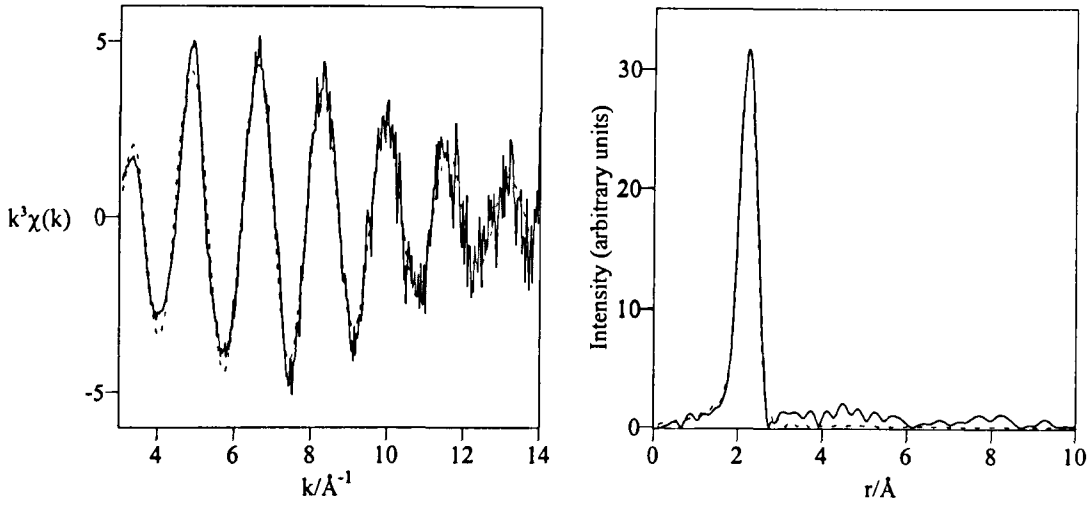

Figure 4.36: Pd K-edge EXAFS and Fourier Transform for palladium sputtered with 5 % chlorine / argon and isolated at 12 K.

r_{Pd-Cl}	$2\sigma^2_{Pd-Cl}$ [a] / Å^2	E_f [b] / eV	N_1 [c]	R
2.268 (3)	0.0115 (8)	-1.7 (6)	2.8(1)	24

[a] *Debye-Waller factor,* [b] *Reflection of differences in experimental and theoretical Fermi levels,* [c] *Co-ordination number.*

Table 4.28: refined EXAFS parameters For palladium sputtered with 5 % chlorine in argon and isolated at 12 K.

A refinement of the co-ordination number produced a value of 2.8, which was thought to be more likely 2 than 3 due to the stability of Pd^{II} in comparison to Pd^{III}. A bond length of 2.268 Å is produced in the refinement which as expected is shorter than the Pd-Cl distance of either of the model compounds. The parameters were then refined with multiple scattering terms included and with the co-ordination number

fixed at 2. The multiple scattering terms included in the refinement result in the appearance of a weak band at double the bond length which acts as evidence of the linearity of the molecule shown in figure 4.36. The band is rather weak in this prediction and is not obviously present above the noise level in the experimentally observed Fourier Transform.

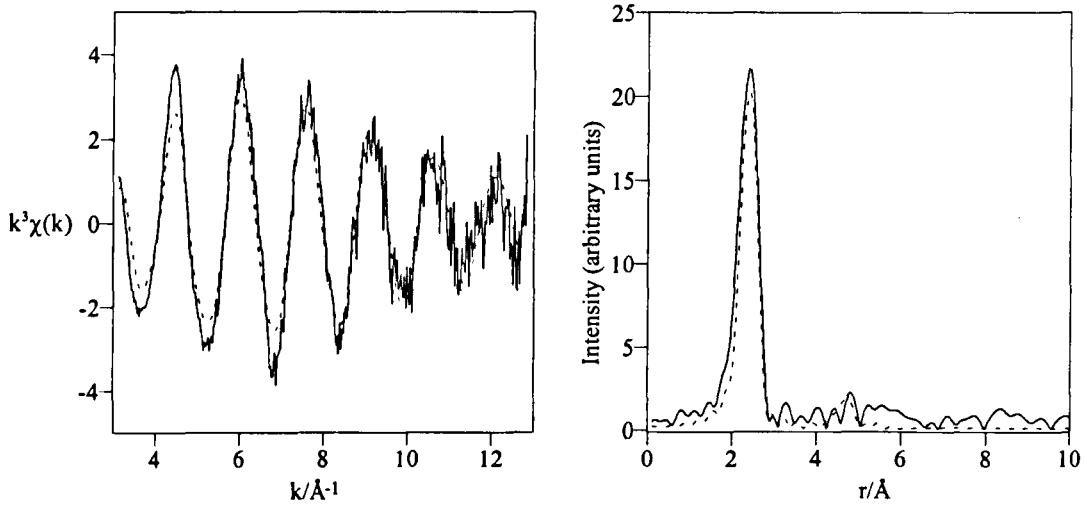

Figure 4.36: Pd K-edge EXAFS and Fourier Transform for palladium sputtered with 5 % chlorine / argon and isolated at 12 K. Including multiple scattering term, with a co-ordination number of 2.

r_{Pd-Cl}	$2\sigma^2_{Pd-Cl}$ [a] / Å²	E_f [b] / eV	R
2.268 (3)	0.0079 (5)	-2.3 (8)	24

[a] Debye-Waller factor, [b] Reflection of differences in experimental and theoretical Fermi levels.

Table 4.29: refined EXAFS parameters For palladium sputtered with 5 % chlorine in argon and isolated at 12 K. Including multiple scattering term, with a co-ordination number of 2.

The XANES spectra observed for the model compounds and after the palladium sputtering experiments are shown in figure 4.37 along with the spectrum observed

from a 0.25 mm thick palladium foil. The edge data presented in the table below are reasonably consistent and the edge steps are of very similar relative intensity after pre-edge background subtraction.

Sample	Edge Position / eV
K_2PdCl_4 in BN at 298 K	11566
$PtCl_2$ in BN at 298 K	11564
Pd in 5 % Cl_2 / Ar at 12 K	11567
Pd in Ar at 12 K	11562
Palladium foil at 298 K	11564

Table 4.30: edge positions for Pd L_3-edge XAFS experiments

Conclusion

The vacuum sublimation of solid state palladium (II) has been shown to result in the direct decomposition of the molecule, with no molecular species being observed in the vapour by mass spectral analysis.

Sputtering palladium foil with a gas mixture of chlorine and argon and trapping the products in a matrix of the discharging gas has been identified as a new route to isolated monomeric palladium chloride molecules. The use of UV-Vis-NIR, infrared and EXAFS spectroscopy has again been employed in an attempt to determine the molecular and geometric structure of the isolated species with varied success. Although vibrational bands still cannot be resolved to obtain the isotopic structure contained within, a tentative assignment of the molecule as $PdCl_2$ can be made. The assignment is based on the previously reported stability of the dichloride along with the experimentally observed spectroscopic evidence described. If the molecule formed is indeed the dichloride as suspected then the infrared data presented strongly suggests that the molecule is linear.

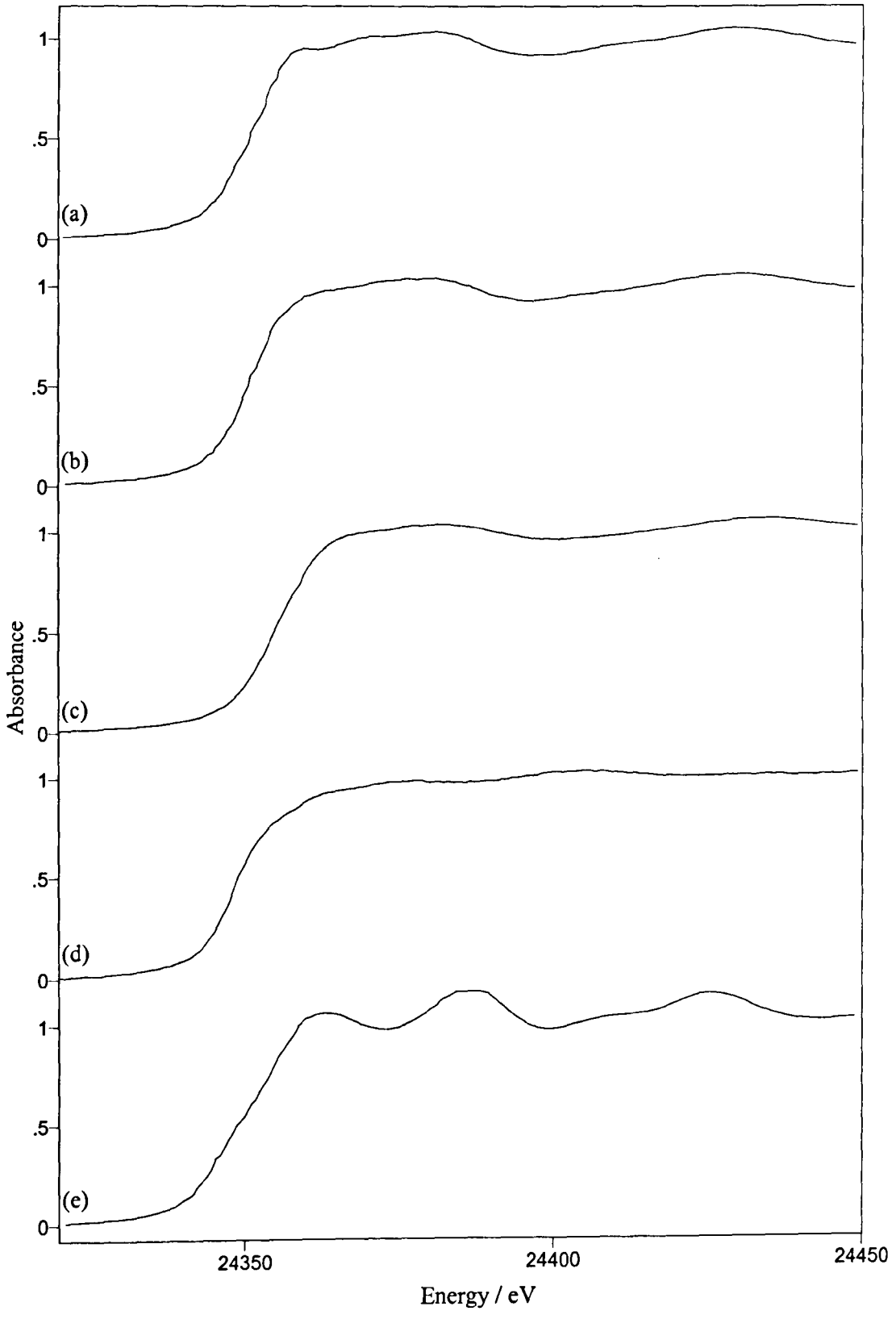

Figure 4.37: Pd K-edge XANES spectra observed in palladium XAFS experiments. (a) K_2PdCl_4 in BN at room temperature, (b) $PdCl_2$ in BN at room temperature, (c) sputtered sample of palladium atoms in a 5 % chlorine in argon matrix at 12 K, (d) sputtered sample of palladium atoms in an argon matrix at 12 K, (e) 0.25 mm palladium foil at room temperature.

Section 4.5: **Complementary Studies - Atomic EXAFS.**

Continuing the investigation of a sputtering source for the isolation of atomic species in cryogenic matrices EXAFS were recorded on samples of platinum and palladium isolated in argon matrices at 12 K. Recently atomic EXAFS has been used to help determine the oxidation state of platinum in catalytic research, as the rate of chemisorption can be monitored by the change in the Pt-edge data.[87]

Figure 4.38 below shows the observed EXAFS and Fourier Transform after the sputter deposition of platinum with argon, with the refined fitting parameters given in the accompanying table. Although the low concentration of atoms in the matrix makes the data particularly noisy, a reasonable fit to the data is still found. The evidence is in reasonable agreement with what would be expected for platinum atoms isolated in an argon matrix. The local environment is shown by the EXAFS to consist of around 14 argon atoms at a distance of 4.02 Å. The co-ordination number is poorly defined, with a large error margin and the degree of thermal and static disorder also large. However, a large proportion of this is most likely due to the poor data quality but does still fit to a platinum atom isolated in an argon matrix site. A co-ordination number of 12 is expected for an atom isolated in the cubic close packed lattice, which is within the error margin of the refined co-ordination number. The bond length of 4.02 Å is clearly too large to be a meaningful bond between platinum and argon but is a reasonable distance to be the sum of the van der Waals radii of adjacent matrix atoms. The Debye-Waller factor is also in reasonably good

agreement with previous studies on krypton isolated in argon matrices which showed 0.03 $Å^2$ to be a reasonable degree of disorder for matrix isolated atomic species.[88]

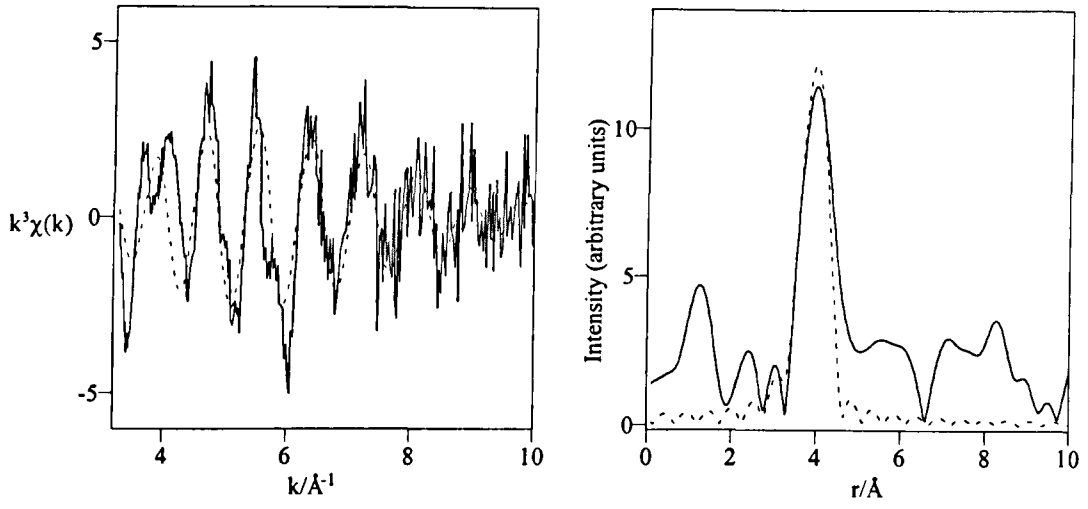

Figure 4.38: Pt L_3-edge EXAFS and Fourier Transform for platinum sputtered with argon and isolated at 12 K.

$r_{Pt\text{-}Ar}$	$2\sigma^2_{Pt\text{-}Ar}$ [a] / Å^2	E_f [b] / eV	N	R
4.02 (2)	0.031 (8)	7 (2)	14 (4)	69

[a] *Debye-Waller factor,* [b] *Reflection of differences in experimental and theoretical Fermi levels,* [c] *co-ordination number.*

Table 4.30: refined EXAFS parameters For platinum sputtered with argon and isolated at 12 K.

In contrast to this the observed EXAFS and Fourier Transform for palladium sputtered with argon and isolated at 12 K is shown in figure 4.39(a) with the refined fitting parameters again given in the accompanying table. In this case strong evidence is presented for the formation of a $PdAr_x$ species, with a co-ordination number of 1 and a bond length of 2.5 Å with a reasonable degree of disorder. For comparison figure 4.39(b) rules out the possibility of the isolation of dimeric species as a very poor fit between experimentally observed and theoretical data is produced.

Experimental evidence observed at the time of deposition also adds to the speculation of the formation of a co-ordinated species. A green glow was observed on the deposition surface during the palladium deposition which was not observed during any other sputtering deposition. The glow observed gradually deteriorated on completion of deposition, but returned again when the matrix was annealed. Spontaneous fluorescence has been observed under similar matrix isolation conditions when depositing silver in an argon matrix,[89] however in that case it was assigned to the photo-relaxation of silver dimers through agglomeration. The EXAFS observed in these experiments clearly show that the formation of dimeric species is not the source of the emission in this case which therefore suggests the formation of a meta-stable complex in the matrix.

The possible formation of metal-inert gas complexes have been studied theoretically, specifically $Au\text{-}Ar^+$ species.[90,91] Work has also been presented that suggests the sputtering discharge is a source of metastable metal ions.[92]

It is therefore reasonable to make a tentative assumption that the sputtering of palladium with argon may result in the formation of a Pd-Ar or $Pd\text{-}Ar^+$ species.

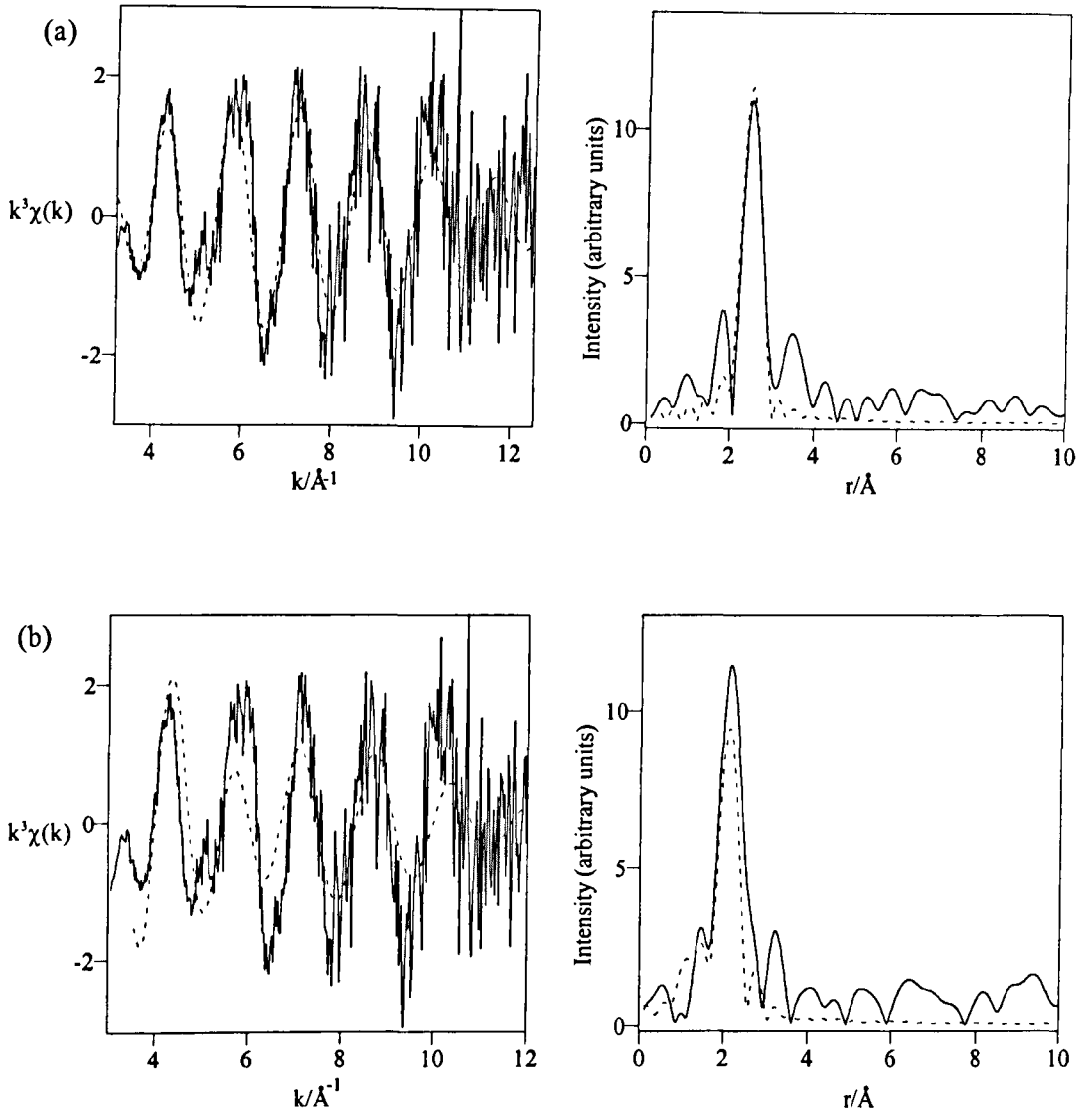

Figure 4.39: Pd K-edge EXAFS and Fourier Transform for palladium atoms isolated in argon at 12 K. (a) Pd-Ar refinement, (b) Pd-Pd refinement.

	r_{Pd-X}	$2\sigma^2_{Pd-X}$ [a] / Å^2	E_f [b] / eV	N_1 [c]	R
Pd-Ar	2.53 (1)	0.010 (3)	-3 (2)	1.2 (2)	51
Pd-Pd	2.22 (1)	0.023 (4)	-2 (2)	1.5 (4)	65

[a] *Debye-Waller factor,* [b] *Reflection of differences in experimental and theoretical Fermi levels,* [c] *co-ordination number.*

Table 4.27: refined EXAFS parameters for Pd-X species isolated in argon at 12 K (X = Ar or Pd).

Conclusion

EXAFS studies on platinum and palladium atoms isolated in argon matrices have provided evidence of both atomic isolation (in the case of platinum) and bond formation (in the case of palladium) between isolated metal and matrix gas atoms.

The results presented in this section are very much in the preliminary stage of the investigation and require more work before the evidence presented can be used to unambiguously confirm the result so far observed. A more intense edge step, provided by increasing the concentration of the isolated species in the matrix, should improve the signal-to-noise and provide better EXAFS data. This is particularly relevant for isolated atoms as the larger interatomic distances require good quality data at high k space.

Section 4.6: **Conclusion**

These studies have shown that the hollow cathode sputtering source is an excellent source for matrix isolated atomic species. Unfortunately, it is also evident that although it works well as an atom source applying this method to the generation of new species is somewhat problematic. Difficulties encountered with the reaction of the atomic species with reactive dopants in the matrix gas provide poor data quality when compared to the clarity of some of the atomic spectra observed. The presence of multiple molecular species, chlorine and unreacted atoms all make the UV-Vis-NIR and EXAFS results difficult to assign unambiguously. The apparent low yield of reaction can also provide low intensity infrared bands, making the underlying isotopic structure of any observed bands very difficult to deduce, especially when coupled with the broadening of the observed bands caused by the presence of chlorine in the matrix. The technique also suffers from the high gas flow rate required to sustain the discharge during deposition, with the net gain in band intensity being negligible after only a relatively short deposition period due to the deterioration of light penetration. Additional impetus for the alteration of the atom source was supplied by the intrinsic difficulty of maintaining the continuous deposition source. The simplicity and clarity of the atomic spectra provided is the only consolation for the general difficulty, in terms of determining the precise experimental conditions, experienced in recording them.

Experiments with other atom sources have provided an alternative route to these new isolated species which may allow depositions to be more controlled and lead to an improvement in the definition of the observed bands. Laser ablation experiments offered evidence of providing an alternative atom source with a suitable

deposition rate, but unfortunately experimental constraints made it difficult to complete these experiments to a meaningful result during the course of this research. Ideally the species generated from the metal target by ablation need to be confirmed by UV-Vis-NIR spectroscopy as the precise conditions that result in the isolation of atoms should be determined before attempting to generate the metal chlorides by this method. The improvements in the experimental set-up required for this technique to be used to its full potential should now be achieved as a laser has recently been provided by The Royal Society based on the work presented in this thesis.

However, these experiments can still be considered to have achieved the initial experimental goals. The monomeric chlorides of gold, platinum and palladium have all been isolated for the first time, with reasonably firm assignment made for matrix isolated $PdCl_2$ and $PtCl_2$. For the gold chloride isolated, assumed at this time to be $AuCl_3$ or $AuCl_2$, it is only an improvement in the data quality that is required before the assignments made in this chapter can be confirmed unambiguously.

The possible assignment of $AuCl_2$ rather than $AuCl_3$ would add some consistency to the work. Platinum and palladium have both been confirmed as forming the dichloride when the atoms are isolated in a chlorine containing argon matrix. This suggests a mechanism of formation of these chlorides, namely the insertion of a metal atom into the chlorine molecule to form the dichloride. If this were the case for all atomic species it would clearly suggest the formation of $AuCl_2$. This could also assist in the understanding of the silver sputtering experiments and the assignment of the species formed.

This new information has merely highlighted the need for an improvement in the quality of the infrared data required to determine the isotope pattern and confirm the structure of the gold chloride formed. The apparent reproducibility of the laser

ablation experiment may well be the key to determining this structure and ultimately lead to a greater understanding of the reactivity and formation mechanism of gold atoms isolated in chlorine containing argon matrices.

Section 4.7: **References.**

[1] W. Fischer and W. Blitz, *Z. Anorg. Allgem. Chem.*, **176**, 81 (1928).

[2] W. Blitz, W. Fischer and R. Juza, *Z. Anorg. Allgem. Chem.*, **176**, 121 (1928).

[3] W. F. C. Ferguson, *Nature*, **120**, 298 (1928).

[4] W. F. C. Ferguson, *Phys. Rev.*, **31**, 969 (1928).

[5] J. Thomsen, *J. Prakt. Chem.*, **13**, 337 (1876).

[6] G. Krüss and F. Schmidt, *Ber. Dtsch. Chem. Ges.*, **20**, 2634 (1887).

[7] J. Thomsen, *J. Prakt. Chem.*, **37**, 105 (1888).

[8] G. Krüss and F. Schmidt, *J. Prakt. Chem.*, **38**, 77 (1888).

[9] J. D. Corbett and L. F. Druding, *J. Inorg. Nucl. Chem.*, **11**, 20 (1959).

[10] E. M. W. Janssen, F. Pohlmann and G. A. Wiegers, *J. Less-Common Met.*, **45**, 261 (1976).

[11] P. N. Kokhanenke, *Ivest. Akad. Nauk. SSSR, Ser. Fiz.*, **15**, 685 (1951).

[12] S. S. Batsanova, M. N. Sokolova and E. D. Ruchkin, *Izv. Akad. Nauk. SSSR, Ser. Khim.*, **9**, 1863 (1971).

[13] I. Ivashentsev and R. I. Timonova, *Russ. J. Inorg. Chem.*, **12**, 1059 (1967).

[14] M. N. Zyryanov and G. A. Khlebnikova, *Izv. Vyssh. Uchlebn. Zaved. Tsvet. Metall.*, **1976**, 163 (1976).

[15] M. N. Zyryanov and G. I. Butanova, *Izv. Vyssh. Uchlebn. Zaved. Tsvet. Metall.*, **1987**, 70 (1987).

[16] J. S. Shannon and J. M. Swan, *Chem. Comm.*, **1965**, 33 (1965).

[17] S. E. James and J. P. Hager, *Metall. Trans. B*, **9B**, 501 (1978).

[18] V. K. Tigarov, E. V. Makarov and V. A. Bryukvin, *Russian Metallurgy*, **1993** (5), 56 (1993).

[19] J. P. Hager and R. B. Hill, *Met. Trans.*, **1**, 2723 (1970).

[20] E. S. Clark, D. H. Templeton and C. H. MacGillavry, *Acta Cryst.*, **11**, 284 (1958).

[21] A. F. Wells, *Structural Inorganic Chemistry,* Oxford: Clarendon Press, p 508 (1947).

[22] P. Schwerdtfeger, P. D. W. Boyd, S. Brienne and A. K. Burrell, *Inorg. Chem.*, **31**, 3411 (1992).

[23] D. M. Adams and R. G. Churchill, *J. Chem. Soc. (A),* **1968**, 2141 (1968).

[24] I. R. Beattie, T. R. Gilson and G. A. Ozin, *J. Chem. Soc. (A),* **1968**, 2765 (1968).

[25] R. Forneris, J. Hiraishi, F. A. Miller and M. Uehara, *Spectrochim. Acta,* **26A**, 581 (1970).

[26] J. Strähle and K. P. Lörcher, *Z. Naturforsch, Teil B,* **29**, 266 (1974).

[27] E. M. W. Janssen, F. Pohlmann and G. A. Wiegers, *J. Less-Common Met.*, **38**, 71 (1974).

[28] L. Capella and C. Schwab, *C. R. Acad. Sc. Paris,* **260**, 4337 (1965).

[29] D. Breitinger and H Leuchtenstern, *Z. Naturforsch, Teil B,* **29**, 806 (1974).

[30] E. Husson, N. Q. Dao and D. K. Breitinger, *Spectrochim. Acta,* **37A**, 1087 (1981).

[31] D. S. Rustad and N. W. Gregory, *Polyhedron,* **10**, 633 (1991).

[32] L. Nalbandian, S. Boghosian and G. N. Papatheodorou, *Inorg. Chem.*, **31**, 1769 (1992).

[33] L. Nalbandian and G. N. Papatheodorou, *Vibrational Spectroscopy,* **4**, 25 (1992).

[34] L. C. O'Brien, A. L. Elliott and M. Dulick, *J. Mol. Spectrosc.*, **194**, 124 (1999).

[35] P. Schwerdtfeger, *Mol. Phys.*, **86**, 359 (1995).

[36] T. Nakajima, T. Suzumura and K. Hirao, *Chem. Phys. Lett.*, **304**, 271 (1999) *and references therein.*

[37] I. R. Beattie, N. Cheetham, M. Gardner and D. E Rogers, *J. Am. Chem. Soc. A,* **1971**, 2240 (1971).

[38] N. A. Young, Massspec, Program to calculate mass spectral data simulations, University of Hull, 1995.

[39] (a) D. M. Gruen and J. K. Bates, *Inorg. Chem.*, **16**, 2450 (1977) *and references therein.*

(b) W. Harbich, S. Fedrigo, F.Meyer, D. M. Lindsay, *Z. Phys. D,* **19**, 157 (1991).

(c) W. Harbich, S. Fedrigo, J. Butter, D. M. Lindsay, J. Lignieres, C. J. Rivoal and D. Kreisel, *J. Chem. Phys.*, **93**, 8535 (1990).

[40] W. F. Howard, Jr. and L. Andrews, *J. Am. Chem. Soc.*, **95**, 2056 (1969).

[41] J. M. Williams and S. W. Peterson, *J. Am. Chem. Soc.*, **91**, 776 (1969).

[42] B. Reffy, M. Kolontis, A. Schulz, T. M. Kapötke and M. Hargittai, *J. Am. Chem. Soc.*, **122**, 3127 (2000).

[43] A. Pantelouris, G. Küper, J. Hormes, C. Feldmann and M. Jansen, *J. Am. Chem. Soc.*, **117**, 11749 (1995).

[44] H. M. Rosenstock and L. K. Brice. *US At. Energy Comm.*, **ORNL-2772**, (1959).

[45] A. W. Gusarov and L. N. Gorochov, *Vest. Mosk. Univ.*, **5**, 14 (1962).

[46] A. Visnapuu and J. W. Jensen, *J. Less-Comm. Met.*, **20**, 141 (1970).

[47] P. Graber and K. G. Weil, *Ber. Berbunsen-Ges.*, **76**, 410 (1972).

[48] L. C. Wagner and R. T. Grimley, *J. Phys. Chem.*, **76**, 2819 (1972).

[49] M. Binnewies, K. Rinke, H. Schäfer, *Z. Anorg. Allg. Chem.*, **395**, 50 (1973).

[50] P. Gräber and G. Weil, *Ber. Berbunsen-Ges.*, **77**, 410 (1973).

[51] E. V. Makarov, V. A. Bryukvin and V. K. Tagirov, *Russ. J. Non-Ferrous Met.*, **38**, 36 (1997).

[52] T. P. Martin and H. Schaber, *J. Chem. Phys.*, **73**, 3541 (1980).

[53] S. Vonbacho, H. Saltsburg and G. P. Ceasar, *J. Electron Spectrosc. and relat. phenom.*, **8**, 359 (1976).

[54] A. W. Potts and M. L. Lyus, *J. Electron Spectrosc. and relat. phenom.*, **13**, 305 (1978).

[55] J. Berkowitz, C. H. Batson and G. L. Goodman, *J. Chem. Phys.*, **71**, 5829 (1980).

[56] E. Apra, E. Stefanovich, R. Dovesi and C Roetti, *Chem. Phys. Lett.*, **186**, 329 (1991).

[57] S. A. Shchukarev, M. A. Oranskaya and T. S. Shemyakina, *Russ. J. Inorg. Chem.*, **1**, 17 (1956) *and references therein.*

[58] J. Krustinsons, *Z. Elektrochem.*, **45**, 83 (1939).

[59] U. Weise, H. Schäfer, H. G. v. Schnering, C. Brendel and K. Rinke, *Angew. Chem. Int Ed.*, **9**, 158 (1970).

[60] A. Landsberg and J. L. Schaller, *J. Less-Comm. Met.*, **23**, 195 (1971).

[61] U. Wosiewitz and H. Schäfer, *J. Less-Comm. Met.*, **32**, 389 (1973).

[62] S. V. Zemskov, Z. I. Zasorina, K. A. Grigorova, V. M. Grankin, V. N. Lyubimov, *Izv. Sib. Otd. Akad. Nauk. SSSR, ser Khim. Nauk.*, **19**, 107 (1974).

[63] M. Degner, B. Holle, J. Kamm, M. F. Pilbrow, G. Thiele, D. Wagner, W. Weigl and P. Woditsch, *Transition Met. Chem.*, **1**, 41 (1975/76).

[64] A. E. Schweitzer and G. T. Kerr, *Inorg. Chem.*, **17**, 2326 (1978).

[65] L. K. Shubochkin, V. I. Gishchin, G. M. Larin and V. A. Kolosov, *Russ. J. Inorg. Chem.*, **19**, 249 (1974).

[66] H. Schäfer and U Wosiewitz, *Z. Anorg. Allgem. Chem.*, **415**, 202 (1975).

[67] H. Schäfer, *Z. Anorg. Allgem. Chem.*, **415**, 217 (1975).

[68] E. V. Makarov, V. A. Bryukvin and V. K. Tagirov, *Russ. J. Non-Ferrous Met.*, **38**, 35 (1997) *and references therein.*

[69] D. H. W. Carstens, W. Brashear, D. R. Eslinger and D. M .Gruen, *Appl. Spectrosc.*, **26**, 184 (1972).

[70] (a) W. Klotzbücher and G. A. Ozin, *Inorg. Chem.*, **15**, 292 (1976).

(b) K. Jansson and R. Scullman, *J. Mol. Spec.*, **61**, 299 (1976).

[71] H. Takazawa, S. Ohba, Y. Saito and M. Sano, *Acta Cryst. B*, **46**, 166 (1990).

[72] A. L. Ankudinov, J. J. Rehr and S. R. Bare, *Chem. Phys. Lett.*, **316**, 495 (2000).

[73] F. Puche, *Compt. Rend.*, **200**, 1206 (1935).

[74] J. Krustinsons, *Z. Elektrochem.*, **44**, 537 (1938).

[75] M. A. Oranskaya and N. A. Mikhailova, *Russ. J. Inorg. Chem.*, **5**, 5 (1960).

[76] W. E. Bell, U. Merten and M. Tagami, *J. Phys. Chem.*, **65**, 510 (1961).

[77] Ya. I. Ivashentsev and R. I. Timonova, *Russ. J. Inorg. Chem.*, **12**, 308 (1967).

[78] N. S. Sidorov, B. G. Karepov and R. K. Nikolaev, *Izv. Akad. Nuak. SSSR, Neorg. Mater.*, **24**, 70 (1988). *English translation available.*

[79] H. Schäfer, U. Weise, K. Rinke, and C. Brendel, *Angew. Chem. Int. Ed. Engl.*, **6**, 253 (1967).

[80] V. K. Tagirov, E. V. Makarov and V. A. Bryukvin., *Russ. J. Inorg. Chem.*, **42**, 688 (1997).

[81] T. P. Martin, *J. Chem. Phys.*, **69**, 2036 (1978).

[82] P. E. M. Siegbahn, *Theo. Chim. Acta*, **87**, 441 (1994).

[83] P. E. M. Siegbahn, *Theo. Chim. Acta*, **88**, 413 (1994).

[84] (a) C. Sugiura, *J. Chem. Phys.*, **62**, 1111 (1975).

(b) W. E. Klotzbucher and G. A. Ozin, *Inorg. Chem.*, **19**, 3767 (1980).

[85] D. Belli Dell'Amico, F. Calderazzo, F. Marchetti and S. Ranello, *Angew. Chem. Int. Ed. Engl.*, **35**, 1331 (1996).

[86] S. A. Gromilov, V. I. Alekseev, I. A. Baidina and S. P. Khranenko, *Zh. Neorg. Khim.*, **39**, 2017 (1994).

[87] *For example:*

i) D. C. Koningsberger, J. de Graaf, B. L. Mojet, D. E. Ramaker and J. T. Miller, *Appl. Catal. A*, **191**, 205 (2000).

[88] I. R. Beattie, N. Binstead, W. Levason, J. S. Ogden, M. D. Spicer and N. A. Young, *High Temp. Sci.*, **26**, 71 (1990).

[89] S. A. Mitchell, J. Farell, G. A. Kenney-Wallace and G. A. Ozin, *J. Am. Chem. Soc.*, **102**, 7702 (1980).

[90] P. Pyykkö, *J. Am. Chem. Soc.*, **117**, 2067 (1995).

[91] J. P. Read and A. D. Buckingham, *J. Am. Chem. Soc.*, **119**, 9010 (1997).

[92] W. S. Taylor, E. M. Spicer and D. F. Barnas, *J. Phys. Chem.*, **103**, 643 (1999).

[93] A. J. Bridgeman, *personal communication* (2001).

Chapter

5

Tellurium Atom Chemistry

Introduction

In the previous chapter transition metal atoms were isolated in reactive matrices as a route to the formation of novel transition metal halides. In this chapter the results of an investigation into the formation of novel tellurium compounds generated in a similar manner, that is the isolation of tellurium atoms in reactive matrices, are described.

An ideal method for the generation of atomic species for matrix isolation experiments would appear to be the furnace evaporation of the pure solid as described previously for the isolation of gold atoms from the bulk metal. However, in the case of tellurium this method is unlikely to produce the required results since the major vapour phase species above heated bulk elemental tellurium are multimer species, with the presence of atomic species being proportionally low even when superheated.[1] Fortunately, tellurium chemistry offers an alternative route to matrix isolated atomic species, that is by the decomposition of a molecular precursor. Hydrogen telluride, H_2Te, is unstable in the presence of light and decomposes to H_2 and Te.[2] A previously reported Mössbauer study on H_2Te isolated in argon at 4.5 K[3] showed that by exposing the sample to UV radiation, decomposition occurs leaving isolated tellurium atoms in the matrix. An added advantage to this generation technique is that previous work[4] has shown that some of the atomic species are in a $^1D_2$ excited state rather than the $^3P_2$ ground state expected for thermally evaporated tellurium atoms. This may in effect increase the reactivity of the isolated tellurium atoms, lowering activation barriers of combination reactions.

This technique of generating matrix isolated tellurium atoms was employed in conjunction with reactive matrices in order to form novel tellurium compounds by matrix host-guest bond formation.

Analysis was completed using FTIR spectroscopy with the MIR region shown in all cases. FIR spectra were recorded routinely but contained no new absorption bands and are therefore not presented. Spectra are often truncated for clarity, with the regions not shown containing only impurity bands with no new features observed in that region on photolysis or annealing.

Section 5.1: **Preparation of Hydrogen telluride**

Hydrogen telluride, H_2Te, can be prepared by the decomposition of metal tellurides with water or acidic solutions.[2] In these experiments it was prepared by the action of water on aluminium telluride, Al_2Te_3:

$$Al_2Te_3 + 6H_2O \longrightarrow 3H_2Te + 2Al(OH)_3$$

a small amount of Al_2Te_3 (Strem, 99.9 %), generally of the order of 25 mg, was placed in a 250 cm^3 round bottom flask in the absence of moisture. The flask was then placed on the distillation apparatus outlined below.

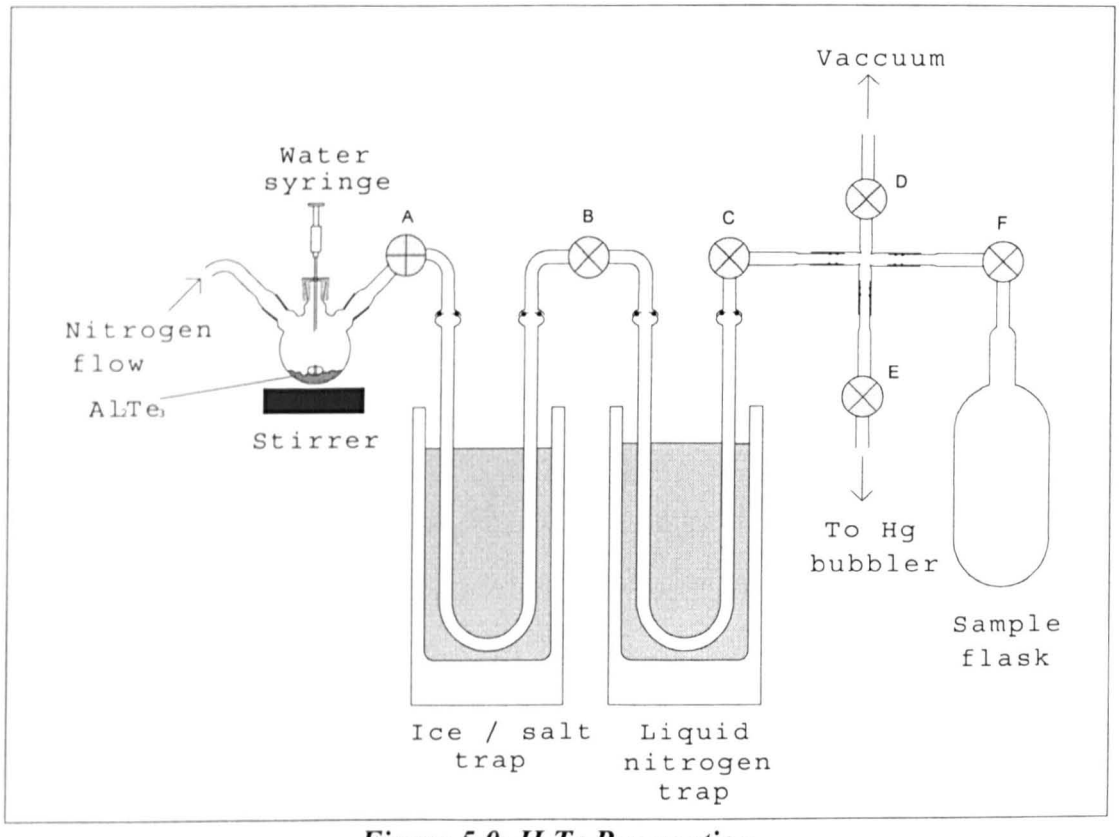

Figure 5.0: H_2Te Preparation

Taps A, B, C and E were opened and nitrogen was flushed through the system and monitored with a mercury bubbler. Two dewars, one containing an ice salt mixture

(258 K) and the other containing liquid nitrogen (77 K) were placed around the 'U-tube' sections of the glassware. Purified water was the added to the Al_2Te_3 with constant stirring under a flowing nitrogen atmosphere. As the H_2Te formed it flowed down the glassware and through the first dewar, which trapped out any moisture, and into the second dewar where it solidified. Once excess water had been added the nitrogen flow was stopped, taps A, B and E were closed. Tap D could now be opened to evacuate the glassware, leaving behind the solidified H_2Te trapped in the 'U-tube' at liquid nitrogen temperature. The product could then be transferred to the evacuated storage vessel by opening tap F, closing tap D and removing the nitrogen trap from the 'U-tube' containing the H_2Te and placing it around the sample flask. The sample flask could then be removed from the vacuum glassware and stored in dry ice (~216 K) in the dark until required further.

The deposition and matrix isolation of hydrogen telluride was then completed as described previously in chapter 3, with the sample cooled using a methylcyclohexane slush bath (172 K) during deposition.

Section 5.2: Isolation and Decomposition of Hydrogen Telluride

Introduction

Hydrogen telluride is reported to be a bent molecule (90°) with a bond length of 1.69 Å in the solid state.[2] A matrix isolation study has previously been employed to confirm the infrared active vibrational modes in the *pseudo* gas phase species.[5]

The following experiments are described to confirm the isolation of molecular H_2Te in an inert matrix and its decomposition on exposure to UV light.

Results and Discussion

Figure 5.1 shows the infrared spectrum observed after the isolation of the vapour above solid hydrogen telluride isolated in nitrogen at 12 K and includes an expansion of the regions containing the infrared active modes of H_2Te. The results are in good agreement with those previously reported for hydrogen telluride isolated in a nitrogen matrix given in table 5.1 along with the gas phase values.

Observed Frequency (N_2 Matrix)	Reported Frequency[5] (N_2 Matrix)	Reported Frequency[6,7] (gas phase)	Assignment
2084.7 cm^{-1}	2085.1 cm^{-1}	2065.27 cm^{-1}	ν_1 (symmetric stretch, A_1)
865.1 cm^{-1}	864.75 cm^{-1}	860.66 cm^{-1}	ν_2 (bend, A_1)
2091.4 cm^{-1}	2091.7 cm^{-1}	2072.11 cm^{-1}	ν_3 (asymmetric stretch, B_1)

Table 5.1: FTIR band assignments for H_2Te in nitrogen at 12 K.

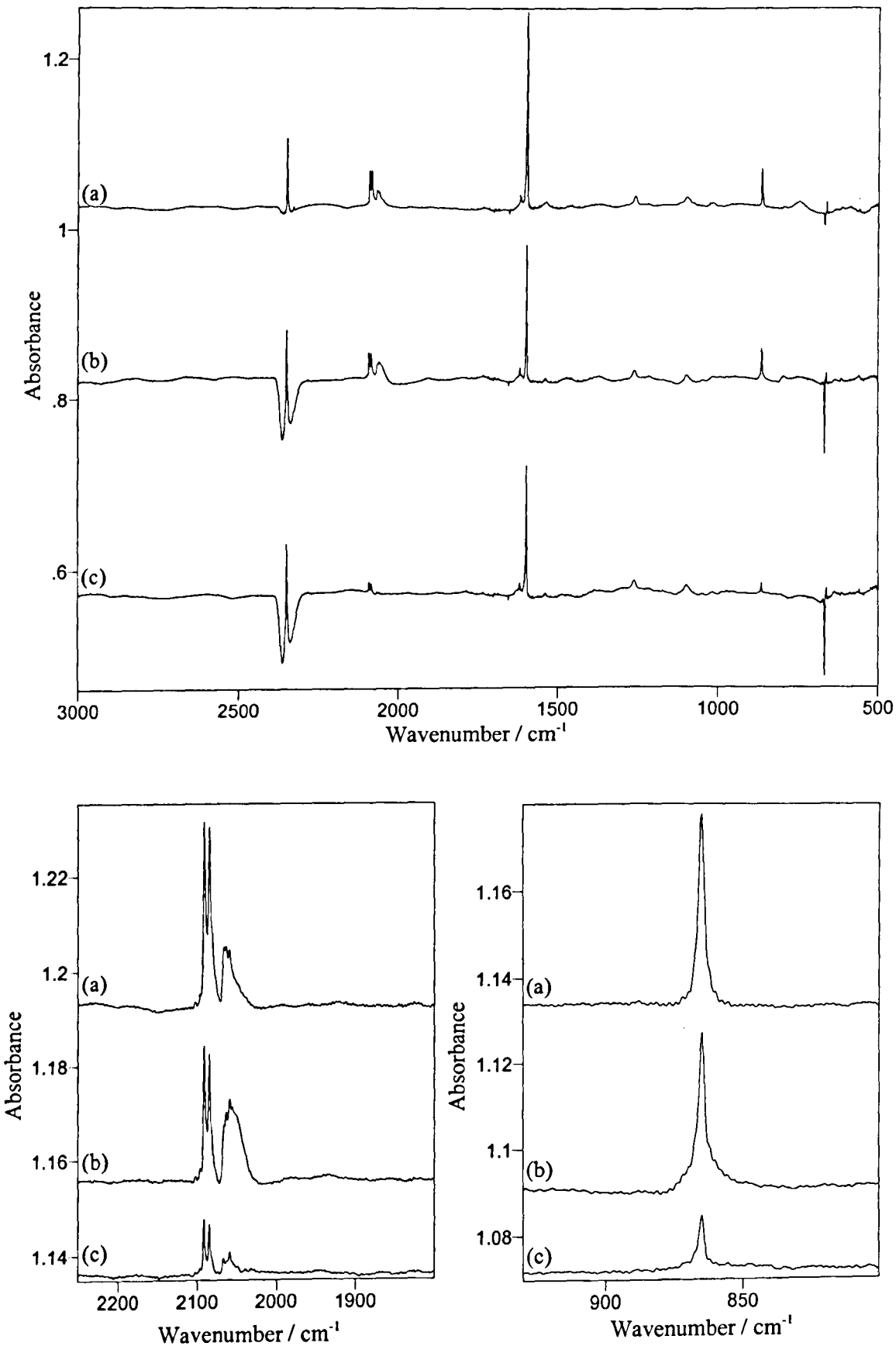

Figure 5.1: H_2Te isolated in nitrogen at 12 K.

a) deposition, b) at 10 K after annealing to 25 K, c) after photolysis with UV light.

The broad feature at around 2064 cm^{-1} was initially thought to be a higher multimer of bulk H_2Te. This assignment was confirmed by annealing experiments which caused a reduction in the intensity of the bands due to isolated H_2Te and an increase in the broad feature suggesting agglomeration of the isolated molecules. On exposure to ultra-violet light a reduction in the intensity of the hydrogen telluride bands is observed showing decomposition of the isolated molecule. No new bands were observed in the spectrum after photolysis, suggesting the decomposed species did not react further, either with themselves or the nitrogen lattice.

The other strong bands present in the spectrum shown in figure 5.1 are due to water (1597.2 cm^{-1}) and carbon dioxide (2351 and 667.7 cm^{-1}) impurities in the sample and the matrix gas. The two weak bands observed at 1260 and 1099 cm^{-1} are presumably due to an interaction between matrix isolated components or nitrogen. These bands undergo no observable change in intensity on annealing or photolysis, suggesting they are unlikely to arise from an interaction between H_2Te and a matrix impurity or the matrix itself. The two bands are common to all spectra and present at proportionally different intensities.

Conclusion

H_2Te has been successfully isolated in a nitrogen matrix with the assignment of the infrared active modes made by comparison with those previously reported. Matrix isolated H_2Te has also been shown to decompose when exposed to UV light suggesting the isolation of Te atoms has been achieved. The assignment of the multimer band has also been confirmed by annealing experiments.

Section 5.3: **Tellurium Oxo Compounds**

Introduction

In order to test the hypothesis that isolated tellurium atoms would form molecular species when isolated in reactive matrices, H_2Te was first isolated and decomposed in oxygen containing matrices in an attempt to form tellurium oxides.

The infrared spectrum of the species produced over solid TeO_2 heated in a Knudsen cell and isolated in argon at 15 K has been previously presented.[8] The major species produced by this method are shown to be TeO, TeO_2 and the dimer molecules of both species.

In the following section the formation of the previously characterised tellurium oxides was investigated by isolating H_2Te in dilute oxygen / argon matrices (2 % O_2) and photo-decomposing the hydrogen telluride to its constituent atoms. These experiments were used to test the applicability of the technique for the generation and isolation of novel tellurium compounds.

Results and Discussion

In the previous section the inert matrix chosen for the isolation of H_2Te was nitrogen. This choice was made as the molecule was characterised by comparison with the previously reported spectrum which was also observed in nitrogen. However, for the experiments involving the addition of a reactive dopant to the matrix gas argon was used as the inert component. This was due to the possible formation of N_xO_y species in nitrogen / oxygen gas mixtures when photolysed, which would distort and complicate the observed spectra.[9]

Figure 5.2 shows the observed infrared spectrum of hydrogen telluride isolated in argon at 12 K along with a expansions of the regions of interest. The bands at 3800 and 1600 cm^{-1} can be immediately assigned to matrix isolated water, with the bands at 2350 and 660 cm^{-1} being due to CO_2. Both of these impurities are likely to originate from the sample and possibly the matrix gas, with additional water impurity supplied from the walls of the vacuum equipment. The observation of these impurities could account for the presence of the weak features at 1239.5 and 1025 cm^{-1} which appear to be present in a similar position in the nitrogen matrix spectrum (figure 5.1) and are probably due to an interaction between the isolated impurities. The bands at 2088 and 867 cm^{-1} are the stretching and bending modes of the isolated H_2Te respectively, which are more complicated than those observed in figure 5.1. In the stretching region of H_2Te the symmetric and asymmetric stretch are identifiable (2088.6 and 2094.8 cm^{-1} respectively) along with the broad multimer band (~ 2060 cm^{-1}). The broad band however appears to have addition features when compared to figure 5.1, namely two well defined, sharp absorption bands at 2061.5 and 2054.5 cm^{-1}. The assignment of these bands is as yet undetermined, although previous work on matrix isolated H_2S provides some useful insights.[10] H_2S has been shown to undergo hindered rotation in argon matrices with the rotational spectra presenting itself as fine structure on the vibration bands. This paper also shows the presence of a sharp, intense band in the multimer region of H_2S which is assigned to the dimer species. It is reasonable to assume therefore that as H_2S rotates so will H_2Te which should provide additional fine structure in the region of the vibrational bands. It is also possible from the previous work on H_2S that these bands are due to isolated dimer and / or trimer species. Figure 5.3 shows an expansion of the H_2Te stretching region during an annealing cycle. The report on the vibrational-rotational spectra of

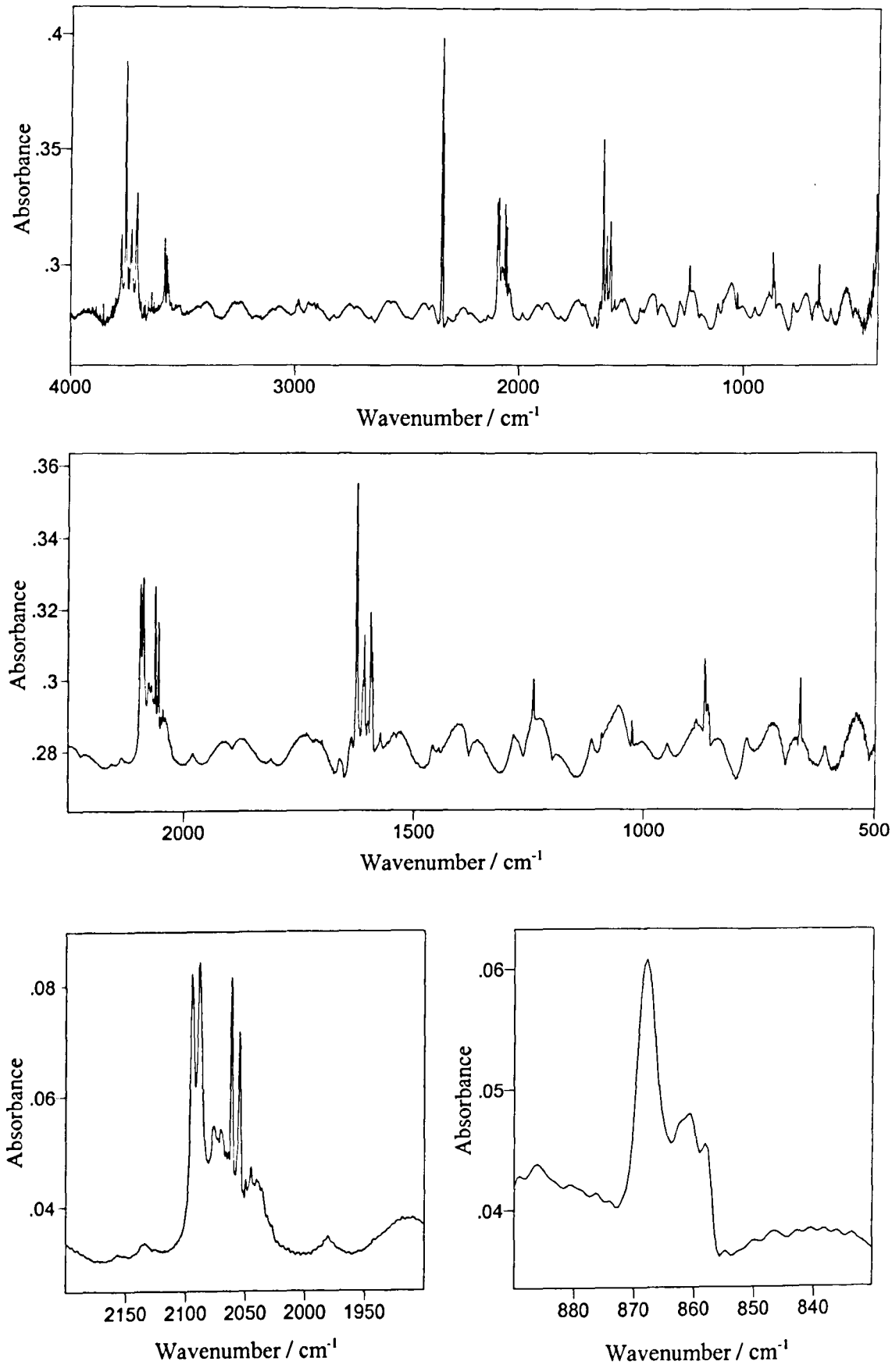

Figure 5.2: H_2Te isolated in argon at 12 K.

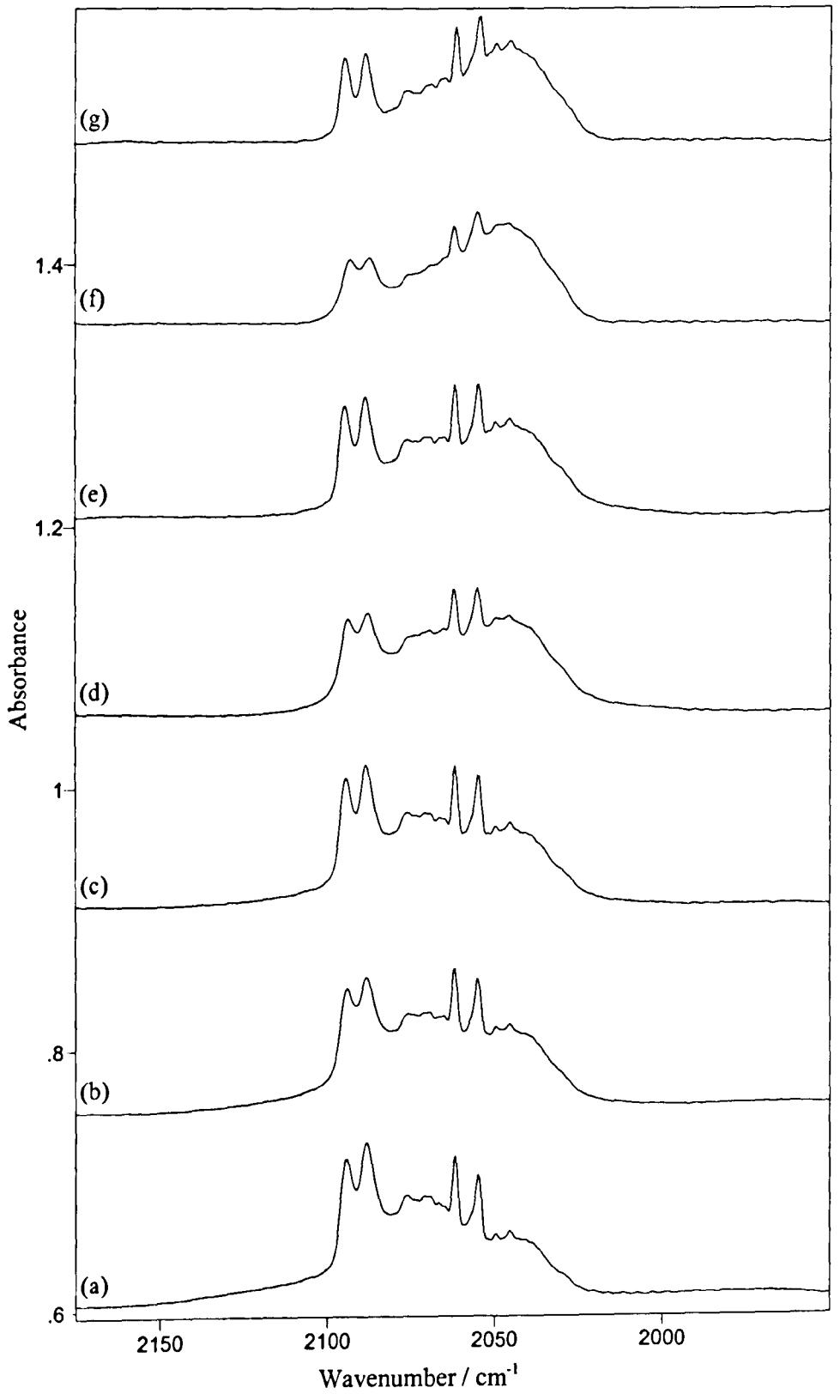

Figure 5.3: H_2Te isolated in argon at 12 K during annealing cycle. (a) 12 K, (b) 20 K, (c) 12 K from 20 K, (d) 25 K, (e) 12 K from 25 K, (f) 30 K, (g) 12 K from 30 K.

matrix isolated H_2S suggested that the rotational structure was removed as the sample was raised to temperatures above 25 K and returned again as the sample was cooled to base temperature (7.5 K in those experiments). This pattern appears to be repeated in the H_2Te annealing experiments shown in figure 5.3 as a reduction in intensity is observed with the sample at 25 and 30 K with the bands returning at base temperature (12 K). It is also evident however that the symmetric and asymmetric stretch of H_2Te undergo a similar reduction in intensity which suggests that these bands arise from the same species. It is expected that the cold temperature of the experiment would only allow the lowest rotational energy levels of the isolated molecule to be populated. It is also likely that any molecular rotation would be restricted by the matrix cage, making matrix rotational data inconsistent with that observed for the true gas phase molecule.[11] The two observed features are therefore likely to be due to the lowest energy transitions similar to those observed for other small molecules in argon matrices, such as H_2O[12] and HCl.[11] In these cases other rotational transitions were at lower energy and are unlikely to be observed in the H_2Te spectra presented here due to the overlap with the multimer band.

In addition to this the bending mode appears to be split into a doublet with peaks at 867 and 861.3 cm^{-1}, although this feature may simply be due to a site effect caused by impurities in the matrix it could also be due rotation fine structure which should also be present on ν_2.

Figure 5.4 shows the infrared spectrum observed when H_2Te was isolated in a 2 % oxygen in argon matrix at 10 K. The initial deposition spectrum observed (figure 5.4(a)) is shown in the region of interest below 1500 cm^{-1}. Along with the H_2Te bending mode at 867 cm^{-1} two other intense bands are also present at 1250 and 810 cm^{-1}. The 1250 cm^{-1} band has already observed in the neat nitrogen and argon matrix

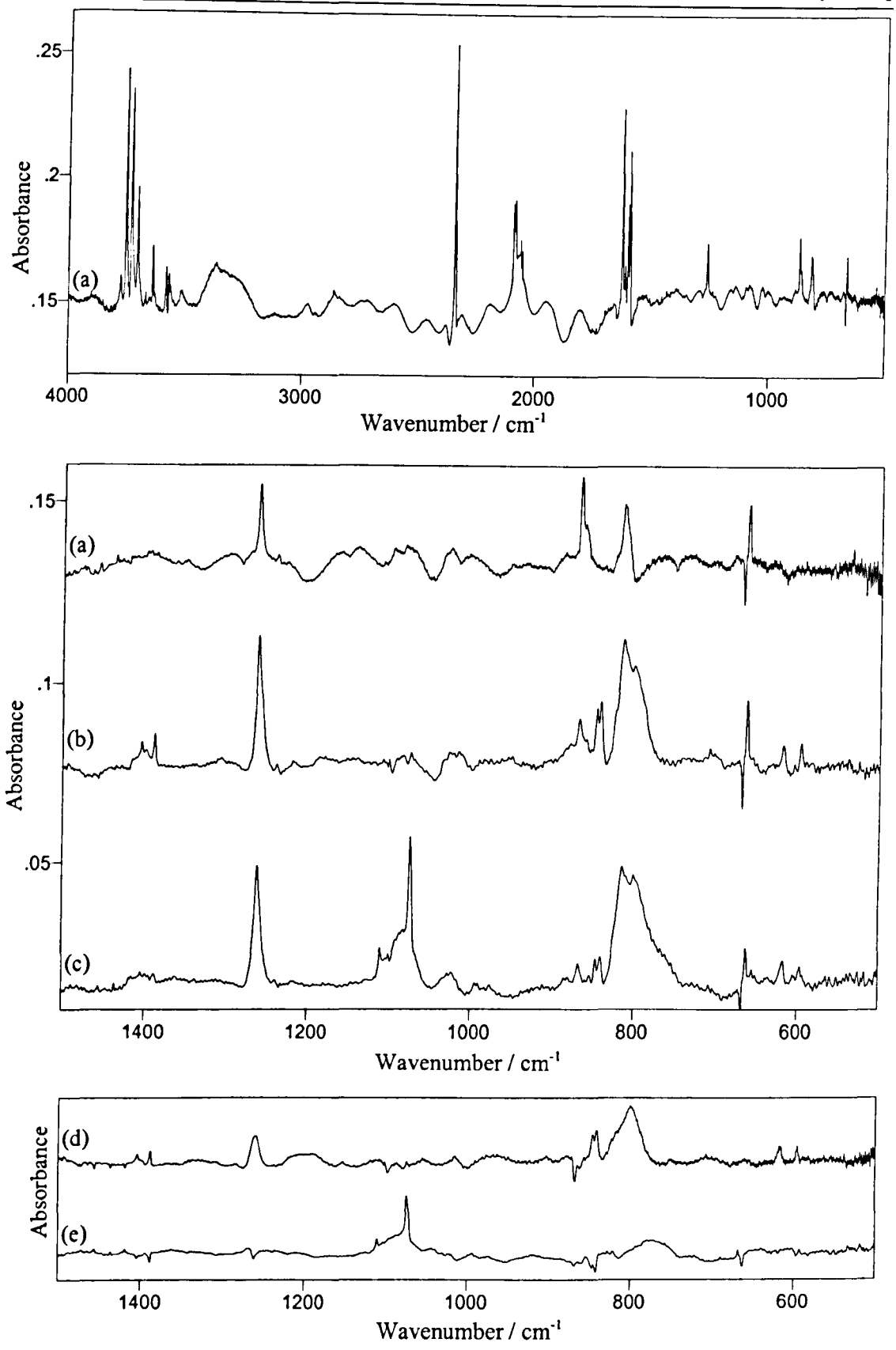

Figure 5.4: H_2Te isolated in 2 % oxygen / argon at 12 K. (a) deposition, (b) after photolysis with UV light, (c) at 12 K after annealing to 25K, (d) and (e) subtraction spectra - deposition from photolysis and photolysis from annealing.

spectra and assigned as being due to the presence of an impurity interaction. This is also likely to be the source of the 810 cm^{-1} band. The presence of this band in the deposition spectrum of oxygen containing matrices and the increase in intensity observed on both annealing and photolysis suggests it is not due to the presence of H_2Te but is more likely to be due to an impurity-oxygen interaction. It is possible however that these bands could be due to the formation of peroxo- and superoxo-species. They are shown in figure 5.5 to be present in proportionally different intensities in different oxygen concentrations and although they are present before photolysis they still may be due to the formation of peroxo- or superoxo- tellurium species. Previous work on matrix isolated NiO_x species has identified the presence of superoxides and peroxides in the region 1200 and 960 cm^{-1} respectively in dilute O_2 / argon matrices.[13] The use of ^{18}O matrices would be required to assist in the characterisation of these bands, but the predicted progression of superoxide to peroxide to oxide is inconsistent with photolysis and annealing evidence provided in these experiments.[14,15]

On photolysis a reduction in the vibrational absorption bands assigned to H_2Te was observed in the infrared spectrum shown in figure 5.4(b). In addition to the reduction in the hydrogen telluride bands new bands are observed in the region below 1500 cm^{-1} which presumably arise from a reaction between the isolated atoms from the dissociated hydrogen telluride and the low concentration of reactive dopant also present in the matrix. The vibrational frequencies of the bands observed are given in table 5.2 below along with possible assignments based on previously reported data.

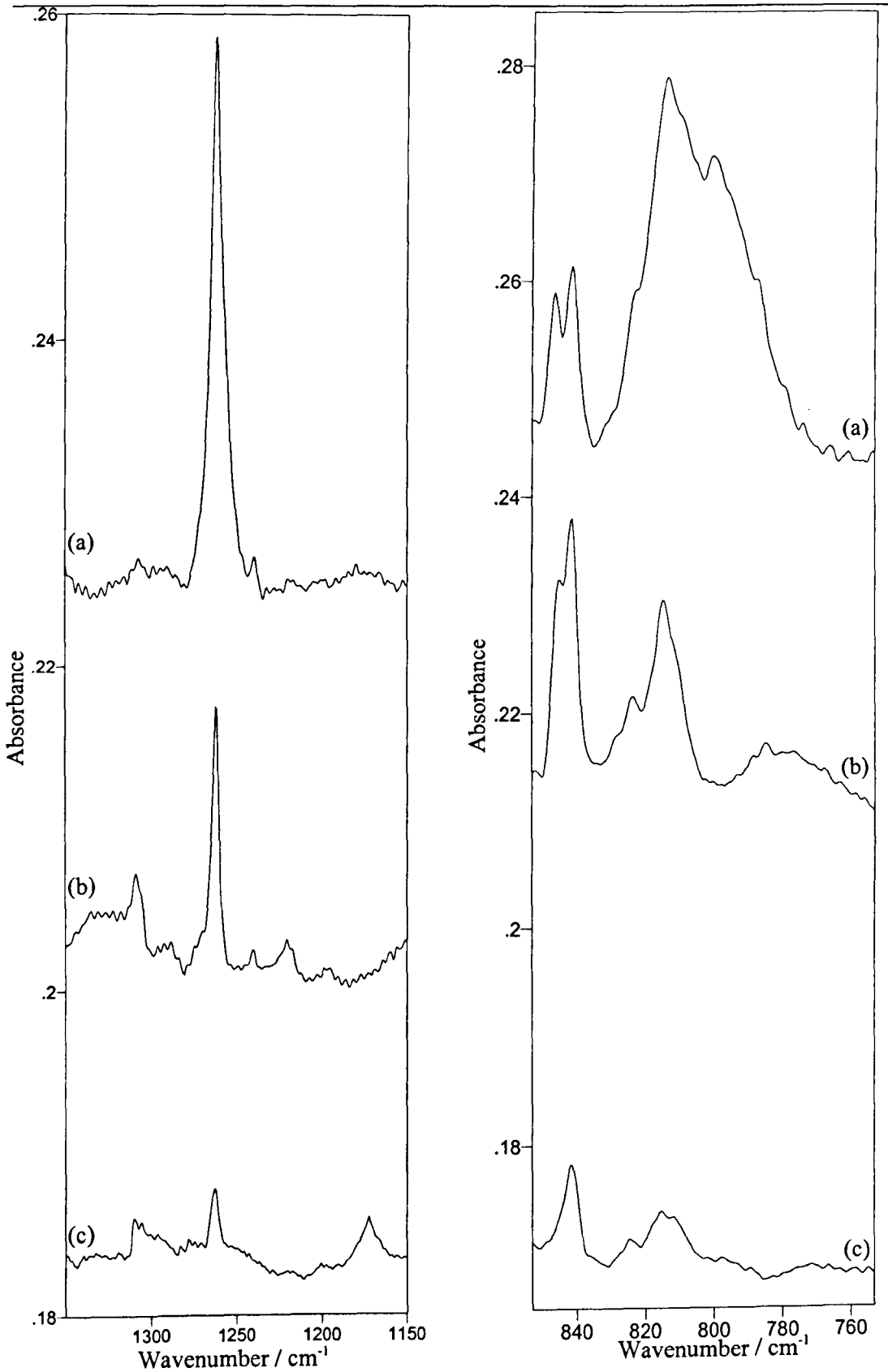

Figure 5.5: variation of intensity of impurity bands in various oxygen / argon matrices at 12 K after photolysis.

(a) 2 % O_2 in argon, (b) 10 % O_2 in argon, (c) neat O_2.

Observed Frequency	Reported Frequency[8]	Assignment
846.2 cm^{-1}	839.4 cm^{-1}	TeO_2 (ν_3)
841.4 cm^{-1}	822.6 cm^{-1}	TeO_2 (ν_1)
800.5 cm^{-1}	787.2 cm^{-1}	TeO (ν)
618.1 / 596.3 cm^{-1}	620 cm^{-1}	$[TeO_2]_{2 \text{ or } 3}$
1388.4 cm^{-1}	1387 cm^{-1}	HO_2[16]

Table 5.2: observed and reported infrared bands for H_2Te in 2 % oxygen / argon at 10 K after photolysis with UV light.

The results show that not only do the dissociated tellurium atoms react with the oxygen in the matrix forming tellurium dioxide but the hydrogen atoms also react to form HO_2.[16] The variation from the literature value is presumably a matrix effect caused by the presence of oxygen in the matrix. The evidence presented also suggests that TeO is formed along with the multimer species $[TeO_2]_x$. The dissociation of O_2 molecules during the photolysis is suggested by the formation of TeO although the mechanism of formation (e.g. photo-dissociation or Te assisted cleavage of the O_2 molecule) is unclear. The presence of the band at 1074 cm^{-1} also remains unassigned, and although it may be due to the formation of a superoxide intermediate. Its growth after annealing to 25 K makes it more likely to be due to the formation of ozone[17,18] which suggests the photo-activation of O_2 molecules by photolysis (literature value 1040 cm^{-1} in argon). This is however a tentative assignment as the band may also be caused by the agglomeration of isolated species which show a reduction in intensity on annealing.

Conclusion

The results presented in this section show that the isolated tellurium atoms from the photo-decomposition of H_2Te will react with dopants in the matrix to form molecular species. Isolation of tellurium atoms in a 2 % oxygen in argon matrix has provided a route to matrix isolated TeO_2 and TeO molecules, with the band positions in reasonable agreement with those previously reported.

The spectra produced are relatively complex due to the presence of impurities in the sample due to problems intrinsic with the sample preparation and storage process and although the use of argon as the inert component of the matrix minimises reaction between the matrix gas and dopant it also provides addition features associated with the isolated hydrogen telluride.

It is possible that experiments using isotopically enriched oxygen could be employed to complete and confirm the characterisation of other isolated species, such as superoxo- and peroxo- compounds. This work was not undertaken as the experimental goals were deemed to have been accomplished by the positive identification of matrix isolated TeO and TeO_2 by the reaction of matrix isolated tellurium atoms and oxygen.

Section 5.4: **Carbonyl Telluride**

Introduction

Carbonyl telluride (OCTe) was first reported in 1944, being formed by passing carbon monoxide over heated tellurium.[19] Although the report contained no experimental or characterisation details it did indicate that it appeared less stable than carbonyl selenide. The only additional literature data available are calculations of the vibrational modes[20] and the proton affinity and structural parameters.[21] No further literature reference to carbonyl telluride has been found, with the structure and composition of OCTe either in the solid or gas phase remaining uncharactersied.

The interest in the identification of carbonyl telluride stems from the catalytic properties of tellurium in organic chemistry. Carbonyl selenide has been identified as an intermediate in the selenium assisted carbonylation of amines.[22] This reaction has also been shown to be catalysed by tellurium,[23] therefore the characterisation and identification of carbonyl telluride should assist in the identification of a potentially important intermediate in tellurium assisted organic transformations.

Results and Discussion.

Hydrogen telluride was first isolated in neat carbon monoxide matrices. Figure 5.6(a) shows the 2000 to 700 cm^{-1} region of the infrared spectrum observed after isolation of H_2Te in neat CO at 10 K. Figure 5.6(b) shows the changes to this region after 15 minutes of photolysis with UV-Vis light. The spectrum is truncated to show only the region below 2000 cm^{-1} since the presence of the various CO

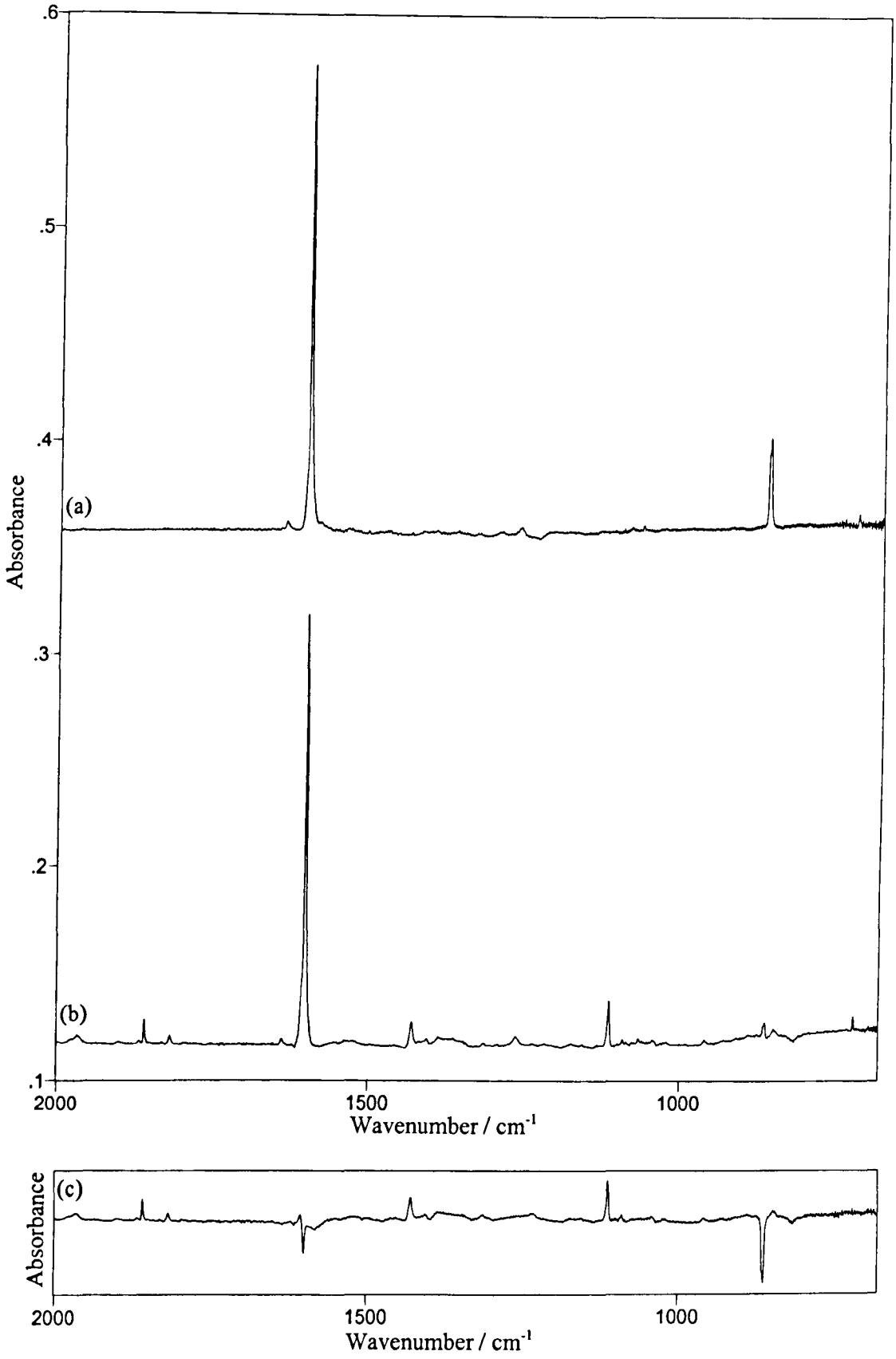

Figure 5.6: H_2Te isolated in carbon monoxide at 10 K.
(a) deposition, (b) after photolysis with UV-Vis light,
(c) subtraction spectrum - photolysis from deposition.

isotopomers obscures the region 2200 to 2000 cm^{-1} which contains the H_2Te stretching modes (ν_1 and ν_3). The deposition and decomposition of the isolated sample was therefore monitored by the presence of the bending mode (ν_2) at 863.0 cm^{-1}. Along with the H_2Te bending mode the deposition spectrum contains one other major feature at 1601.6 cm^{-1} which is simply assigned as matrix isolated water. On photolysis a number of new bands are observed along with the depletion of the H_2Te bending mode, suggesting the formation of new molecular species due to the dissociation of hydrogen telluride.

Since the target molecule is carbonyl telluride, the first area of interest is the $\nu_{C\text{-}O}$ region, that is the region around 2000 cm^{-1}. An expansion of the region 2000 to 1680 cm^{-1} is shown in figure 5.7. The expansion shows new features present at 1965.3, 1859.5, 1818.8 and 1736 cm^{-1} which are presumably due to complexation of the dissociated atoms of hydrogen telluride and the matrix itself. The band at 1859.5 cm^{-1} can be assigned as the C-O stretching frequency of HCO which has been previously reported at 1862 cm^{-1} in a CO matrix.[24] The immediate identification of this molecule and also the assignment of the band at 1736 cm^{-1} to the ν_2 band of H_2CO (previously assigned at 1740.3 cm^{-1} in a nitrogen matrix)[25] provides evidence of the dissociation of H_2Te and the reaction of the dissociated atoms to form matrix isolated molecules. This leaves the vibrational band at 1965.3 cm^{-1} as the major unassigned feature remaining in the ν_{CO} region with the band at 1818.8 cm^{-1} also unassigned at this stage. To assist in the complete characterisation of the bands present after photolysis of H_2Te in a carbon monoxide matrix experiments using isotopically enriched CO were employed. Figure 5.8 shows the ν_{CO} region of H_2Te isolated in neat carbon monoxide after 15 minutes of photolysis using $^{12}C^{16}O$, $^{13}C^{16}O$, and $^{12}C^{18}O$ to determine the sensitivity of the isolated species to carbon and oxygen

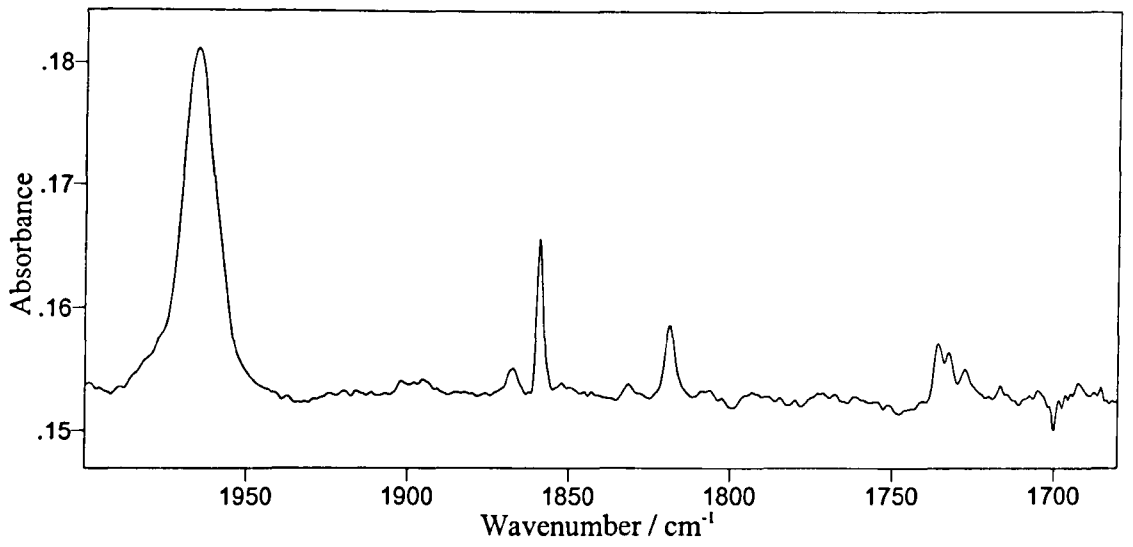

Figure 5.7: products formed after the photo-decomposition of H_2Te in CO at 10 K - expansion.

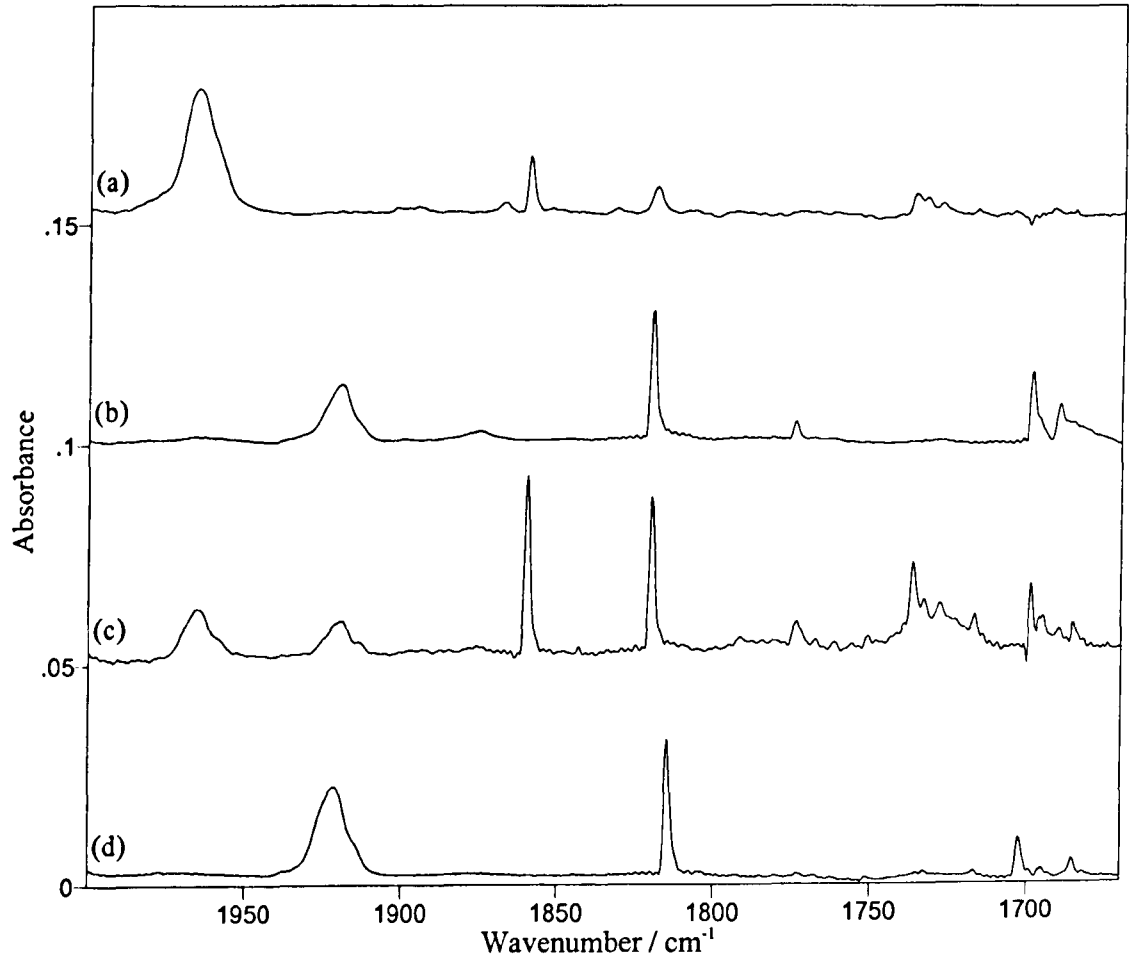

Figure 5.8: products formed after the photo-decomposition of H_2Te in CO at 10 K.

(a) $^{12}C^{16}O$, (a) $^{13}C^{16}O$, (a) $^{12}C^{16}O$ and $^{13}C^{16}O$ (1:1), (a) $^{12}C^{18}O$,

isotopes. These experiments confirmed the presence of HCO and H_2CO and further provided evidence that only one carbonyl group is present. This was confirmed as the bands observed in the $^{12}C^{16}O$ experiment were sensitive to both carbon and oxygen isotopes and each provided only one isotopic counterpart. The 1819 cm^{-1} band (in ^{12}CO) has a very weak $^{12}C^{18}O$ counterpart at which is too weak to be observed in figure 5.8. When a 1 : 1 mixture of $^{12}C^{16}O$ and $^{13}C^{16}O$ was used each band showed a ^{12}C and a ^{13}C isotopomer in roughly equal intensities. This strongly suggests that each band is due to the presence of a species containing only one carbonyl group. The frequencies for the bands observed in the isotopic enrichment experiments are given in table 5.4, with those assigned as being due to HCO and H_2CO in good agreement with the previously reported values.[24,25]

Observed Frequency $^{12}C^{16}O$	Observed Frequency $^{13}C^{16}O$	Observed Frequency $^{12}C^{18}O$	Assignment
1736 cm^{-1}	1698.8 cm^{-1}	1702.8 cm^{-1}	H_2CO
1859.5 cm^{-1}	1819.8 cm^{-1}	1814.7 cm^{-1}	HCO
1818.8 cm^{-1}	1773.9 cm^{-1}	1773 cm^{-1}	-
1965.3 cm^{-1}	1919.2 cm^{-1}	1921.4 cm^{-1}	-

Table 5.4: observed vibrational frequencies of the products formed after photolysis of H_2Te in isotopic CO matrices (ν_{CO} region)

The new bands which appear on photolysis in figure 5.6 occurring below 1600 cm^{-1} which remain unassigned are thought to be due to molecule formation caused by the photolysis of water in CO. Namely the band at 1112.7 cm^{-1} which appears on photolysis is likely to be due to the formation of HCO_2H[27] and the band at 1429.5 cm^{-1} possibly being due to the formation of HO_2.[16] The relative intensity of

these bands has also been seen to vary from experiment to experiment when compared to the bands in the ν_{CO} region.

Figure 5.9 shows and expansion of the ν_{CO} region of the infrared spectrum observed when H_2Te was isolated in a 1 % CO / argon matrix at 12 K after photolysis. The absence of the absorption bands due to HCO and H_2CO is consistent with previous work which has shown that HCO is only formed in dilute CO / argon matrices when vac-UV photolysis rather than UV-Vis photolysis is employed.[26,27] This simplifies this spectral region a great deal, with only the 1970 cm^{-1} band present in sufficiently large intensity as to be observed.

A deuterated sample of hydrogen telluride was then prepared and isolated in a 1 % CO in argon matrix, with the observed spectrum presented in figure 5.10 showing the region below 1550 cm^{-1} to highlight the presence of the D_2Te before and after photolysis. The bands observed in the deposition spectrum show the presence of matrix isolated D_2Te along with a significant proportion of HDTe and H_2Te. The bending mode is the most diagnostic guide to the extent of isotopic enrichment due to the overlap of HDTe and D_2Te modes in the stretching region. This shows that the preparation method has not been thorough in removing all traces of hydrogen from the deuterated sample but is significantly isotopically enriched as to assist in the characterisation. A comparison of the experimentally observed bands for H_2Te, HDTe and D_2Te with literature values is given in table 5.5.

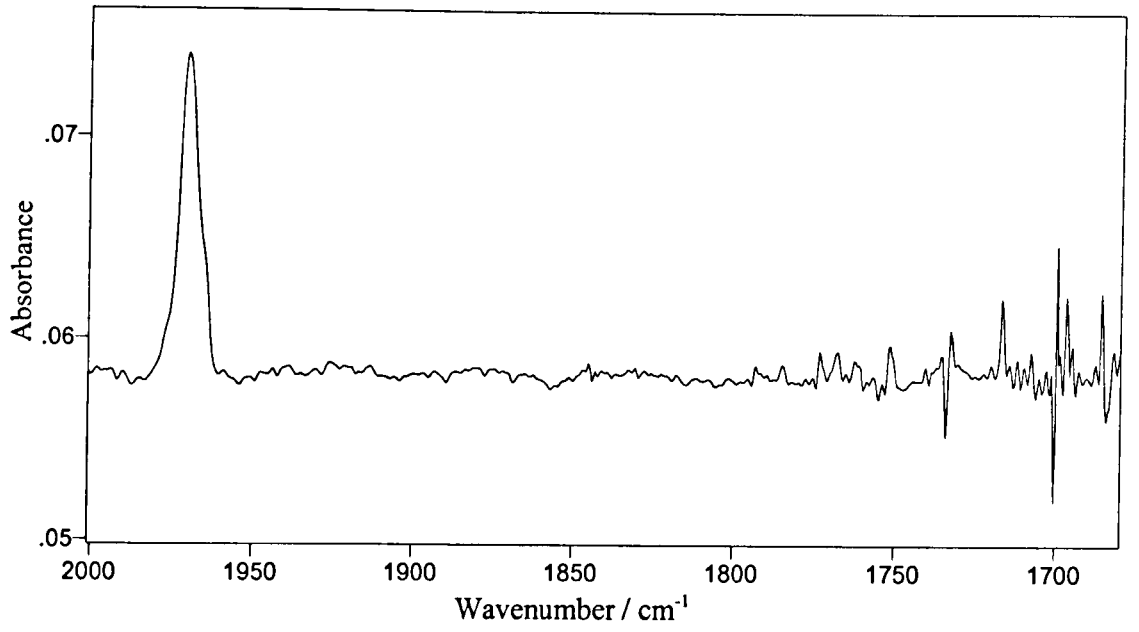

Figure 5.9: H_2Te isolated in 1 % CO / argon after photolysis with UV-Vis light - expansion of ν_{CO} region.

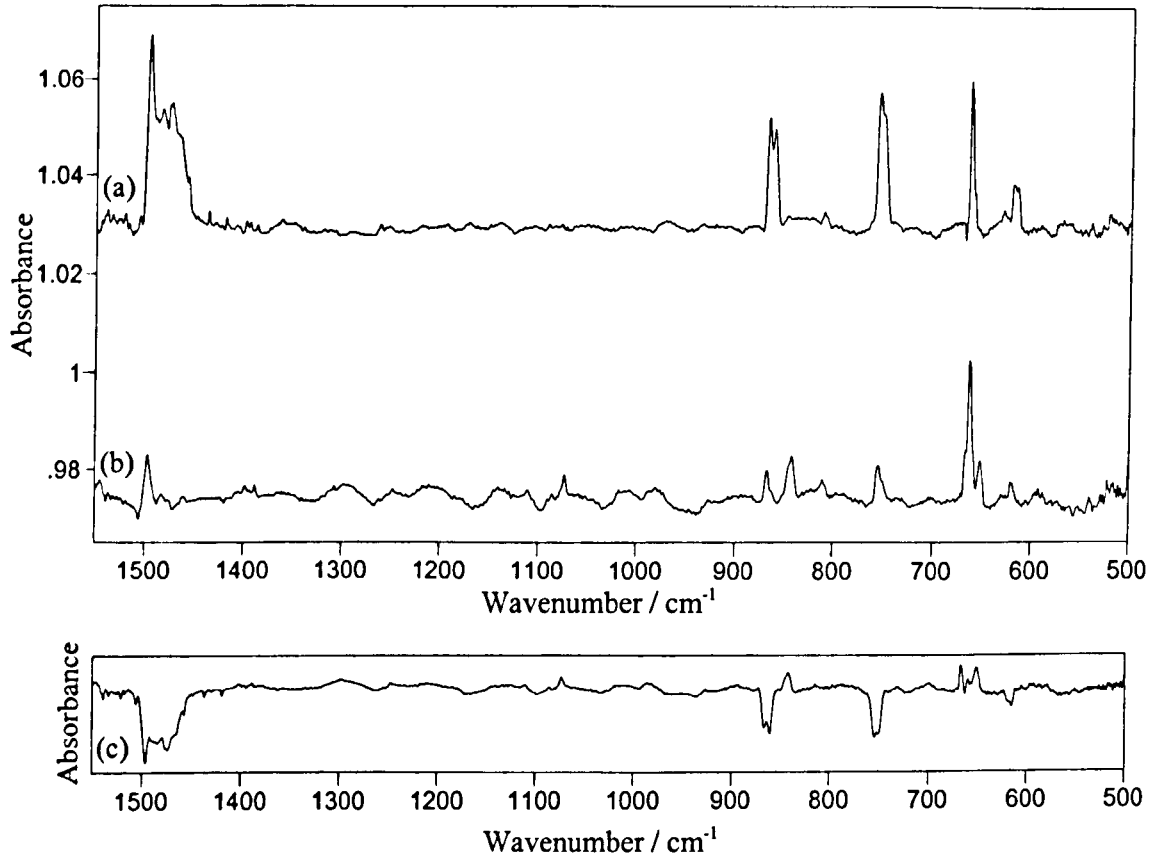

Figure 5.10: D_2Te isolated in 1 % CO / argon at 12 K.
(a) deposition, (b) after 15 minutes UV-Vis photolysis,
(c) subtraction spectrum - photolysis from deposition

Assignment	Observed Frequencies			Reported Frequencies*		
	ν_1 / cm^{-1}	ν_2 / cm^{-1}	ν_3 / cm^{-1}	ν_1 / cm^{-1}	ν_2 / cm^{-1}	ν_3 / cm^{-1}
H_2Te	2087.5	866.8	2090.9	2085.1	864.75	2091.7
HDTe	1496†	754.3	2087.4	1498.2	753.15	2088.35
D_2Te	1496†	620	1496†	1496.1	618.2	1501.6

* *Frequencies previously reported in nitrogen.*[5]

† *The broad band at 1496 was not resolved sufficiently to identify the precise frequencies.*

Table 5.5 Vibrational frequencies for deuterated hydrogen telluride observed in 1 % CO / argon matrices compared with previously reported values.

Figure 5.11 shows a comparison of the ν_{CO} region of the 1 % CO matrix containing H_2Te and the H_2Te / HDTe / D_2Te mixture. Clearly no deuterated counterpart of the 1970.2 cm^{-1} is present in the spectrum showing the species does not contain hydrogen. The shift of this band from 1965 cm^{-1} in neat CO to 1970 cm^{-1} in 1 % CO is easily assigned as a matrix shift.

Therefore the band at 1970 cm^{-1} is formed by the dissociation of hydrogen telluride which has been shown to result in matrix isolated tellurium and hydrogen (and possibly HTe as an intermediate). The band is sensitive to carbon and oxygen isotopes but not to the presence of deuterium. This identifies the molecule to be a carbonyl which does not contain hydrogen and since it is formed from the decomposition of hydrogen telluride must therefore contain tellurium. The presence of only two isotopomers in a 1 : 1 ratio in the ^{12}CO : ^{13}CO matrix experiments identifies only one carbonyl group is present in the molecule. From this information the vibrational band at 1965 cm^{-1} in neat ^{12}CO and 1970 cm^{-1} in 1 % CO / argon can be unambiguously assigned as the C-O stretching frequency of matrix isolated OCTe.

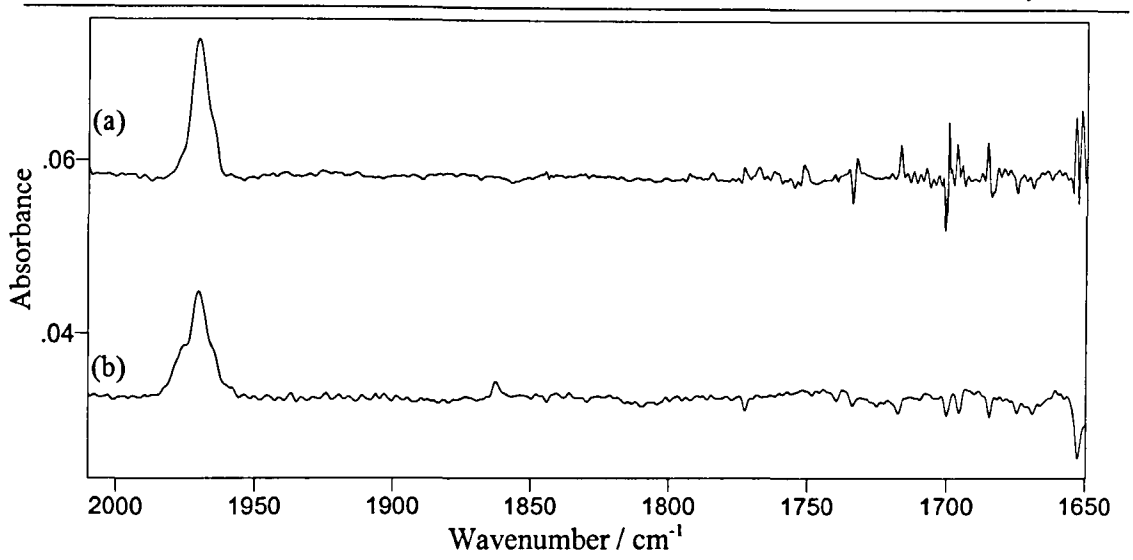

Figure 5.11: expansion of the ν_{CO} region after photolysing the sample for 15 minutes with UV-Vis light. (a) H_2Te and (b) D_2Te isolated in 1 % CO / argon at 12 K.

Assignment	$^{16}O^{12}CM$	$^{16}O^{13}CM$	$^{18}O^{12}CM$
ν_{CO} OCTe (observed)	1965.3 cm^{-1}	1919.2 cm^{-1}	1921.4 cm^{-1}
ν_{CO} OCTe (DFT)	1981 cm^{-1}	1933 cm^{-1}	1939 cm^{-1}
ν_{CO} OCSe (reported)	2023.5 cm^{-1}	1973.8 cm^{-1}	1983.5 cm^{-1}

OCSe and OCTe (DFT) values quoted as gas phase data, OCTe (observed) values are in a neat CO matrix.

Table 5.6: frequencies of the ν_{CO} modes for OCM isotopomers (where M = Te or Se).

This assignment is confirmed by the comparison of the observed bands assigned to OCTe with those previously reported for OCSe[28] and DFT calculations on the predicted vibrational bands of OCTe[29] given in table 5.6 above. DFT calculations also predict that the intensity of the ν_{CTe} and δ_{OCTe} modes would be too low to be observed in the experimental spectra.

This leaves only the 1819 cm^{-1} band unassigned at this stage. The band appears to show similar isotopic ratio as those observed for HCO and H_2CO, with

further deuteration experiments in neat ^{12}CO showing the band to be sensitive to hydrogen isotopes and shifting to 1799 cm^{-1}. From this data it is assumed that the band is most likely to be due to interactions between the isolated HCO or H_2CO species and the impurities in the matrix, for example the formation of the formylperoxy radical $[HC(O)OO]_2$ (previously assigned at 1820 cm^{-1} in a neat O_2 matrix[30]).

Conclusion

The spectroscopic identification of OCTe has been completed for the first time, with the ν_{CO} mode identified at 1965.3 cm^{-1} for $O^{12}CTe$ in a neat CO matrix. The energy shifts observed for the various CO isotopomers are also reported. The photolytic decomposition of H_2Te to tellurium atoms has been identified as an excellent source of tellurium atoms for use in cryochemical synthesis, however impurities in the sample of H_2Te complicate the observed spectra and may lead to the formation of unwanted target molecule-impurity complexes.

Section 5.5: **References**

[1] P. Hassanzadeh, C. Thompson and L. Andrews, *J. Phys. Chem.*, **96**, 8246 (1992) *and references therein.*

[2] D. M. Chizhikov and V. P. Shchastlivyi, *Tellurium and Tellurides,* Collet's Ltd, London (1970) - English translation by E. M. Elkin.

[3] P. H. Barrett, P. A. Montano and J. B. Mann, *Phys. Rev. B,* **14**, 4755 (1976).

[4] R J. Donovan, D. J. Little and J. Konstantatos, *J. Photochem.*, **1**, 86 (1972/3).

[5] N. A. Young, *PhD Thesis,* University of Southampton (1988).

[6] J-M. Flaud, M. Betrencourt, Ph. Arcas, H. Bürger, O. Polanz and W. J. Lafferty, *J. Mol. Spec.*, **182**, 396 (1997).

[7] J-M. Flaud, Ph. Arcas, H. Bürger, O. Polanz and L. Halonen§, *J. Mol. Spec.*, **183**, 310 (1997).

[8] D. W. Mucnow, J. W. Hastie, R. Hauge, R. Bautista and J. L. Margrave, *Trans. Faraday Soc.*, **65**, 3210 (1969).

[9] W. B. DcMoore and N. Davidson, *J. Am. Chem. Soc.*, **81**, 5896 (1959).

[10] E. Isoniemi, M. Petterson, L. Khriachtchev, J. Lundell and M. Räsänen, *J. Phys. Chem.*, **103**, 679 (1999).

[11] H. E. Hallam (editor), *Vibrational Spectroscopy of Trapped Species,* Wiley-Interscience, London (1973).

[12] R. L. Redington and D. E. Milligan, *J. Chem. Phys.*, **39**, 1276 (1963).

[13] A. Citra, G. V. Chertihin, L. Andrews and M. Neurock, *J. Phys. Chem. A,* **101**, 3109 (1997).

[14] M. Moskovits and G. A. Ozin (editors), *Cryochemistry,* Wiley-Interscience, Toronto, (1974).

[15] M. J. Almond and A. J. Downs, *J. Chem. Soc. Dalton Trans.*, **1998**, 809 (1998).

[16] D. W. Smith and L. Andrews, *J. Chem. Phys.*, **60**, 81 (1974).

[17] L. Andrews and R. C. Spiker, Jr., *J. Phys. Chem.*, **76**, 3208 (1972),

[18] M. Spoliti, S. Nunziante Cesaro and B. Mariti, *J. Chem. Phys.*, **59**, 985 (1973).

[19] P. L. Robinson and K. R. Stainthorpe, *Nature,* **153**, 24 (1944).

[20] L. H. Jones, *Inorg. Chem.*, **6**, 429 (1967).

[21] P. G. Jasien and W. J. Stevens, *J. Chem. Phys.*, **83**, 2984 (1985).

[22] N. Sonoda, *Pure Appl. Chem.*, **65**, 699 (1993).

[23] N. Kambe, K. Kondo, H. Ishii and N. Sonoda, *Bull. Chem. Soc. Jpn.*, **54**, 1460 (1981).

[24] D. E. Milligan and M. E. Jacox, *J. Chem. Phys.*, **41**, 3032 (1964).

[25] B. Nelander, *J. Chem. Phys.*, **73**, 1026 (1980).

[26] D. E. Milligan and M. E. Jacox, *J. Chem. Phys.*, **51**, 277 (1969)

[27] D. E. Milligan and M. E. Jacox, *J. Chem. Phys.*, **54**, 927 (1971).

[28] K. Sucoka, Y. Hamada and H. Uehara, *J. Mol. Spectrosc.*, **127**, 370 (1988).

[29] A. J. Bridgeman, N. Harris and N. A. Young, *Chem. Comm.*, **2000**, 1241 (2000).

[30] T.-L. Tso and E. K. C. Lee, *J. Phys. Chem.*, **88**, 5465 (1984).

Chapter

6

Carbonyl Complexes of 3d Transition Metal Bromides

Introduction

Previous work has shown that the geometry of some isolated transition metal dibromides can differ depending on the matrix gas used.[1] Evidence presented in the work also suggested that isolation of MBr_2 species in reactive matrices such as CO may lead to the formation of novel carbonyl complexes of the metal dibromides. The experiments were based on the isolation of the sublimation products of the solid metal bromides in neat CO matrices for characterisation by FTIR, UV-Vis-NIR and XAFS.

In a continuation of this previous work the structure and properties of the carbonyl complexes formed by the isolation of some 3d transition metal dibromide molecules in carbon monoxide matrices was investigated. Further data presented on the FIR spectra (including the region 200 to 100 cm^{-1} not previously reported), results of photolysis experiments and the infrared spectra observed after the isolation of these species in dilute CO in argon matrices are given to reconfirm and in some cases reassign the previously reported data.

The aim in continuing this investigation was to determine the vibrational stretching frequency of the CO stretching modes of the carbonyl dibromide complexes (previously obscured in neat CO matrices by the presence of free CO and isolated CO-impurity complexes) and also to investigate the presence of any further infrared active modes at low energy. In addition to this, the use of photolysis and annealing cycles was to be employed to determine the stability of the complexes formed and the identification of any further photochemical or thermochemical products.

The remainder of the chapter describes a continuation of this research, with a preliminary investigation into chromium bromide carbonyl complexes which were not investigated in the initial research due to the sublimation products of the solid being composed of multiple species.

Table 6.1 shows the most likely geometry of the carbonyl dibromide species formed in this study, with the active IR vibrational modes for each point group also given. This data was used as the basis for the assignments made in the original work[1] with isotopic enrichment used to confirm the characterisation.

Complex	Point Group	Vibration	Symmetry
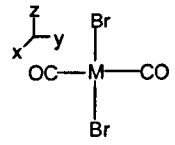	D_{2h}	$\delta_{M\text{-}C\text{-}O}$ out of plane	B_{3u}
		$\delta_{M\text{-}C\text{-}O}$ in plane	B_{1u}
		$\nu_{M\text{-}C}$, ν_{CO}	B_{2u}
		$\nu_{M\text{-}Br}$	B_{1u}
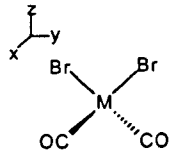	C_{2v}	$\delta_{M\text{-}C\text{-}O}$ out of plane	B_1
		$\delta_{M\text{-}C\text{-}O}$ in plane	A_1
		$\delta_{M\text{-}C\text{-}O}$ in plane	B_2
		$\nu_{M\text{-}C}$ symmetric, ν_{CO}	A_1
		$\nu_{M\text{-}C}$ asymmetric, ν_{CO}	B_1
		$\nu_{M\text{-}Br}$ symmetric	A_1
		$\nu_{M\text{-}Br}$ asymmetric	B_2
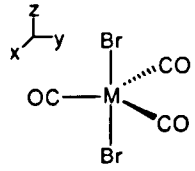	D_{3h}	$\delta_{M\text{-}C\text{-}O}$ out of plane	A_2''
		$\delta_{M\text{-}C\text{-}O}$ in plane	E'
		$\nu_{M\text{-}C}$, ν_{CO}	E'
		$\nu_{M\text{-}Br}$	A_2''
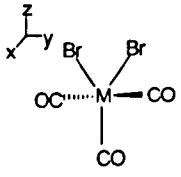	C_{2v}	$\delta_{M\text{-}C\text{-}O}$ (C) in plane	B_2
		$\delta_{M\text{-}C\text{-}O}$ (C) in plane	B_1
		$\delta_{M\text{-}C\text{-}O}$ (C) out of plane	A_1
		$\delta_{M\text{-}C\text{-}O}$ (T) out of plane	B_1
		$\delta_{M\text{-}C\text{-}O}$ (T) in plane	B_2
		$\nu_{M\text{-}C}$ (C) asymmetric, ν_{CO}	B_1
		$\nu_{M\text{-}C}$ (T) asymmetric , ν_{CO}	A_1
		$\nu_{M\text{-}C}$ (C) symmetric, ν_{CO}	A_1
		$\nu_{M\text{-}Br}$ asymmetric	B_2
		$\nu_{M\text{-}Br}$ symmetric	A_1
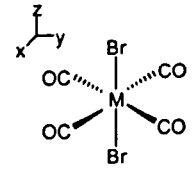	D_{4h}	$\delta_{M\text{-}C\text{-}O}$ out of plane	A_{2u}
		$\delta_{M\text{-}C\text{-}O}$ in plane	E_u
		$\nu_{M\text{-}C}$, ν_{CO}	E_u
		$\nu_{M\text{-}Br}$	A_{2u}
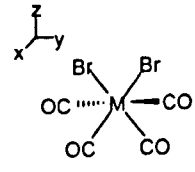	C_{2v}	$\delta_{M\text{-}C\text{-}O}$ (T) out of plane	B_1
		$\delta_{M\text{-}C\text{-}O}$ (C) in plane	A_1
		$\delta_{M\text{-}C\text{-}O}$ (C) out of plane	B_2
		$\delta_{M\text{-}C\text{-}O}$ (T) in plane	A_1
		$\delta_{M\text{-}C\text{-}O}$ (T) in plane	B_2
		$\delta_{M\text{-}C\text{-}O}$ (C) in plane	B_1
		$\nu_{M\text{-}C}$ (C) asymmetric, ν_{CO}	B_1
		$\nu_{M\text{-}C}$ (C) symmetric, ν_{CO}	A_1
		$\nu_{M\text{-}C}$ (T) asymmetric, ν_{CO}	B_2
		$\nu_{M\text{-}C}$ (T) symmetric, ν_{CO}	A_1
		$\nu_{M\text{-}Br}$ asymmetric	B_2
		$\nu_{M\text{-}Br}$ symmetric	A_1

(in plane (yz), out of plane (xy), C / T - cis / trans to Br)

Table 6.1: IR active modes of $M(CO)_xBr_2$ (x = 2 to 4).

Section 6.1: **Iron Carbonyl Dibromide**

The infrared spectrum observed on the isolation of $FeBr_2$ in neat CO matrices has been unambiguously assigned to the formation of *trans*-$[Fe(CO)_4Br_2]$,[1] although the *cis*- isomer has also been spectroscopically characterised.[2] This is analogous to the isolation of $FeCl_2$ which has also been shown to form *trans*-$[Fe(CO)_4Cl_2]$ in CO matrices.[3] The assignments given in previous work are listed in the table below along with the observed experimental results shown in figure 6.1.

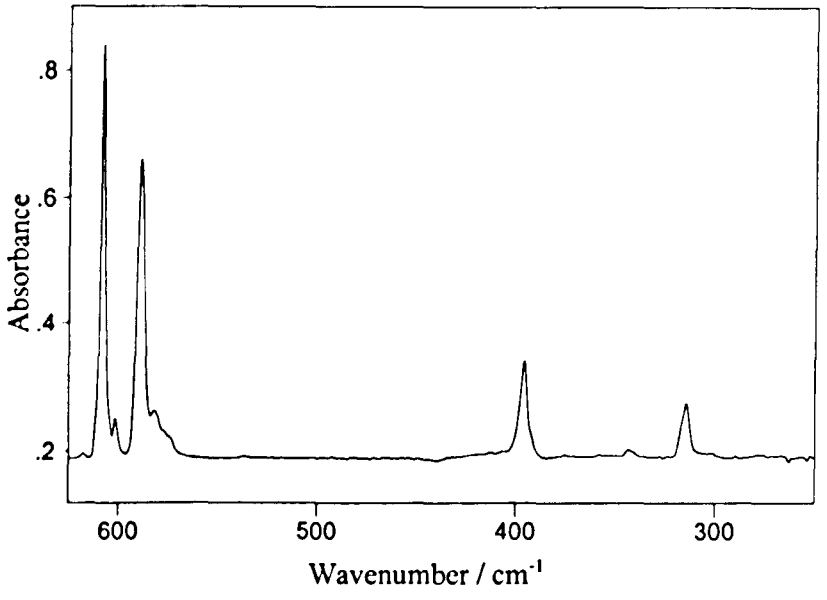

Figure 6.1: $FeBr_2$ isolated in a CO matrix at 12 K.

Reported Frequency (cm^{-1})[1]	Observed Frequency (cm^{-1})	Assignment[1]
608.7	608.4	$\delta_{Fe\text{-}C\text{-}O}$ (A_{2u})
589.0	589.1	$\delta_{Fe\text{-}C\text{-}O}$ (E_u)
394.5	395.6	$\nu_{Fe\text{-}C}$ (E_u)
317.3, 314.1	314.3	$\nu_{Fe\text{-}Br}$ (A_{2u})

Table 6.2: infrared data for $FeBr_2$ isolated in a CO matrix.

The results confirm the formation of *trans*-$[Fe(CO)_4Br_2]$ by the isolation of $FeBr_2$ in neat CO matrices. No changes in intensity were observed after broad band photolysis and / or annealing (to 25 K). Figure 6.2 shows the observed bands in the far and mid infrared regions of $FeBr_2$ isolated in a 1 % CO / argon matrix at 12 K. The frequencies of the observed bands are listed in table 6.3 below.

Observed Frequency	Previous Assignment[1]*
341.8 cm^{-1}	
367.8 cm^{-1}	
374.6 cm^{-1}	
382.3 cm^{-1}	
385.5 cm^{-1}	ν_{Fe-Br} (site)
399.7 cm^{-1}	ν_{Fe-Br}
583.8 cm^{-1}	
594.2 cm^{-1}	
610.5 cm^{-1}	
617.6 cm^{-1}	
2090.9 cm^{-1}	
2101.6 cm^{-1}	

**previous assignment in argon*

Table 6.3: infrared data for $FeBr_2$ isolated in a 1 % CO in argon matrix at 12 K.

In the FIR region a subtraction of the experimental spectra observed after annealing from that of the initial deposition shows a reduction in all the major bands present. The bands observed at 399.2 and 385.9 cm^{-1} which are shown by the subtraction spectrum to undergo the greatest reduction in relative intensity are easily assigned to the ν_{Fe-Br} stretching mode of $FeBr_2$ isolated in argon and in a second matrix site, previously reported at 399.7 and 385.5 cm^{-1} respectively.[1] The other bands could also be due to other argon / carbon monoxide site effects.

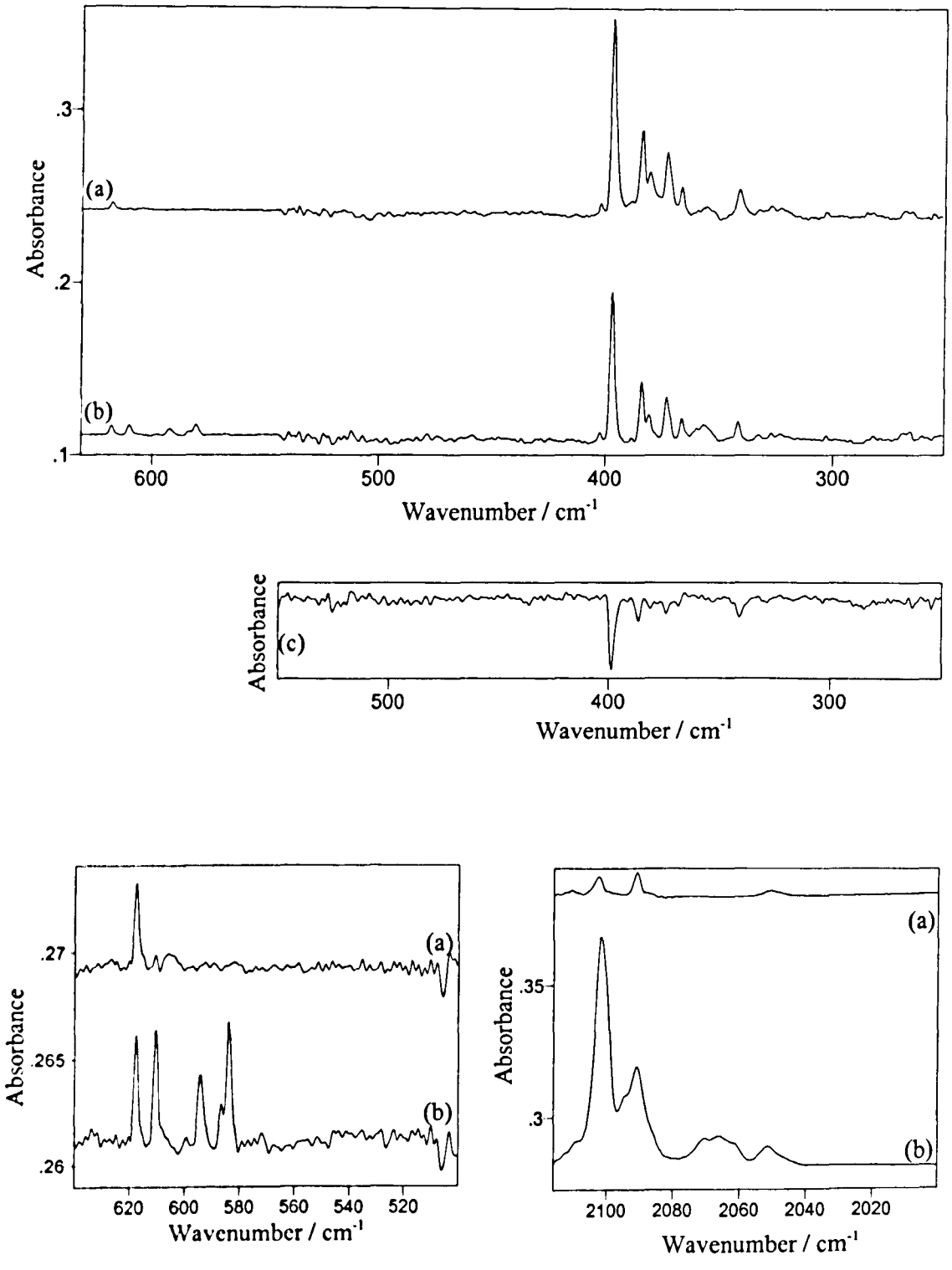

Figure 6.2: $FeBr_2$ isolated in a 1 % CO in argon matrix at 12 K. FIR with expansion of 640 to 550 cm^{-1} region and truncated MIR spectrum. (a) deposition, (b) annealing, (c) spectral subtraction of deposition from annealing to show the changes on warming the spectrum.

The appearance of new bands in the region around 600 cm^{-1} after annealing suggests that new species are being formed in conjunction with a reduction in isolated $FeBr_2$ molecules. This infers that as the matrix is annealed CO molecules migrate through the matrix and interact with the isolated $FeBr_2$ molecules resulting in the formation of carbonyl complexes. This would account for the reduction in intensity of the low energy modes observed and the growth of new bands in the higher energy region of the FIR spectrum. These bands are also accompanied by the increase of a band in the $\nu_{C\text{-}O}$ stretching region at 2101.6 cm^{-1}. The second band present at 2090.9 cm^{-1} is observed in all 1 % CO / argon matrix spectra and is assigned to ^{13}CO. It would also be expected that these new bands should be accompanied by new bands present in the FIR region corresponding to the $\nu_{Fe\text{-}Br}$, $\nu_{Fe\text{-}C}$ and possibly other deformation modes of the complex formed, as observed in the neat CO matrix. Although these bands are not obviously evident, it is likely they are present but merely too weak to be observed. In the neat CO spectrum the bands at 600 cm^{-1} are of much greater relative intensity than those at lower energy assigned to the $\nu_{Fe\text{-}Br}$ and $\nu_{Fe\text{-}C}$ modes. The low intensity of the bands observed around 600 cm^{-1} in the 1 % CO matrix spectrum suggests that by simple comparison of relative intensities the lower energy modes associated with these bands would be too weak to be observed.

The new bands that appear on annealing in the region of 600 cm^{-1} can therefore be assigned to the formation of a carbonyl complex. The nature of the dilute CO matrix could facilitate the formation of a lower co-ordinated carbonyl complex rather than the tetracarbonyl complex formed in neat CO matrices. This could explain the presence of extra bands in this region.

Figure 6.3 shows the change observed in these bands to assist in their assignment, with the spectral subtraction also being shown. The band at 617.6 cm^{-1}

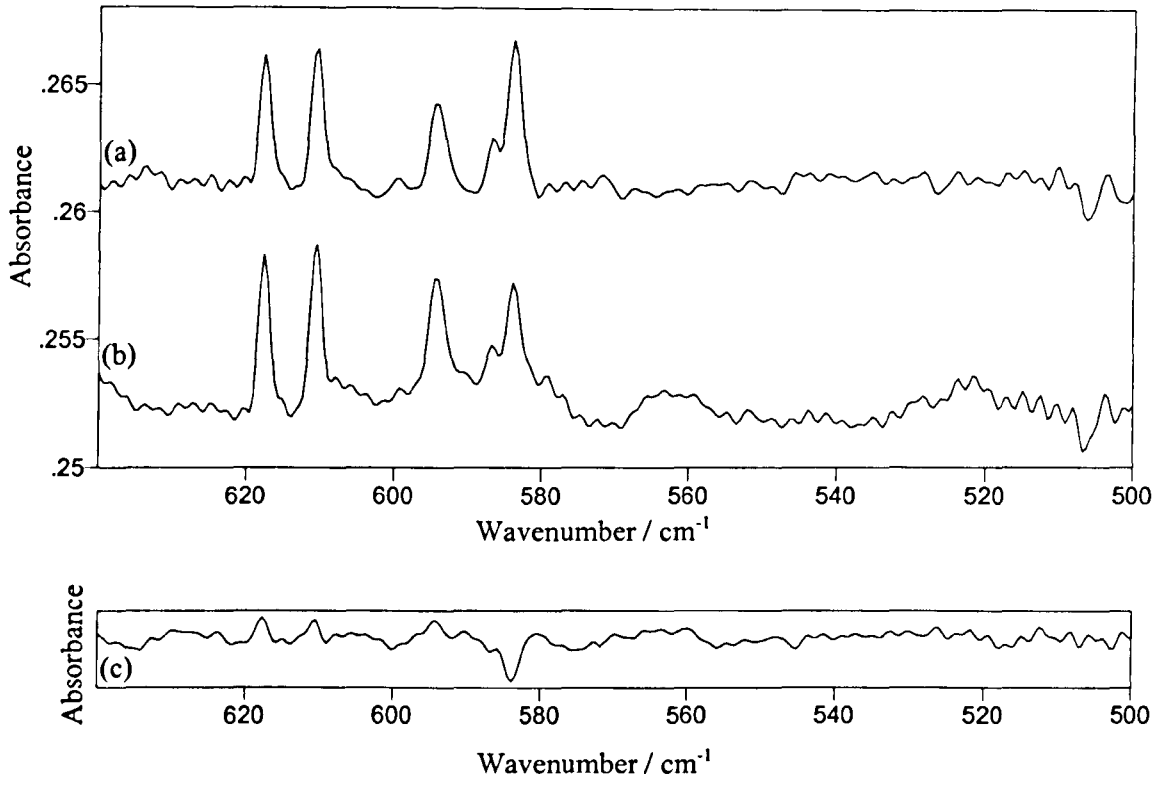

Figure 6.3: IR spectra showing the effects of photolysis with visible light on $FeBr_2$ isolated in 1% CO / argon at 12 K.

(a) at 12 K after annealing to 25 K, (b) after exposure to visible light for 10 minutes, (c) spectral subtraction of visible photolysis from annealing.

has been observed in other 1% CO in argon matrix spectra and can therefore be assigned to the presence of some low level impurity. Visible photolysis can be seen to reduce the intensity of the band at 583.8 cm^{-1} (and possibly the accompanying shoulder at 586.7 cm^{-1}) while the other bands at 610.5 and 594.2 cm^{-1} can be seen to undergo very little change. This confirms that the 583 cm^{-1} band is due to the presence of a different species to the features at 610 and 594 cm^{-1}. By comparison with the neat CO spectra it is therefore reasonable to assign these two bands as the two $\delta_{Fe\text{-}C\text{-}O}$ modes of *trans*-$[Fe(CO)_4Br_2]$ with the other band at 583 cm^{-1} likely to arise from the presence of a lower co-ordinated carbonyl complex.

Figure 6.4 shows the presence of bands at around 2160 cm^{-1}. The band present at 2148.8 cm^{-1} is present in all 1 % CO / argon spectra and is assigned as due to the presence of a CO-impurity complex, most likely a $OC\text{-}H_2O$ species. The remaining bands may be the result of an impurity interaction, such as OC-HBr which has been previously observed at 2152.4 cm^{-1}.[4] This probably corresponds to the broad band observed in these spectra at 2153.9 cm^{-1}. The remaining bands are thought to be due to the interaction of the isolated $FeBr_2$ with the CO molecules present in the matrix. The band at 2165.4 cm^{-1} which is reduced on annealing is consistent with the formation of a non-classical carbonyl complex. A classical metal carbonyl (M-CO) bond has a significant σ and π component (as CO is a σ donor and a π acceptor) with the π component (π backbonding) being the transfer of electron density from metal d_π orbitals to CO π^* orbitals. When CO ligands are only weakly bound the amount of π backbonding is less, this shortens the C-O bond which results in an increase in ν_{CO}.[5] The previously reported examples of non-classical metal carbonyls offer a tentative assignment to the bands occurring at high frequency to molecular CO. This would explain the reduction in intensity observed on annealing

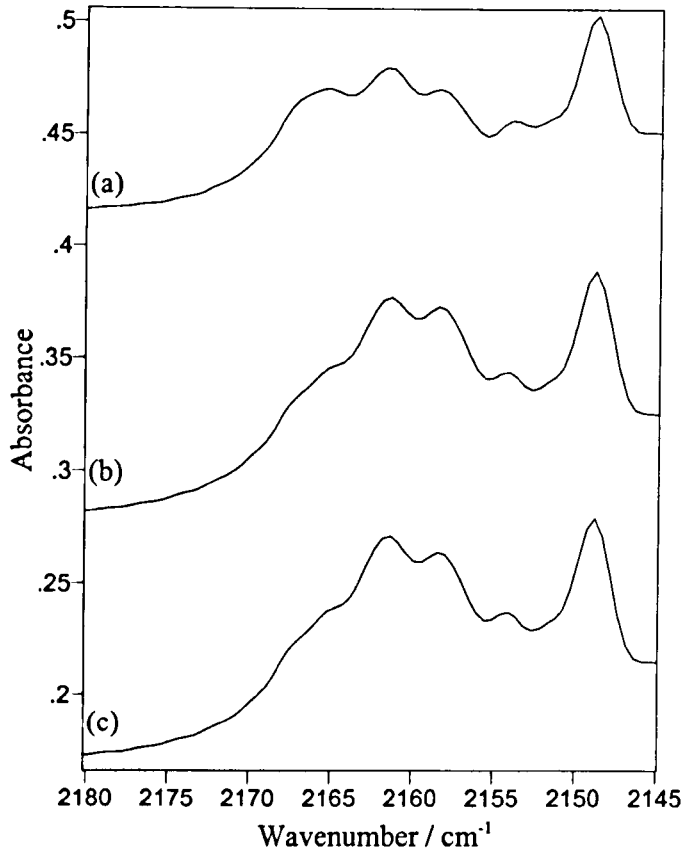

Figure 6.4: MIR spectra showing effects of annealing and photolysis on the non-classical carbonyl region of $FeBr_2$ isolated in 1% CO / argon at 12 K.
(a) deposition (b) at 12 K after annealing to 25 K,
(c) after exposure to broad band photolysis.

as warming the matrix facilitates the association of isolated molecules. The remaining two bands at 2161.6 and 2158.4 cm^{-1} show the opposite behaviour as they increase in intensity on annealing. This makes it unlikely that these bands are due to the formation of a non-classical carbonyl complex. The bands are clearly metal dependent as they are not observed in other 1 % CO / argon matrix spectra, but without further experiments theses bands remain unassigned. The possibility that these bands indicate the presence of the *cis*- complex which has a ν_{CO} mode at 2149.5 cm^{-1}[2] is discredited by the absence of the more intense bands expected at lower frequency, in particular the band at 2073.6 cm^{-1}.

Conclusion

The major species formed in neat CO matrices, namely *trans*-$[Fe(CO)_4Br_2]$, is considered to again be the most likely product in 1 % CO / argon matrices. From the observed spectra of $FeBr_2$ isolated in 1 % CO argon it has been shown that complexation of the isolated sample occurs when the matrix is warmed. The presence of a greater number of bands than expected points to the formation of a second species, with the associated bands being determined through photolysis and annealing experiments. The ν_{CO} stretching mode for $[Fe(CO)_4Br_2]$ has also been identified at 2101.6 cm^{-1}.

The presence of other bands in the ν_{CO} region at high frequency to free CO offers evidence for the formation of carbonyl complexes with matrix impurities and the possible formation of a non-classical iron carbonyl complex.

Section 6.2: **Cobalt Dibromide**

In the previous study on the products formed on the isolation of $CoCl_2$ in CO matrices by Beattie *et al.*[3] the major species was proposed to be *trans*-$[Co(CO)_4Cl_2]$. The results of the previous study on $CoBr_2$ are presented in table 6.4 along with the assignments given. The observed experimental values corresponding to those previously reported are also given in the table. It was found that the major product formed on isolation of cobalt dibromide vapour in CO matrices was the *trans*-$[Co(CO)_2Br_2]$ complex (with the presence of the tetrahedral complex implied as a secondary product present in lower concentration). Therefore there remains some doubt as to the true nature of the species formed when cobalt halides are isolated in CO matrices. The aim of this work was to try to resolve these inconsistencies and confirm the structure and geometry of the carbonyl bromide formed.

Observed Frequency (cm^{-1})	**Reported Frequency (cm^{-1})[1]**	**Assignment[1]**
516.4	517.2	*trans*-$[Co(CO)_2Br_2]$ $\delta_{Co\text{-}C\text{-}O}$ (B_{1u})
498.0	499.0	*tet*-$[Co(CO)_2Br_2]$ $\delta_{Co\text{-}C\text{-}O}$
451.0	451.1	*trans*-$[Co(CO)_2Br_2]$ $\delta_{Co\text{-}C\text{-}O}$ (B_{2u})
404.9	404.9	*trans*-$[Co(CO)_2Br_2]$ $\nu_{Co\text{-}C}$ (B_{3u})
332.4	331.1	*tet*-$[Co(CO)_2Br_2]$ $\nu_{Co\text{-}Br}$
306.1	304.3	*trans*-$[Co(CO)_2Br_2]$ $\nu_{Co\text{-}Br}$ (B_{1u})
294.0	294.4	*tet*-$[Co(CO)_2Br_2]$ $\delta_{Co\text{-}C\text{-}O}$
210.7	210.0	*tet*-$[Co(CO)_2Br_2]$ $\nu_{Co\text{-}C}$

Table 6.4: IR assignments for cobalt carbonyl dibromide.

The IR spectrum observed on the isolation of $CoBr_2$ in neat CO is given in figure 6.5. The spectra were recorded in the far infrared only (600 to 50 cm^{-1}) to identify the presence of any weaker bending modes at low energy that could not be observed under previous experimental conditions. For this reason a longer deposition time (around 3 hours) was employed, such that the vibrational bands previously observed around 520 cm^{-1} were almost fully absorbing. The bands are still shown in the figure and the intensity changes observed are believed to be an accurate representation of the intensity change, but probably not quantitatively.

On photolysis of the isolated product a relative intensity change was observed in the IR bands. This intensity change, best shown by the subtraction spectrum in figure 6.5(e), not only confirms the presence of two species present in the matrix as previously assigned but also suggests conversion between the two on exposure to visible and ultraviolet light. As the sample is exposed to ultra-violet light a reduction in intensity is evident in the three bands at 332.4, 294.0 and 210.7 cm^{-1} assigned to the presence of *tet*-$[Co(CO)_2Br_2]$ and accompanied by an increase in the intensity of the remainder of the bands. The fourth band assigned to the tetrahedral complex (at 499 cm^{-1}) in the initial work shows inconsistent photolytic behaviour, associating this band with the second species rather than the tetrahedral complex. This is most clearly evident in the subtraction spectrum (figure 6.5(e)). On exposure to visible light the intensity change is reversed as those bands due to *tet*-$[Co(CO)_2Br_2]$ increase in intensity and the remainder of the bands are reduced. The isotopic data presented in the initial report made exact assignment of the bands difficult, as when mixed isotope experiments were used (^{12}CO and ^{13}CO 1:1) the bands were difficult to identify unambiguously due to their low intensity and the overlap of some of the more intense bands.

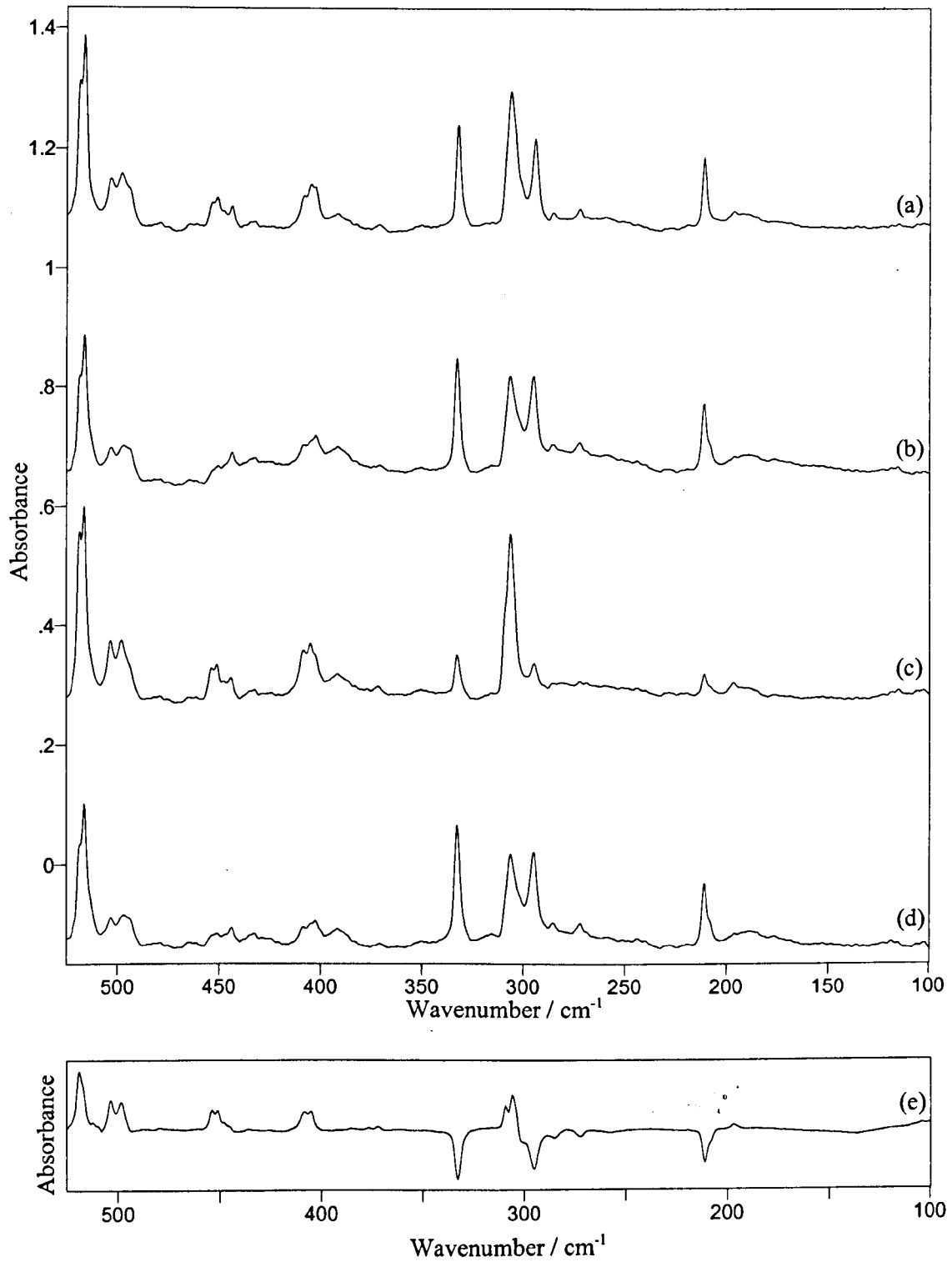

Figure 6.5: IR spectra observed after the isolation of $CoBr_2$ in CO at 18 K. (a) deposition, (b) after photolysis with visible light, (c) after photolysis with UV light, (d) after photolysis with visible light, (e) subtraction spectrum - visible photolysis from UV photolysis (c-b).

The assignment of the major species as the tetrahedral complex appears accurate, with theoretical evidence[6] supporting the identification of the tetrahedral complex with no infrared active absorption bands above 400 cm^{-1}. The weak band evident at 271.9 cm^{-1} which appears to undergo similar photolytic behaviour could be a fourth expected infrared active mode of the tetrahedral complex. The presence of two distinct species in of $[Co(CO)_xBr_2]$ is clearly evident from the spectra shown in figure 6.5, with exposure to visible and ultra violet light causing a conversion between the two species. The second species assigned previously to fit with the observed isotopic data was the *trans-* square planar complex. The use of photolysis in these experiments has identified that one of the bands previously assigned to the tetrahedral complex (at 499 cm^{-1}) is in fact due to the presence of the second species. This makes it highly unlikely that the second species present is the *trans-* square planar complex as there are now five infrared bands associated with the species, where only four active infrared bands are expected (see table 6.1). It is therefore assumed that the square planar complex formed is more likely to be *cis-*$[Co(CO)_2Br_2]$ than *trans-* due to the number of observed vibrational bands. This is consistent with previous work in which it has been shown that this conversion between the tetrahedral and square planar complex can be promoted by photolysis.[7]

As is expected the UV-Vis-NIR spectrum observed when two species are present is more complicated, although again the photolysis experiments can be used to identify the observed transitions associated with the two species present due to the conversion observed in the IR experiments. Figure 6.6 shows the UV-Vis spectrum observed on the isolation of $CoBr_2$ in CO. The three major features appear in the charge transfer region and are very strong, which makes their photolytic behaviour difficult to determine with respect to accurately assigning them to a particular species

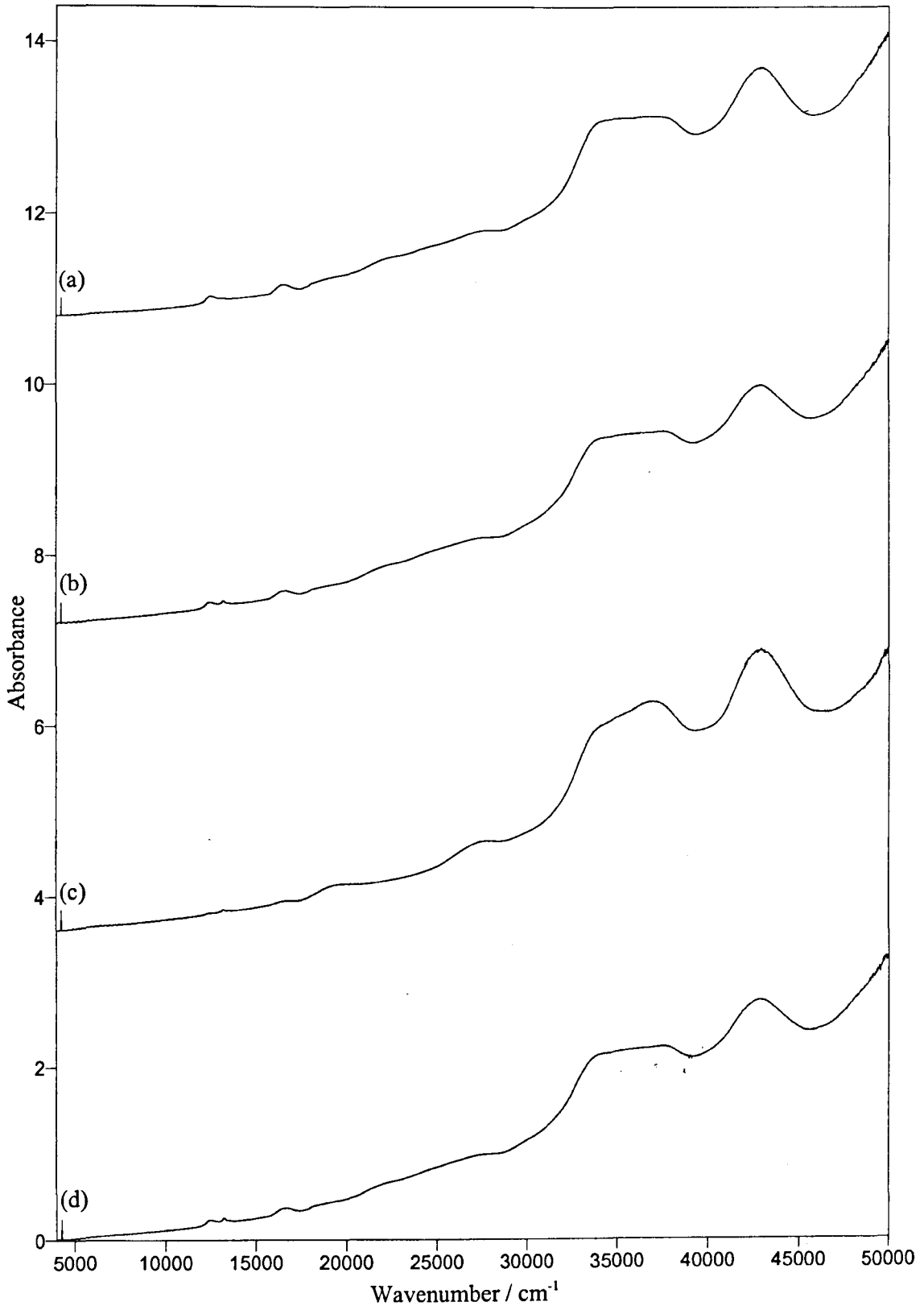

Figure 6.6: UV-Vis-NIR spectra observed after the isolation of $CoBr_2$ in CO at 18 K.

(a) deposition, (b) after photolysis with visible light,

(c) after photolysis with UV light, (d) after photolysis with visible light.

although some intensity change is observed. The bands at 43000 and 37000 cm^{-1} show an increase after exposure to visible light associating them with the tetrahedral complex. The opposite is true for the 34100 cm^{-1} band which shows a reduction in intensity after exposure to visible light, associating this band with the presence of the square planar molecule. An expansion of the region below 30000 cm^{-1} is given in figure 6.7 along with the spectra observed after photolysis to highlight the changes in those bands which were previously identified as d-d transitions of both tetrahedral and *trans*-$[Co(CO)_2Br_2]$ in order to assign the bands to the square planar or tetrahedral isomers. From previous work on Co^{II} complexes the pseudo-tetrahedral complex would be expected to have three d-d transition from the $^4A_2$ ground state (to $^4T_2$, $^4T_1(F)$ and $^4T_1(P)$ excited states) occurring in the region 6000 to 16000 cm^{-1}. These transitions can therefore be assigned to those bands at 12470, 13200 and the weak band at 22100 cm^{-1} which all show a reduction in intensity after exposure to UV light. The assignments are based on the observation of the IR bands assigned to the same species undergoing similar photolytic behaviour. The growth of broad bands at 19600 and 27700 cm^{-1} on exposure to UV light leads to their assignment as being due to the d-d transition of the square planar complex. This behaviour appears conclusive, but some doubt remains over the band at 13200 cm^{-1}. This band shows the same photolysis behaviour as the other assigned to the square planar complex, but also shows clear growth on exposure to visible light in figure 6.7(b), while the others show no observable change. This suggests the possibility that this band may be due to the presence of another species rather than *cis*-$[Co(CO)_2Br_2]$.

The infrared spectrum given in figure 6.8 is that observed after the isolation of $CoBr_2$ vapour in a 1 % CO in argon matrix at 12 K. The FIR spectrum shows the presence of the isolated dibromide at 397.7 cm^{-1} (previously reported at 398.6 cm^{-1} in

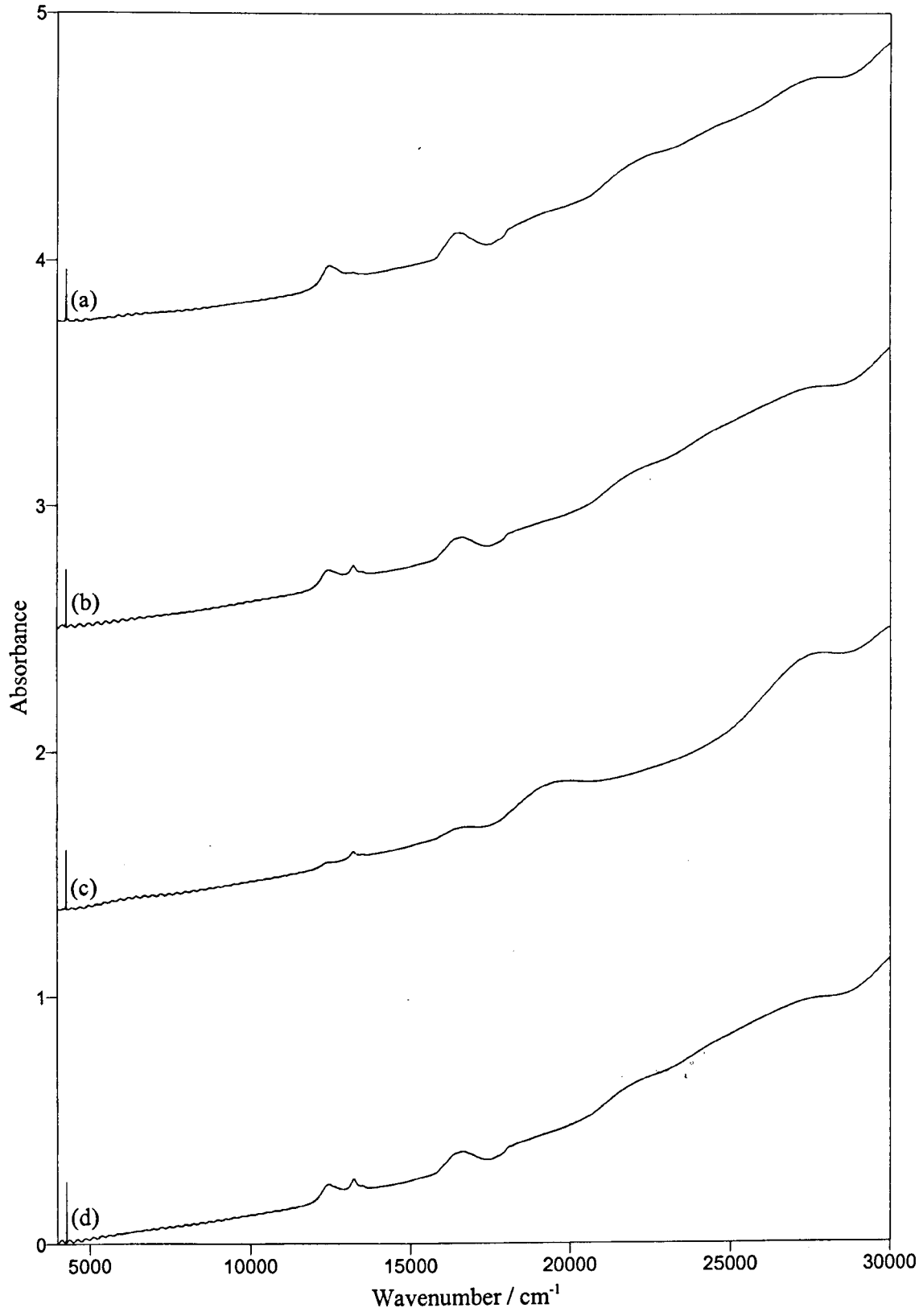

Figure 6.7: Expansion of UV-Vis-NIR spectrum of $CoBr_2$ in CO at 12 K.
(a) deposition, (b) after photolysis with visible light,
(c) after photolysis with UV light, (d) after photolysis with visible light.

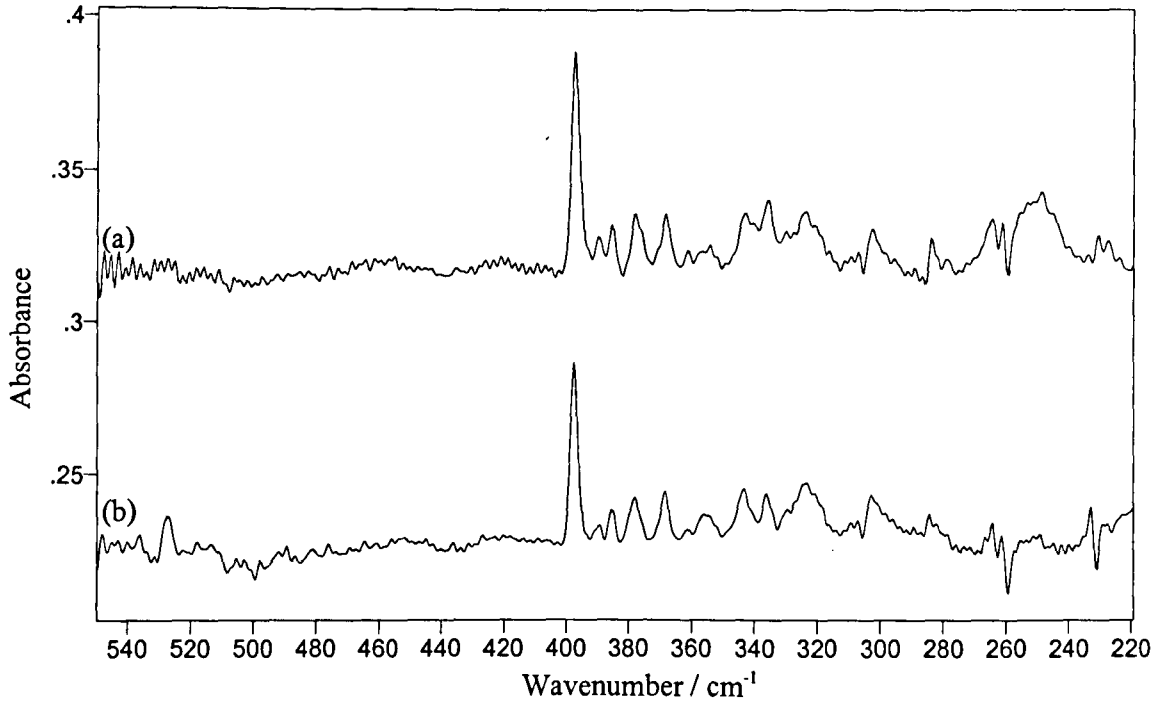

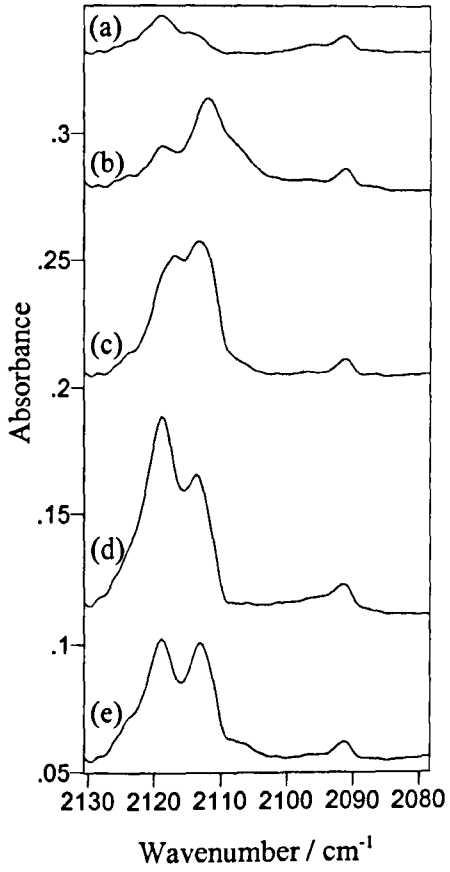

Figure 6.8: IR spectrum of $CoBr_2$ isolated in 1 % CO / argon at 12 K. (a) deposition, (b) after photolysis with visible light, (c) after photolysis with UV light, (d) at 12 K after annealing to 25 K, (e) after broad band photolysis.

argon)[1] along with a large number of other weak bands. Similar to the results discussed earlier, these bands may be due the presence of isolated $[Co(CO)_xBr_2]$ complexes and / or the dibromide molecule isolated in a number of different matrix sites. The FIR bands show negligible changes on annealing and photolysis, which makes their assignment speculative. This is unhelpful but not completely unexpected as it has been seen in previous results that the low energy modes of the carbonyl complexes formed are of such low intensity they are unlikely to be unambiguously assigned in 1 % CO matrices.

A truncated section of the MIR spectrum is also given in figure 6.8 to show the development of a new band in the ν_{CO} region of the spectrum. The MIR spectrum shows two distinct bands at 2118.8, 2112.8 in addition to the ^{13}CO band at 2091.2 cm^{-1}. The changes undergone by these bands in figure 6.8 is clear, with exposure to visible and UV light again appearing to cause a conversion between the 2118.8 and 2112.8 cm^{-1} bands. This photolysis behaviour allows the bands at 2118.8 and 2112.8 cm^{-1} to be assigned as the ν_{CO} stretching modes of the *cis*-square planar and tetrahedral $[Co(CO)_2Br_2]$ complexes respectively.

Bands were again present at higher frequency of 'free' CO in the MIR and are shown in figure 6.9. The photolysis and annealing behaviour suggest that both bands are affected by visible and UV light, with annealing showing an increase in the intensity of the 2165.4 cm^{-1} band and very little effect on the 2181.8 cm^{-1} band. This behaviour is inconsistent with that expected for a non-classical complex as discussed earlier and it is thought the bands may be due to the association of CO molecules with a decomposition or multimer species. The remainder of the MIR spectrum contained no other new bands other than those already assigned as being due to the presence of impurities and their interaction with the CO in the matrix.

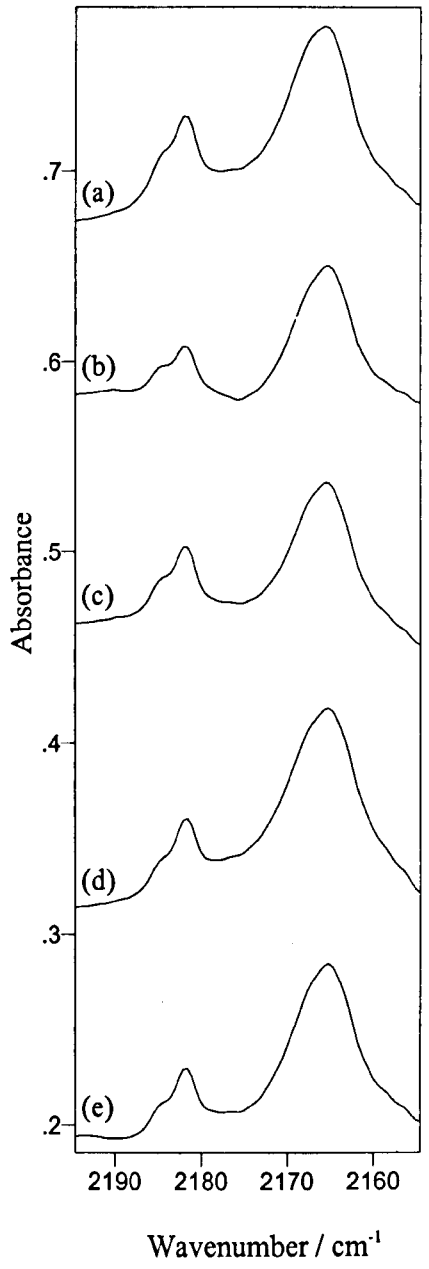

Figure 6.9: MIR spectrum of $CoBr_2$ isolated in 1 % CO / argon at 12 K. (a) deposition, (b) after photolysis with visible light, (c) after photolysis with UV light, (d) at 12 K after annealing to 25 K, (e) after broad band photolysis,

Conclusion

The isolation of $[Co(CO)_2Br_2]$ in a CO matrix has been completed and the characterisation of the *cis*-square planar and tetrahedral complexes confirmed. Photolysis experiments have shown that a conversion occurs between the two isomers, with *cis*-$[Co(CO)_4Br_2]$ being shown to be converted to *tet*-$[Co(CO)_2Br_2]$ on exposure to visible light, with the reverse intensity change occurring on exposure to UV light. This therefore leads to a reassignment of the previous data given in table 6.4 as outlined in table 6.5 below.

***cis*-$[Co(CO)_4Br_2]$**	***tet*-$[Co(CO)_2Br_2]$**
2118.8 cm^{-1}	2112.8 cm^{-1}
516.4 cm^{-1}	332.4 cm^{-1}
468.0 cm^{-1}	294.0 cm^{-1}
451.0 cm^{-1}	210.7 cm^{-1}
404.9 cm^{-1}	
306.1 cm^{-1}	

Table 6.5: IR data for the two isomers of $[Co(CO)_2Br_2]$.

Section 6.3: **Nickel Dibromide**

Previous work has shown that the isolation of $NiBr_2$ in CO matrices results in the formation of a four co-ordinate nickel carbonyl bromide complex.[1] Results suggest the product formed is a mixture of *trans*-$[Ni(CO)_2Br_2]$ and *tet*-$[Ni(CO)_2Br_2]$. The spectra given in figure 6.10 were recorded after a long deposition time (around 3 hours) as they were intended to be used for the identification of very weak, low energy IR bands occurring below 200 cm^{-1}. Similar to the results with cobalt, this meant that the bands above 500 cm^{-1} were almost completely absorbing but are still included as they are clearly affected by the photolysis experiments. Table 6.6 gives the previously reported infrared data and the assignments made along with the corresponding frequencies of the bands observed in these experiments.

Reported Frequency (cm^{-1})[1]	**Observed Frequency (cm^{-1})**	**Assignment[1]**
518.7	518.3	*trans*-$[Ni(CO)_2Br_2]$ $\delta_{Ni\text{-}C\text{-}O}$ (B_{1u})
502.4	501.4	*tet*-$[Ni(CO)_2Br_2]$ $\delta_{Ni\text{-}C\text{-}O}$
455.5	455.4	*trans*-$[Ni(CO)_2Br_2]$ $\delta_{Ni\text{-}C\text{-}O}$ (B_{3u})
410.8	410.9	*trans*-$[Ni(CO)_2Br_2]$ $\nu_{Ni\text{-}C}$ (B_{2u})
354.9	354.8	*tet*-$[Ni(CO)_2Br_2]$ $\delta_{Ni\text{-}C\text{-}O}$
346.8	343.8	*trans*-$[Ni(CO)_2Br_2]$ $\nu_{Ni\text{-}Br}$ (B_{1u})
319.2	319.4	*tet*-$[Ni(CO)_2Br_2]$ $\nu_{Ni\text{-}Br}$
252.2	258.4	*tet*-$[Ni(CO)_2Br_2]$ $\nu_{Ni\text{-}Br}$

Table 6.6: observed and previously reported IR data for $NiBr_2$ isolated in CO.

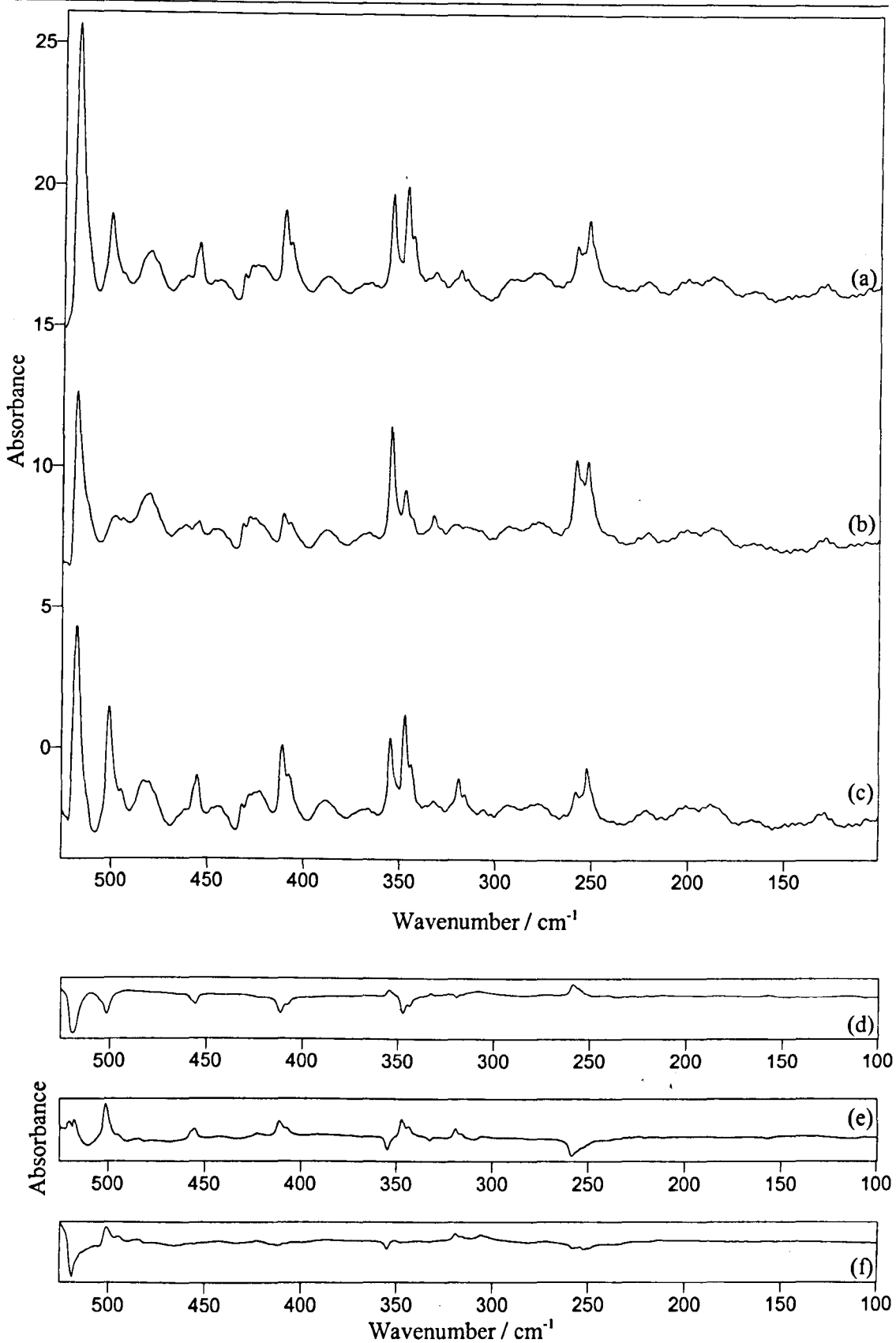

Figure 6.10 : $NiBr_2$ isolated in CO at 12 K. (a) deposition, (b) after photolysis with visible light, (c) after photolysis with UV light, (d) subtraction spectrum - (b) from (a), (e) subtraction spectrum - (c) from (b), (f) subtraction spectrum (c) from (a).

As in the case of cobalt, more than one species is evidently present, with the changes in intensity on exposure to visible and UV light shown by the subtraction spectra in figure 6.10(d) clearly showing a photolytic conversion similar to that discussed in the previous section. This identifies a conversion of the complex between tetrahedral and square planar as the sample area is exposed to differing frequencies of light, with conversion to the tetrahedral complex again being promoted by visible photolysis.

The values given in table 6.4 correspond in reasonable agreement with those observed in these experiments. However, the photolysis experiments contradict some of the assignments made in the previous work and suggest the presence of a third species. The changes observed on photolysis from figure 6.10(f) in the subtraction spectra show that although a conversion occurs, the relative intensities are different in the deposition spectrum and that observed after visible and UV photolysis. The subtraction spectrum shows that of the bands which are increased in intensity some are present at greater relative intensity than others when compared to the original deposition spectrum. This also clearly shows that the bands above 500 cm^{-1} are due to different species as the relative intensity of both bands after photolysis is significantly different. Additional experiments have also shown that these bands have different relative intensities on deposition.

Visible photolysis causes an increase in the bands at 355, 333 and 258 cm^{-1} as all the other bands present can be seen to be reduced. This behaviour is then reversed as the sample is exposed to UV light. The difference spectra comparing the UV photolysis with the deposition spectrum (figure 6.10(f)) further identifies that the bands at 500, 320 and 252 cm^{-1} have all undergone a relative intensity increase when compared to the other bands in the deposition spectrum. Clearly this behaviour suggests the presence of three distinct molecular species.

The band at 520 cm^{-1} is evidently associated by photolysis behaviour with the bands at 455, 411 and 344 cm^{-1} and is at its most abundant in the deposition spectrum. On exposure to visible light this species is then converted to the second species as the bands at 355, 333 and 258 cm^{-1} increase in intensity. This is accompanied by a reduction in intensity of those bands associated with the third species at 500, 320 and 252 cm^{-1}. On exposure to UV light the intensity of the bands associated with the second species is reduced, with the intensity of the bands associated with the other two species showing a marked increase, although the third species clearly shows a larger increase than the first. It is therefore suggested that the deposition spectrum is reasonably consistent with the previous report[1] with both the tetrahedral and square planar complexes being present. On exposure to visible light the square planar complex is converted to the tetrahedral complex as was observed in the case of cobalt. Again theoretical work[6] suggests that the tetrahedral complex has no infrared active $\delta_{M\text{-}C\text{-}O}$ vibrational modes expected above 400 cm^{-1} which is consistent with the assignments made here. It is therefore proposed that UV photolysis converts the tetrahedral complex back to the square planar complex as both *cis*- and *trans*- isomers.

It is reasonable to assume therefore that the three species present correspond to the tetrahedral and both *cis*- and *trans*- square planar complexes with the *trans*- complex formed as the major component on deposition but being converted to the tetrahedral complex on exposure to visible light. When the tetrahedral complex is exposed to UV light it returns back to the square planar geometry, but can reasonably be converted to both *cis*- and *trans*-$[Ni(CO)_2Br_2]$. This explains the presence of three distinct species in the infrared spectrum and the relative intensity differences observed after photolysis. For completeness figure 6.11 shows the extended

photolysis cycle, with visible and UV photolysis being employed in sequence to show the continued conversion between tetrahedral and square planar complexes without any further significant decomposition of isolated species.

As with the case of the cobalt dibromide in CO the isotopic data presented in the previous work is difficult to use in the assignment due to the low intensity of some bands and the problems associated with overlapping bands.

The infrared data for the three isomers of $[Ni(CO)_2Br_2]$ are given in table 6.7 below. The table shows the expected number of bands present for the *trans*- square planar complex, with fewer bands than expected evident for the other two complexes. These bands are expected to be of much lower relative intensity when compared to the other vibrational modes and may be too weak to be observed in these spectra.

tet-$[Ni(CO)_2Br_2]$	*trans*-$[Ni(CO)_2Br_2]$	*cis*-$[Ni(CO)_2Br_2]$
354.8 cm^{-1}	518.3 cm^{-1}	501.4 cm^{-1}
332.7 cm^{-1}	455.4 cm^{-1}	319.4 cm^{-1}
258.4 cm^{-1}	410.9 cm^{-1}	252.2 cm^{-1}
	343.8 cm^{-1}	

Table 6.7: IR data for the three isomers of $[Ni(CO)_2Br_2]$.

The UV-Vis-NIR spectra shown in figure 6.12 confirms the presence of two charge-transfer bands for both complexes. The presence of the strong band at 37600 cm^{-1} and the band at 33860 cm^{-1} which substantially reduce on exposure to visible light associates these features with the square planar complex. These are accompanied by the appearance of the two features at 35600 and 42200 cm^{-1} which are presumably charge transfer bands of the tetrahedral complex. The UV-Vis-NIR spectra also show two further intriguing characteristics. Firstly, it is evident from

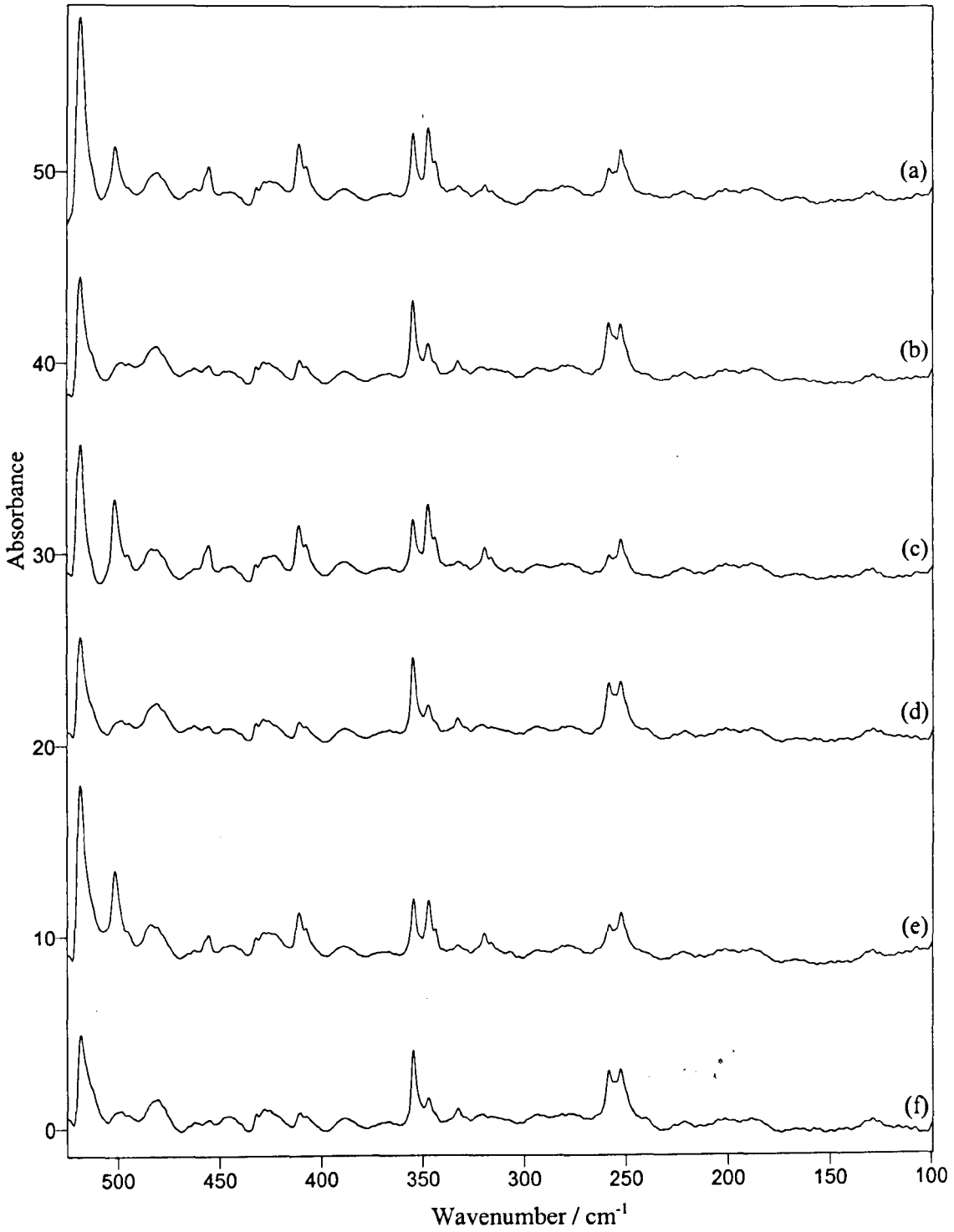

Figure 6.11 : $NiBr_2$ isolated in CO at 12 K - photolysis cycle. (a) deposition, (b) after photolysis with visible light, (c) after photolysis with UV light, (d) after photolysis with visible light, (e) after photolysis with UV light, (f) after photolysis with visible light.

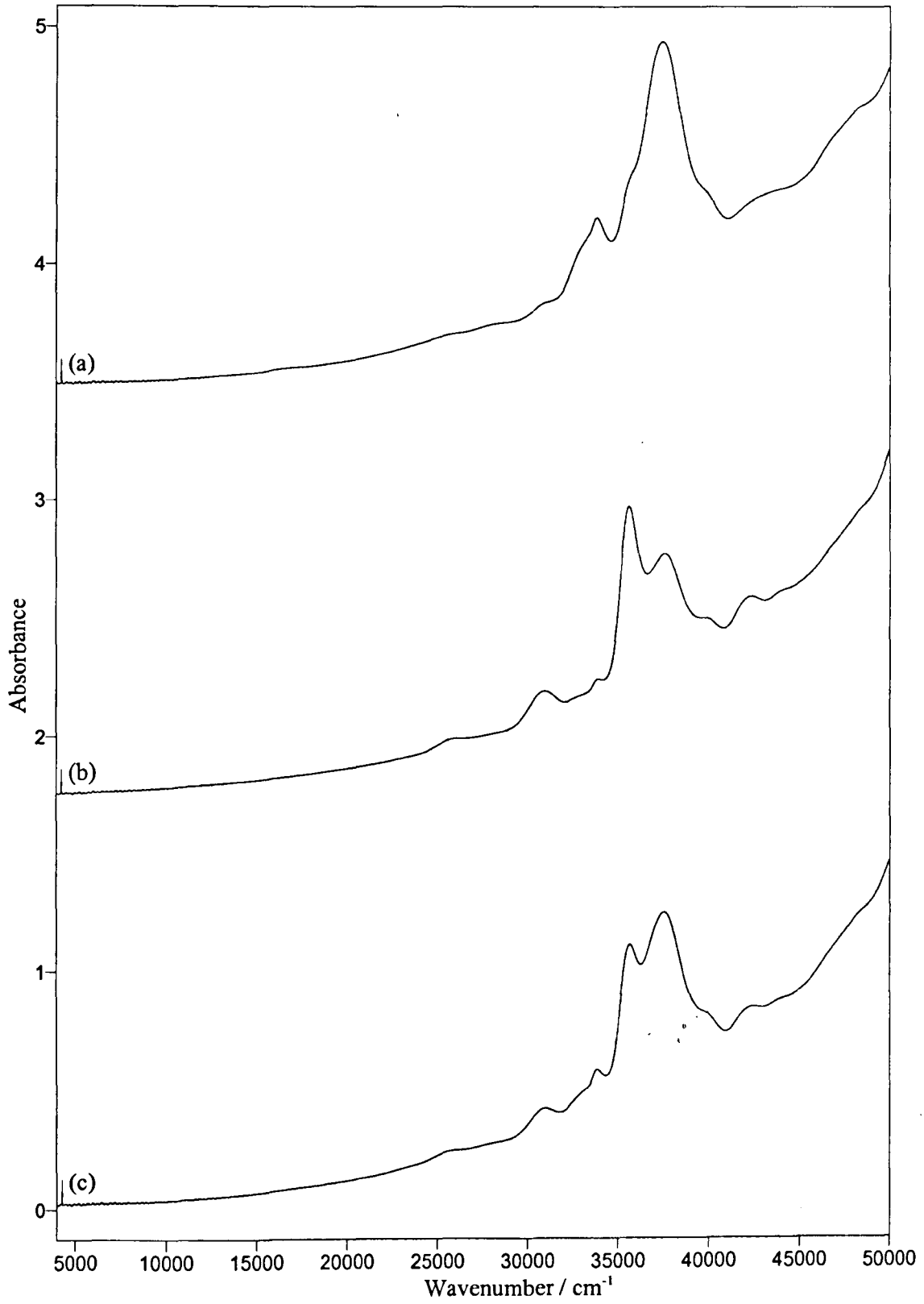

Figure 6.12: UV-Vis-NIR spectrum of $NiBr_2$ in CO at 12 K.
(a) deposition, (b) after photolysis with visible light,
(c) after photolysis with UV light.

comparison of the relative intensities of the charge transfer bands associated with either complex that the square planar complex is clearly prevalent in the original deposition. This is then substantially reduced as it is apparently converted to the tetrahedral complex on exposure to visible light. Although the square planar complex is then seemingly reformed on exposure to UV light the bands associated with the tetrahedral complex remain in a reasonable intensity although still somewhat reduced by the photolysis. This is reasonably consistent with the behaviour observed in the infrared spectra.

An expansion of the region below 30000 cm^{-1} where the d-d transitions are expected to occur (figure 6.13) shows evidence of bands at 25800 and 30960 cm^{-1} which appear on visible photolysis. Although this associates them with the tetrahedral complex this contradicts previous work which has shown the d-d transitions for Ni^{II} square planar complexes appear at much lower energy (< 21000 cm^{-1}).[8] This means that these bands are more likely to be charge transfer in origin than d-d transition, with the associated features of the low energy transitions presumably being too weak to be observed in the spectra presented.

The IR spectrum observed when $NiBr_2$ was isolated in 1 % CO in argon matrices is given in figure 6.14. The FIR spectrum is shown on deposition and after an annealing cycle, which resulted in the marginal decrease in intensity of the major features at 418.7 and 413.7 cm^{-1}. These bands correspond to the nickel isotope pattern on the ν_{asym} stretching mode of $NiBr_2$ isolated in an argon matrix, previously assigned at 423.5 (^{58}Ni), 418.3 (^{60}Ni) and 413.4 cm^{-1} (^{62}Ni). This was accompanied by a slight decrease in all other bands present. It is therefore likely that the remainder of the FIR bands at lower energy to the major $NiBr_2$ bands are associated with the isolated dibromide molecule, most probably in a different matrix site, rather than a

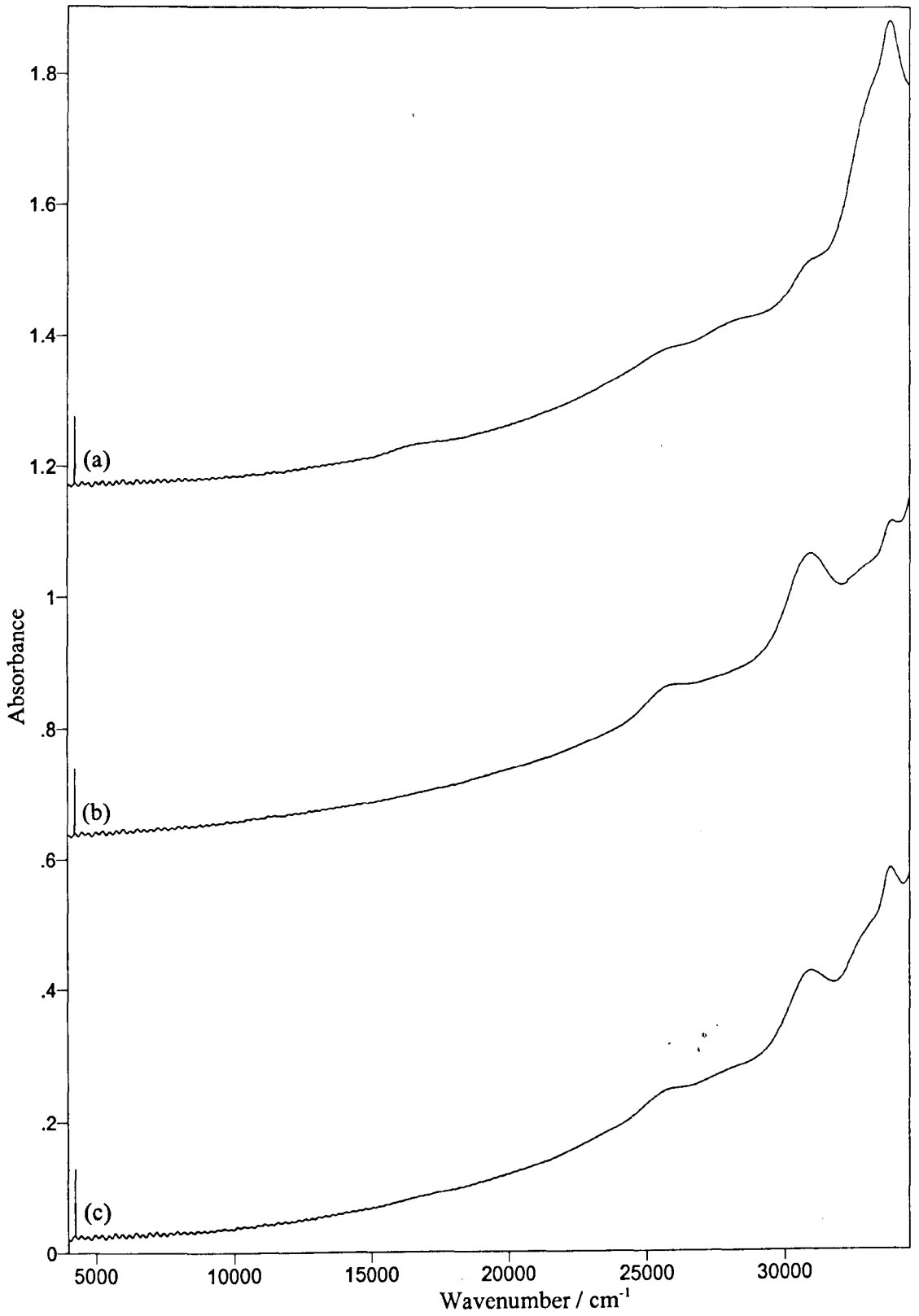

Figure 6.13: Expansion of UV-Vis-NIR spectrum of $NiBr_2$ in CO at 12 K.
(a) deposition, (b) after photolysis with visible light,
(c) after photolysis with UV light.

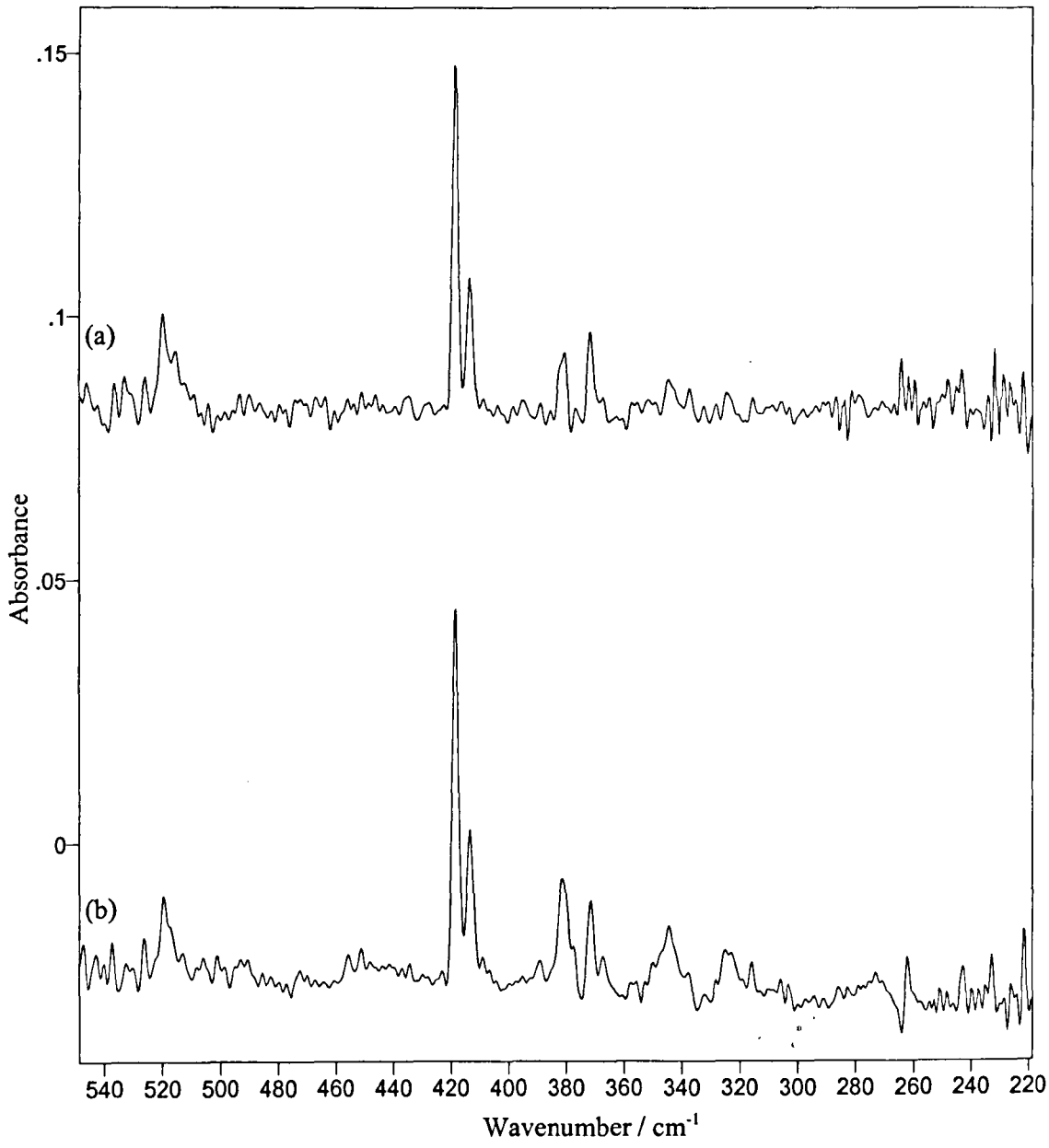

Figure 6.14: FIR spectrum of $NiBr_2$ isolated in 1 % CO / argon at 12 K. (a) deposition, (b) at 12 K after annealing to 25 K.

carbonyl complex. However this leaves the band at 519.7 cm^{-1} which shows no evident change on photolysis or annealing unassigned. By comparison of the 1 % CO / Ar and neat CO spectra for $NiBr_2$ it is possible that this band corresponds to that of the $\delta_{Ni\text{-}C\text{-}O}$ mode of *trans*-$[Ni(CO)_2Br_2]$ (observed in neat CO at 518.3 cm^{-1}) with the energy shift of 1.4 cm^{-1} easily accounted for by the perturbing effects of using a dilute CO / argon matrix rather than a neat carbon monoxide matrix. If this band is indeed the bending mode of the *trans*- complex then it would also explain the absence of any other bands in the FIR, since this band is clearly the most intense of the vibrations in the FIR, making the other low energy stretching and deformation modes too low in intensity to be observed. Unfortunately the low intensity of the feature and the relatively high noise level in this region of the spectrum made the results of photolysis inconclusive. However, it may be considered that since the experiments in neat CO strongly point towards the preferential formation of the *trans*- complex in the deposition, plus the fact that the isolated $NiBr_2$ unit in an argon matrix is linear, then the assignment of this band to that of the $\delta_{Ni\text{-}C\text{-}O}$ mode of *trans*-$[Ni(CO)_2Br_2]$ is reasonable.

A truncated view of the MIR spectra observed on deposition and after annealing (to 25 K) and photolysis are shown in figure 6.15 with the changes observed highlighted by the subtraction spectra (e, f and g). The spectra are again truncated for clarity. The MIR spectrum in figure 6.15 presents 2 major features at 2090.9 and 2074.0 cm^{-1}. The band at 2090.9 cm^{-1} is assigned as being due to ^{13}CO in the matrix, leaving the band at 2074 cm^{-1} which appears on annealing to be assigned as the ν_{CO} mode of the $[Ni(CO)_2Br_2]$ complex. The subtraction spectra in figure 6.15 show that further photolysis had no effect on either band making further characterisation difficult. Since the formation of $[Ni(CO)_2Br_2]$ is expected by the co-

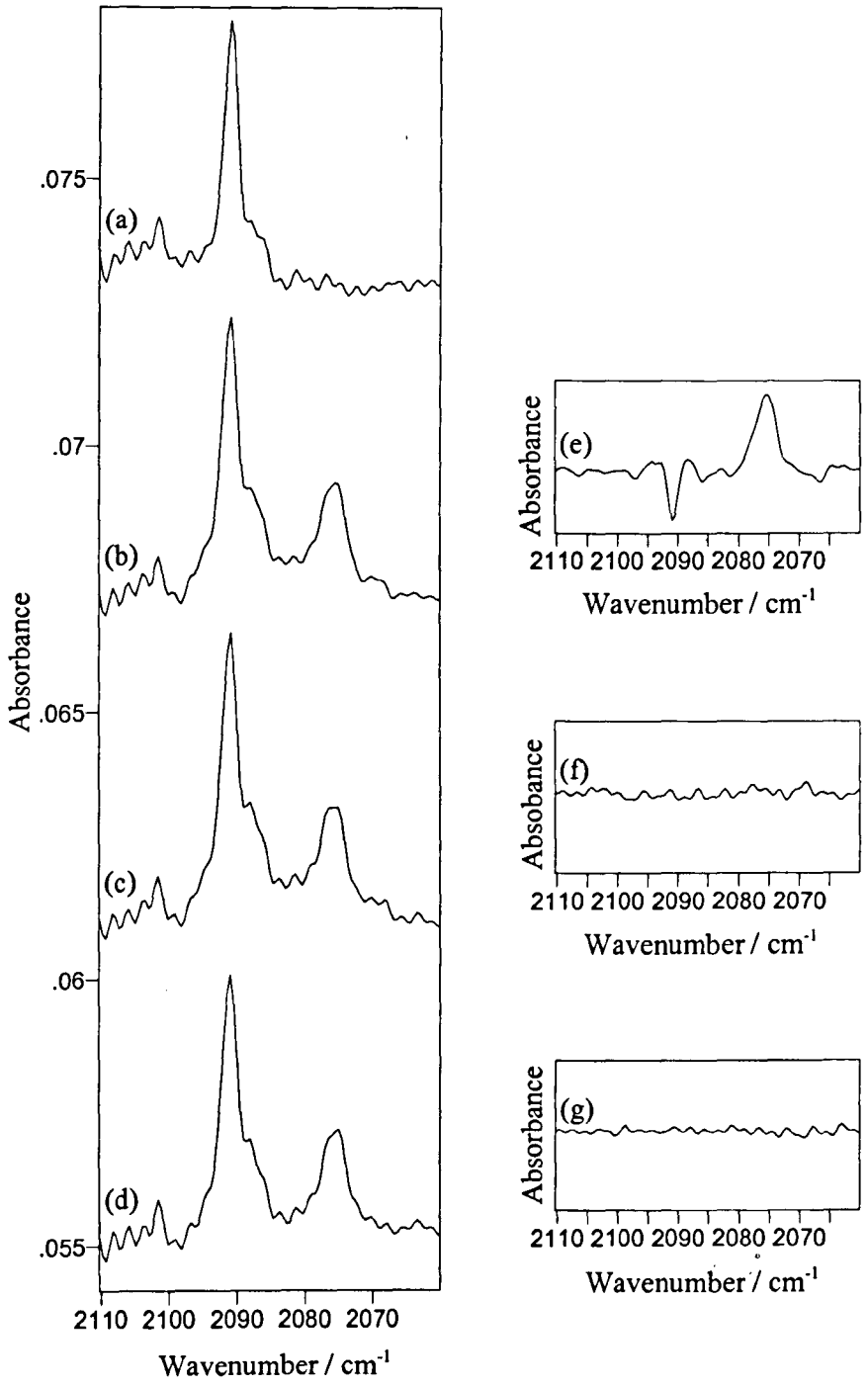

Figure 6.15: MIR spectrum of $NiBr_2$ isolated in 1 % CO / argon at 12 K.
(a) deposition, (b) at 12 K after annealing to 25 K,
(c) after photolysis with visible light, (d) after photolysis with UV light,
(e) subtraction spectrum - (a) from (b), (f) subtraction spectrum - (b) from (c),
(g) subtraction spectrum - (c) from (d).

ordination of CO molecules to isolated $NiBr_2$, it is possible that the observed behaviour is due to the co-ordination of CO molecules to form the dicarbonyl complex on annealing. This behaviour cannot be linked to the FIR bands as only one band (at 519.7 cm^{-1}) is present but too low in intensity in a noisy spectral region to observe such a subtle change. However, the band at 520 cm^{-1} is clearly present in both the deposition and annealing spectra, whereas the 2074 cm^{-1} band does not appear until the sample is warmed. This clearly suggests that these two bands do not arise from the same species and it is therefore impossible to assign the ν_{CO} mode to a specific $[Ni(CO)_2Br_2]$ species at this time.

Again the region to high frequency of free CO contains new features. In this case one major band is present at 2175.5 cm^{-1}. The band is shown in figure 6.16 along with the effect of photolysis and annealing and the appropriate subtraction spectra. Although the band undergoes a slight intensity change it is not consistent to associate this band with the presence of a non-classical carbonyl complex and as in the case of cobalt it is assumed to be the co-ordination of CO to a dissociation or agglomeration product.

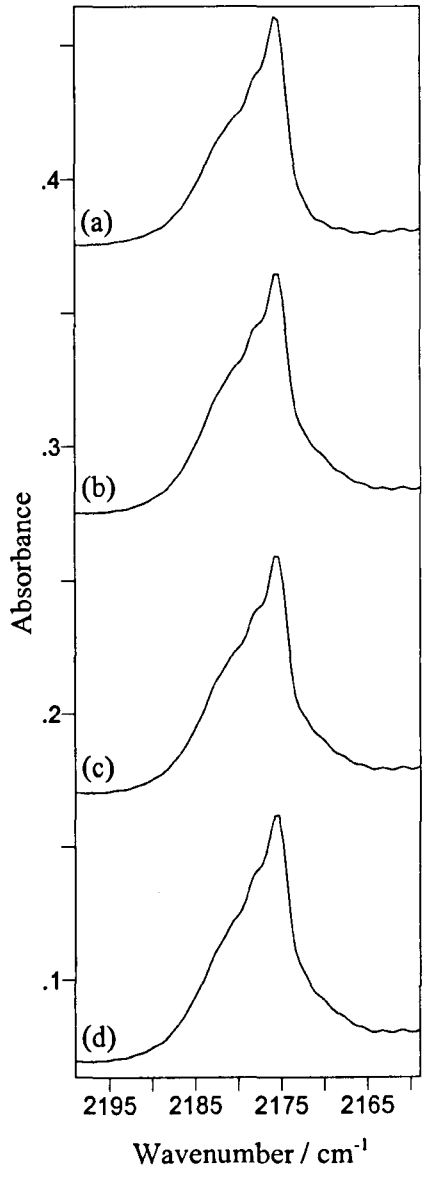

Figure 6.16: MIR spectrum of $NiBr_2$ isolated in 1 % CO / argon at 12 K. (a) deposition, (b) after photolysis with visible light, (c) after photolysis with UV light, (d) at 12 K after annealing to 25 K.

Conclusion

The identification of the FIR modes for the square planar and tetrahedral $[Ni(CO)_2Br_2]$ complexes isolated in a CO matrix has been confirmed by photolysis of the isolated sample. A conversion between the two isomers has been identified on exposing the sample to visible and UV light (with the formation of the tetrahedral complex being promoted by exposure to visible light). The presence of both *cis*- and *trans*-$[Ni(CO)_2Br_2]$ has also been identified, with the *trans*- complex appearing prevalent in the initial deposition and the proportion of the *cis*- complex apparently increasing after conversion of the tetrahedral complex. This has lead to the reassignment of the vibrational bands made in the previously reported experiments.[1] The use of 1 % CO in argon matrices has also been used to identify a band thought to be due to the ν_{CO} mode of $[Ni(CO)_2Br_2]$, unfortunately inconsistent annealing and photolysis behaviour has not allowed this band to be assigned to a specific isomer of the complex.

The full characterisation of the infrared bands may require further isotopic data in conjunction with extensive photolysis experiments before the assignments made can be confirmed.

Section 6.4: **Zinc and Manganese Dibromide**

The previous results presented on matrix isolated zinc and manganese dibromide are given in tables 6.8 and 6.9 below. The evidence presented showed that no new metal carbonyl bromide complexes were formed by the isolation of these species in CO matrices.[1]

The current investigation confirmed this assessment, with only the metal-halide stretching frequency observed in neat CO matrices. The FIR spectra observed after the isolation of zinc dibromide and manganese dibromide in a neat CO matrix is shown in figures 6.17 and 6.18, along with the FIR spectra observed in 1 % CO / argon matrices. The frequencies observed are presented in the tables below and show reasonable agreement with those previously identified as the asymmetric metal-halide stretching frequency of the isolated molecules.

Reported Frequency (cm^{-1})[1]		Observed Frequency (cm^{-1})		Assignment[1]
CO	**Argon**	**CO**	**1 % CO in argon**	
	410.1		409.8	$\nu_{Zn\text{-}Br}$ - ^{64}Zn
	405.6		405.4	$\nu_{Zn\text{-}Br}$ - ^{66}Zn
	401.4		401.1	$\nu_{Zn\text{-}Br}$ - ^{68}Zn
			383.5	?
			379.4	?
			376.0	?
325.5		232.2	328.6	$\nu_{Zn\text{-}Br}$
220.5		211.3		$\nu_{Zn\text{-}Br}$ - site

? *probably due to the presence of multimer or matrix site effect.*

Table 6.8: infrared data for matrix isolated $ZnBr_2$

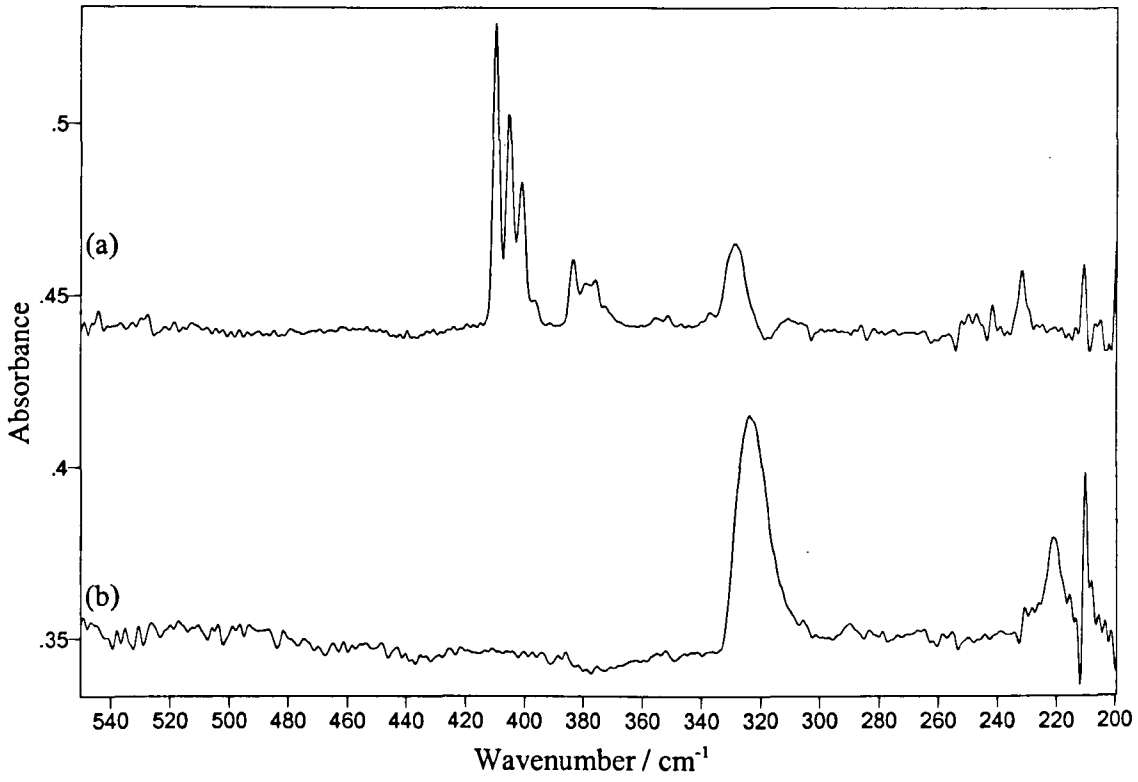

Figure 6.17: $ZnBr_2$ isolated in (a) 1 % CO / argon and (b) neat CO at 12 K.

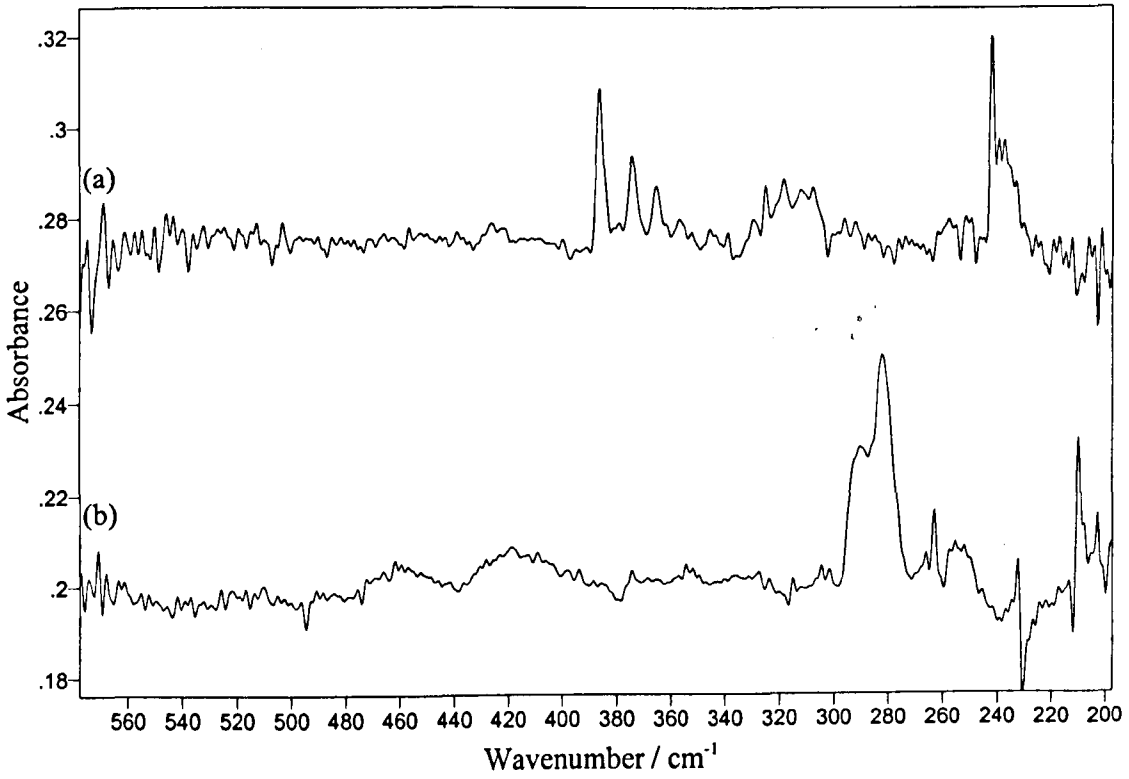

Figure 6.18: $MnBr_2$ isolated in (a) 1 % CO / argon and (b) neat CO at 12 K.

Reported Frequency (cm^{-1})[1]		Observed Frequency (cm^{-1})		Assignment[1]
CO	**Argon**	**CO**	**1 % CO in argon**	
	387.3		386.4	ν_{Mn-Br} - argon site
	374.0		374.5	ν_{Mn-Br} - 2nd site
			365.5	ν_{Mn-Br} - 3rd site
294.7		290.7	318.7	ν_{Mn-Br} - CO site
283.2		282.3		ν_{Mn-Br} - 2nd site

Table 6.9: infrared data for matrix isolated $MnBr_2$

A truncated view of the MIR regions for both manganese and zinc dibromides in 1 % CO / argon spectra are given in figures 6.19 and 6.20. No bands were observed in the ν_{CO} region at lower frequency to CO, but again bands were observed at high frequency. In both cases one major band dominates the region, at 2194.1 cm^{-1} for manganese and 2185.5 cm^{-1} for zinc. Both these bands are observed to undergo a reduction in intensity after the matrix is warmed to 25 K. This reduction in intensity is accompanied by the growth of a number of weak, broad absorption bands, the values of which are given in table 6.10.

Manganese	Zinc	Intensity Change on Annealing
2194 cm^{-1}	2185.5 cm^{-1}	Decrease
2188 cm^{-1}	2196.6 cm^{-1}	Increase
2176.5 cm^{-1}	2188.1 cm^{-1}	Increase
2162.8 cm^{-1}	2161.1 cm^{-1}	Increase

Table 6.10: Wavelengths of observed MIR bands and the effect of annealing.

The decrease in intensity on annealing of one band in each case would suggest that these bands may well be due to the formation of a non-classical carbonyl

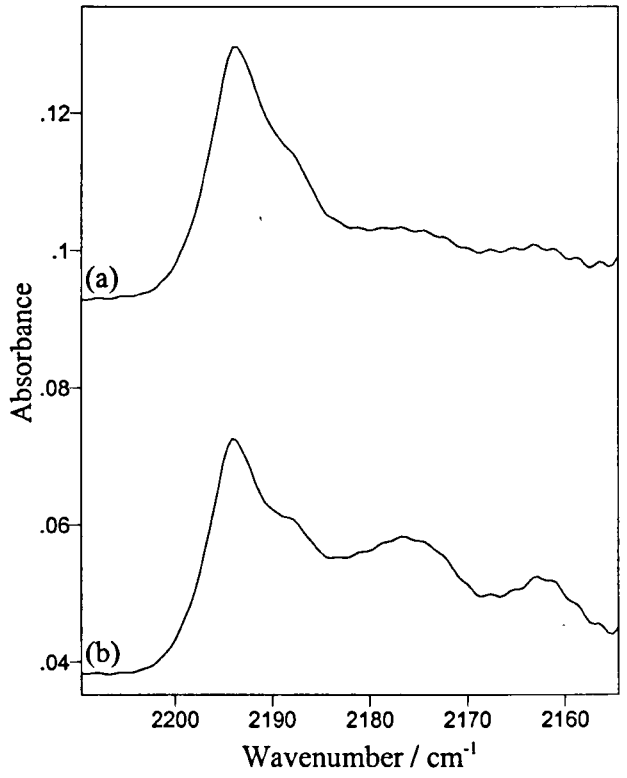

Figure 6.19: truncated MIR spectra of $MnBr_2$ in a 1 % Co /Ar matrix at 12 K. (a) deposition, (b) at 12 K after annealing to 15 K.

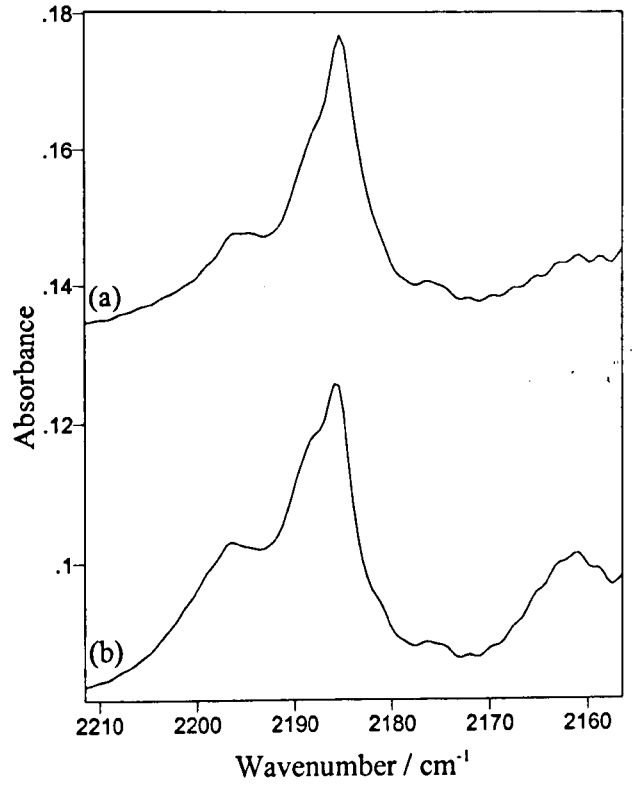

Figure 6.20: truncated MIR spectra of $ZnBr_2$ in a 1 % Co /Ar matrix at 12 K. (a) deposition, (b) at 12 K after annealing to 15 K.

complex which, as discussed earlier, are expected to undergo a reduction in intensity as the matrix is warmed and molecules can co-ordinate fully. The increase of the other bands in this region in each case is also inconsistent with the formation of non-classical carbonyls, but is reasonably consistent with the results from the other transition metal dibromides already discussed in this chapter. As stated earlier, it is not possible to completely assign these bands with only the current data available, but they are most likely due to the interaction of impurities or decomposition and agglomeration products with CO.

These results confirm that no complexation occurs between the isolated molecules and the matrix when $ZnBr_2$ and $MnBr_2$ are isolated in CO containing matrices. The result using 1 % CO/ argon matrices concur with this statement, although evidence does exist in the MIR region that some CO molecules may interact with the metal bromide molecules and a low level of co-ordination may occur.

Section 6.5: **Chromium Bromide**

The aim of the experiments outlined in this section was to isolate molecular chromium (II) bromide in an inert matrix. Once identified the molecule was then to be isolated in CO matrices to identify any possible $[Cr(CO)_xBr_2]$ species which may be formed.

The matrix isolation infrared spectrum of $CrBr_2$ in argon has been presented with the molecule identified as most likely being linear.[9] This work showed that heating chromium metal in the presence of bromine (the route used in the preparation of the 3d transition metal dibromides described in the previous sections) resulted in the formation of solid $CrBr_3$. The isolated sublimation products of $CrBr_{3(s)}$ were then identified as $CrBr_4$, $CrBr_3$ and $CrBr_2$. The formation of these gas phase species by sublimation was found to be temperature dependent, with $CrBr_4$ formed at the lowest sublimation temperature (500 °C). An increase in temperature was then shown to lead to the isolation of $CrBr_3$, however with preheating the temperature could then be increased (~ 650 °C) to result in the isolation of $CrBr_2$. These molecules were never isolated as single species and were always accompanied by the isolation of bromine in the matrix. Mass spectral studies also presented suggested the predominance of $CrBr_3$ in the vapour.

Previous work has identified the formation of $CrCl_2$ by the heating of silver chloride with chromium powder with no notable presence of silver chloride in the matrix.[3] The following section describes a similar route to matrix isolated chromium dibromide, that is the heating of silver bromide and chromium powder, with the products isolated in inert matrices to identify the chromium bromide species being

formed. This method was chosen as a source of chromium bromide as it was hoped that as in the case of chromium chloride the vapour would be predominately Cr^{II} with negligible traces of Cr^{III} and Cr^{IV} and with no isolated Br_2 present. The isolation of a single species was desirable since the further investigation of the interaction between matrix isolated $CrBr_2$ and the CO matrix would be overcomplicated by the presence of higher chromium bromides or bromine.

Results and Discussion

a) Inert Matrices.

The infrared spectrum observed after 60 minutes of deposition at sublimation temperature (600 °C) with the sublimate isolated in an argon matrix at 10 K is shown in figure 6.21. The spectrum is in good agreement with that previously present for the sublimation product of $CrBr_{3(s)}$ in argon.[9] The bands at 362.3 and 375.6 cm^{-1} can be clearly assigned to $CrBr_2$ and $CrBr_4$ respectively by simple comparison to the previously observed spectra as shown in table 6.11. The presence of the band at 357.5 cm^{-1} was initially considered to be due to the chromium isotope pattern, but on closer examination it appears similar to a band observed in a previous report on $CrCl_2$[10] and is thought to be due to a site effect. Although the presence of $CrBr_2$ and $CrBr_4$ is clear, no evidence for the presence of $CrBr_3$ was found.

It would appear from this initial spectrum in argon that the attempt to form a single matrix isolated chromium dibromide species has been unsuccessful due to the presence of a band due to matrix isolated $CrBr_4$. However, by comparison of the argon matrix spectrum with that observed in a nitrogen matrix (figure 6.22) this may not be the case. The previous report on matrix isolated chromium bromides had indicated that $CrBr_4$ was prevalent at lower sublimation temperatures and after

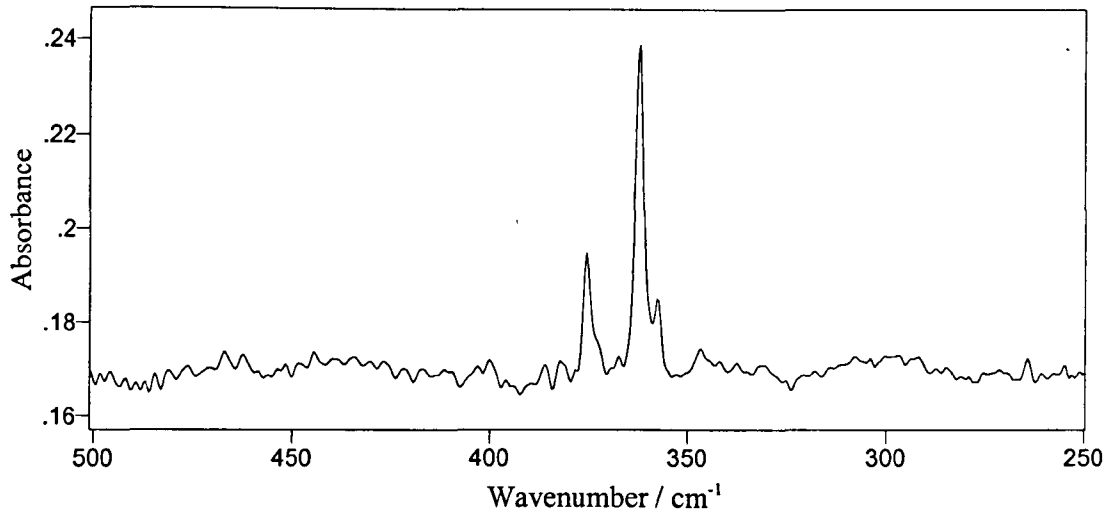

Figure 6.21: sublimation products of chromium powder and silver chloride isolated in argon at 10 K.

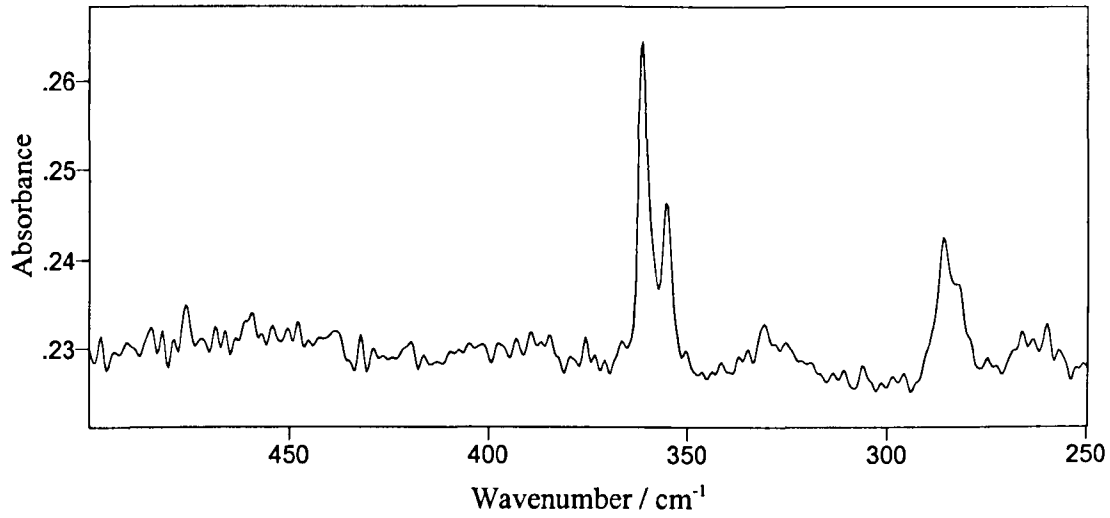

Figure 6.22: sublimation products of chromium powder and silver chloride isolated in nitrogen at 10 K.

Assignment	Reported in Ar	Observed in Ar	Observed in N_2
$CrBr_4$	375.5 cm^{-1}	375.6 cm^{-1}	-
$CrBr_3$	393 cm^{-1}	-	-
$CrBr_2$	362 cm^{-1}	362.3 cm^{-1}	361.3 cm^{-1}
$CrBr_2$ (2^{nd} site)	-	357.5 cm^{-1}	355.1 cm^{-1}

Table 6.11: vibrational frequencies of matrix isolated $CrBr_x$ (x=2 to 4).

preheating was found to disproportionate to a greater extent, increasing the amount of matrix isolated $CrBr_3$ and $CrBr_2$. It is therefore not inconceivable that the initial stages of these experiments involving the heating of chromium and silver bromide that some $CrBr_4$ would be present, but removed after significant preheating. This could explain the lack of $CrBr_4$ in the nitrogen spectrum shown in figure 6.22 which was recorded immediately after the argon experiment. The nitrogen spectrum also shows another broad band below 300 cm^{-1} (285.8 cm^{-1}) which remains unassigned. The band could possibly be due to a dimer or higher multimer species, although previous work suggests the dimer bands should be present at around 340 cm^{-1} it could also be interacting with the nitrogen matrix which would probably cause a significant shift in the vibrational frequency. The presence of monomeric $CrBr_2$ is again clear by comparison with the argon spectrum, the small frequency shift undergone by the vibrational mode on changing from an argon to a nitrogen matrix suggests little or no interaction between the molecular species and the matrix which discounts the formation of $Cr(N_2)_xBr_2$ complexes. It is notable from table 6.2 that the band at 357.5 cm^{-1} in argon which was tentatively assigned to a site effect undergoes a greater energy shift than the major vibrational band. This suggests it is very unlikely to be part of the chromium isotope pattern as an identical energy shift would be expected and therefore adds further evidence for the assignment of this band as $CrBr_2$ in a second matrix site.

To gain more information on the nature of the gas phase species produced by the sublimation of silver bromide and chromium a mass spectral study was undertaken on the remaining sample after the matrix isolation experiments were completed. The mass spectrum produced provided evidence of the presence of $CrBr^+$ and $CrBr_2^+$ ions but no evidence was found of the higher bromides or dimeric

species. The mass spectrum was also able to highlight the absence of silver in the vapour. This confirms that after initial preheating the major vapour phase species produced was $CrBr_2$.

b) CO Matrices.

Previous work on $CrCl_2$ has identified the formation of $[Cr(CO)_4Cl_2]$ by the isolation of molecular $CrCl_2$ in neat CO and dilute CO / argon matrices.[3] The infrared spectrum observed after the isolation of the vapour above heated chromium powder and silver bromide in neat CO at 10 K is given in figure 6.23. Immediately observable is the presence of new bands in the FIR region indicating some form of interaction. The band at 310.5 cm^{-1} is most likely to be the $\nu_{M\text{-}Cl}$ stretching mode since a reasonably large matrix shift would be expected from the value observed in the argon matrix (based on previous metal bromide data[1]). Simple comparison with the spectra observed for $[Cr(CO)_4Cl_2]$ in CO[3] allows the tentative assignment of the band at 539 cm^{-1} to the $\delta_{M\text{-}C\text{-}O}$ bending mode of a carbonyl complex with remaining bands at 363.5 cm^{-1} and 263.5 cm^{-1} being the $\nu_{M\text{-}C}$ and $\nu_{M\text{-}Br}$ stretching modes respectively. This leaves only the second $\delta_{M\text{-}C\text{-}O}$ mode unassigned which DFT calculations have predicted to be much weaker in intensity compared to the other vibrational modes.[6] This assignment is obviously somewhat tentative and based merely on comparison between experimental observation and previous reports.

The observed spectrum is also consistent with that expected for *trans*-$[Cr(CO)_2Br_2]$, but theoretical work suggests the formation of this is less likely than the octahedral complex due to their relative stabilities. The work also predicts that although more than three infrared active bands are expected they are low intensity and therefore may be lost in the spectral noise. To complete the characterisation of

the FIR bands further experimentation is required using isotopic enrichment and high resolution, although as in these experiments it is unlikely that the bands will resolve further due to the perturbing nature of the CO matrix.

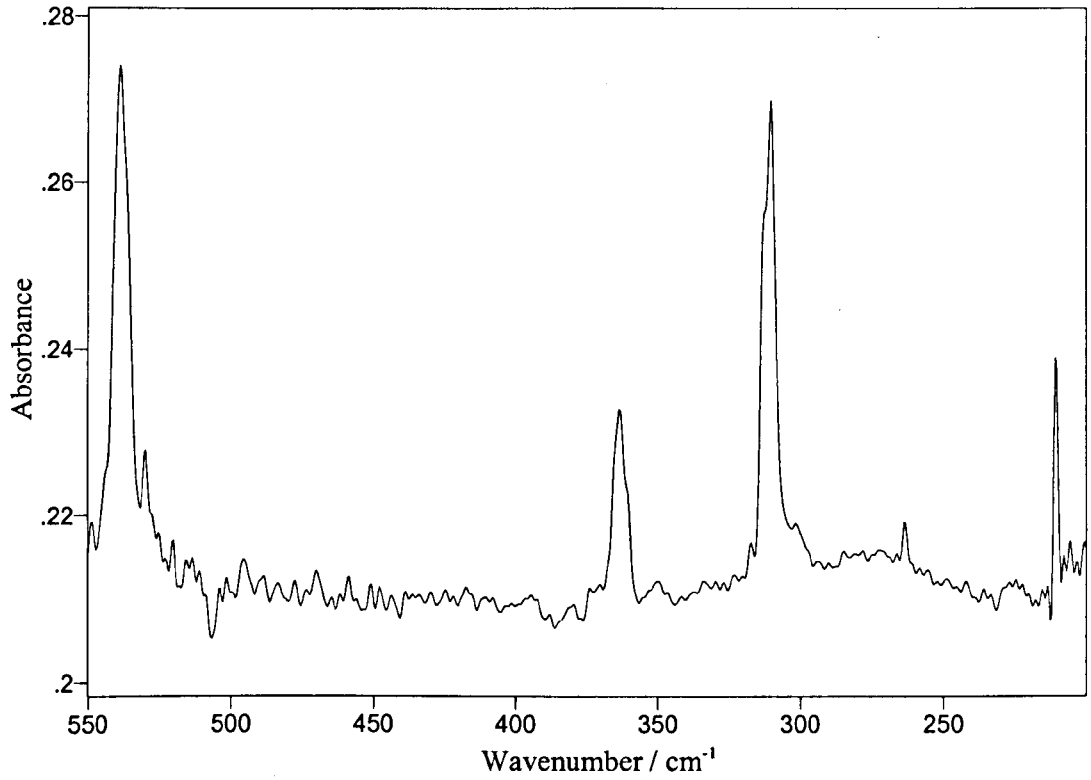

Figure 6.23: FIR spectrum observed after the isolation of the vapour above heated chromium powder and silver bromide in neat CO at 10 K.

To assign the $\nu_{C\text{-}O}$ stretching mode experiments with 1 % CO in argon matrices were employed. This dilution was required to simplify the ν_{CO} region which in neat CO matrices is almost completely masked by the presence of CO isotopomers and CO-impurity complexes. Figure 6.24 shows the observed far infrared spectrum of $CrBr_2$ in a 1 % CO in argon along with the neat argon matrix spectra for comparison. The band positions are listed in table 6.12 accompanying figure 6.24.

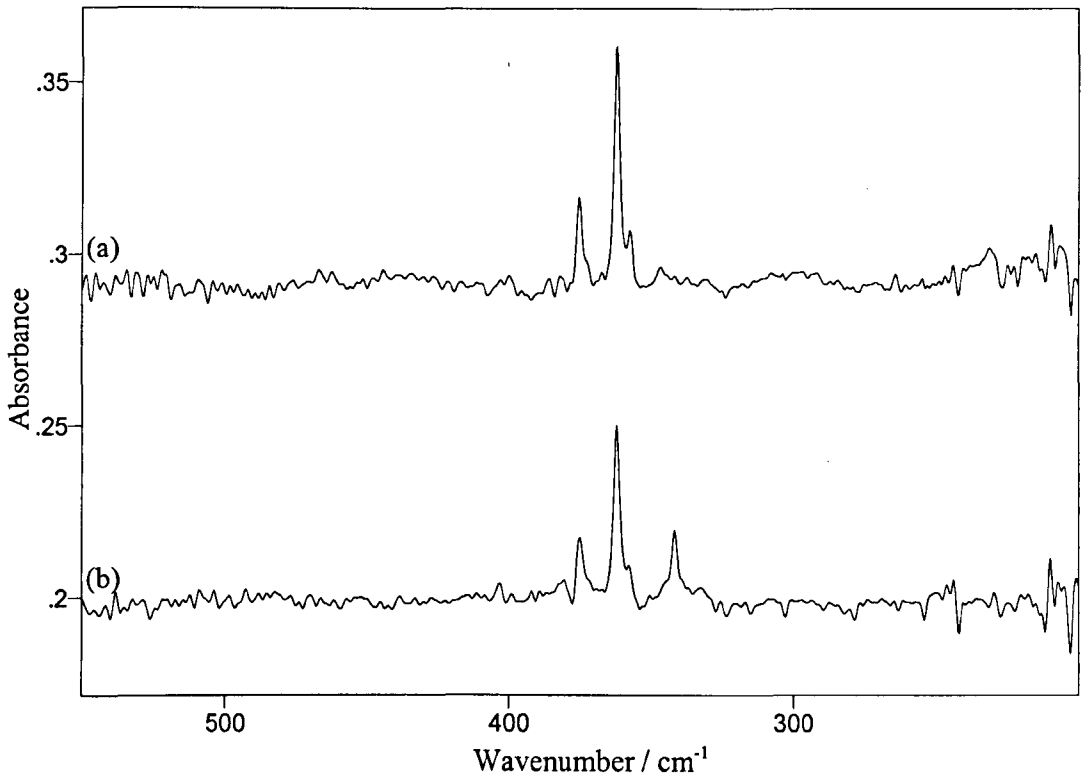

Figure 6.24: FIR spectrum observed after the isolation of the vapour above heated chromium powder and silver bromide at 10 K (a) in argon, (b) in 1 % CO / argon.

Argon Matrix	1 % CO in an Argon Matrix	CO Matrix
	403.3 cm^{-1}	539 cm^{-1}
375.5 cm^{-1}	375.1 cm^{-1}	363.5 cm^{-1}
362.3 cm^{-1}	362.1 cm^{-1}	310.5 cm^{-1}
357.3 cm^{-1}	357.7 cm^{-1}	263.5 cm^{-1}
	341.8 cm^{-1}	

Table 6.12: infrared data for $CrBr_2$ isolated in argon and CO containing matrices at 12 K.

In addition to the band assigned as the M-Br stretch of the dibromide at 362.1 cm^{-1} a new band is observed at 341.8 cm^{-1} which could be due to the dimer, expected at around 340 cm^{-1}, although it may also be a site effect from the isolation of a $CrBr_2$ molecule in a CO / argon site. The spectrum also shows evidence for the continued presence of tetrabromide in the band at 375.1 cm^{-1}. There is also the suggestion of a weak band at 403.3 cm^{-1} which could be considered as being due to the tribromide, previously reported at 393.1 cm^{-1}. These are the most simple assignments to make based on previously reported spectra, but contradict the findings of the mass spectrometry experiments. Since the observations of the FIR spectra in neat CO provide strong evidence for the interaction between CO and isolated $CrBr_2$ the possibility that these bands are in fact a result of interaction between isolated molecules and CO must be investigated further. A previous matrix isolation study on CrF_2 in CO / argon has identified the presence of new bands in the region surrounding the $\nu_{Cr\text{-}F}$ mode of the isolated molecule which are assigned to the formation of a carbonyl complex.[15]

Figure 6.25 shows the effect of annealing (to 25 K) and photolysis (broad band) on the FIR spectrum. The possibility that the FIR spectrum contains only bands due to the presence of chromium bromide species with chromium in different oxidation states is discredited by these annealing and photolysis experiments. On annealing the band at 362.1 cm^{-1} decreases in intensity, while the other bands present undergo no intensity change which can be observed above the spectral noise. Since there is no free bromine (312 cm^{-1} in argon,[9] gas phase fundamental at 318 cm^{-1}[11]) in the matrix it is unlikely that the presence of $CrBr_3$ and $CrBr_4$ would increase while the amount of $CrBr_2$ is reduced. In addition, little effect is shown by the band at 341.8 cm^{-1} making it unlikely that this band is due to the presence of the dimer since

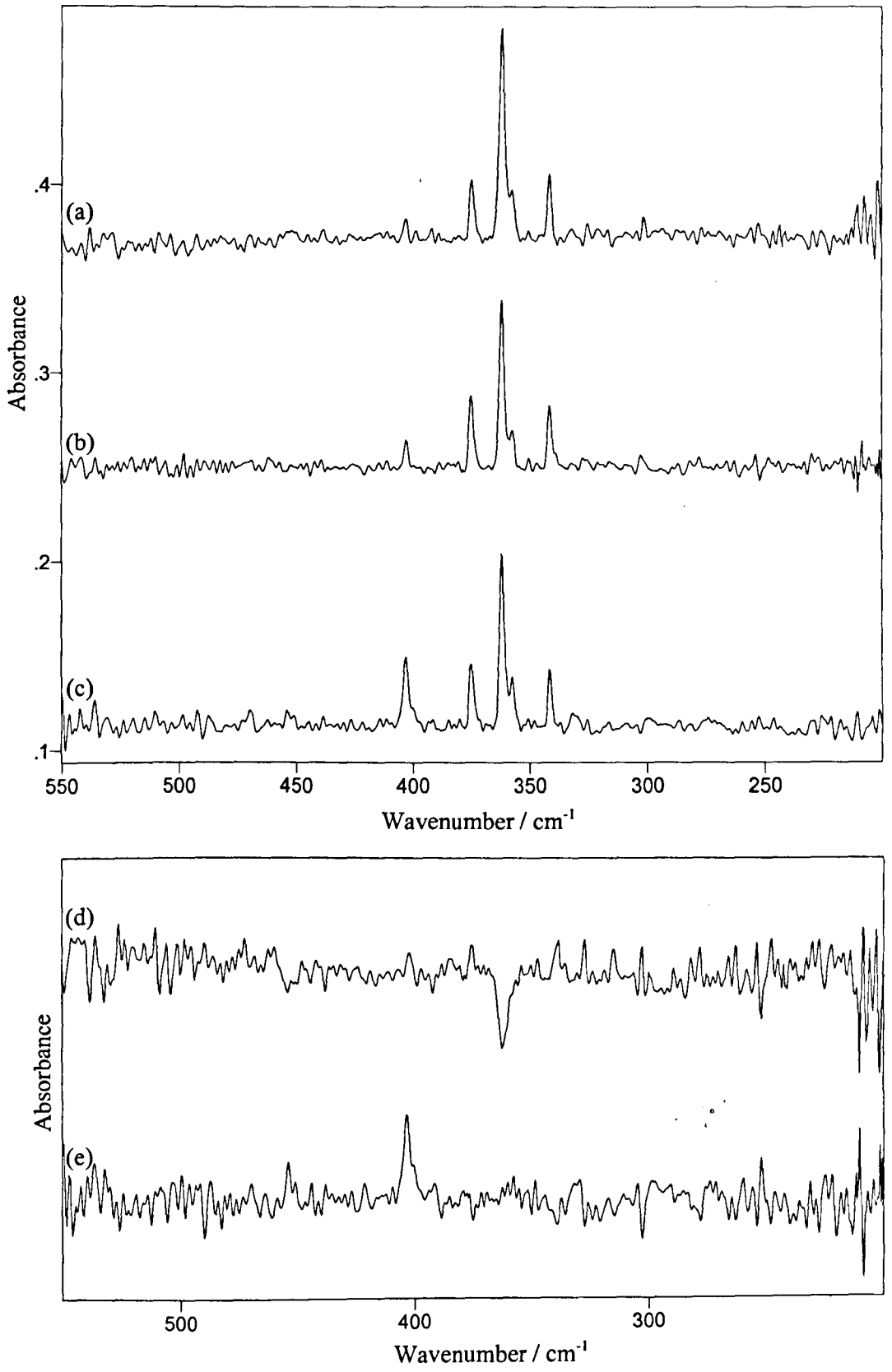

Figure 6.5: far infrared spectrum observed after the isolation of the vapour above heated chromium powder and silver bromide in 1 % CO in argon at 10 K. (a) deposition, (b) at 10 K after annealing to 25 K, (c) after photolysis, (d) subtraction spectrum - (a) from (b), (e) subtraction spectrum (c) from (b)

the presence of multimer species would most probably be increased on annealing, as warming the matrix generally leads to agglomeration and the increase in intensity of dimer and higher multimer bands. In dilute CO matrices warming the matrix should also lead to the formation of new carbonyl complex as the CO molecules interact with other isolated species present. It is therefore likely that as the matrix is annealed the $CrBr_2$ present interacts with the CO to form a chromium carbonyl dibromide complex. This would result in the observed decrease in intensity of the major M-Br vibrational mode which corresponds to the vibrational stretching frequency of an isolated $CrBr_2$ molecule accompanied by an increase in the $\nu_{M\text{-}Br}$ vibrational mode of the carbonyl complex formed. The growth of the other bands suggest they may be the results of an interaction between the isolated molecule and the CO present in the matrix. On photolysis the band at 403.3 and 362.1 cm^{-1} are observed to increase while the other bands show a slight decrease.

In the previous sections exposure to visible and ultraviolet light has been seen to cause interconversion between isomers, but it is also known to decompose carbonyl complexes.[12] It is therefore possible that the two bands at 375.1 and 341.8 cm^{-1} are due to the formation of a carbonyl complex which can be converted or decomposed by photolysis. The increase of the band due to molecular $CrBr_2$ may support the decomposition theory, showing an increase in free $CrBr_2$ as the CO molecules are removed from the complex. However, the continued growth of the band at 403.3 cm^{-1} on photolysis supports the interconversion between isomers, as it is unlikely that this band is due to anything other than a carbonyl complex.

The MIR spectra also shown in figure 6.26, the region 2160 to 2120 cm^{-1} is excluded from the spectral plot as it contains only bands due to the presence of CO and CO-impurity complexes. The MIR spectra confirms this assignment of carbonyl

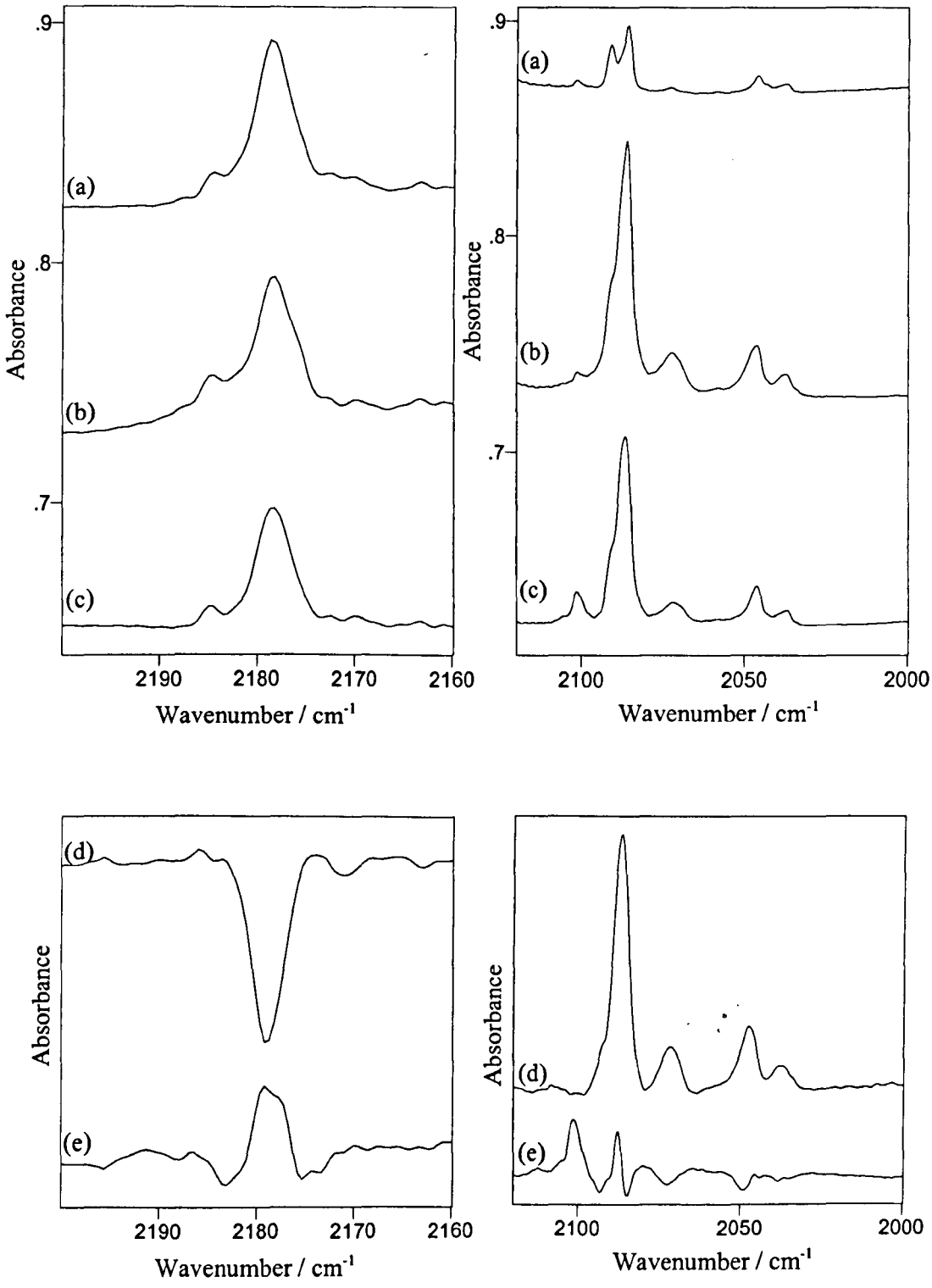

Figure 6.26: mid infrared spectrum observed after the isolation of the vapour above heated chromium powder and silver bromide in 1 % CO in argon at 10 K. (a) deposition, (b) at 10 K after annealing to 25 K, (c) after photolysis, (d) subtraction spectrum - (a) from (b), (e) subtraction spectrum (c) from (b)

complexation, with the band present at high frequency to free CO (2178.6 cm^{-1}) probably arising from the formation of a non-classical carbonyl complex. The previously reported examples of non-classical metal carbonyls still only offer a tentative assignment to the bands occurring at high frequency to molecular CO. The large increase in the band at 2086.2 cm^{-1} on annealing is presumably due to the formation of the carbonyl complex on annealing as CO molecules migrate within the matrix. This band is also observed to undergo a slight reduction in intensity on photolysis.

The MIR spectrum of $CrCl_2$ in dilute CO / argon matrices[3] also identifies the presence of a band at 2188 cm^{-1} which was assigned to presence of a non-classical carbonyl complex of $[Cr(CO)_xCl_2]$, with x most likely being 1. On annealing the growth of a band at 2086 cm^{-1} was noted and assigned as the ν_{CO} mode of the octahedral complex (x = 4). These assignments were based on earlier work[13] in which it was shown that where more than one ν_{CO} mode is present the highest frequency component corresponds to MCl_2 interacting with largest number of CO molecule (except when non-classical carbonyls may be present). It is therefore assumed that the remaining bands at lower frequency must be due to the formation of lower co-ordinated carbonyl complexes. Comparison with figure 6.26 shows a similar pattern in the MIR. For Cr^{II} both octahedral and square planar complexes are known[14] with the study on $CrCl_2$ using EXAFS to show the preference of the formation of the octahedral complex.

The number of ν_{CO} bands present in the MIR can assist in the identification of these species and in this case suggests the formation of octahedral $[Cr(CO)_4Br_2]$ in neat CO matrices. To confirm these assignment experiments involving the use of isotopically enriched CO are required. Unfortunately those experiments may not

clarify the situation either, as the presence of the various CO isotopomers would impede the interpretation required to complete the characterisation. Especially when using ^{12}CO / ^{13}CO mixtures, which often provide the most diagnostic results. Without isotopic data the assignments made are somewhat tentative and based only on the proportionality of the relative band intensity and previous reports.

It is possible therefore that the band present at 2179 cm^{-1} is the ν_{CO} mode of a non-classical carbonyl complex with the weaker band present at higher frequency (2184.5 cm^{-1}) being due to the interaction of $CrBr_2$ with fewer CO molecules. The observation of the presence of the band at 2086 cm^{-1} on annealing can therefore be assigned as due to the presence of the octahedral complex *trans*-$[Cr(CO)_4Br_2]$ with the behaviour of both bands on annealing and photolysis possibly explained on the basis of conversion between classical and non-classical complexes as CO molecules are attached (annealing) and disconnected (photolysis). If the complex formed on annealing is assumed to be the octahedral complex it therefore follows that in an environment where the presence of ligand molecules is at saturation (i.e. in a CO matrix) the most stable, fully co-ordinated complex will form. This allows the tentative assignment of the bands observed in neat CO matrices as the $[Cr(CO)_4Br_2]$ molecule.

Conclusion

The presence of new bands in the FIR spectrum suggests the complexation of isolated $CrBr_2$ molecules with the CO matrix forming a chromium carbonyl dibromide. Analysis of the far and mid infrared spectra of chromium bromide also offer evidence of the formation of a carbonyl complex on annealing which appears to be decomposed on photolysis. Although the number and positioning of the observed

bands is similar to that previously observed for similar transition metal carbonyl halides in neat CO, in particular *trans*-$[Cr(CO)_4Cl_2]$, the assignments made are still tentative at this stage although do appear to be consistent with the formation of *trans*-$[Cr(CO)_4Br_2]$. The use of 1 % CO in argon matrices has identified one major ν_{CO} mode at 2086 cm^{-1} with the presence of other MIR bands in the same region suggesting the formation of lower co-ordinated carbonyl complexes, although these bands show similar behaviour on photolysis as the band assigned to *trans*-$[Cr(CO)_4Br_2]$ and may therefore be related to the same species. A further investigation involving the use of CO isotopes and perhaps even varied concentrations of carbon monoxide in argon are required before the characterisation of the isolated complex as *trans*-$[Cr(CO)_4Br_2]$ can be unambiguously confirmed. Increasing the concentration of CO in the dilute matrices may also assist in the assignments.

The experiments involving the isolation of $CrBr_2$ in isotopically enriched CO matrices which are required to complete the characterisation are currently being undertaken. They are not present in this chapter due to time constraints set on the completion of the study.

Section 6.6: **Conclusion**

The carbonyl complexes formed on isolation of some 3d transition metal bromides in CO containing matrices has been investigated in a continuation of previous work.

The results concur with previous work which identifies the formation of $[Fe(CO)_4Br_2]$, $[Co(CO)_2Br_2]$ and $[Ni(CO)_2Br_2]$ in neat CO matrices after the isolation of the associated metal bromide.[1] One major species is evident for iron (*trans*-$[Fe(CO)_4Br_2]$), but in the case of cobalt and nickel multiple species are thought to be present, with photolysis experiments being used to convert between the tetrahedral and square planar complexes in both cases. In the case of nickel, bands are assigned to both *trans*- and *cis*-$[Ni(CO)_2Br_2]$, whereas cobalt only offers evidence of the formation of *cis*-$[Co(CO)_2Br_2]$ along with the tetrahedral complex. the use of 1 % CO in argon matrices to determine the position of the ν_{CO} mode for the various isomers has been accomplished with moderate success. Although a band in the correct region has been identified in each case, the low intensity of the FIR bands make the assignment to a particular isomer more difficult. As in the original work the isolation of zinc and manganese dibromide has not been found to result in the formation of a classical carbonyl complex.

Chromium dibromide has also been isolated in CO, leading to the formation of a carbonyl compound. At this stage the species is tentatively assigned to *trans*-$[Cr(CO)_4Br_2]$, with experiments using isotopically enriched CO required to confirm this unambiguously. This work was not completed due to the time constraints associated with the period of study.

In each case there is evidence for the formation of non-classical carbonyl complexes. The ν_{CO} modes of these complexes are present at higher frequency than the ν_{CO} modes of the classical carbonyl complexes and are difficult to analyse further due to the presence of CO-impurity complexes.

The values for the ν_{CO} modes of the complexes observed in these experiments are listed in the table below for comparison.

Complex	Observed Wavelength
$[Fe(CO)_4Br_2]$	2101.7 cm^{-1}
$[Ni(CO)_2Br_2]$	2074 cm^{-1}
cis-$[Co(CO)_2Br_2]$	2118.8 cm^{-1}
tet-$[Co(CO)_2Br_2]$	2112.8 cm^{-1}
$[Cr(CO)_4Br_2]$	2086.2 cm^{-1}

Table 6.13: ν_{CO} modes for various carbonyl complexes in a 1 % CO in argon matrix.

Section 6.7: **References**

[1] O. M. Wilkin, *PhD. Thesis,* The University of Hull (1999).

[2] E. W. Robertson, O. M. Wilkin and N. A. Young, *Polyhedron,* **19**, 1493 (2000).

[3] I. R. Beattie, P. J. Jones and N. A. Young, *J. Am. Chem. Soc.,* **114**, 6146 (1992).

[4] L. Andrews, R. T. Arlinghaus and G. L. Johnson, *J. Chem. Phys.,* **78**, 6347 (1983).

[5] S. H. Strauss, *J. Chem. Soc., Dalton Trans.,* **2000**, 1 (2000).

[6] M. D. Haynes, *MChem Report,* The University of Hull (2000).

[7] R. G. Wilkins, *Kinetics and Mechanisms of Reactions of Transition Metal Complexes,* 2nd Edition, VCH, Cambridge (1991).

[8] *For example:* M Goodgame, D. M. L. Goodgame and F. A. Cotton, *J. Am. Chem. Soc.,* **83**, 4161 (1961).

[9] P. D. Gregory and J. S. Ogden, *J. Chem. Soc., Dalton Trans.,* **1995**, 1423 (1995).

[10] J. S. Ogden and R. S. Wyatt, *J. Chem. Soc., Dalton Trans.,* **1987**, 859 (1987).

[11] W. Holzer, W. F. Murphy and H. J. Bernstein, *J. Chem. Phys.,* **52**, 399 (1970).

[12] P. S. Braterman, *Metal Carbonyl Spectra,* Academic Press, London (1975).

[13] R. H. Hauge, S. E. Gransden and J. L. Margrave, *J. Chem. Soc., Dalton Trans.,* **1979**, 745 (1979).

[14] J. Jub, L. F. Lockworthy, D. C. Poveyand G. W. Smith, *Polyhedron,* **8**, 1825 (1989) *and references therein.*

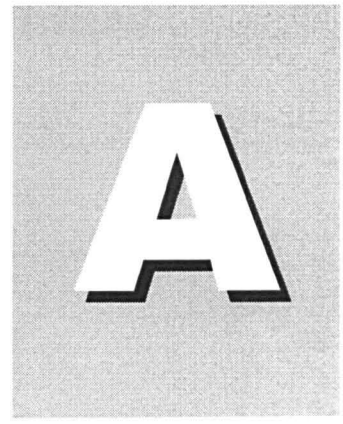

Appendix

Appendix A: **Vacuum Chamber Designs**

a) UV-Vis-NIR Experiments

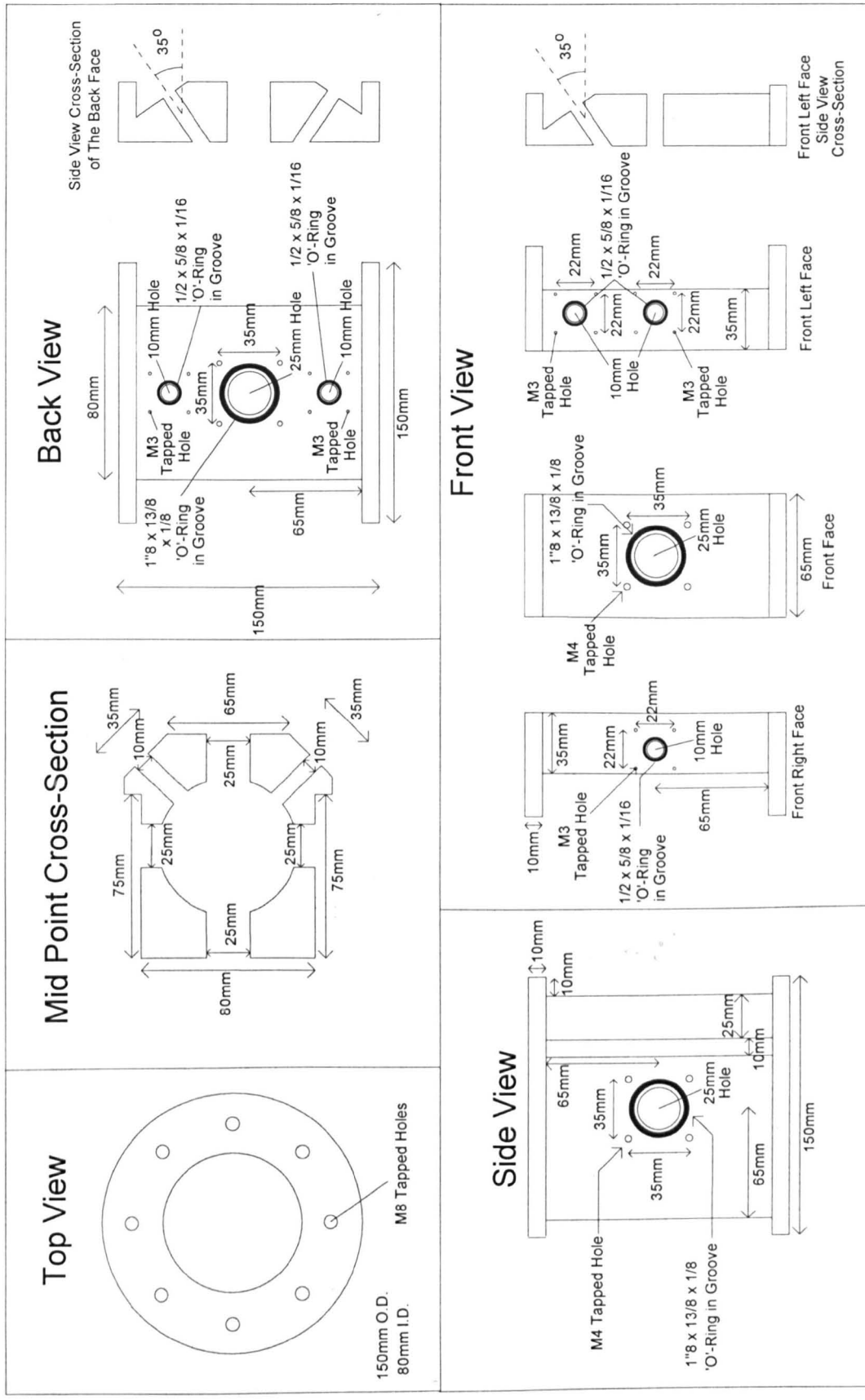

b) FIR at Daresbury Laboratories Station 13.3.